Universidade de Aveiro
2022

Université de Bretagne Sud

Miguel Jorge Guimarães de Oliveira

Efficient Strategies to Speed Up Material Characterization and Parameter Identification for Virtual Forming of Metallic Sheets

Estratégias de Caracterização Material e Identificação de Parâmetros para Conformação Virtual de Chapas Metálicas

Stratégies Efficaces en Caractérisation des Matériaux et Calibration de Modèles Mécaniques pour la Conception Virtuelle des Tôles Métalliques

Universidade de Aveiro
2022

Université de Bretagne Sud

Miguel Jorge Guimarães de Oliveira

Efficient Strategies to Speed Up Material Characterization and Parameter Identification for Virtual Forming of Metallic Sheets

Estratégias de Caracterização Material e Identificação de Parâmetros para Conformação Virtual de Chapas Metálicas

Stratégies Efficaces en Caractérisation des Matériaux et Calibration de Modèles Mécaniques pour la Conception Virtuelle des Tôles Métalliques

Tese em cotutela apresentada à Universidade de Aveiro para cumprimento dos requisitos necessários à obtenção do grau de Doutor em Engenharia Mecânica pela Universidade de Aveiro e *Docteur en Mécanique des Solides, des Matériaux, des Structures et des Surfaces* pela Université de Bretagne Sud, realizada sob a orientação científica do Doutor António Gil D'Orey de Andrade Campos, Professor Auxiliar com Agregação do Departamento de Engenharia Mecânica da Universidade de Aveiro, e da Doutora Sandrine Thuillier, *Professeur des Universités* da Université de Bretagne Sud.

REPÚBLICA PORTUGUESA
CIÊNCIA, TECNOLOGIA E ENSINO SUPERIOR
fct Fundação para a Ciência e a Tecnologia
CENTRO 2020
UNIÃO EUROPEIA Fundo Social Europeu
Région BRETAGNE
ESAFORM
European Commission

o júri

presidente

Doutor Óscar Emanuel Chaves Mealha
Professor Catedrático, Universidade de Aveiro

vogais

Doutor Bertrand Langrand
Diretor de Investigação, Office National d'Etudes et de Recherches Aérospatiales

Doutor Sam Coppieters
Professor Associado, Katholieke Universiteit Leuven

Doutor Luís Filipe Martins Menezes
Professor Catedrático, Universidade de Coimbra

Doutora Gabriela Tamara Vincze
Professora Auxiliar, Universidade de Aveiro

Doutor Robertt Angelo Fontes Valente
Professor Associado, Universidade de Aveiro

Doutora Sandrine Thuillier
Professora Catedrática, Université de Bretagne Sud

Doutor António Gil D'Orey de Andrade Campos
Professor Auxiliar com Agregação, Universidade de Aveiro

agradecimentos

Ao Professor Doutor António Andrade-Campos e à Professora Doutora Sandrine Thuillier, pelo desafio lançado e confiança demonstrada no meu trabalho. A vossa orientação, enorme disponibilidade, compreensão e amizade foram fundamentais para o sucesso deste trabalho. O meu muito obrigado.

A todos aqueles que me acolhem na Universidade de Aveiro desde sempre, o meu sincero agradecimento. Aos colegas do M9'Calibre, por criarem um grupo de trabalho divertido, com importantes momentos de discussão científica e de lazer promovidos. Em especial, ao Doutor João Martins, que desde o primeiro dia foi um constante apoio e exemplo para mim. Agradeço a sua disponibilidade nas nossas discussões que muito contribuiram para o sucesso deste trabalho.

A todos aqueles que me receberam na Université Bretagne Sud, onde realizei uma grande parte deste trabalho. Os períodos vividos em Lorient muito contribuiram para o desenvolvimento deste trabalho, e enorme crescimento pessoal. Em especial, gostaria de agradecer ao Amine Lagroum, à Cynthia Tayeh, e ao Federico Amenini pela amizade desde o primeiro dia. *Merci à tous!*

A todos aqueles que me receberam na Università Politecnica delle Marche, onde tive oportunidade de realizar uma parte deste trabalho. Ao Professor Doutor Marco Rossi e ao Doutor Atillio Lattanzi, a vossa disponibilidade e conhecimento transmitido em muito me enriqueceram. De salientar, também, as experiências vividas e pessoas que conheci durante os três meses em Ancona. Em especial, ao Gabrielle Buratti, colega de casa e amigo, pela amizade e conversas proporcionadas. *Grazie a tutti!*

À Fundação para a Ciência e Tecnologia, pelo apoio financeiro concedido através da bolsa de doutoramento SFRH/BD/143665/2019. Agradeço, também, o apoio financeiro concedido pela associação ESAFORM e pela Région Bretagne durante o período de mobilidade na Università Politecnica delle Marche.

À minha familía, cuja presença é fundamental na minha vida e a quem devo grande parte daquilo que sou como pessoa. Aos meus pais, pelo apoio incondicional e compreensão que só eles conseguem dar. À minha irmã e ao Luís, pela amizade, carinho e compressão. Aos meus sobrinhos, Afonso e Francisca, que são o meu maior orgulho e motivo de enorme felicidade.

À Luísa, por sempre me apoiar e também questionar para que possa tornar-me uma melhor pessoa. A tua força, motivação, e compreensão foram peças essenciais para o sucesso desta etapa.

keywords

constitutive models, inverse methodologies, parameter identification, heterogeneous mechanical tests, optimization algorithms, volume reconstruction

abstract

The mechanical design of sheet metal forming parts tends to be more virtual, reducing delays and manufacturing costs. Reliable numerical simulations can also lead to optimized metallic parts using accurately calibrated advanced constitutive models. Thus, the aim of this thesis is to improve the representation of the mechanical behavior of the material in the numerical model, by developing efficient and accurate methodologies to calibrate advanced constitutive models.

A recent trend in material characterization is the use of a limited number of heterogeneous mechanical tests, which provide more valuable data than classical quasi-homogeneous tests. Yet, the design of the most suitable tests is still an open question. To that extent, an overview of heterogeneous mechanical tests for metallic sheets is provided. However, no standards exist for such tests, so specific metrics to analyze the achieved mechanical states are suggested and applied to four tests. Results show that the use of various metrics provides a good basis to qualitatively and quantitatively evaluate heterogeneous mechanical tests.

Due to the development of full-field measurement techniques, it is possible to use heterogeneous mechanical tests to characterize the behavior of materials. However, no analytical solution exists between the measured fields and the material parameters. Inverse methodologies are required to calibrate constitutive models using an optimization algorithm to find the best material parameters. Most applications tend to use a gradient-based algorithm without exploring other possibilities. The performance of gradient-based and -free algorithms in the calibration of a thermoelastoviscoplastic model is discussed in terms of efficiency and robustness of the optimization process.

Often, plane stress conditions are assumed in the calibration of constitutive models. Nevertheless, it is still unclear whether these are acceptable when dealing with large deformations. To further understand these limitations, the calibration of constitutive models is compared using the virtual fields method implemented in 2D and 3D frameworks. However, the 3D framework requires volumetric information of the kinematic fields, which is experimentally difficult to obtain. To address this constraint, an already existing volume reconstruction method, named internal mesh generation, is further improved to take into account strain gradients in the thickness. The uncertainty of the method is quantified through virtual experiments and synthetic images.

Overall, the impact of this thesis is related to (i) the importance of establishing standard metrics in the selection and design of heterogeneous mechanical tests, and (ii) enhancing the calibration of advanced constitutive models from a 2D to a 3D framework.

palavras chave

modelos constitutivos, metodologias inversas, identificação de parâmetros, ensaios mecânicos heterogéneos, algorimos de otimização, reconstrução volúmica

resumo

O projeto mecânico de peças por conformação de chapas metálicas tende a ser mais virtual, reduzindo atrasos e custos de produção. Simulações numéricas confiáveis também podem levar a peças optimizadas usando modelos constitutivos avançados calibrados com precisão. Assim, o objetivo desta tese é melhorar a representação do comportamento mecânico do material no modelo numérico, através do desenvolvimento de metodologias eficientes e precisas para a calibração de modelos constitutivos avançados.

Uma tendência recente na caracterização de materiais é o uso de um número limitado de ensaios mecânicos heterogéneos, que fornecem dados mais valiosos do que os ensaios clássicos quase-homogéneos. No entanto, a concepção de ensaios mais adequados ainda é uma questão em aberto. Este trabalho detalha os ensaios mecânicos heterogêneos para chapas metálicas. No entanto, não existem ainda normas para estes ensaios, pelo que métricas específicas para analisar os estados mecânicos são sugeridas e aplicadas a quatro ensaios. Os resultados mostram que o uso de várias métricas disponibiliza uma boa base para avaliar ensaios mecânicos heterogéneos.

Devido ao desenvolvimento de técnicas de medição de campo total, é possível utilizar ensaios mecânicos heterogéneos para caracterizar o comportamento dos materiais. No entanto, não existe uma solução analítica entre os campos medidos e os parâmetros do material. Metodologias inversas são necessárias para calibrar os modelos constitutivos usando um algoritmo de otimização para encontrar os melhores parâmetros do material. A maioria das aplicações tende a usar um algoritmo baseado em gradiente sem explorar outras possibilidades. O desempenho de vários algoritmos na calibração de um modelo termoelastoviscoplástico é discutido em termos de eficiência e robustez do processo de otimização.

Frequentemente, são utilizadas condições de estado plano de tensão na calibração de modelos constitutivos, hipótese que é questionada quando se trata de grandes deformações. A calibração de modelos constitutivos é comparada usando o método de campos virtuais implementado em 2D e 3D. No entanto, a implementação 3D requer informações volumétricas dos campos cinemáticos, o que é experimentalmente difícil de obter. Um método de reconstrução volúmica já existente é melhorado para considerar os gradientes de deformação ao longo da espessura. A incerteza do método é quantificada através de ensaios virtuais e imagens sintéticas.

No geral, o impacto desta tese está relacionado com (i) a importância de estabelecer métricas na seleção e concepção de ensaios mecânicos heterogéneos, e (ii) promover desenvolvimentos na calibração de modelos constitutivos avançados de 2D para 3D.

mots clés

modèles de comportement, méthodologies inverses, identification de paramètres, essais mécaniques hétérogènes, algorithmes d'optimisation, reconstruction volumique

résumé

La conception mécanique des pièces métalliques tend à être plus virtuelle, réduisant les délais et les coûts de fabrication. Des simulations numériques fiables peuvent conduire à des pièces optimisées en utilisant des modèles mécaniques avancés calibrés avec précision. Ainsi, l'objectif de cette thèse est d'améliorer la représentation du comportement mécanique du matériau dans le modèle numérique, en développant des méthodologies efficaces et précises pour calibrer des modèles de comportement avancés.

Une tendance récente dans la caractérisation des matériaux est l'utilisation d'un nombre limité d'essais mécaniques hétérogènes, qui fournissent des données plus riches que les essais classiques quasi-homogènes. Pourtant, la conception des tests les plus adaptés reste une question ouverte. Ce travail détaille les essais mécaniques hétérogènes pour les tôles métalliques. Cependant, aucune norme n'existe pour de tels tests, ainsi des métriques spécifiques pour analyser les états mécaniques sont suggérées et appliquées à quatre tests. Les résultats montrent que l'utilisation de diverses métriques fournit une bonne base pour évaluer des essais mécaniques hétérogènes.

L'utilisation des essais mécaniques hétérogènes pour caractériser le comportement des matériaux est rendue possible par des mesures de champ. Cependant, aucune solution analytique n'existe entre les champs mesurés et les paramètres du matériau. Des méthodologies inverses sont nécessaires pour calibrer les modèles de comportement à l'aide d'un algorithme d'optimisation afin de déterminer les meilleurs paramètres de matériau. Un algorithme basé sur le gradient est très fréquemment utilisé, sans explorer d'autres possibilités. La performance de plusieurs algorithmes dans la calibration d'un modèle thermoélastoviscoplastique est discutée en termes d'efficacité et de robustesse du processus d'optimisation.

Souvent, des conditions de contraintes planes sont supposées dans la calibration des modèles, hypothèse qui est remise en cause dans le cas de forte localisation des déformations. La calibration de modèles de comportement est comparée à l'aide de la méthode des champs virtuels développée dans les cadres 2D et 3D. Cependant, le cadre 3D nécessite des informations volumétriques des champs cinématiques, ce qui est expérimentalement difficile à obtenir. Une méthode de reconstruction volumique déjà existante est encore améliorée pour prendre en compte les gradients de déformation dans l'épaisseur. L'incertitude de la méthode est quantifiée par des expériences virtuelles, à l'aide d'images de synthèse.

Dans l'ensemble, l'impact de cette thèse est lié à (i) l'importance d'établir des métriques dans la sélection et la conception d'essais mécaniques hétérogènes, et (ii) à faire progresser la calibration de modèles de comportement avancés d'un cadre 2D à un cadre 3D.

Contents

1 Introduction

1.1 Motivation

The mechanical design of sheet metal forming parts tends to be more and more virtual, by numerical simulation. The sheet metal forming industry is economically driven, so it is only natural that one of their main goals is to decrease associated delays and costs in the manufacturing process. Nevertheless, designing better products and improving their performance by using innovative materials is also crucial (Adams and Askenazi 1999). This is only possible due to the major developments in simulation and computational systems that have allowed every engineer access to, for example, finite element analysis (FEA) software. This leads to the development of many computational tools, some of general application and others tailored for specific tasks. In the scope of sheet metal forming, computational analysis software is meaningless without accurate information on the part being manufactured, ranging from something as simple as the initial blank dimensions to how the material behaves. Generally, industrial processes use phenomenological constitutive models to characterize the material behavior from a macroscopic description (Banabic 2010). Compared to the alternative micromechanical models based on the crystallographic texture of the material, the phenomenological approach is much simpler, easier to implement, and computationally efficient. Their accuracy depends much on the model's ability to reproduce the real behavior under several mechanical states and deformation amplitudes. Advanced phenomenological models can describe multiple phenomena, but require the determination of many material parameters. This leads to exhaustive experiments and complicated methodologies (Yoshida and Uemori 2002; Cazacu et al. 2006; Reyne and Barlat 2022). Therefore, the topic of parameter identification of constitutive models has received increased attention due to the need for reliable input data (Banabic et al. 2020).

Conventionally, the parameters of constitutive models are determined from experimental data acquired by standard mechanical tests, such as uniaxial, biaxial and shear tests (Kuwabara et al. 1998; Boger et al. 2005; Vincze et al. 2005). An advantage of these tests over other methods is the relatively straightforward way to obtain the stress-strain curves required to calibrate constitutive models. These tests generate quasi-homogeneous strain and stress fields, only describing the material behavior for a specific mechanical state, ranging from uniaxial compression to biaxial tension (Oliveira et al. 2022b). Therefore, to characterize the material behavior for different mechanical states, additional tests need to be carried out. For example, to calibrate an advanced plasticity model describing the material anisotropy under various mechanical states, 13 quasi-homogeneous tests are required (Barlat et al. 2005). Moreover, the stress field generated by

these tests does not resemble the multiple mechanical states simultaneously observed in many sheet metal forming processes (Thuillier et al. 2010; Banabic 2010).

Recently, the development of non-contacting full-field measurement techniques has led to advances in experimental testing (Grédiac and Hild 2012). Instead of obtaining a single stress-strain curve out of a mechanical test, these techniques allow the extraction of complete coordinates field from the surface of the specimen, which can then be used to calculate derived quantities, such as displacements or strains. One of the most widespread techniques is the digital image correlation (DIC) technique, which correlates the evolution of a pattern applied to the surface of the specimen (Sutton et al. 2009). Consequently, these advances opened up the opportunity to explore new test configurations, with the goal of obtaining more mechanical data from a single mechanical test (Rossi et al. 2022b). Since then, many so-called heterogeneous mechanical tests have been proposed (Aquino et al. 2019). These tests are distinguished by complex specimen geometries that achieve heterogeneous strain field. In general, the tests are either uniaxial or biaxial loading, with a few exceptions. Moving from homogeneous to heterogeneous mechanical tests will eventually allow the reduction of experiments to characterize a material behavior, as well as improving the quality of the calibrated models (Teaca et al. 2010; Pottier et al. 2011). However, designing heterogeneous tests is a complicated task, proven by the increased complexity of the most recent methodologies to arrive at such geometries (Souto et al. 2017). For example, one test was proposed by using a test simulator to generate synthetic images (Rossi et al. 2016a), and another by using topology optimization (Barroqueiro et al. 2020). The scientific community seems not yet fully convinced of the advantages of heterogeneous mechanical tests. There is a strong need to establish ways to evaluate existing and novel methodologies, as well as clear standards for the so-called "Material Testing 2.0" (Pierron and Grédiac 2021).

Due to the heterogeneity of such tests, it is no longer possible to directly obtain the stress-strain relationship from experimental data. Thus, inverse methodologies to identify the material parameters were developed, where an iterative procedure is employed (Cooreman et al. 2007; Andrade-Campos et al. 2022). Among several inverse methodologies, the most widely used is the finite element model updating (FEMU) since its publication by Kavanagh and Clough (1971). In FEMU, a finite element model of the real test configuration is modeled, and the material parameters are iteratively updated by repeatedly performing a FEA until a close correspondence between numerical simulations and real experiments is achieved. Although this methodology is popular, it incurs high computational effort due to many simulations required. Moreover, having the information of the real boundary conditions may be delicate and is also a drawback of FEMU. As an example, Kacem et al. (2021) has shown the influence of boundary conditions for rupture tests. More recently, the virtual fields method (VFM) has been largely investigated and efficiently used in various applications (Pierron and Grédiac 2012). The VFM is derived from the principle of virtual work (PVW), which is a statement of equations of equilibrium in the weak form. One interesting feature of the VFM is that it directly uses the actual displacement field acquired during the experimental test, and, by means of special virtual fields, it does not require to reproduce the boundary conditions of the real test. An overview of inverse methodologies based on full-field measurements can be found in Avril et al. (2008b), where the authors conclude that the inverse methods are highly sensitive to errors in the experimental data. Martins et al. (2018a) has compared the performance of, among others, the FEMU and the VFM, concluding that the latter provides the best compromise between the final solution and computational effort.

A key feature common to all inverse methodologies is the requirement for an optimization procedure to update the material parameters. A general-purpose optimization algorithm is commonly employed, but as of yet, there is no clear consensus on this topic (Andrade-Campos et al. 2007; de-Carvalho et al. 2011; Kowalewski and Gajewski 2019).

Often, the material behavior of thin sheet metals is conveniently characterized using plane

stress constitutive models (Hill 1990; Vegter and van den Boogaard 2006), provided the specimen thickness is small relative to its width and height. This leads to simplification of identification procedures, such as the use of two-dimensional (2D) instead of three-dimensional (3D) finite element models with the FEMU. Nevertheless, it also leads to considerable improvement in its computational efficiency. However, when dealing with thick plates and necking at large deformations, plane stress assumptions may no longer be valid. Indeed, after necking, a triaxial stress state develops and eventually leads to rupture of the material (Bridgman 1952; Hill 2001). As a result, the hardening behavior beyond the point of diffuse necking is usually extrapolated from the pre-necking information, but can lead to large errors in the predicted stress-strain curve. Moreover, the triaxial state developed in the necking region is not used, but represents rich mechanical information that could improve the material characterization. These limitations and the use of plane stress conditions can also be linked with the limitations of DIC, which only provide the kinematic fields on the surface of the material. An alternative technique, named digital volume correlation (DVC), could potentially reconstruct the 3D kinematic fields over the whole volume (Bay et al. 1999). However, this technique requires highly advanced and costly experimental apparatus and is limited to materials that present a heterogeneous microstructure, such as wood or composites. Moreover, the application of inverse methodologies up to rupture, and in particular the VFM, has not been extensively investigated. A few studies using the VFM in a 2D framework have shown that its validity after necking is violated (Kim et al. 2013; Martins et al. 2021). This means the model does not accurately predict the behavior of the material after necking. Therefore, there is a need and interest in extending the VFM to a 3D framework (Rossi and Pierron 2012a), to provide a more accurate representation of the data.

1.2 Objectives

This thesis deals with the development of efficient and accurate methodologies for robust numerical characterization and proper determination of the material parameters for advanced constitutive models. As already established, this field concerns many topics that need to be addressed to make further advances. Concerning the virtual forming of metallic sheets, the parameter identification of constitutive models can be divided in three pillars, which can be understood as necessary steps of the process: (i) material testing, including the mechanical tests, experimental and numerical techniques to acquire and reconstruct the kinematic fields; (ii) constitutive models, used to describe different phenomena of material behavior; and (iii) inverse methodologies, employed in the identification of the material parameters governing the constitutive models (see Figure 1.1).

In many cases, there are research groups solely dedicated to the development of constitutive models, while other groups are more focused on researching inverse methodologies. Although each of these pillars is often investigated separately, they are not independent and can each contribute to the entire process. The process is a multiplicative system (Farnam Street 2016), which means that if one pillar fails, it will undoubtedly jeopardize the successful outcome of the parameter identification. One could say that the integration of all these pillars is the essence of the "Material Testing 2.0" paradigm. This thesis will not only provide an overview of the field, but will also contribute to each pillar by expanding on current research.

As such, a critical topic is the design of heterogeneous mechanical tests that achieve several mechanical states and a wide range of deformation. To gain a better understanding, an overview of heterogeneous mechanical tests reported in the literature is the starting point. Furthermore, it can still be quite difficult to select the most appropriate test based on qualitative or quantitative metrics. Recently, there have been a few studies that have tackled this problem, but their approaches are mostly quantitative and complex from an implementation point of view. In this thesis, a contribution is made by suggesting standard metrics, based on the strain and stress fields, to qualitatively evaluate the richness of heterogeneous mechanical tests. It is expected that these

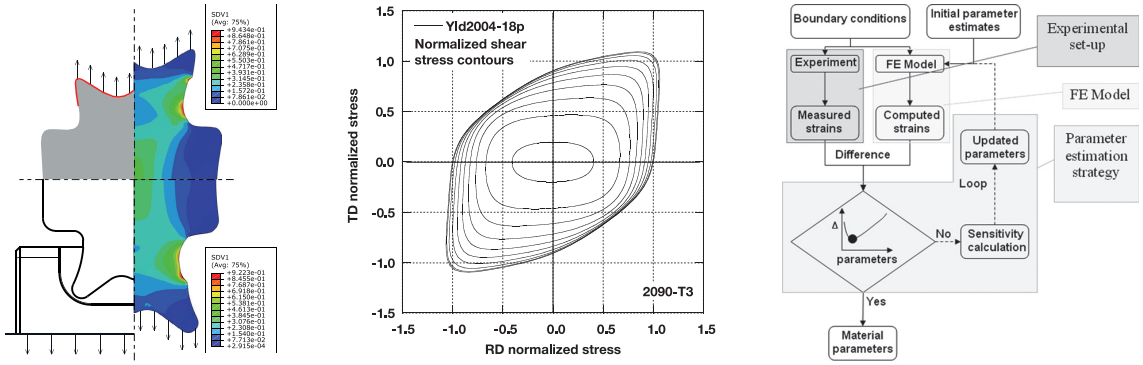

(a) (b) (c)

Figure 1.1 Illustrative images of the three pillars addressed in this thesis: (a) material testing (Aquino et al. 2019), (b) constitutive models (Barlat et al. 2005), and (c) inverse methodologies (Cooreman et al. 2007).

metrics will be used after any experiment or numerical simulations, providing a way to easily compare different studies.

The topic of constitutive models can be further divided in the development and selection of the models. The former is important to accurately describe different material phenomena, and will be crucial for the development of a new generation of materials. However, selecting the correct model to describe a given phenomenon might be as important. A model might be well calibrated, but not adequate to describe the material behavior, leading to unreliable numerical simulations. Therefore, there is a great need in the scientific and industrial communities for indicators and tools that help select constitutive models. Nevertheless, the numerical implementation of constitutive models can be an arduous task, requiring expertise and time. To bridge the gap between selection and implementation, this thesis aims to explore the use of an open source library of constitutive models and contribute to its spread among the scientific community.

A largely developed topic is the use of inverse methodologies, in particular the FEMU and the VFM. While the latter is not yet fully adopted and is restricted to highly specialized research groups, the former is already established in the scientific community. Both methods need an optimization algorithm to find the best material parameters. However, studies tend to use a gradient-based least squares algorithm, or default algorithms in a given programming language, without knowledge of its characteristics. Therefore, this thesis investigates the use of different optimization algorithms within the FEMU. These algorithms are compared regarding their efficiency and robustness. It is expected to contribute to the definition of more efficient optimization strategies.

Perhaps the VFM is the inverse methodology that creates the biggest interest nowadays in the scientific community. The computational efficiency and direct use of experimental data in the identification procedure are its major advantages. Its use within a 2D framework has already been largely investigated, because the VFM is still limited to surface measurements. However, the VFM is not inherently limited, but rather the experimental techniques to acquire volume kinematic fields inside the material. By further developing and proposing new techniques to reconstruct the deformation field inside the material, the use of the VFM in a 3D framework is promoted. Therefore, this thesis aims to contribute to the enhancement of a numerical method able to reconstruct the kinematic fields inside the material. In the future, it is expected to use this method in combination with the VFM to more accurately describe the material behavior up to rupture. Until then, the VFM can be extended to a 3D framework and its use investigated within a numerical approach. By investigating the limitations of the VFM in 2D and 3D frameworks, we can learn more about the VFM and how it can be improved.

1.3 Scientific Contributions

The studies developed during this thesis have led to contributions to scientific and industrial communities through the publication of articles in international journals and conference proceedings. The contributions made as a first author are as follows:

P1. Oliveira MG, Thuillier S, Andrade-Campos A. Analysis of heterogeneous tests for sheet metal mechanical behavior. *Procedia Manufacturing*, 47:831–838, 2020.

P2. Oliveira MG, Martins JMP, Coelho B, Thuillier S, Andrade-Campos A. On the optimization efficiency for the inverse identification of constitutive model parameters. *Proceedings of the 24th International ESAFORM Conference on Material Forming*, Liège, Belgium, 14-16 April, 2021.

P3. Oliveira MG, Thuillier S, Andrade-Campos A. Evaluation of heterogeneous mechanical tests for model calibration of sheet metals. *The Journal of Strain Analysis for Engineering Design*, 57(3):208–224, 2022.

P4. Oliveira MG, Lattanzi A, Thuillier S, Andrade-Campos A, Rossi M. Error estimation of the 3D reconstruction of a displacement field from DIC measurements. *Key Engineering Materials*, 926:2129–2136, 2022.

In addition, the following contributions were made as a second author:

1. Ha GX, Oliveira MG, Andrade-Campos A, Manach PY, Thuillier S. Prediction of coupled 2D and 3D effects in springback of copper alloys after deep drawing. *International Journal of Material Forming*, 14(5):1171–1187, 2021.
2. Andrade-Campos A, Bastos N, Conde M, Gonçalves M, Aquino J, Lourenço R, Martins JMP, Oliveira MG, Prates P, Rumor L. On the inverse identification methods for forming plasticity models using full-field measurements. *IOP Conference Series: Materials Science and Engineering*, 1238:012059, 2022.

Moreover, these contributions would not have been possible without the development of computational tools. Although some parts of the software were based on others, a large part was originally developed in Python and Fortran, combining the accessibility of a modern programming language with the speed and efficiency of one of the oldest. All of these software programs are available open source and are listed as follows:

S1. Unified Material Model Driver for Plasticity
Available at: https://github.com/migueljgoliveira/unified-material-model-driver-for-plasticity

S2. Heterogeneous Tests Post-Processing
Available at: https://github.com/migueljgoliveira/heterogeneous-tests-post-processing

S3. Finite Element Model Updating
Available at: https://github.com/migueljgoliveira/finite-element-model-updating

S4. Internal Mesh Generation
Available at: https://github.com/migueljgoliveira/internal-mesh-generation

S5. Stereo-Vision Simulator
Available at: https://github.com/migueljgoliveira/stereo-vision-simulator

S6. Virtual Fields Method
Available at: https://github.com/migueljgoliveira/virtual-fields-method

1.4 Thesis Outline

This chapter provides an overview of the contents addressed in this thesis. Therefore, every chapter has its own introduction as well as a review of the current state of the art. Including the present chapter, this thesis is divided in eight chapters, which are outlined in Figure 1.2 and organized as follows:

Chapter 1 Introduces the motivation for this thesis by highlighting the latest developments and technological challenges in the field. Enumerates the scientific contributions of this thesis and describes its content.

Chapter 2 Introduces fundamental mathematical concepts applied to the constitutive modeling of elastoplasticity. Several yield criteria and hardening laws used throughout this thesis are presented and mathematically described. Additionally, an open source user subroutine library for plasticity models is presented and its use investigated.

Chapter 3 Presents a literature survey of heterogeneous mechanical tests by focusing on the type and amount of mechanical information provided. Moreover, the tests are classified according to the loading type, either uniaxial, biaxial or other.

Chapter 4 Discusses the use of standard metrics to evaluate heterogeneous mechanical tests. All these metrics are calculated from the stress and strain tensors. A metric named rotation angle is also suggested to evaluate the sensitivity of tests to anisotropy. To illustrate the approach, four heterogeneous mechanical tests are selected from the literature and numerically evaluated through the use of the suggested metrics.

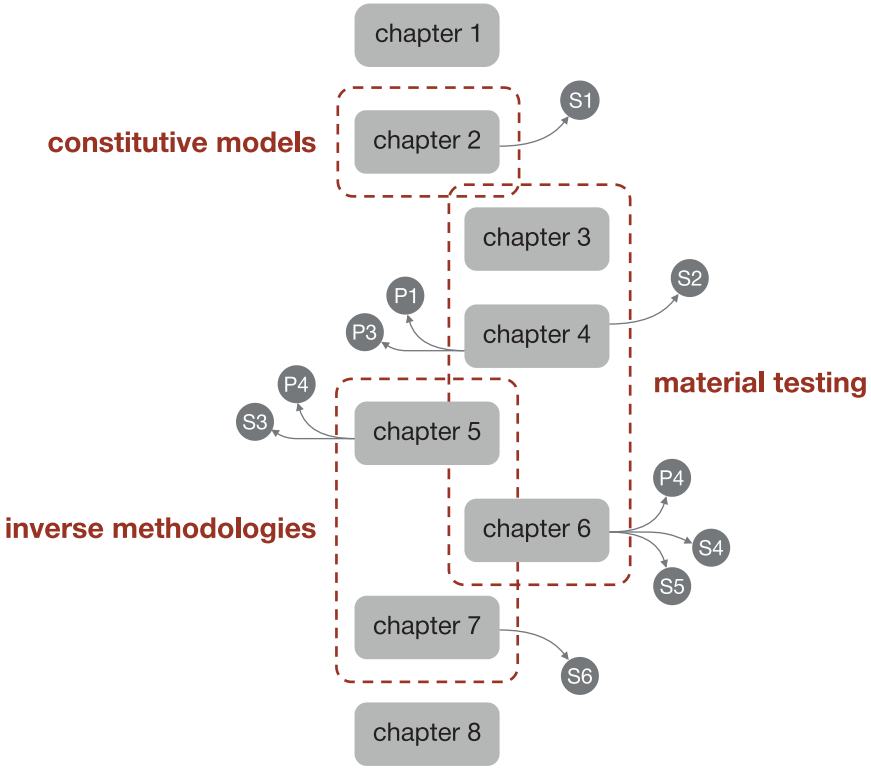

Figure 1.2 Schematic of the thesis structure, including chapters and scientific contributions.

Chapter 5 Compares the use of optimization algorithms, one gradient-based and two gradient-free algorithms, in the inverse identification of constitutive model parameters. To avoid unnecessary implementation and take advantage of highly developed programming languages, the optimization algorithms available in Python's optimization libraries are used. A FEMU based approach is developed and implemented in the calibration of a thermoelastoviscoplastic model. The results are discussed in terms of efficiency and robustness of the optimization process.

Chapter 6 Investigates a numerical method able to reconstruct the volume displacement field inside a flat specimen. This method can potentially enable the material characterization at large deformations and up to rupture. However, its inherent error was not yet fully investigated, and improvements are proposed to address possible sources of error. Moreover, the uncertainty of the method is evaluated through a simulated 3D test and the measurement chain associated with a virtual stereo-DIC system composed of four cameras.

Chapter 7 Extends and investigates the use of VFM in a 3D framework, and compares it with a 2D framework. For that purpose, a code is developed in Python programming language, coupled with its optimization library, and uses an open source user subroutine for the stress reconstruction. The prediction of the load and the identification of the Swift hardening law are analyzed and compared for both frameworks.

Chapter 8 Presents, globally, the main conclusions and contributions of this thesis. Furthermore, outlines some perspectives of potential future developments following the thematics addressed.

2 Constitutive Modeling

2.1 Introduction

Material modeling in mechanics is the description of the mechanical behavior of materials through mathematical models, also known as constitutive models, based on physical and empirical evidence. In practice, the stress tensor acting on a material body is obtained from constitutive models, as a function of the deformation history. For each material, different constitutive models might be required to describe its unique behavior. In fact, a complete characterization of the material behavior might require the description of different phenomena, such as anisotropy, strain hardening behavior, rupture, or Bauschinger's effect (BANABIC ET AL. 2020). Consequently, the development and selection of the constitutive model can play a major role in accurately predicting the material's behavior.

One of the most important phenomena of sheet metal characterization is the anisotropic behavior that some materials exhibit. This phenomenon is mainly related to the crystallographic structure of the materials, which is affected by thermomechanical processes and is characterized by the symmetry of the mechanical properties with respect to three orthogonal planes. The intersection lines of the symmetry planes are the orthotropic axes, and in the case of rolled sheet metals, their orientations are defined as (see Figure 2.1): rolling direction (RD), transverse direction (TD), and normal direction (ND).

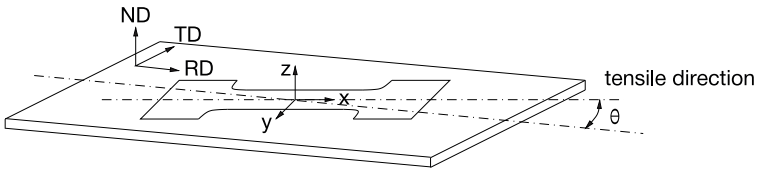

Figure 2.1 Orthotropic axes of rolled sheet metals, respectively, rolling direction (RD), transverse direction (TD), and normal direction (ND). Tensile test specimen represented on the sheet metal at an angle θ from the RD (van den Boogaard 2002).

In sheet metal forming processes, anisotropy can have a big effect on predicting the drawing limits of the sheet. As such, a parameter known as the Lankford strain ratio or coefficient r_θ was introduced to measure the material anisotropy (LANKFORD ET AL. 1950). This parameter is defined as the ratio of the specimen's width strain ε_{yy} to the thickness strain ε_{zz}, along with different material orientations θ as

$$r_\theta = \frac{\varepsilon_{yy}}{\varepsilon_{zz}}. \tag{2.1}$$

When the material demonstrates isotropic behavior, r_θ will be equal to 1 for any value of θ between 0° and 90°. Therefore, in order to quantify the material anisotropic behavior, several uniaxial tensile tests are usually performed with the material at different orientations. The three most common orientations are 0°, 45°, and 90° from the RD.

In sheet metal forming, materials generally present a linear elastic behavior at the initial stages of deformation. However, after a given amount of deformation, the material might undergo irreversible deformations and not recover its initial configuration. In this case, the material has deformed plastically, and the stress-strain relationship is no longer linear. Different phenomena are responsible for governing transition from the elastic to the plastic regime, as well as controlling the deformation.

In the following sections, the theoretical basis of constitutive models adopted throughout this thesis is described. Emphasis is given to the used constitutive models describing each material's mechanical behavior, though many others could have been presented. Afterwards, an open source library of plasticity models is investigated.

2.2 Linear Elasticity

A material body that regains its initial shape after being submitted to an external force is said to be in the elastic regime. In this case, the material body only undergoes elastic deformations (Dunne and Petrinic 2005). It is then possible to determine the material body's linear state of stress through Hooke's law, which corresponds to

$$\boldsymbol{\sigma} = \mathbf{D}\boldsymbol{\varepsilon}^{e} \tag{2.2}$$

where $\boldsymbol{\sigma}$ represents the Cauchy stress tensor, and $\boldsymbol{\varepsilon}^{e}$ is the elastic strain tensor, both defined in the (x, y, z) coordinate system (see Figure 2.1). According to the Voigt notation, this relationship can be rewritten as

$$\begin{bmatrix} \sigma_{xx} \\ \sigma_{yy} \\ \sigma_{zz} \\ \sigma_{xy} \\ \sigma_{xz} \\ \sigma_{yz} \end{bmatrix} = \mathbf{D} \begin{bmatrix} \varepsilon^{e}_{xx} \\ \varepsilon^{e}_{yy} \\ \varepsilon^{e}_{zz} \\ 2\varepsilon^{e}_{xy} \\ 2\varepsilon^{e}_{xz} \\ 2\varepsilon^{e}_{yz} \end{bmatrix}, \tag{2.3}$$

where $\mathbf{D}$ is the elasticity matrix in three dimensions. The elasticity matrix depends on the material's elastic constants, the Young's modulus E and the Poisson's ratio ν, as

$$\mathbf{D} = \frac{E}{(1+\nu)(1-2\nu)} \begin{bmatrix} 1-\nu & \nu & \nu & 0 & 0 & 0 \\ \nu & 1-\nu & \nu & 0 & 0 & 0 \\ \nu & \nu & 1-\nu & 0 & 0 & 0 \\ 0 & 0 & 0 & \frac{1-2\nu}{2} & 0 & 0 \\ 0 & 0 & 0 & 0 & \frac{1-2\nu}{2} & 0 \\ 0 & 0 & 0 & 0 & 0 & \frac{1-2\nu}{2} \end{bmatrix}. \tag{2.4}$$

2.3 Plasticity

An elastoplastic material is characterized by, after a certain level of stress, undergoing irreversible deformations (plasticity). Therefore, the material's behavior is elastic up to an elastic limit, corresponding to the yield stress σ_y, after which the material presents a plastic strain. In the case of metals, made up of many crystals in which atoms are organized regularly, the origin of plasticity is associated with crystal slip. It results that many important phenomena are observed in macroscopic plasticity (DE BORST ET AL. 2012):

1. plastic slip does not lead to volume change, known as the incompressibility condition of plasticity;
2. plastic slip is a shearing process, thus, hydrostatic stress can often be assumed not to influence plastic strain;
3. plastic yielding is often considered an isotropic process.

Experimentally, the stress-strain behavior of an elastoplastic material is classically determined from a uniaxial tensile test, as schematically represented in Figure 2.2.

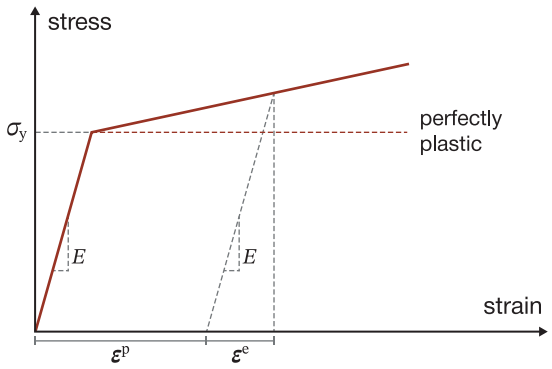

Figure 2.2 Schematic representation of the classical stress-strain relationship of an elastoplastic material from a uniaxial tensile test. The classical additive decomposition of strain into elastic and plastic parts is also represented.

In Figure 2.2, the linear elastic behavior of the material is observed up to σ_y. From this point onward, the material is on the plastic regime. If the stress does not increase further with the increase of strain, it is said the material is perfectly plastic, even though that is usually not the case with sheet metals. On the other hand, when the stress increases with the development of plastic strain, the material undergoes a phenomenon known as strain hardening. If the specimen is unloaded at a given strain in the plastic regime (after the yield stress point), it would cease to deform plastically and present a linear decreasing stress-strain relationship equal to E. Once the stress is zero, the material recovers some strain, known as the elastic strain $\boldsymbol{\varepsilon}^e$, while other remains, known as the plastic strain $\boldsymbol{\varepsilon}^p$. Consequently, the total strain $\boldsymbol{\varepsilon}$ is equal to the sum of the elastic and plastic strains as

$$\boldsymbol{\varepsilon} = \boldsymbol{\varepsilon}^e + \boldsymbol{\varepsilon}^p. \tag{2.5}$$

Equation 2.5 is known as the classical additive decomposition of strain, which is convenient in the definition of mathematical models that, separately, describe the physical phenomena of elasticity and plasticity. Generally, to describe the plastic behavior, a few elements are required:

1. a yield criterion, expressing the relationship between stress components at the onset of plastic yielding;

2. an associated flow rule, expressing the relationship between strain- and stress-rate;
3. a hardening law, describing the evolution of the yield surface with plastic deformation.

2.3.1 Yield Criterion

As mentioned above, the yield criterion expresses the relationship between stress components at the onset of plastic yielding. Consequently, it is also responsible for determining the transition between the elastic and plastic regimes (DE SOUZA NETO ET AL. 2008). Generically, the yield criterion can be defined in an implicit function as

$$\phi(\boldsymbol{\sigma}, \bar{\varepsilon}^{\mathrm{p}}) = \bar{\sigma}(\boldsymbol{\sigma}) - \sigma_{\mathrm{y}}(\bar{\varepsilon}^{\mathrm{p}}) = 0, \tag{2.6}$$

where $\bar{\sigma}$ is the equivalent stress, and $\bar{\varepsilon}^{\mathrm{p}}$ is the equivalent plastic strain governing the hardening behavior. Mathematically, Equation 2.6 represents a surface in the 3D space, known as yield surface, which is necessarily closed, smooth, and convex. Therefore, a given material point is on the plastic regime when $\phi(\boldsymbol{\sigma}, \bar{\varepsilon}^{\mathrm{p}}) = 0$, while $\phi(\boldsymbol{\sigma}, \bar{\varepsilon}^{\mathrm{p}}) < 0$ is associated to the elastic regime. It should be noted that the condition $\phi(\boldsymbol{\sigma}, \bar{\varepsilon}^{\mathrm{p}}) > 0$ is not admissible and has no physical meaning.

Yield criteria can be differentiated for their ability to describe the material anisotropic behavior. On the one hand are the isotropic yield criteria, often used to describe the behavior of a material that behaves similarly in all directions under a given loading state. On the other hand, if the material presents a different behavior depending on the loading direction, it is said to be anisotropic, and specific yield criteria able to describe this behavior are required. Additionally, yield criteria can also be differentiated as micromechanical or phenomenological. The first approach is based on the mechanism of plastic deformation in metallic crystals at the microscopic level, while the latter corresponds to the macroscopic description of the mechanical behavior. Compared to microscopic criteria, the latter are simpler, easier to implement, and lead to computationally efficient numerical simulations. In the field of sheet metal forming, several authors are solely dedicated to the development of novel yield criteria, comprehensively presented in BANABIC (2010). Throughout this thesis, only phenomenological yield criteria are considered, and the ones used are presented.

von Mises

The von Mises isotropic yield criterion was independently proposed by HUBER (1904) and VON MISES (1913), and later developed by HENCKY (1924). The criterion is based on the observation that hydrostatic pressure cannot induce plastic yielding of the material, thus often known as J_2-plasticity. The von Mises yield criterion can be expressed in terms of the deviatoric Cauchy stress tensor $\mathbf{s}$ as

$$\bar{\sigma} = \sqrt{\frac{3}{2}\mathbf{s} : \mathbf{s}}, \tag{2.7}$$

with

$$\mathbf{s} = \boldsymbol{\sigma} - \frac{1}{3}\mathrm{tr}(\boldsymbol{\sigma})\mathbf{I}, \tag{2.8}$$

where $\mathbf{I}$ represents the second order identity tensor, and $\mathrm{tr}(\boldsymbol{\sigma})$ represents the trace of the Cauchy stress tensor. The criterion can be expressed in terms of the normal and shear stress components, and can be written as

$$2\bar{\sigma}^2 = (\sigma_{\mathrm{xx}} - \sigma_{\mathrm{yy}})^2 + (\sigma_{\mathrm{yy}} - \sigma_{\mathrm{zz}})^2 + (\sigma_{\mathrm{zz}} - \sigma_{\mathrm{xx}})^2 + 6(\sigma_{\mathrm{xy}}^2 + \sigma_{\mathrm{xz}}^2 + \sigma_{\mathrm{yz}}^2). \tag{2.9}$$

Hill 1948

The Hill 1948 anisotropic yield criterion was proposed as a generalization of the von Mises criterion (HILL 1948). Because of its simplicity and physical meaning, it is one of the most used yield criterion to describe the anisotropic behavior of metals. It can be expressed as

$$\bar{\sigma}^2 = F(\sigma_{yy} - \sigma_{zz})^2 + G(\sigma_{zz} - \sigma_{xx})^2 + H(\sigma_{xx} - \sigma_{yy})^2 + 2L\sigma_{yz}^2 + 2M\sigma_{xz}^2 + 2N\sigma_{xy}^2, \tag{2.10}$$

where F, G, H, L, M, and N are material-dependent parameters describing the anisotropic behavior. In plane stress conditions ($\sigma_{zz} = \sigma_{xz} = \sigma_{yz} = 0$), the parameters are reduced to F, G, H, and N. These four parameters can also be obtained as a function of the Lankford strain ratios r_0, r_{45}, and r_{90}, respectively, evaluated at 0°, 45°, and 90° from the RD of the sheet metal, according to:

$$F = \frac{r_0}{(1+r_0)r_{90}}; \quad G = \frac{1}{1+r_0}; \quad H = \frac{r_0}{1+r_0}; \quad N = \frac{(r_0+r_{90})(2r_{45}+1)}{2r_{90}(1+r_0)}. \tag{2.11}$$

The Hill 1948 yield criterion reduces to the von Mises yield criterion when $F = G = H = 0.5$ and $L = M = N = 1.5$.

Yld2000-2d

The Yld2000-2d anisotropic yield criterion describes the anisotropic behavior of a material under plane stress conditions (BARLAT ET AL. 2003). It can be expressed as

$$2\bar{\sigma}^a = \left|X_1' - X_2'\right|^a + \left|2X_2'' + X_1''\right|^a + \left|2X_1'' + X_2''\right|^a, \tag{2.12}$$

where a is a material-dependent parameter, usually, assuming the values of 6 or 8, depending on the crystallographic structure of the material, respectively, body-centred cubic (BCC) or face-centred cubic (FCC). X_i' and X_i'' ($i = 1, 2$) are the eigenvalues of the tensors $\mathbf{X}'$ and $\mathbf{X}''$ obtained after two linear transformations on the stress tensor. These transformations can be directly determined from $\boldsymbol{\sigma}$ as

$$\mathbf{X}' = \mathbf{L}'\boldsymbol{\sigma} \quad \text{and} \quad \mathbf{X}'' = \mathbf{L}''\boldsymbol{\sigma}, \tag{2.13}$$

where $\mathbf{L}'$ and $\mathbf{L}''$ are the linear transformation tensors defined as

$$\mathbf{L}' = \begin{bmatrix} L_{11}' \\ L_{12}' \\ L_{21}' \\ L_{22}' \\ L_{66}' \end{bmatrix} = \frac{1}{3} \begin{bmatrix} 2 & 0 & 0 \\ -1 & 0 & 0 \\ 0 & -1 & 0 \\ 0 & 2 & 0 \\ 0 & 0 & 3 \end{bmatrix} \begin{bmatrix} \alpha_1 \\ \alpha_2 \\ \alpha_7 \end{bmatrix}, \tag{2.14}$$

and

$$\mathbf{L}'' = \begin{bmatrix} L_{11}'' \\ L_{12}'' \\ L_{21}'' \\ L_{22}'' \\ L_{66}'' \end{bmatrix} = \frac{1}{9} \begin{bmatrix} -2 & 2 & 2 & -2 & 0 \\ 1 & -4 & -4 & 4 & 0 \\ 4 & -4 & -4 & 1 & 0 \\ -2 & 8 & 2 & -2 & 0 \\ 0 & 0 & 0 & 0 & 0 \end{bmatrix} \begin{bmatrix} \alpha_3 \\ \alpha_4 \\ \alpha_5 \\ \alpha_6 \\ \alpha_8 \end{bmatrix}, \tag{2.15}$$

with α_k ($k = 1, ..., 8$) the anisotropy coefficients representing the material-dependent parameters. It is worth noting that when all coefficients are equal to 1 and $a = 2$, the Yld2000-2d criterion reduces to the von Mises criterion.

Yld2004-18p

The Yld2004-18p is an advanced non-quadratic yield criterion (BARLAT ET AL. 2005) given by

$$4\bar{\sigma}^a = \sum_{i=1}^{3}\sum_{j=1}^{3}\left|\tilde{\mathbf{S}}_i' - \tilde{\mathbf{S}}_j''\right|^a, \tag{2.16}$$

where a is a material-dependent parameter, $\tilde{\mathbf{S}}_i'$ and $\tilde{\mathbf{S}}_j''$ are the principal values of the tensors $\tilde{\mathbf{s}}'$ and $\tilde{\mathbf{s}}''$ defined by two linear transformations on $\mathbf{s}$ as

$$\tilde{\mathbf{s}}' = \mathbf{C}'\mathbf{s} \quad \text{and} \quad \tilde{\mathbf{s}}'' = \mathbf{C}''\mathbf{s}, \tag{2.17}$$

where $\mathbf{C}'$ and $\mathbf{C}''$ are the matrices containing the 18 anisotropy coefficients, with the form of $\mathbf{C}$ as

$$\mathbf{C} = \begin{bmatrix} 0 & -c_{12} & -c_{13} & 0 & 0 & 0 \\ -c_{21} & 0 & -c_{23} & 0 & 0 & 0 \\ -c_{31} & -c_{32} & 0 & 0 & 0 & 0 \\ 0 & 0 & 0 & c_{44} & 0 & 0 \\ 0 & 0 & 0 & 0 & c_{55} & 0 \\ 0 & 0 & 0 & 0 & 0 & c_{66} \end{bmatrix}. \tag{2.18}$$

Similarly to the Yld2000-2d criterion, the exponent a usually assumes the values of 6 or 8, depending on the crystallographic structure of the material, respectively, BCC or FCC (LOGAN AND HOSFORD 1980). When the coefficients are all equal to 1 and $a = 2$ (or 4), the Yld2004-18p yield criterion reduces to the von Mises criterion.

2.3.2 Associated Flow Rule

The associated flow rule is valid in the theory of plasticity for the generality of metallic materials. A plasticity law is said to be associated if the same potential is used to describe the plastic behavior in terms of yield surface and plastic deformation. As the material deforms plastically after the onset of plastic yielding, the normality hypothesis is used to determine the direction of plastic flow. This hypothesis determines that the plastic strain rate $\dot{\boldsymbol{\varepsilon}}^{\mathrm{p}}$ develops in a direction normal to the tangent of the yield surface (see Figure 2.3) and is given by

$$\dot{\boldsymbol{\varepsilon}}^{\mathrm{p}} = \dot{\lambda}\frac{\partial \phi}{\partial \boldsymbol{\sigma}}, \tag{2.19}$$

where the magnitude is determined by the plastic multiplier $\dot{\lambda}$ and the direction by $\partial\phi/\partial\boldsymbol{\sigma}$. The determination of $\dot{\lambda}$ is based on the condition that during plastic loading a given material point remains on the yield surface, also known as the consistency condition.

2.3.3 Hardening Law

The hardening law regulates the evolution of the yield surface after the onset of plastic yielding according to the evolution of plastic deformation as a function of the equivalent plastic strain $\bar{\varepsilon}^{\mathrm{p}}$. The yield surface evolution is usually associated with three types of hardening laws (see Figure 2.4):

1. isotropic hardening;
2. kinematic hardening;
3. mixed hardening.

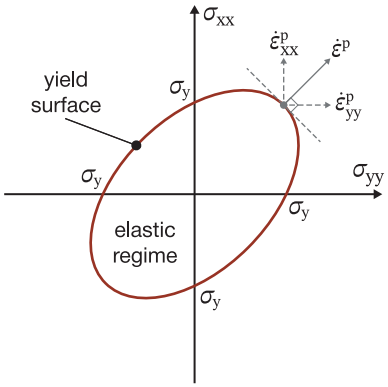

Figure 2.3 Schematic representation of the von Mises yield surface in the principal stress space for plane stress conditions. The plastic strain rate is represented in a normal direction to the tangent of yield surface.

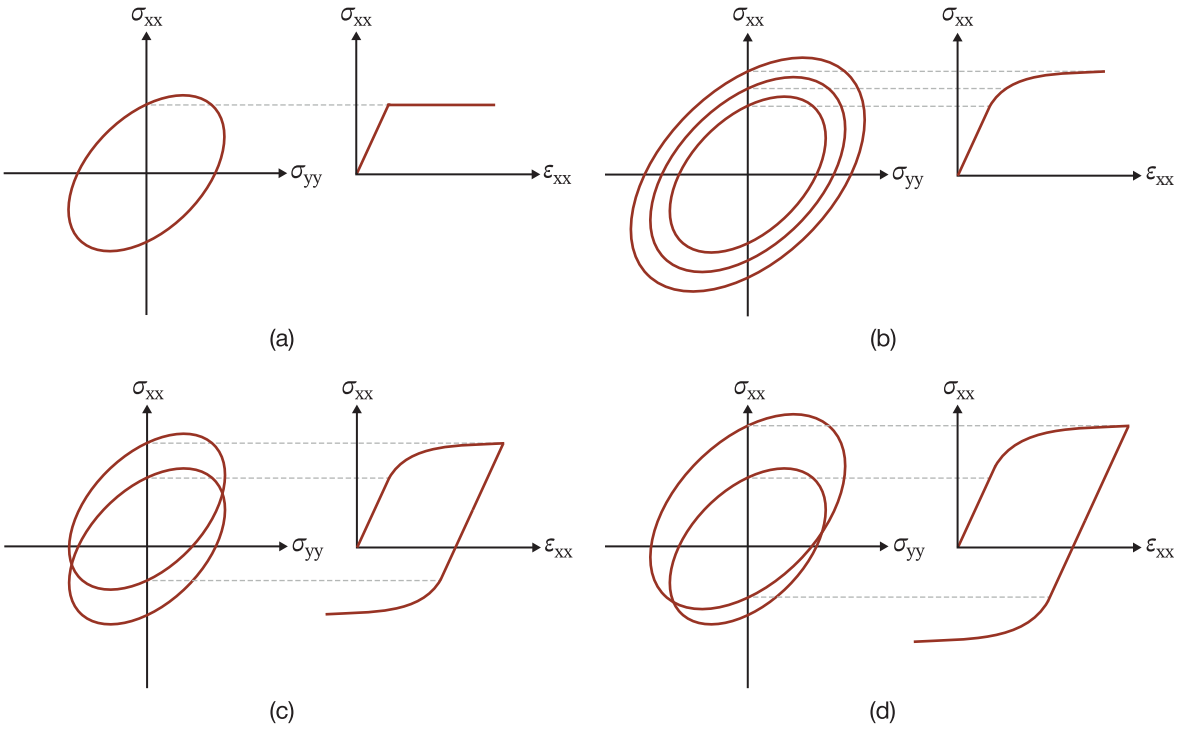

Figure 2.4 Schematic representation of the evolution of the von Mises yield surface and stress-strain relationship (a) without strain hardening, and for different types of hardening: (b) isotropic hardening, (c) kinematic hardening, and (d) mixed hardening.

In isotropic hardening, the development of plastic deformation results exclusively from the uniform expansion of the yield surface in all directions, while its center is kept fixed throughout the loading path. On the other hand, in kinematic hardening, the development of plastic deformation results only from the translation of the yield surface in the stress space. Lastly, in mixed hardening, the development of plastic deformation combines both isotropic and kinematic hardening laws, leading to simultaneous expansion and translation of the yield surface.

Many models exist to describe the isotropic hardening behavior of metallic materials (such as Ludwick). One of the most known and used models is the Swift's law, given as

$$\sigma_y = K(\varepsilon_0 + \bar{\varepsilon}^p)^n, \tag{2.20}$$

with

$$\varepsilon_0 = \left(\frac{\sigma_0}{K}\right)^{\frac{1}{n}}, \tag{2.21}$$

where K, ε_0, n, and σ_0 are material-dependent parameters, respectively, the strength coefficient, the initial yield strain, the strain-hardening exponent, and the initial yield stress.

Another well known isotropic hardening law is the Voce's law, given as

$$\sigma_y = \sigma_0 + Q[1 - \exp(-b\bar{\varepsilon}^p)], \tag{2.22}$$

where Q and b are material-dependent parameters.

The Johnson-Cook model can describe the hardening behavior of metals under various temperatures and strain rates (Johnson and Cook 1983). A decoupled formulation characterizes the model, because it describes the yield stress evolution by taking into account strain hardening, temperature, and strain rate effects as independent phenomena. The model can be written as

$$\sigma_y = [A + B(\bar{\varepsilon}^p)\, n]\left[1 - \left(\frac{T - T_{tr}}{T_m - T_{tr}}\right)^m\right]\left[1 + C\ln\left(\frac{\dot{\bar{\varepsilon}}^p}{\dot{\varepsilon}_0}\right)\right], \tag{2.23}$$

where A, B, and n are material-dependent parameters describing the strain hardening behavior. The effects of temperature are described by the temperature T, the transition temperature T_{tr} (governing the threshold of temperature effect), the melting temperature T_m, and the exponent m. Lastly, the strain rate sensitivity is described by the parameters C and $\dot{\varepsilon}_0$, defining the threshold of strain rate dependence.

Kinematic hardening is typically used to predict the Bauschinger effect, often observed in materials subject to cyclic loading. Also, when considering mixed hardening, the generic yield function from Equation 2.6 takes the form of

$$\phi(\boldsymbol{\sigma}, \boldsymbol{\alpha}, \bar{\varepsilon}^p) = \bar{\eta}(\boldsymbol{\sigma} - \boldsymbol{\alpha}) - \sigma_y(\bar{\varepsilon}^p) = 0, \tag{2.24}$$

where $\bar{\eta}$ is the equivalent stress as a function of the tensor $\boldsymbol{\eta} = \boldsymbol{\sigma} - \boldsymbol{\alpha}$. The back stress tensor $\boldsymbol{\alpha}$ describes the kinematic hardening and is defined in the stress space analogously to the stress tensor. To account for the need to describe the hardening behavior under cyclic loading, several models have been proposed, such as by Prager (1955), Ziegler (1959), or the more advanced by Yoshida and Uemori (2002).

The kinematic hardening model considered in this study is based on the additive contribution of several back stress terms as proposed by Chaboche (1986), following a modification of the model originally proposed in 1966 by Frederick and Armstrong (2007). This model defines the evolution of the back stress tensor $\dot{\boldsymbol{\alpha}}$ as

$$\dot{\boldsymbol{\alpha}} = \sum_{i=1}^{n} \dot{\boldsymbol{\alpha}}_i = \sum_{i=1}^{n} \left(\frac{2}{3} c_i \dot{\boldsymbol{\varepsilon}}^p - \gamma_i \boldsymbol{\alpha}_i \dot{\bar{\varepsilon}}^p\right), \tag{2.25}$$

where c_i and γ_i ($i = 1, ..., n$) are material-dependent parameters, $\dot{\boldsymbol{\varepsilon}}^p$ is the plastic strain rate (see Equation 2.19) and $\dot{\bar{\varepsilon}}^p$ is the equivalent plastic strain rate. Additionally, this model has also been formulated based on the stress tensor as

$$\dot{\boldsymbol{\alpha}} = \sum_{i=1}^{n} \dot{\boldsymbol{\alpha}}_i = \sum_{i=1}^{n} \left(\frac{c_i}{\bar{\eta}} \boldsymbol{\eta} - \gamma_i \boldsymbol{\alpha}_i\right) \dot{\bar{\varepsilon}}^p. \tag{2.26}$$

According to Carbonnière et al. (2009), this formulation leads to an uncoupling between the initial anisotropy and the hardening behavior, which is not the case when using the original formulation based on the plastic strain tensor.

2.4 Unified Material Model Driver for Plasticity

The Unified Material Model Driver for Plasticity (UMMDp) was developed by the Japan Association for Nonlinear Computer Aided Engineering (JANCAE)[1] It is an open source user subroutine library for plasticity models that supports various anisotropic yield criteria, isotropic and kinematic hardening laws. Moreover, it is compatible with several FEA software: Abaqus/Standard, ANSYS, ADINA, LS-DYNA, and MARC (see Figure 2.5). The structure of the UMMDp is modular, flexible, and relatively easy for any user to implement their own models into the library. Although this library could have a huge potential, few validations are reported, and none outside the original contributions are found yet (Takizawa et al. 2018; Oide et al. 2018; Inoue et al. 2018; Ida et al. 2018).

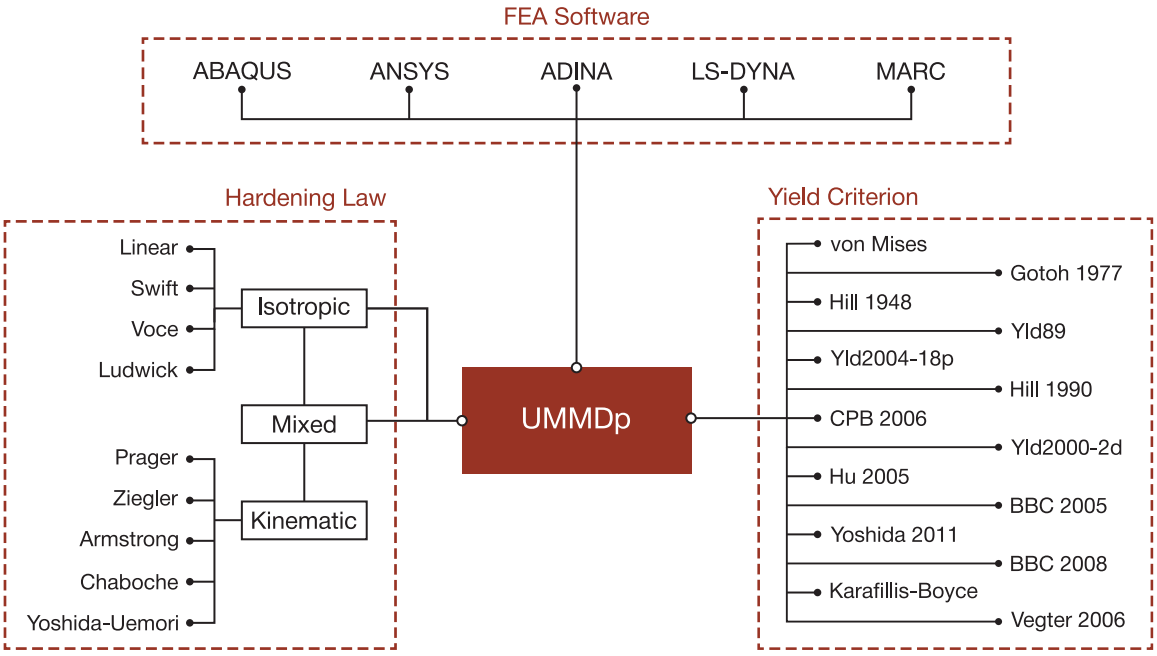

Figure 2.5 Framework of the UMMDp, including the compatible FEA software, the yield criteria and hardening laws.

With this study, it was intended to start exploring the capabilities of the UMMDp, as well as validate its use with Abaqus/Standard (Dassault Systèmes 2019). To validate a few models, a user material subroutine (UMAT), developed for Abaqus/Standard in the scope of previous doctoral theses, is used as a reference (Grilo et al. 2013; Grilo 2015; Souto 2015). This UMAT implements the Yld2004-18p anisotropic yield criterion, various isotropic hardening laws, and the non-linear kinematic hardening law composed of three back stress terms from Equation 2.26. This UMAT has already been successfully used in the identification of material parameters (Grilo et al. 2016; Souto et al. 2015b; Pradeau et al. 2016), thus constitutes a reliable reference in the validation of the UMMDp. For simplicity, the latter UMAT is hereon designated as UMAT_Yld2004_Mixed. Nevertheless, the built-in constitutive models provided by Abaqus/Standard are used as a second reference, hereon designated as Std_Aba.

Initially, the implementation of the Yld2004-18p anisotropic yield criterion is discussed by analyzing differences between the formulation in the UMMDp and the UMAT_Yld2004_Mixed.

[1]The JANCAE, a non-profit organization, has held lectures twice a year for four days each since 2001 to provide training on theories and technology related to nonlinear simulation for researchers and engineers engaged in various computer-aided engineering (CAE) businesses. Since 2009, as one of the subcommittee activities, it has developed and verified the user subroutine library the UMMDp (https://www.jancae.org/annex/annexUMMDe/index.html).

Afterwards, FEA simulations of homogeneous tests and a deep drawing cup test are performed to validate the UMMDp and analyze its computational efficiency.

2.4.1 Formulation of Yld2004-18p

Concerning the formulation of the Yld2004-18p anisotropic yield criterion implemented in the UMMDp and the UMAT_Yld2004_Mixed, there are two important details to discuss: (i) the order of the anisotropy coefficients, and (ii) the formulation of the yield criterion. Firstly, it is important to note that in the formulation of Yld2004-18p in the UMMDp, the order of the anisotropy coefficients differs from the one in the original formulation (see Equation 2.18). This difference is related to the Voigt notation of the Cauchy stress tensor, which is given by (σ_{xx}, σ_{yy}, σ_{zz}, σ_{yz}, σ_{xz}, σ_{xy}) in the original formulation and by (σ_{xx}, σ_{yy}, σ_{zz}, σ_{xy}, σ_{yz}, σ_{xz}) in the UMMDp, while the formulation in the UMAT_Yld2004_Mixed is known to be the same as in the original formulation. This difference in the Voigt notation changes the order of the anisotropy coefficients c_{44}, c_{55}, and c_{66} as

$$\underbrace{\begin{Bmatrix} c_{66} \\ c_{44} \\ c_{55} \end{Bmatrix}}_{\text{Barlat et al. (2005)}} \equiv \underbrace{\begin{Bmatrix} c_{44} \\ c_{55} \\ c_{66} \end{Bmatrix}}_{\text{UMMDp}} \equiv \underbrace{\begin{Bmatrix} c_{66} \\ c_{44} \\ c_{55} \end{Bmatrix}}_{\text{UMAT\_Yld2004\_Mixed}} . \tag{2.27}$$

Secondly, in the original formulation of the yield criterion, the value 4 in the left hand side of Equation 2.16 is constant. However, in the formulation of the UMMDp, this value takes the form of a coefficient R, herein named coefficient of equivalent stress, and defined as

$$R\bar{\sigma}^a = \sum_{i=1}^{3}\sum_{j=1}^{3} \left|\tilde{\mathbf{S}}_i' - \tilde{\mathbf{S}}_j''\right|^a . \tag{2.28}$$

In the UMMDp, the coefficient depends on the values of the material parameters c_{12}, c_{13}, c_{21}, c_{23}, c_{31}, and c_{32}, and is computed according to

$$R = \sum_{i=1}^{3}\sum_{j=1}^{3} \left|B_i' - B_j''\right|^a , \tag{2.29}$$

with

$$\begin{aligned}
B_1 &= 2\sqrt{p}\cos\left(\frac{\theta}{3}\right) + H_1, \\
B_2 &= 2\sqrt{p}\cos\left(\frac{\theta + 4\pi}{3}\right) + H_1, \\
B_3 &= 2\sqrt{p}\cos\left(\frac{\theta + 2\pi}{3}\right) + H_1, \\
p &= H_1^2 + H_2, \\
q &= \frac{1}{2}\left(2H_1^3 + 2H_1H_2 + 2H_3\right), \\
\theta &= \arccos\left(\frac{q}{p^{3/2}}\right), \\
H_1 &= \frac{1}{9}\left(c_{12} + c_{13} + c_{23} - 2c_{21} + c_{32} - 2c_{31}\right), \\
H_2 &= \frac{1}{27}\left[\left(c_{23} - 2c_{21}\right)\left(c_{32} - 2c_{31}\right) + \left(c_{32} - 2c_{31}\right)\left(c_{12} + c_{13}\right) + \left(c_{12} + c_{13}\right)\left(c_{23} - 2c_{21}\right)\right], \\
H_3 &= \frac{1}{54}\left(c_{12} + c_{13}\right)\left(c_{23} - 2c_{21}\right)\left(c_{32} - 2c_{31}\right).
\end{aligned} \tag{2.30}$$

The latter set of equations was deduced from the source code files of the UMMDp. The scientific background for this formulation is not documented, but it appears to be related to assuming σ_y as the yield stress in the RD. This assumption can be imposed by the following condition as

$$\frac{\sigma_{xx}}{\bar{\sigma}} = \left(\frac{3^a R}{\xi}\right) = 1, \tag{2.31}$$

where ξ depends on the anisotropy coefficients as

$$\begin{aligned}\xi = &|c'_{12} + c'_{13} - c''_{12} - c''_{13}|^a + |c'_{12} + c'_{13} + 2c''_{21} - c''_{23}|^a + |c'_{12} + c'_{13} - 2c''_{31} - c''_{32}|^a \\ &+ |c'_{23} - 2c'_{21} - c''_{12} - c''_{13}|^a + |c'_{23} - 2c'_{21} + 2c''_{21} - c''_{23}|^a + |c'_{23} - 2c'_{21} + 2c''_{31} - c''_{32}|^a \\ &+ |c'_{32} - 2c'_{31} - c''_{12} - c''_{13}|^a + |c'_{32} - 2c'_{31} + 2c''_{21} - c''_{23}|^a + |c'_{32} - 2c'_{31} + 2c''_{31} - c''_{32}|^a .\end{aligned} \tag{2.32}$$

According to Equation 2.16, for a given set of material parameters with $R = 4$, it is not guaranteed that Equation 2.31 is satisfied. In the formulation of the UMMDp, the value of R can be calculated from the material parameters, thus satisfying Equation 2.31. This approach is more practical in terms of the identification procedure, as it reduces the number of externally imposed constraints. For example, Güner et al. (2012) and Martins et al. (2019) both used such constraint in the identification of the material parameters of the Yld2000-2d yield criterion, to obtain σ_y as the yield stress in the RD.

To validate this assumption, a comparison between both formulations is performed with $\sigma_{xx} = 100$ MPa, and the material parameters reported by Souto et al. (2015b) presented in Table 2.1, with the exponent a equal to 6. The obtained results are presented in Table 2.2, where it is observed that in the original formulation of the yield criterion, Equation 2.31 is not satisfied, whereas in the formulation of the UMMDp it is, with $R = 4.215$. Although the formulation of the UMMDp calculates R, it is possible to manually assign its value to 4. Therefore, to fairly compare the UMMDp with the UMAT_Yld2004_Mixed, the constant value of 4 is adopted in all the following analysis.

Additionally, the order of the anisotropy coefficients in $\mathbf{C}'$ and $\mathbf{C}''$ is analyzed with a simple validation test. A prescribed stress tensor $\boldsymbol{\sigma}$ is given as input to the yield criterion, and the

Table 2.1 Material parameters for the Yld2004-18p yield criterion used in the verification of the coefficient of equivalent stress (Souto et al. 2015b). All parameters are dimensionless.

	Parameter								
Term	c_{12}	c_{13}	c_{21}	c_{23}	c_{31}	c_{32}	c_{44}	c_{55}	c_{66}
$\mathbf{C}'$	1.264	0.974	1.242	1.049	0.579	0.708	1.000	1.000	1.365
$\mathbf{C}''$	0.792	0.672	0.838	0.929	0.996	0.768	1.000	1.000	0.678

Table 2.2 Comparison of the Yld2004-18p anisotropic yield criterion formulation between the original formulation and the UMMDp, under uniaxial tensile loading.

	Formulation	
Parameter	Barlat et al. 2005	UMMDp
ξ [–]	3072.416	3072.416
R [–]	4.000	4.215
$\sigma_{xx}/\bar{\sigma}$ [–]	0.991	1.000
$\bar{\sigma}$ [MPa]	100.875	100.000

resulting equivalent stress $\bar{\sigma}$, first and second derivatives of the yield criterion represented by, respectively, $\partial\phi/\partial\boldsymbol{\sigma}$ and $\partial^2\phi/(\partial\boldsymbol{\sigma})^2$, are analyzed. By manually prescribing a stress tensor as input to the yield criterion, it is possible to successfully compare its formulation. However, when running a numerical simulation with a FEA software, the input is more difficult to control, and it would be equal to both the UMAT_Yld2004_Mixed and the UMMDp. The material parameters used in this verification are presented in Table 2.3, according to the values reported for the material 6111-T4 by Barlat et al. (2005), with $a = 8$.

Table 2.3 Set of Yld2004-18p material parameters used in the verification of the coefficients order (Barlat et al. 2005). All parameters are dimensionless.

	Parameter								
Term	c_{12}	c_{13}	c_{21}	c_{23}	c_{31}	c_{32}	c_{44}	c_{55}	c_{66}
$\mathbf{C}'$	1.241	1.078	1.216	1.223	1.093	0.889	0.501	0.557	1.349
$\mathbf{C}''$	0.775	0.922	0.765	0.793	0.918	1.027	1.115	1.112	0.589

In Table 2.4, the prescribed input stress tensor and the results of first and second derivatives of both the UMAT_Yld2004_Mixed and the UMMDp, with and without modifications, are presented. In all formulations, the order of the anisotropy coefficients is maintained according to Equation 2.31. Nevertheless, the position of the prescribed stress tensor out-of-plane components

Table 2.4 Comparison of the first and second derivatives of the yield criterion, for a given stress tensor, for the UMAT_Yld2004_Mixed and the UMMDp, with and without modifications. The highlighted values correspond to the differences between formulations.

	Input	**Output**	
Formulation	σ [MPa]	$\frac{\partial\phi}{\partial\sigma}$ [–]	$\frac{\partial^2\phi}{(\partial\sigma)^2}$ [–]
UMAT_Yld2004_Mixed	$\begin{bmatrix} -149 \\ -5 \\ 35 \\ -12 \\ -19 \\ 204 \end{bmatrix}$	$\begin{bmatrix} -0.632 \\ 0.266 \\ 0.366 \\ -0.168 \\ -0.120 \\ 1.205 \end{bmatrix}$	$\begin{bmatrix} 0.004 & -0.002 & -0.001 & 0.000 & 0.000 & 0.003 \\ -0.002 & 0.003 & -0.001 & 0.001 & 0.000 & -0.001 \\ -0.001 & -0.001 & 0.002 & 0.000 & 0.000 & -0.001 \\ 0.000 & 0.001 & 0.000 & 0.017 & -0.002 & 0.001 \\ 0.000 & 0.000 & 0.000 & -0.002 & 0.008 & 0.000 \\ 0.003 & -0.001 & -0.001 & 0.001 & 0.000 & 0.002 \end{bmatrix}$
UMMDp			
without modification	$\begin{bmatrix} -149 \\ -5 \\ 35 \\ -12 \\ 204 \\ -19 \end{bmatrix}$	$\begin{bmatrix} -0.632 \\ 0.266 \\ 0.366 \\ -0.168 \\ 1.205 \\ -0.120 \end{bmatrix}$	$\begin{bmatrix} 0.004 & -0.002 & -0.001 & 0.000 & 0.003 & 0.000 \\ -0.002 & 0.003 & -0.001 & 0.001 & -0.001 & 0.000 \\ -0.001 & -0.001 & 0.002 & 0.000 & -0.001 & 0.000 \\ 0.000 & 0.001 & 0.000 & 0.017 & 0.001 & -0.002 \\ 0.003 & -0.001 & -0.001 & 0.001 & 0.002 & 0.000 \\ 0.000 & 0.000 & 0.000 & -0.002 & 0.000 & 0.008 \end{bmatrix}$
with modification	$\begin{bmatrix} -149 \\ -5 \\ 35 \\ -12 \\ -19 \\ 204 \end{bmatrix}$	$\begin{bmatrix} -0.632 \\ 0.266 \\ 0.366 \\ -0.168 \\ -0.120 \\ 1.205 \end{bmatrix}$	$\begin{bmatrix} 0.004 & -0.002 & -0.001 & 0.000 & 0.000 & 0.003 \\ -0.002 & 0.003 & -0.001 & 0.001 & 0.000 & -0.001 \\ -0.001 & -0.001 & 0.002 & 0.000 & 0.000 & -0.001 \\ 0.000 & 0.001 & 0.000 & 0.017 & -0.002 & 0.001 \\ 0.000 & 0.000 & 0.000 & -0.002 & 0.000 & 0.002 \\ 0.003 & -0.001 & -0.001 & 0.001 & 0.000 & 0.008 \end{bmatrix}$

σ_{xz} and σ_{yz} had to be changed using the UMMDp without modification, to obtain the same value of equivalent stress ($\bar{\sigma} = 355.769$) as the UMAT_Yld2004_Mixed. However, by changing the order of σ_{xz} and σ_{yz}, it led to differences in the first and second derivatives out-of-plane components. These differences are not in terms of values, but rather in terms of the positions at which they appear, which are consistent with the positions σ_{xz} and σ_{yz} in the prescribed stress tensor.

Although the latter situation is not documented in the UMMDp, it is understood that the formulation used in the yield criterion cannot be the same for each software for which the UMMDp is prepared for, as shown in Table 2.5 that there are two different orders of Voigt notation used by the software. Abaqus/Standard (Dassault Systémes 2014) and ADINA (ADINA R&D 2021) share the first type of notation, while LS-DYNA (Livermore Software Technology 2021), ANSYS (ANSYS, Inc. 2021) and MARC share the second. Because the software used in this study is Abaqus/Standard, the formulation of the yield criterion in the UMMDp is modified according to the Voigt notation of the stress tensor used in this FEA software (σ_{xx}, σ_{yy}, σ_{zz}, σ_{xy}, σ_{xz}, σ_{yz}), resulting in a new relation of the anisotropy coefficients c_{44}, c_{55} and c_{66} as

$$\left\{\begin{matrix} c_{44} \\ c_{55} \\ c_{66} \end{matrix}\right\}_{\text{Barlat et al. 2005}} \equiv \left\{\begin{matrix} c_{44} \\ c_{55} \\ c_{66} \end{matrix}\right\}_{\text{UMMDp}} \equiv \left\{\begin{matrix} c_{44} \\ c_{55} \\ c_{66} \end{matrix}\right\}_{\text{UMAT\_Yld2004\_Mixed}} . \tag{2.33}$$

With the modification applied to the yield criterion in the UMMDp, the results of equivalent stress, first and second derivatives are now identical for the UMAT_Yld2004_Mixed and the UMMDp (see Table 2.4). Therefore, the modification is validated and maintained in all subsequent analyses. It is recommended that the Voigt notation be verified for the other yield criteria implemented in the UMMDp, taking into account the software to be used. In addition, future modifications to the UMMDp can include an automatic detection of the software and change the Voigt notation accordingly.

Table 2.5 Convention of Voigt notation for each finite element software prepared for the UMMDp.

Software	Voigt notation
ABAQUS/Standard	σ_{xx} σ_{yy} σ_{zz} σ_{xy} σ_{xz} σ_{yz}
ADINA	σ_{xx} σ_{yy} σ_{zz} σ_{xy} σ_{xz} σ_{yz}
LS-DYNA	σ_{xx} σ_{yy} σ_{zz} σ_{xy} σ_{yz} σ_{xz}
ANSYS	σ_{xx} σ_{yy} σ_{zz} σ_{xy} σ_{yz} σ_{xz}
MARC	σ_{xx} σ_{yy} σ_{zz} σ_{xy} σ_{yz} σ_{xz}

2.4.2 Numerical Validation

After implementing the modifications to the UMMDp, it is possible to directly compare the results of the Std_Aba, the UMAT_Yld2004_Mixed and the UMMDp by using FEA simulations. With that purpose, single-element homogeneous tests and a deep drawing cup test are used in this validation. The results are compared for the von Mises yield criterion and the Yld2004-18p yield criterion, using the parameters from Table 2.3. In addition, a mixed hardening law, composed of the Voce law, is used for isotropic hardening (see Equation 2.22), and the non-linear kinematic hardening law of Equation 2.26 is used for the kinematic hardening, using the material parameters presented in Table 2.6. The latter material parameters were identified from real experiments of a DC04 mild steel with 0.7 mm of thickness in Souto et al. (2015b).

Table 2.6 Material parameters of the Voce isotropic hardening law and kinematic hardening law used in numerical simulations (Souto et al. 2015b).

Isotropic hardening			Kinematic hardening					
σ_0 [MPa]	Q [MPa]	b [–]	c_1/γ_1 [MPa]	γ_1 [–]	c_2/γ_2 [MPa]	γ_2 [–]	c_3/γ_3 [MPa]	γ_3 [–]
100.0	110.3	5.92	44.57	22.85	106.2	258.38	5629.7	0.0258

Single-Element Homogenous Tests

Three types of homogeneous tests, namely, tensile, shear and biaxial, are modeled using a single 3D element of 1 mm^3 with boundary conditions according to Figure 2.6. The use of single element models, particularly in the tensile and shear tests, is justified by the homogeneous strain distributions commonly observed in real experiments, using classical tests. In the case of the biaxial test, it has been previously shown, compared to a bulge test, that the evolution of the strain tensor components ε_{xx} and ε_{yy} is approximately identical (Souto 2015). The numerical models are displacement-driven, with imposed displacements of 0.6 mm for the tensile and shear tests, and 0.4 mm in each direction for the biaxial test. In addition, the 8-node brick element with reduced integration (C3D8R) is used.

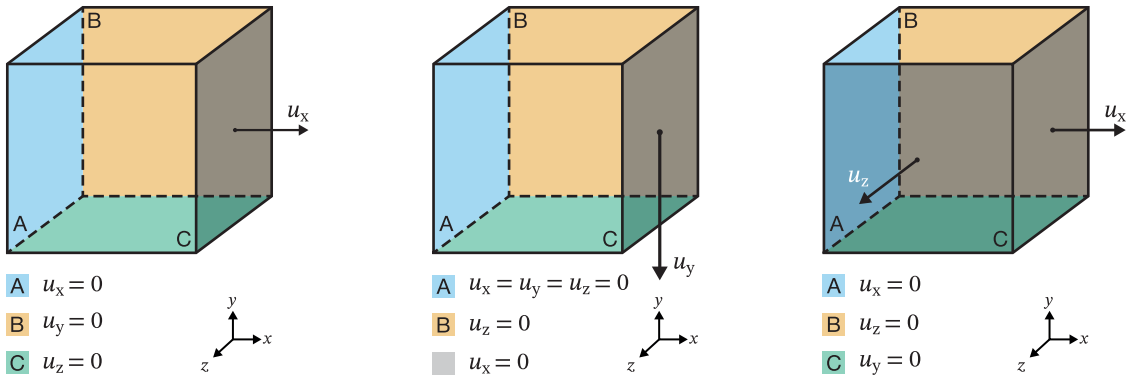

Figure 2.6 Boundary conditions applied on the numerical models of the single-element homogeneous: (a) tensile, (b) shear, and (c) biaxial.

The three tests are each performed with three combinations of constitutive models, namely, using the von Mises yield criterion with mixed hardening, using the Yld2004-18p yield criterion with isotropic hardening at 0° from RD, and using the Yld2004-18p yield criterion with mixed hardening at 0° from RD. In the first case, all three user material subroutines are used. However, in the other two cases only the UMMDp and the UMAT_Yld2004_Mixed are used, because Std_Aba allows the use of Yld2004-18p. The evolution of strain and stress tensor components was analyzed and compared. In particular, the evolution of $\varepsilon_{xx} - \sigma_{xx}$, $\varepsilon_{xx} - \varepsilon_{yy}$, and $\varepsilon_{xx} - \varepsilon_{zz}$ are presented for the tensile and the biaxial tests, while the evolution of $\sigma_{xy} - \varepsilon_{xy}$ is presented for the shear tests. Nevertheless, all the results are identical independently of which user material subroutine is used, thus validating its use for this particular application. For that reason, in Figure 2.7, the shown curves are representative of all user material subroutines correspondent.

Deep Drawing Cup Test

Additionally, it is recommended to compare the results of each user material subroutine for a more complex model, as well as their convergence efficiency. For that purpose, a deep drawing

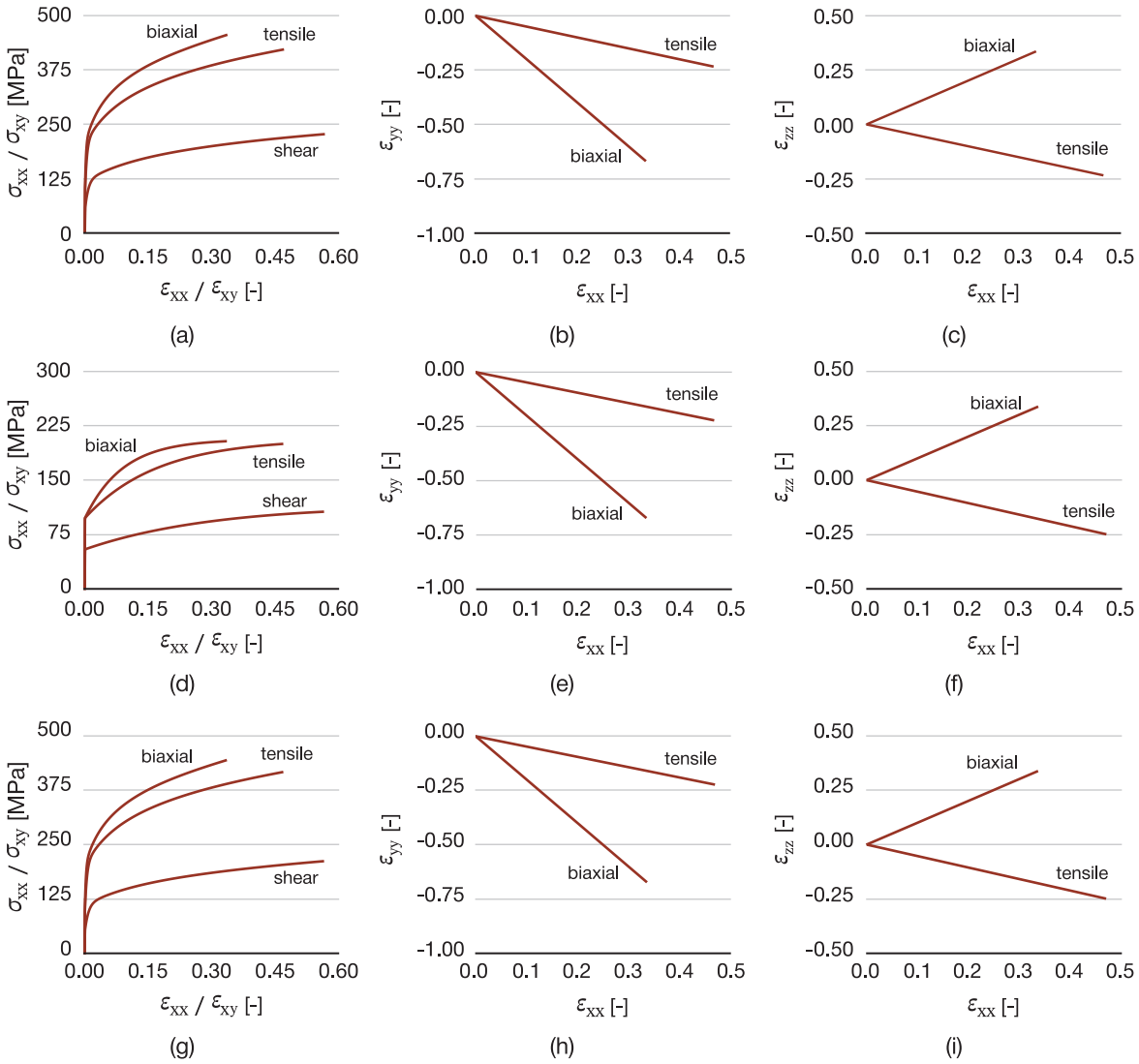

Figure 2.7 Results of the numerical simulations of homogeneous tensile, shear and biaxial tests using the three user material subroutines represented by ε_{xx} - σ_{xx} and ε_{xy} - σ_{xy} (left), ε_{xx} - ε_{yy} (center), and ε_{xx} - ε_{zz} (right) using: (a)–(c) the von Mises yield criterion with mixed hardening, (d)–(f) the Yld2004-18p yield criterion with isotropic hardening at 0° from RD, and (g)–(i) the Yld2004-18p yield criterion with mixed hardening at 0° from RD.

cup test is carried out using the setup presented in Figure 2.8a, for a sheet 0.7 mm thick. The FEA simulation is displacement-driven with an imposed vertical displacement of 15 mm in the punch, considering an implicit integration scheme using Abaqus/Standard. To reduce the computational cost of the simulation, only one quarter of the blank is modeled by assuming symmetry conditions. In addition, the finite element mesh of the blank is built using the 8-node brick elements with reduced integration (C3D8R). The mesh presents two regions of varying element size, one coarse in the center region and in contact with the punch, therefore not achieving considerable deformation, and another finer in regions withstanding higher deformations (see Figure 2.8b). The blank is also built with 4 elements through the thickness, leading to a total of 47 011 elements. The tools, namely the die, the punch and the blank holder, are modeled as analytical rigid surfaces. The contact between the blank and the tools is assumed to present a friction coefficient of 0.06 and modeled using the Coulomb friction model. Moreover, a force of 15 kN is applied on the blank holder.

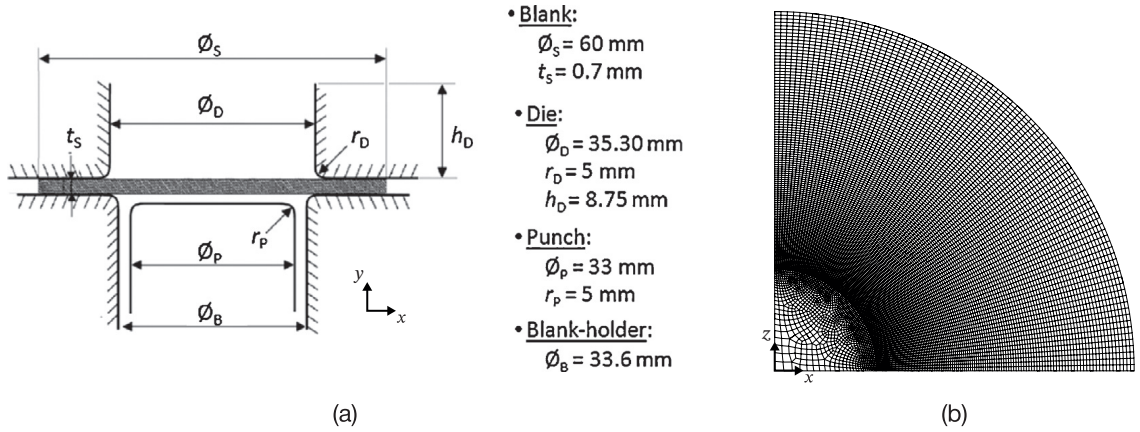

Figure 2.8 Schematic of the deep drawing cup test (dimensions in mm): (a) setup and geometry (Souto et al. 2015b) and (b) finite element mesh used in the blank.

Two FEA simulations are performed using two combinations of constitutive models, namely, one using the von Mises yield criterion with a mixed hardening law (test 1), and another using the Yld2004-18p yield criterion with a mixed hardening (test 2). The results of major strain ε_1, minor strain ε_2, and total back stress tensor component α_{xx} are analyzed for each user material subroutine and presented in Figure 2.9. Similarly to the homogeneous tests, it is observed that the results for the deep drawing cup test are identical between the UMMDp, the UMAT_Yld2004_Mixed, and the Std_Aba, thus a single map representative of the three user material subroutines is shown in Figure 2.9. It should be noted that the finite element mesh of test 2 is highly distorted at the end of the test, as no rupture criterion has been considered. Nevertheless, this simulation is still valid for comparison purposes.

Analyzing the convergence and computational time of the UMAT_Yld2004_Mixed and the UMMDp, it is important to refer that both are implemented with a backward-Euler scheme with a

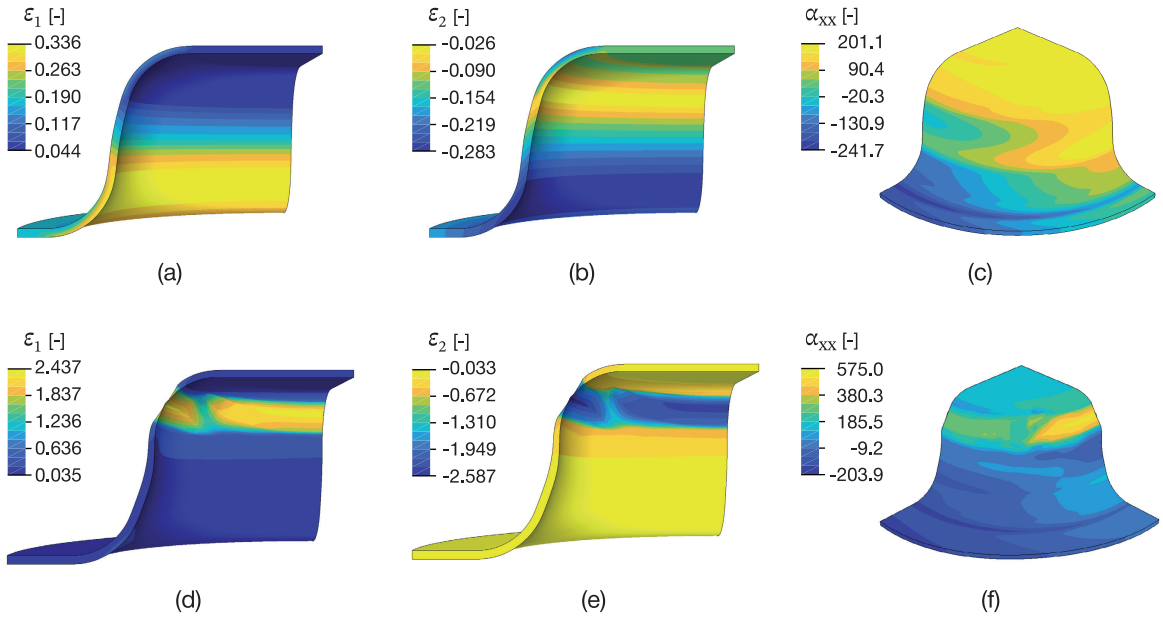

Figure 2.9 Maps of the major strain ε_1 (left), minor strain ε_2 (center), and total back stress tensor component α_{xx} (right) of the deep drawing cup simulations at the last time instant for (a)–(c) test 1 and (d)–(f) test 2.

sub-incremental method. However, it is unclear if the algorithm is implemented with the same conditions, and the computation of the consistent tangent matrix is not identical. What is known is that the code complexity in the UMMDp is higher than in the UMAT_Yld2004_Mixed. Some examples are: (i) the implementation of the yield criteria in the UMMDp is programmed using arrays, while in the UMAT_Yld2004_Mixed the differential equations are previously derived in an external software and then implemented in the subroutine in the form of scalar operations; (ii) in the UMMDp, the user can select the level of printing information during the analysis, so that every time a printing option is available, the subroutine must check the level required by the user, while in UMAT_Yld2004_Mixed, the amount of printing is low, and it should be commented if the user does not wish it to be printed; and (iii) a large number of yield criteria, isotropic and kinematic hardening laws are available in the UMMDp, and the subroutine is required to select each option every time it is called. On the other hand, in UMAT_Yld2004_Mixed, there are only available options for selecting the isotropic hardening law.

All simulations required 2032 increments for the step corresponding to the displacement of the punch, and the number of cutbacks was identical in each increment.

In terms of the computational time, the total central processing unit (CPU) time required by both user material subroutines is analyzed for test 2. In this case, the UMMDp is approximately 14 % slower than the UMAT_Yld2004_Mixed (see Table 2.7). To verify the influence of the *if* programming conditions on the selection of constitutive models and the printing, a new simulation is performed, named UMMDp_Simplified, where these conditions are removed. Now, the UMMDp_Simplified is approximately 11 % slower than the UMAT_Yld2004_Mixed, which represents a relatively good improvement.

Table 2.7 Total CPU time of the deep drawing cup test 2.

User material subroutine	Time [h]
UMMDp	53.946
UMMDp_Simplified	52.614
UMAT_Yld2004_Mixed	47.544

However, the computational gap is significant, and it is therefore relevant to investigate if it is related to the stress integration algorithm or programming efficiency. For that purpose, it is monitored for a single element of the model, from the first yield increment onward, the number of Newton-Raphson (NR) iterations in the global equilibrium per increment, the number of sub-increments in the stress integration scheme, and the number of NR iterations in the stress integration scheme, per increment. Moreover, the ratio of NR iterations between the UMMDp and the UMAT_Yld2004_Mixed is used in the analysis. Values above 1 mean the UMAT_Yld2004_Mixed required more NR iterations than the UMMDp, and vice versa. The CPU time required per increment is also monitored for the same element.

In Figure 2.10a, the number of NR iterations in the global equilibrium per increment is presented. However, this analysis shows that the two subroutines are identical. On the other hand, analyzing the results for the ratio of NR iterations presented in Figure 2.10b, it is observed that the UMAT_Yld2004_Mixed requires more iterations, particularly in the late stages of the test. The same is observed on average through the test, as the average value 1.037 indicates.

Regarding the number of NR iterations in the stress integration scheme, a large difference between the two user material subroutines is observed (see Figure 2.11a). Analyzing Figure 2.12b, where above the threshold are the points where the UMAT_Yld2004_Mixed takes more iterations than the UMMDp and *vice versa*, the average ratio of 2.624 indicates the ability of the UMMDp to converge faster than the UMAT_Yld2004_Mixed. Further observing the results of the sub-

increments required in each NR iteration (see Figure 2.11d), it is interesting to observe that the UMMDp only requires one sub-increment per NR iteration in each increment, while the UMAT_Yld2004_Mixed requires at least two sub-increments and a maximum of 15.

From these results, it is possible to conclude that the UMMDp presents higher levels of efficiency, even though the total CPU time was higher than the UMAT_Yld2004_Mixed. The

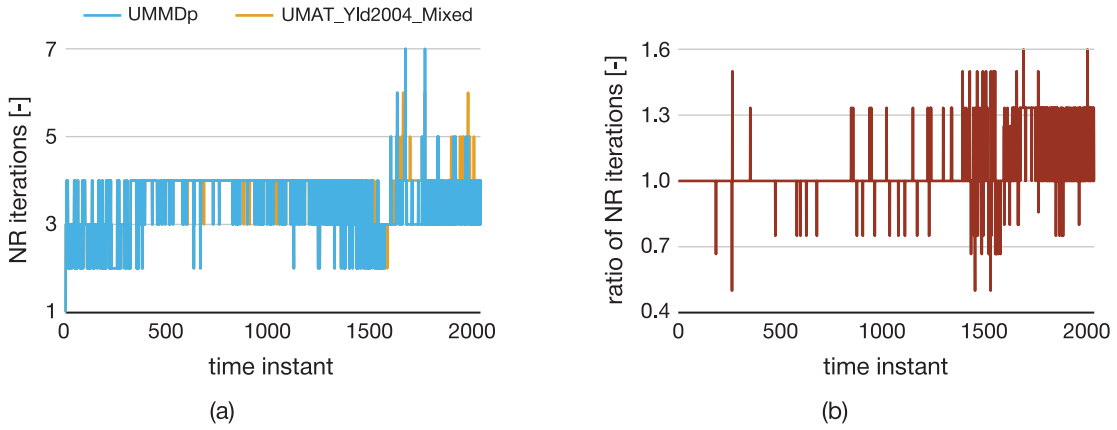

Figure 2.10 Results for global equilibrium of (a) NR iterations and (b) ratio of NR iterations, per increment, of the deep cup drawing test with the Yld2004-18p yield criterion and a mixed hardening law.

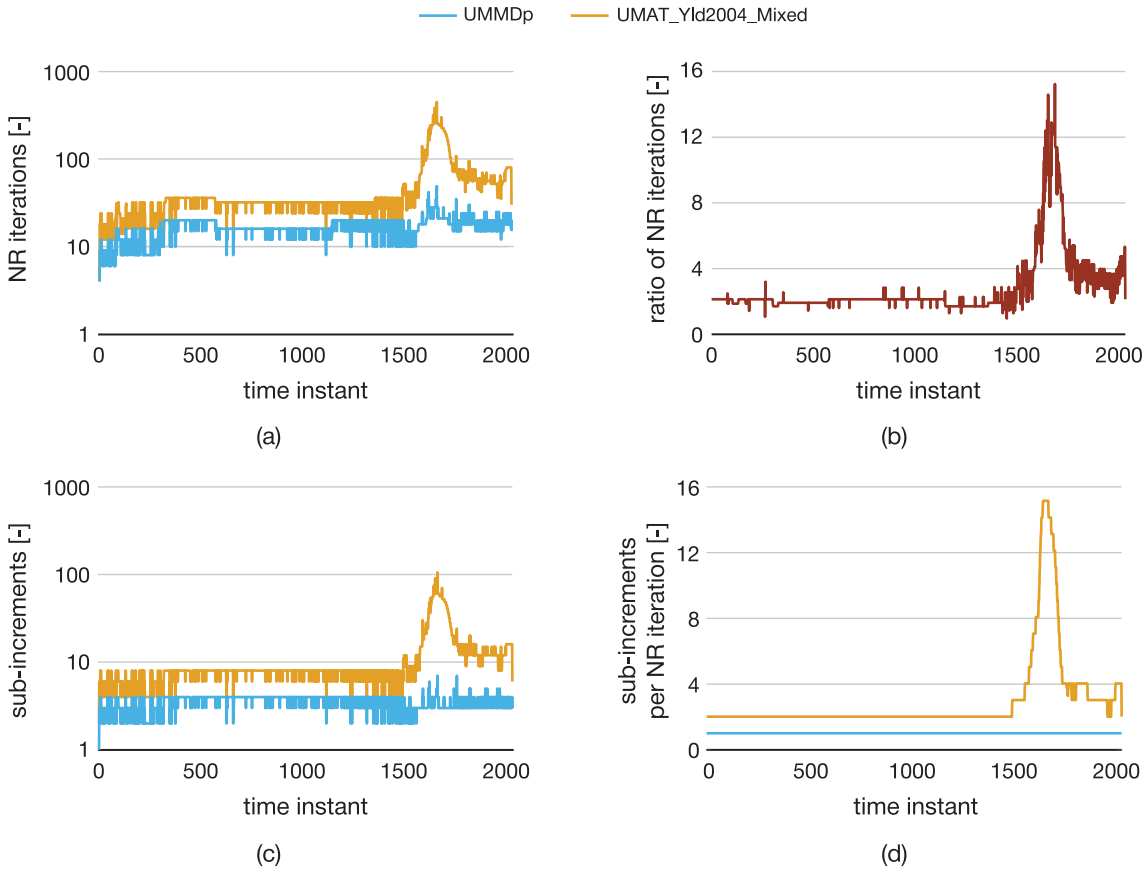

Figure 2.11 Results for stress integration scheme of (a) NR iterations, (b) ratio of NR iterations per increment, (c) sub-increments, and (d) sub-increments per NR iteration, per increment, of the deep cup drawing test using the Yld2004-18p yield criterion with mixed hardening.

results of the CPU time per increment presented in Figure 2.12a show that the UMMDp is slower than UMAT_Yld2004_Mixed, and that the simplification in the code does not improve the CPU time considerably. In Figure 2.12b, the ratio of the CPU time of the UMAT_Yld2004_Mixed by the UMMDp is represented, where the values above 1 mean the UMAT_Yld2004_Mixed is slower than the UMMDp and vice versa. It is possible to see the differences in the CPU time. Overall, the UMMDp requires fewer iterations than UMAT_Yld2004_Mixed to converge to the solution, but the difference in CPU time is significantly in favor of the UMAT_Yld2004_Mixed. Thereby, it is possible to assume that this difference is related to the programming efficiency of the material user subroutines, and not to the algorithm's efficiency.

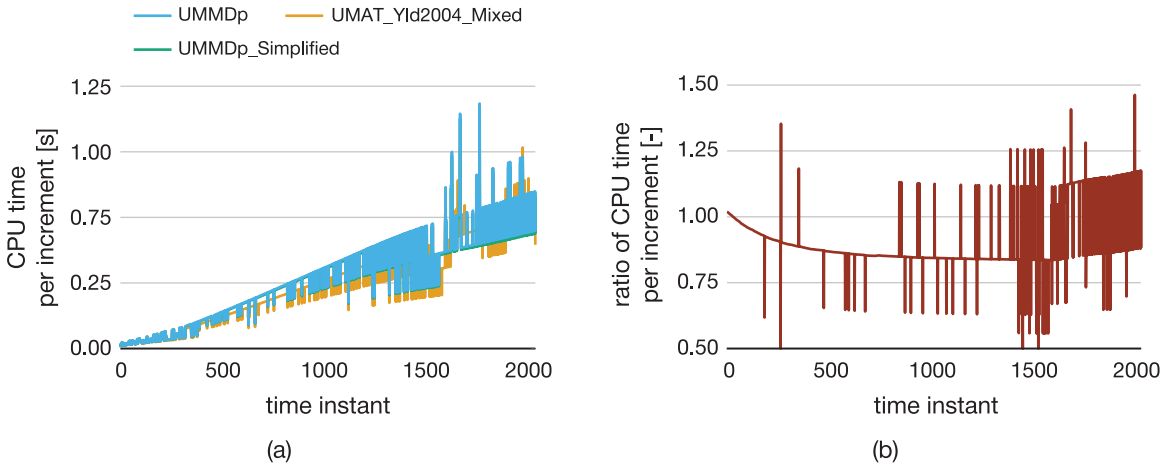

Figure 2.12 Results for stress integration scheme of (a) CPU time and (b) ratio of the CPU time, per increment, of the deep cup drawing test using the Yld2004-18p yield criterion with mixed hardening.

2.4.3 Conclusions

The UMMDp is a valuable open source library to FEA software thanks to its wide range of constitutive models. Even though it presents great potential, it still lacks numerical validations of the implemented models. The Yld2004-18p yield criterion in the UMMDp presented an interesting formulation of the yield criterion, which might be of great use in material parameter identifications. However, the observed incoherence between the Voigt notation of the stress tensor used in its formulation and the FEA software conventions is of great importance. When accounting for the implemented modifications to the Yld2004-18p, the results are similar to the user material subroutine used as reference, validating its formulation. The analyzed kinematic hardening law in the UMMDp also presents similar results to the user material subroutines used as reference, validating its formulation. Finally, the numerical simulations performed validate the use of Yld2004-18p yield criterion, isotropic and kinematic hardening laws in the UMMDp. Even though the UMMDp proved significantly slower in the deep drawing cup test than the reference, it is nevertheless advantageous, as it enables the use of complex yield criteria, without the need to implement them from zero. Therefore, the UMMDp will be used for the remainder of studies of this thesis.

3 Overview of Heterogeneous Mechanical Tests

3.1 Introduction

To decrease associated delays and costs, the mechanical design of sheet metal forming parts tends to be nowadays more and more virtual, by using numerical simulation. Therefore, the characterization of materials has received increased attention due to the need for precise input data to computational analysis software. The material mechanical behavior is numerically described through constitutive equations and material parameters. Conventionally, the identification of material parameters is achieved using standard quasi-homogeneous mechanical tests (Rusinek and Klepaczko 2001; An et al. 2004; Gilles et al. 2011). In this approach, the strain field is quasi-homogeneous for tensile conditions along the gauge part of the sample before necking occurs, and in shear conditions, the heterogeneity is negligible, which is restrictive. Moreover, from a single classical test, it is difficult to extract many material parameters, requiring several tests to identify many parameters of a single constitutive model. As such, the number of material parameters to identify might range from only 3, considering an isotropic material using the von Mises yield criterion with the Swift hardening law (Reis et al. 2017). On the other hand, some studies have identified many material parameters. For example, in Souto et al. (2015b), 24 parameters are identified for an highly anisotropic material using the Yld2004-18p yield criterion with a mixed hardening law.

More recently, research has focused on alternative identification methods based on heterogeneous strain fields, measured using full-field experimental techniques (Prates et al. 2016; Pierron and Grédiac 2021). The accuracy of these alternative methods depends on three main issues: (i) the geometry of the specimen to be used, (ii) the choice of an appropriate measurement technique of the strain field and (iii) the definition of an identification strategy. By using these techniques, it is possible to extract a greater amount and variety of information from the strain field developed during the test. Ideally, the use of a single heterogeneous test could be sufficient to characterize the material behavior (Rossi et al. 2022b). However, the selection of a geometry that demonstrates a rich strain field, both in type and amount of information, is still a topic under research (Thoby et al. 2022). Additionally, the use of full-field measurement techniques requires inverse methodologies to determine the material parameters of a given constitutive model. The identification procedure consists of minimizing the gap between experimental and numerical data, measured by an objective function, for example, defined in a least square form. In sheet metal

characterization, the thickness of the material is generally small, of the order of a few millimeters or below, and stress levels in the ND to the sheet plane are most of the time neglected. In addition, measuring deformation perpendicular to the plane of the sheet is a difficulty in conventional DIC techniques. For that reason, studies investigating the material's behavior tend to assume that it presents isotropic behavior in the ND to the sheet plane.

To evaluate the richness of the test, studies generally use the major and minor stresses diagram, and the major and minor strains diagram, in the sheet plane, respectively, illustrated in Figures 3.1a and 3.1b. Both types of representation illustrate the mechanical state observed at different material points of the test. In the case of the major and minor stresses diagram, the mechanical states are represented by the ratio of minor stress σ_2 by major stress σ_1. For example, at $\sigma_2/\sigma_1 = 1$ corresponds to an equibiaxial state, and at $\sigma_2/\sigma_1 = -1$ to a shear state. In the case of the major and minor strains diagram, the mechanical states are represented by the ratio of minor strain ε_2 by major strain ε_1. For example, at $\varepsilon_2/\varepsilon_1 = 1$ corresponds to a equibiaxial state, and at $\varepsilon_2/\varepsilon_1 = -0.5$ to a uniaxial state.

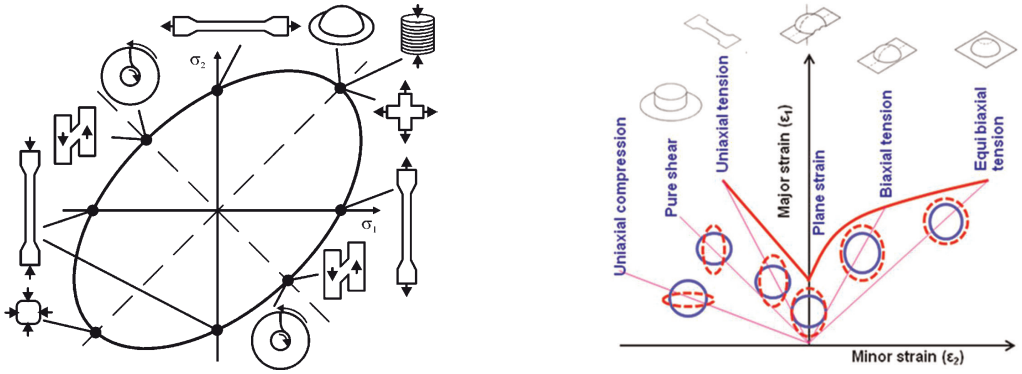

(a) (b)

Figure 3.1 Different mechanical states reached during testing of sheet metal defined in the (a) major and minor stresses diagram (Brosius et al. 2011), and (b) major and minor strains diagram (Paul et al. 2013), in the sheet plane.

One of the goals of using heterogeneous mechanical tests is to apply them in the identification of material parameters with inverse methodologies. Therefore, the following sections provide an overview of heterogeneous mechanical tests reported in the literature, with a focus on the type and quantity of information. Details of applications to identify the material parameters are also provided if applicable. The tests are presented chronologically in order of their publication, and are distinguished between uniaxial, biaxial, and out-of-plane loading. The latter tests are more complex, requiring advanced experimental apparatus with contact between the material and tools. Therefore, friction exists and should be accounted for. On the other hand, the first and second type of tests are simpler, and no contact is required between the material and the tools. Additionally, no occurrence of out-of-plane of shear stresses is observed, that is, the tests are insensitive to the material parameters associated with these stresses. For each test, a description of the geometry, materials and constitutive models used will be provided when this information is available. In some cases, the studies do not explain how the test has been designed or selected, so no information is reported.

3.2 Uniaxial Loading Tests

MEUWISSEN (1998) was one of the pioneer studies that used heterogeneous mechanical tests for the characterization of sheet metals through a mixed numerical-experimental methodology. In this study, an irregular specimen with two holes was used, both in virtual and real experiments, to

estimate the parameters of constitutive models (see Figure 3.2a). One of the conclusions of the study was that the test leads to richer mechanical information, although with a single test it was impossible to characterize all the anisotropic properties of the materials. Additionally, Meuwissen et al. (1998) also proposed a shear-like specimen to investigate the material characterization of an aluminum alloy with 0.5 mm of thickness (see Figure 3.2b). These tests were selected so that the strain and stress levels in the materials varied over a wide range. However, it is unclear how the geometry was obtained. Later, the shear-like specimen was also used to characterize a dual-phase steel (Haddadi and Belhabib 2012) and a pure titanium with 0.5 mm of thickness (Pottier et al. 2011).

Kajberg and Lindkvist (2004) designed a specimen with a narrow part in the middle to control the location of plastic instabilities (see Figure 3.2c). This way, it was possible to focus the acquisition cameras in this region and achieve better spatial resolution. The test achieved high values of equivalent plastic strain (around 0.75), leading to a successful characterization of the hardening behavior up to large strains.

Belhabib et al. (2008) and Haddadi and Belhabib (2012) proposed a heterogeneous tensile test for the identification of material parameters of a dual-phase steel with 1 mm of thickness using full-field measurements (see Figure 3.2d). The specimen consists of a hybrid geometry between a classical tensile test and a plane tensile test, and was designed with the aim of presenting: (i) large strain heterogeneity in the gauge area; (ii) large strain paths diversity; and (iii) good sensitivity of the strain fields to the material parameters. The study performed real experiments using this test, but from the available data, it is not easy to identify the type of strain paths achieved.

Robert et al. (2012) investigated the use of the specimens proposed by Meuwissen et al. (1998) and Belhabib et al. (2008) to identify the material parameters of Hill 1948 yield criterion and Ludwig isotropic hardening law for a 2024-T3 aluminum alloy. Through real experiments, it was observed that the range of strain paths is located between uniaxial tension and plane strain for both specimens. The maximum major strain values observed are approximately 0.20 and 0.16 (concentrated in the notches), respectively, for the specimen of Belhabib et al. (2008) and Meuwissen et al. (1998). The study concludes that for this specific material, the specimen proposed by Belhabib et al. (2008) exhibited similar strain paths, but for higher values of strain and a better distribution over the surface of the specimen.

Avril et al. (2008c), Pierron et al. (2010), Rossi et al. (2016b), and Marek et al. (2017) investigated the use of a double notched specimen with similar geometries to characterize the material parameters using VFM (see Figure 3.2e). According to Rossi et al. (2016b), this shape is often used because it can produce a heterogeneous strain field, is easy to machine, and, in plasticity, allows to have a large zone of the specimen under plastic deformation. However, Rossi et al. (2016b), observe that the adopted notched specimens generate states of stress covering only a small part of the yield surface, so that a good identification of material parameters of Hill 1948 yield criterion is obtained using a 45° specimen or the combination of 0° and 90° angle from RD.

Cooreman (2008) proposed two perforated specimens of different geometric complexity to identify the material parameters of the Hill 1948 yield criterion and the Swift hardening law (see Figures 3.2f and 3.2g). In total, there were 6 material parameters to identify. By comparing the identification against a traditional approach using multiple conventional uniaxial tensile tests, the study showed that using a single heterogeneous test yields better results. The study concluded that mechanical tests should be proposed according to the forming process, which will be employed afterwards.

Kim et al. (2014) investigated four different geometries of heterogeneous tests (see Figure 3.3) that should present very heterogeneous stress states from a uniaxial load, and that the relative errors between the identified parameters using the VFM and the input values in the FEA simulations should be less than 1 %. The study considers the latter condition important, because the

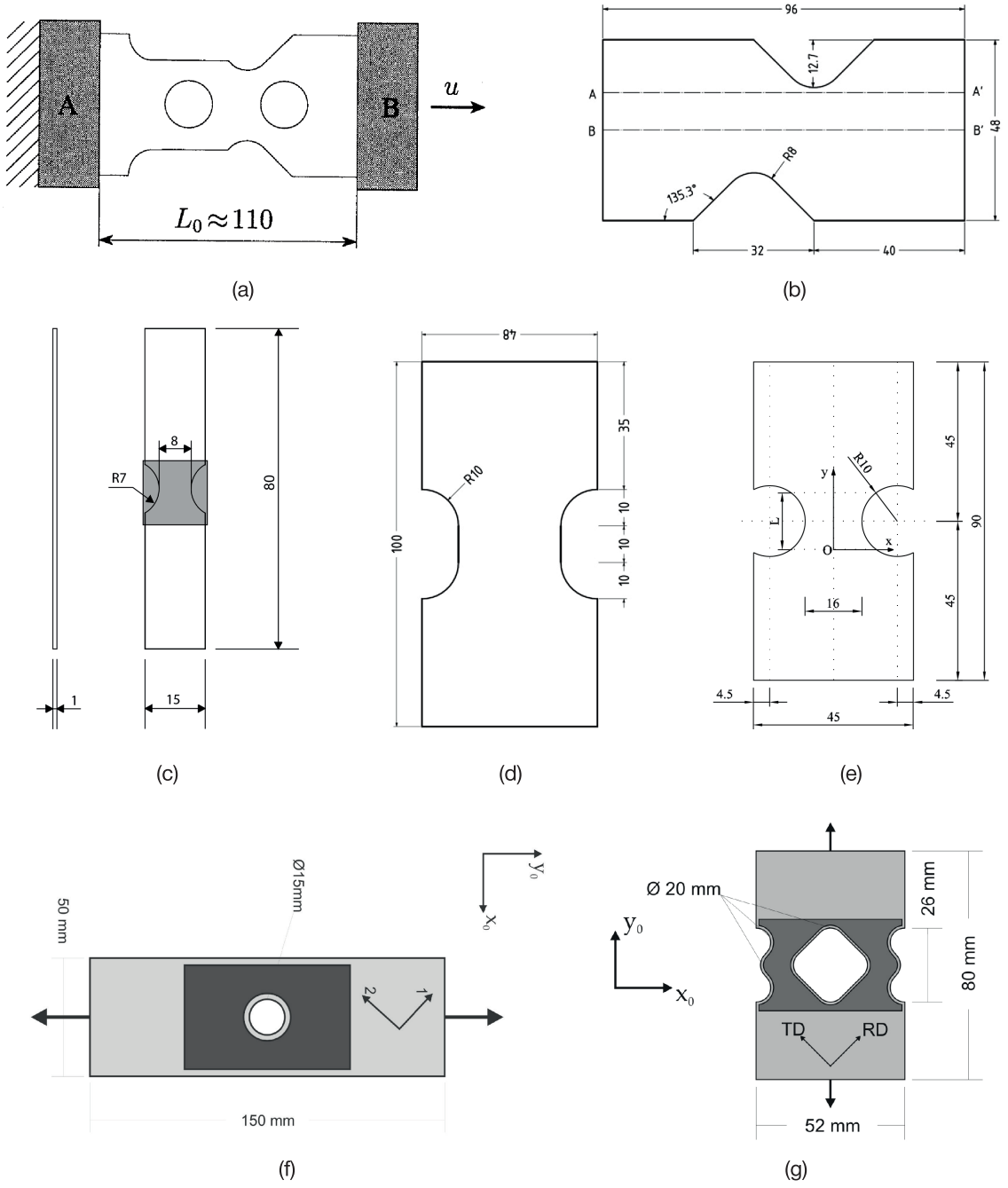

Figure 3.2 Geometry of uniaxial loading specimens (dimensions in mm): (a) Meuwissen (1998), (b) Meuwissen et al. (1998), (c) Kajberg and Lindkvist (2004), (d) Belhabib et al. (2008), (e) Pierron et al. (2010), and (f)–(g) Cooreman (2008).

identification was unsuccessful in various geometries, producing heterogeneous stress states due to high strain concentration in a few elements. Geometry A exhibits various stress distributions, from biaxial tension, uniaxial tension and pure shear to uniaxial compression. Though this geometry yields satisfactory identification results, this specimen tends to buckle in the experiments. Geometry B exhibits a similar stress distribution to geometry A, and the identification results were successful, even though it is considered that the specimen will eventually buckle when imposing a large displacement. Geometry C exhibits biaxial stress states in the central area between the two holes. However, in the experiments, it was found that necking occurs prematurely in the hole areas,

leading to unsuccessful identification. Geometry D exhibits a stress distribution mainly concentrated over the uniaxial tension range. The identification using this geometry was unsuccessful, as the specimen does not provide sufficient information to identify each material parameter. Finally, the study combined two tests of geometry B in different directions, and the identification results are satisfying. Although applied to dynamic testing, Fu et al. (2021) designed a specimen similar to geometry B, named M-shaped specimen.

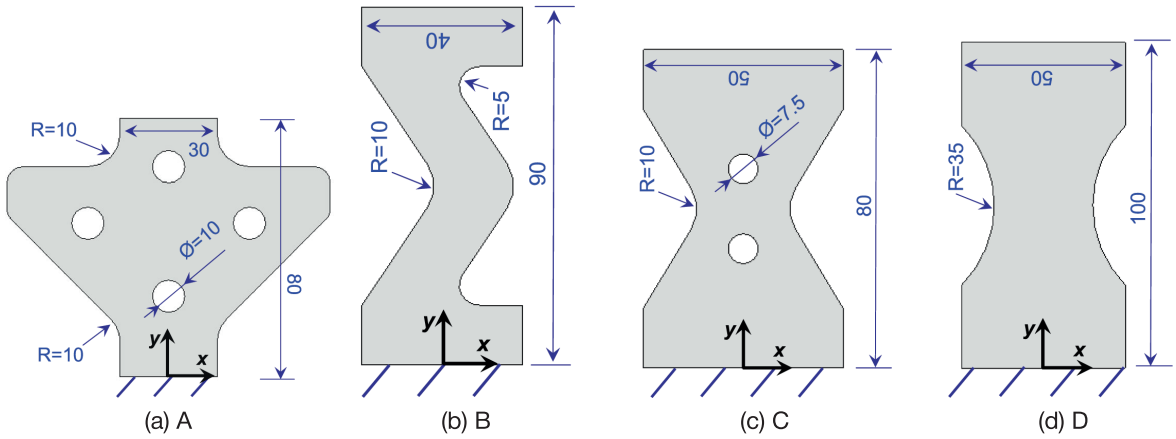

Figure 3.3 Geometry of the specimens (dimensions in mm) proposed by Kim et al. (2014).

Goga (2014) proposed a specimen for plane stress analysis, which only requires a uniaxial testing machine (see Figure 3.4a). Due to its geometry, the specimen exhibits tension in the vertical arm and compression in the horizontal one. The geometry was numerically and experimentally investigated for an aluminum alloy, and appears to exhibit various mechanical states. However, the test was only carried out in the elastic regime.

Rossi et al. (2016a) proposed a couple of specimens based on a numerical procedure that relies on a test simulator that can generate synthetic images similar to the ones obtained during an actual test, to identify the hardening behavior of sheet metals with the VFM. The external shape of the specimen is fixed, while in the zone of measurement, there are two notches whose geometries are defined according to 7 independent design variables (see Figure 3.4b). The study proposes a few geometries (with different variables) considered optimal geometries, which present a diffuse plastic strain distribution, while non-optimal geometries exhibit a strain concentration only close to the notches.

Souto et al. (2017) proposed a specimen, known as butterfly test, based on an optimization procedure of the outer shape (see Figure 3.4c). A dedicated indicator guides the optimization that quantifies, among others, the heterogeneity of strain states (Souto et al. 2015a). Later, Aquino et al. (2019) investigated the experimental application of the specimen to characterize a 0.7 mm thick mild steel. One interesting aspect of this test is that the shape of the top boundary is created using special grips with the desired shape. To avoid sliding between the specimen and the grips, special patterned contact marks were used in the jaws. The study performs experiments and numerical simulations of the test, observing that the range of principal strains distribution is between shear and close to plane strain, but most of the specimen is the uniaxial tension region. The maximum value of major strain observed is approximately 0.8, but only a few points are observed in this range. Most material points are concentrated for values lesser than 0.4. The identification procedure uses two different material orientations (0° and 90° from the RD), and the results show that the identified parameters can reproduce the real material behavior.

Jones et al. (2018) proposed a specimen to investigate the identification of material parameters of a viscoplastic material model for a 1.5 mm thick stainless steel, using the VFM (see

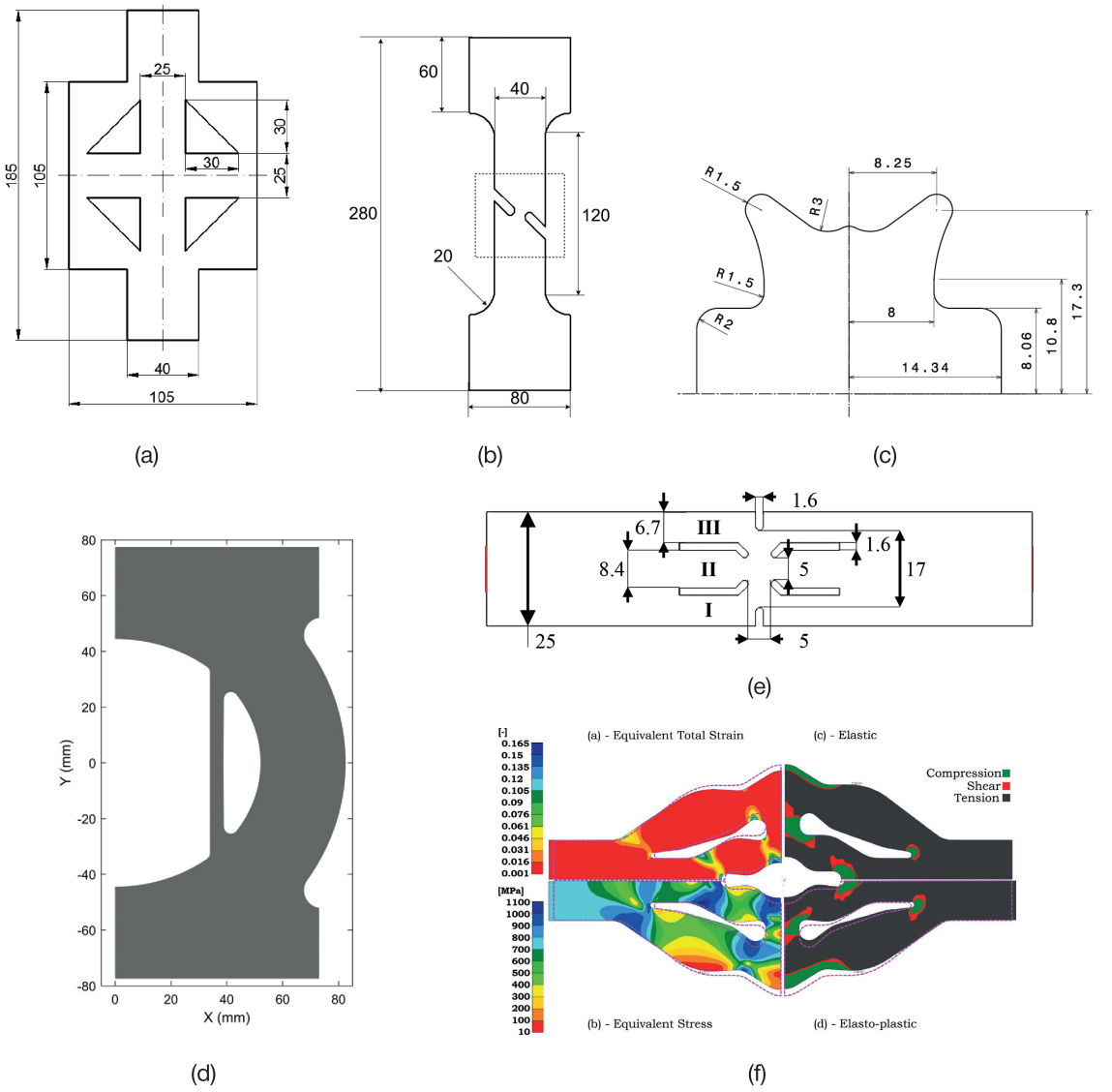

Figure 3.4 Geometry of uniaxial tensile specimens (dimensions in mm): (a) Goga (2014), (b) Rossi et al. (2016a), (c) half-shape of Souto et al. (2017), (d) Jones et al. (2018), (e) Küsters and Brosius (2019), and (f) Barroqueiro et al. (2020).

Figure 3.4d). The study designed the specimen via an iterative process, starting with an initial shape selected by engineering intuition, and then performing a finite element analysis of the specimen using the reference material model parameters. Afterwards, the design is manually adjusted until the geometry met the following criteria: (i) maximize stress heterogeneity, (ii) maximize range of strain rates, (iii) minimize large gradients in stress or strain near sample edges, (iv) restrict the geometry to planar, but with arbitrarily complex in-plane geometry, while preventing buckling, and (v) be a uniaxial loading test. Strain paths that occur in the specimen are not presented, as the study does not explore in detail the characteristics of the optimized specimen.

Küsters and Brosius (2019) developed a specimen to achieve various stress states in the plastic regime (see Figure 3.4e). This test is intended to be used in damage characterization, and has also been designed to achieve more than one failure mode in each experiment.

Barroqueiro et al. (2020) developed an innovative methodology to design heterogeneous mechanical tests from topology optimization and a dedicated indicator. The goal was to design tests promoting uniformity of equivalent stress, while simultaneously achieving uniaxial tension,

uniaxial compression and shear stress states. Following this innovative methodology, a specimen mainly achieving tensile stress states was obtained (see Figure 3.4f). The geometry has already been experimentally investigated, but huge buckling was observed.

Fu et al. (2020) proposed a specimen, named bridge-like, that exhibits balanced heterogeneous stress states (see Figure 3.5a). This test was designed based on the plate buckling theory to avoid significant buckling under compressive loadings. One important aspect of their study focused on avoiding the use of buckling devices, because they block the field of view during experiments. The test has been experimentally validated under cycling loadings and has shown to not be liable to buckle within a reasonable range of in-plane compression. The study also performed a calibration of the Hill 1948 yield criterion and a non-linear mixed hardening law, and found that by combining two tests with different material orientations, it yielded accurate and robust results.

Maček et al. (2020) developed a heterogeneous test that primarily achieves a biaxial stress state away from free edges, to avoid difficulties with DIC measurements (see Figure 3.5b). Additionally, the study also wanted to avoid any stress concentrations or high strain gradients. Their goal was to use this test to identify only biaxial related parameters of the Yld2000-2d yield criterion, in combination with classic uniaxial tensile tests. One issue was the pronounced buckling of the upper and lower bridges during experimental tests.

Another specimen designed by topology optimization was proposed by Chamoin et al. (2020) to maximize the sensitivity of displacement fields to material parameters (see Figure 3.5c). The obtained geometry was directly manufacturable. Both numerical and experimental results that confirm the validity of the methodology were obtained. However, this study is only applied to fir wood and the identification of a shear modulus.

Conde et al. (2021) used shape optimization methodologies to design a perforated specimen (see Figure 3.5d). In this study, the exterior geometry was fixed, and only the interior shape was optimized to maximize stress heterogeneity. The obtained specimen demonstrates to achieve stress states ranging from uniaxial tension to compression. Although this specimen has not yet been experimentally validated, it has already been successfully applied to the identification of material parameters of Swift hardening law (Conde et al. 2022).

Zhang et al. (2022a) designed a new specimen using shape optimization of the exterior notches by maximizing the heterogeneity of strain states (see Figure 3.5e). Interestingly, this study uses the same indicator as proposed by Souto et al. (2015a). This specimen has shown to achieve strain states located between shear to uniaxial tension, though closer to the latter. Additionally, the study validated the use of this test to successfully identify the material parameters of the Hill 1948 and the Yld2000-2d yield criteria.

Gonçalves et al. (2022) extended the study of Barroqueiro et al. (2020) to plasticity and obtained new geometries (see Figure 3.5f). A large part of the specimen presents strain states between uniaxial compression and uniaxial tension. In terms of equivalent plastic strain, it is observed that the highest values are concentrated in small regions and away from regions of uniaxial tension. So far, this test has not yet been applied in the identification of material parameters or experimentally validated.

Chapelier et al. (2022) developed an innovative methodology that leads to the improvement of existing specimens, instead of generating new geometries from scratch. This methodology is based on a non-invasive CAD-inspired optimization strategy, which relies on univariate spline tools to update the finite element model mesh. An example is shown in Figure 3.5g, where the shape and position of holes are optimized to improve the sensitivity of the tests to material parameters of a given model.

Many uniaxial loading tests exist, as shown by the 25 different tests here presented. It is expected that this number continues to increase, as studies will continue to design tests using even

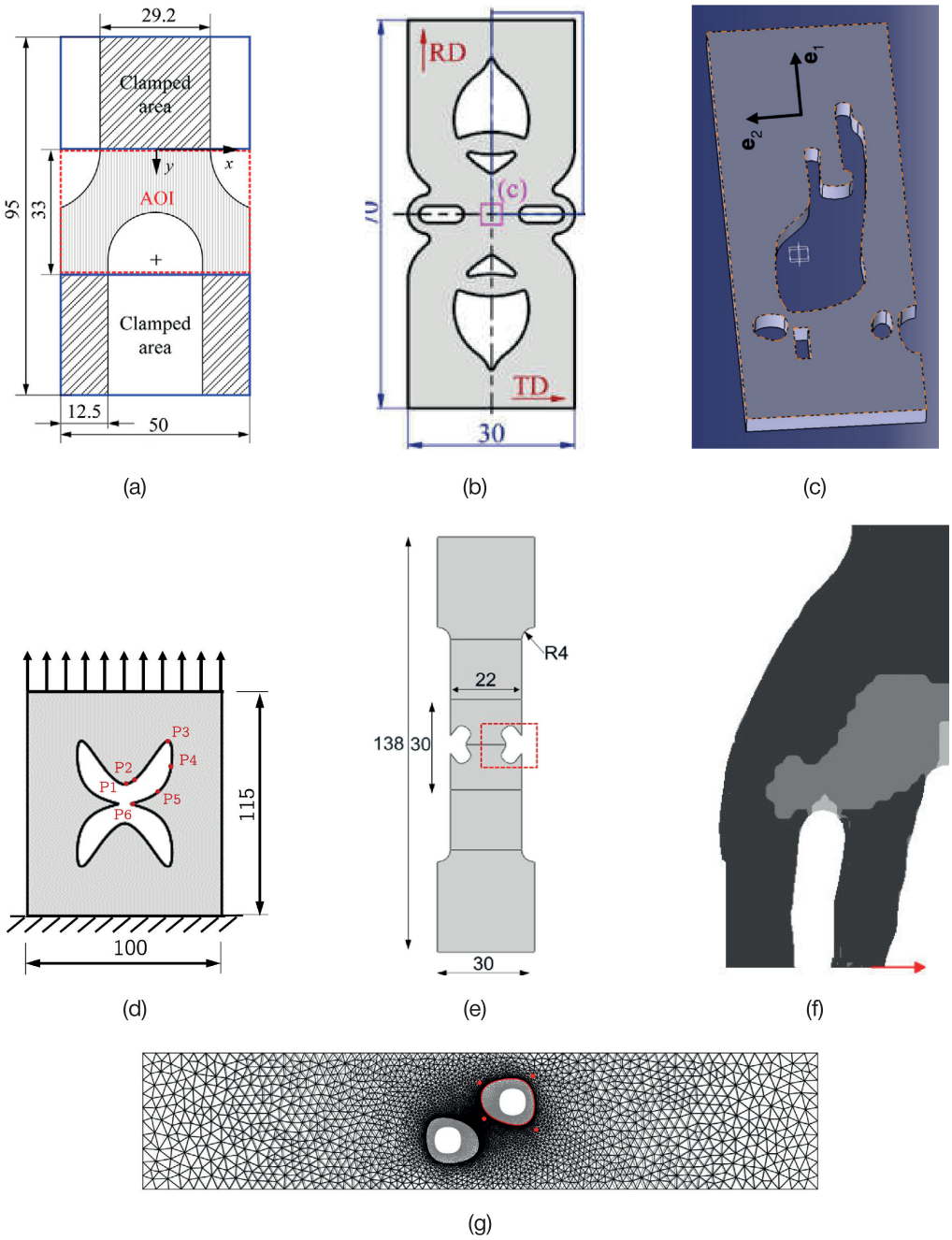

Figure 3.5 Geometry of the specimens proposed : (a) Fu et al. (2020), (b) Maček et al. (2020), (c) Chamoin et al. (2020), (d) Conde et al. (2021), (e) Zhang et al. (2022a), (f) quarter-shape of Gonçalves et al. (2022), and (g) Chapelier et al. (2022).

more innovative methodologies. The first heterogeneous tests used, in general, simple notches or holes, while nowadays irregular shapes and multiple holes are more prominent. If future tests follow the trend here observed, the complexity of the specimens will increase. This will lead to the need for advanced manufacturing processes and complex experimental apparatus, such as buckling devices. However, selecting the best test is not an easy task due to lack of comparative studies using suitable metrics. The following section provides an overview of biaxial loading tests.

3.3 Biaxial Loading Tests

The use of a cruciform specimen, coupled with full-field displacement or strain measurements, has gained interest in the development of inverse identification strategies. In general, this test allows reaching strain paths ranging from uniaxial tension (in the arms region of the specimen) to equibiaxial tension (in the center region of the specimen), and high strain gradients from the center region of the specimen to the end of the arms region. Also, by changing the load or displacement ratio over the two normal loading axes, several biaxial stress states in the central region of the specimen can be achieved. However, this type of test only allows obtaining low values of equivalent plastic strain before rupture occurs. Nevertheless, by loading the specimen in two directions (RD and TD), it is possible to characterize a larger spectrum of the material anisotropy compared to most uniaxial loading tests (Hannon and Tiernan 2008).

Makinde et al. (1992) pioneered the development of heterogeneous mechanical tests to tackle the lack of suitable standard biaxial loading tests. The study designed a cruciform specimen using a statistical method of factorial and response surface designs in combination with FEA simulations. The resulting geometry presents a circular reduced central region (see Figure 3.6a), and the stress and strain states distribution was better than other geometries.

Yu et al. (2002) designed an optimal shape of a cruciform specimen by manually adjusting the geometrical parameters. The specimen was designed to obtain a uniform stress distribution in the central region and achieve large deformations. The geometry presents a chamfer on the arms and on the central region (see Figure 3.6b). Moreover, different strain paths in the central region, ranging from uniaxial tension to biaxial tension, can be obtained by adjusting the velocity of boundary conditions.

Cooreman (2008) proposed a biaxial test on a perforated cruciform specimen (see Figure 3.6c) to simultaneously identify the material parameters of Hill 1948 anisotropic yield criterion and Swift isotropic hardening law to describe the plastic behavior of a dual-phase steel with 0.8 mm of thickness. The study performed an experimental test with this specimen using DIC and use of 7 load steps in the identification procedure. The isovalues distribution of strain at the last step show that the test presents considerable heterogeneity, though the levels of strain in the RD and the TD are relatively low. On the other hand, the levels of shear strain are considerably high. Additionally, the obtained values of equivalent plastic strain at the end of the last load step are low (approximately 0.23), indicating that this test might not adequately represent the higher strain values that occur in sheet metal forming operations. The results of the Swift hardening law are satisfactory, except for the parameter controlling the initial yield strain, which was justified by the lack of information close to the yield point.

Zidane et al. (2010) investigated several cruciform specimen geometries and identified a promising one for which necking appears in the central region. Based on the most promising geometry, an optimized geometry was manually proposed by adjusting two geometrical parameters (see Figure 3.6d). This geometry concentrates and achieves stress states between uniaxial tension and biaxial tension in the central region, and has been numerically and experimentally validated for an aluminum alloy.

Teaca et al. (2010) designed two cruciform specimens that achieve a wide range of mechanical states and are highly sensitive to the material anisotropy (see Figure 3.7). to identify the material parameters of an advanced anisotropic yield criterion for two materials with 1 mm of thickness. The material characterization is performed for stress paths ranging from uniaxial to plane strain tension with the specimen UT/PST and from uniaxial to equibiaxial tension with the specimen UT/EBT. For the UT/PST specimen, average mechanical states in the arms (RD region) and connecting parts between arms are close to uniaxial tension and plane strain tension, respectively. In the case of the UT/EBT specimen, mechanical states along the RD vary between equibiaxial tension in the center and uniaxial tension in the central ligament of the arm. According

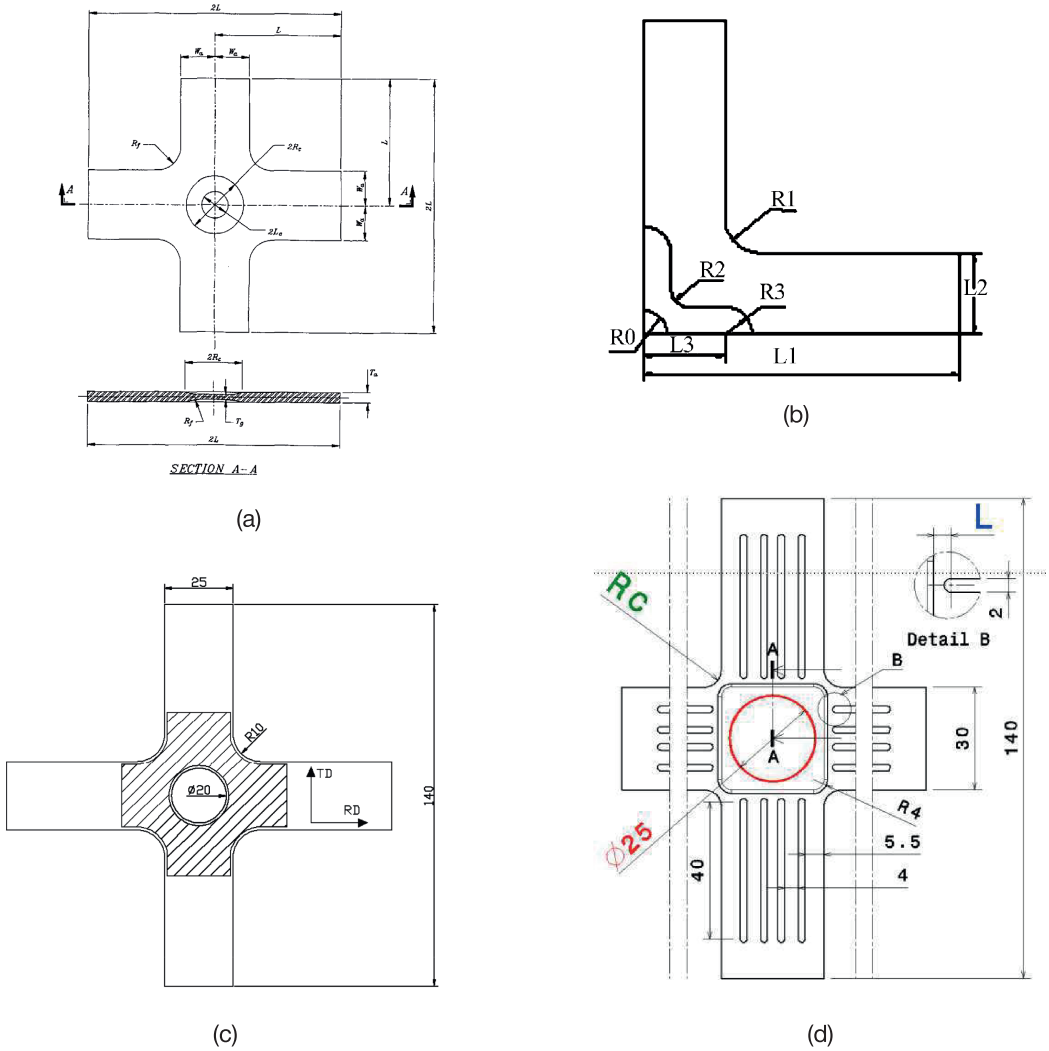

Figure 3.6 Geometry of biaxial loading specimens (dimensions in mm): (a) Makinde et al. (1992), (b) quarter-shape of Yu et al. (2002), (c) Cooreman (2008), and (d) Zidane et al. (2010).

to the study, the main advantage of both specimens is the multiple mechanical states achieved in a single biaxial test, allowing the reproduction of mechanical states close to those encountered in industrial sheet metal forming processes. Nevertheless, the observed mechanical states and deformation levels are similar to those observed in other cruciform specimens.

SCHMALTZ AND WILLNER (2014) explored the usability of the biaxial test on three cruciform specimen geometries (see Figure 3.8), promoting different types of heterogeneous strain fields. The study identified the material parameters of the Hill 1948 yield criterion and an isotropic hardening law for a 2 mm thick steel. The first geometry is designed to present a homogeneous strain distribution in the center region of the specimen, without using slits or perforations (G#1). The second geometry presents the same shape as the first, but with a hole in the center region of the specimen to generate an heterogeneous strain distribution (G#2), and the third geometry is designed so that under biaxial tensile conditions, the center region rotates, generating tension, shear and compressive stresses (G#3). Additionally, the study performed a fourth test to generate more compressive stresses (G#4), using the same geometry as G#2, but loaded by compressive forces in the y direction and by tensile forces in the x direction. From the experimentally determined strain state, tests G#2 and G#3 present a wide range of strain distributions comparatively to test G#1 in

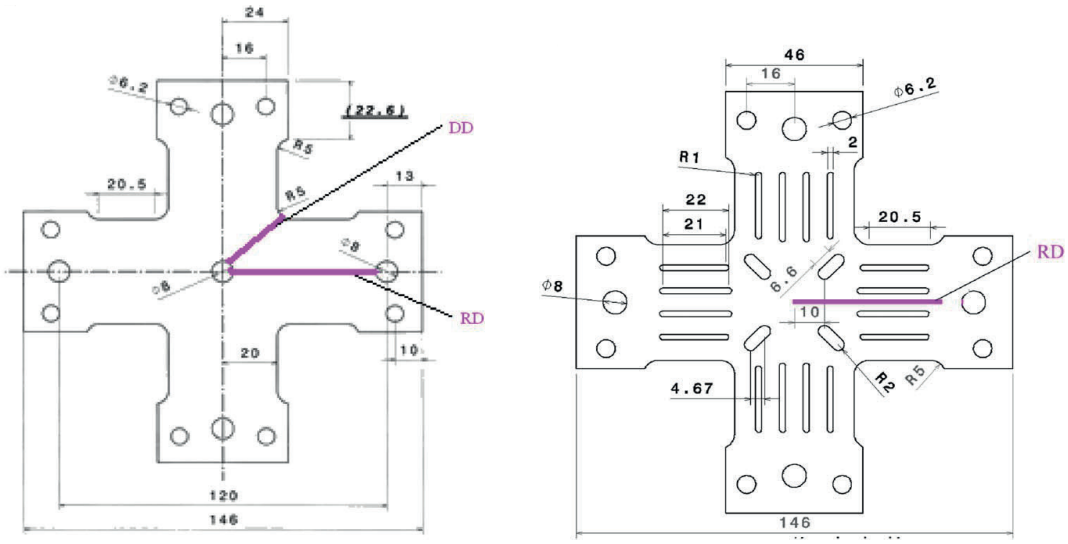

(a) UT/PST (b) UT/EBT

Figure 3.7 Geometry of the biaxial loading specimens (dimensions in mm) proposed by Teaca et al. (2010).

the tensile spectrum, with test G#2 also presenting some equibiaxial tension state, though with relatively small values of major and minor strains. On the other hand, test G#4 presents a strain distribution mainly in the shear state, with both dominant tensile and compressive components. The study concludes that the test G#4 should yield the best identification results, though this is not observed later in their identification. The study argues that the implemented model does not take into account that the real material behavior in the compression region is different compared to the one in the tensile direction, and does not include kinematic or anisotropic hardening.

PRATES ET AL. (2014) proposed an inverse methodology for determining the material parameters of the Hill 1948 yield criterion and the Swift hardening law from a single biaxial tensile test using an optimized 1 mm thick cruciform specimen (see Figure 3.9a). The geometry of this specimen was designed to reproduce heterogeneous strain paths observed in sheet metal forming operations. The specimen geometry demonstrated to cover a range of strain paths from equibiaxial tension to uniaxial tension. The proposed specimen was not experimentally tested, and the numerical results show that at the center of the specimen, the equivalent plastic strain presents low values of approximately 0.03, while the maximum values of approximately 0.3 are obtained

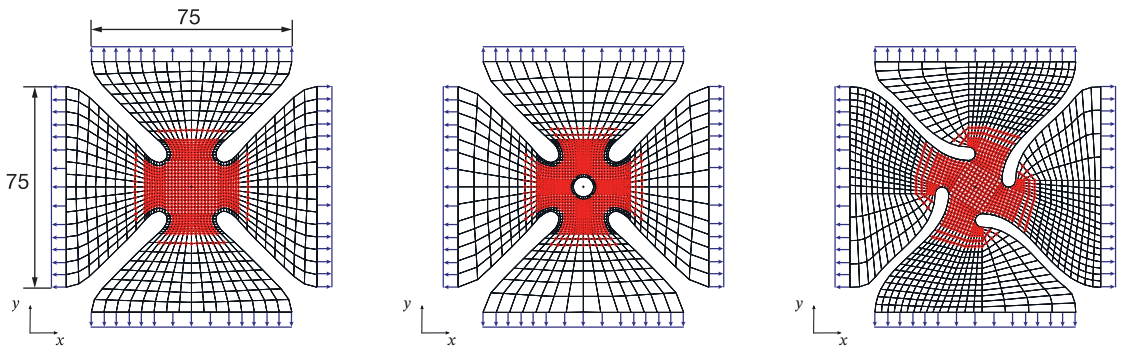

(a) G#1 (b) G#2 (c) G#3

Figure 3.8 Geometry of the biaxial loading specimens (dimensions in mm) proposed by Schmaltz and Willner (2014).

along the arms of the specimen. Moreover, the study performed a sensitivity study using five virtual materials (variations of the parameters of the constitutive models). The results showed that variations in the material parameters of the hardening law did not influence the strain paths, but in the anisotropic material parameters could lead to substantial differences.

Liu et al. (2015) designed an optimized cruciform sample with a thickness-reduced central zone and four slots at each arm (see Figure 3.9b), to characterize the hardening behavior of an aluminum alloy with 2 mm of thickness. The optimized geometry was obtained from a parametric study of five variables controlling the position of notches and slots. The use of a thickness-reduced central zone and slots at each arm in biaxial tensile specimens is to concentrate strains in the central zone, avoiding strain localization at notches. The study performed an experimental test of the specimen using DIC to calculate the strain fields on the surface. The equivalent strain reaches 0.30 just before crack, and the principal strains are about 0.16 for the major strain and 0.14 for the minor strain in the center of the specimen. The maximum deformation is observed in the fillet between the flat central zone and the non-reduced thickness zone on the central axis of the specimen (TD). Although the maximum equivalent plastic strain is relatively high, the range of strain paths is not wide – mainly between equibiaxial and uniaxial stress – therefore not providing a wide variety of strain paths required to characterize the material states in sheet metal forming operations. The study attempted to identify the hardening behavior of the material using three distinct yield criteria (one isotropic and two anisotropic), and the results are relatively good. However, it was not investigated the potential of the specimen to identify the material parameters of anisotropic yield criteria.

Zhang et al. (2015) investigated the use of a cruciform specimen without slits or perforations (see Figure 3.9c) to identify the material parameters of anisotropic yield criteria for an aluminum alloy and a dual-phase steel, respectively, with 1 mm and 1.75 mm of thickness. The experimental results of the designed cruciform specimen show that the observed strain path is nearly equibiaxial for both materials in the central region. It then changes gradually along the diagonal direction to nearly uniaxial tension near the corner. Overall, the observed strains are relatively small for both materials, and the range of strain paths is not good enough to characterize the anisotropic behavior of a given material.

Martins et al. (2019) investigated the use of the same geometry as Zhang et al. (2015), as well as some variations to identify the material parameters of the Hill 1948 and the Yld2000-2d yield criteria with the Swift isotropic hardening law using virtual experimental data of a mild steel and an aluminum alloy. The study concluded that the original geometry proposed by Zhang et al. (2015) lacks information for shear stress states for the mild steel using the Hill 1948 yield criterion, and that using the adapted geometry (see Figure 3.9d), an increase of areas with shear states is observed. Then, an identification of the material parameters for the aluminum alloy using the Yld2000-2d yield criterion was carried out using the adapted geometry. The results show that the adapted test is sensitive to the material, because the shear paths are different comparatively to the mild steel. Also, the plastic behavior of the aluminum alloy leads to more information near plane strain, but leads to a decrease of information in the shear region. From these two studies, it is essential to note that the richness of the test seems to depend significantly on the used material. Therefore, it is of utmost importance to analyze the richness of a test for more than one material.

Kim et al. (2021) designed a cruciform specimen that generates combined tension and shear states on in the gauge section. The specimen shape is based on the combination of a general cruciform specimen and a simple shear specimen (see Figure 3.9e). Its geometry was optimized by evaluating several shapes restricted by geometrical constraints to avoid generating plastic deformation outside the gauge section (Kim et al. 2022). The optimize shape showed large stress concentrations near the fillets, but provided good stress uniformity in the central region for different combinations of force ratio, leading to either a predominant tension or shear state.

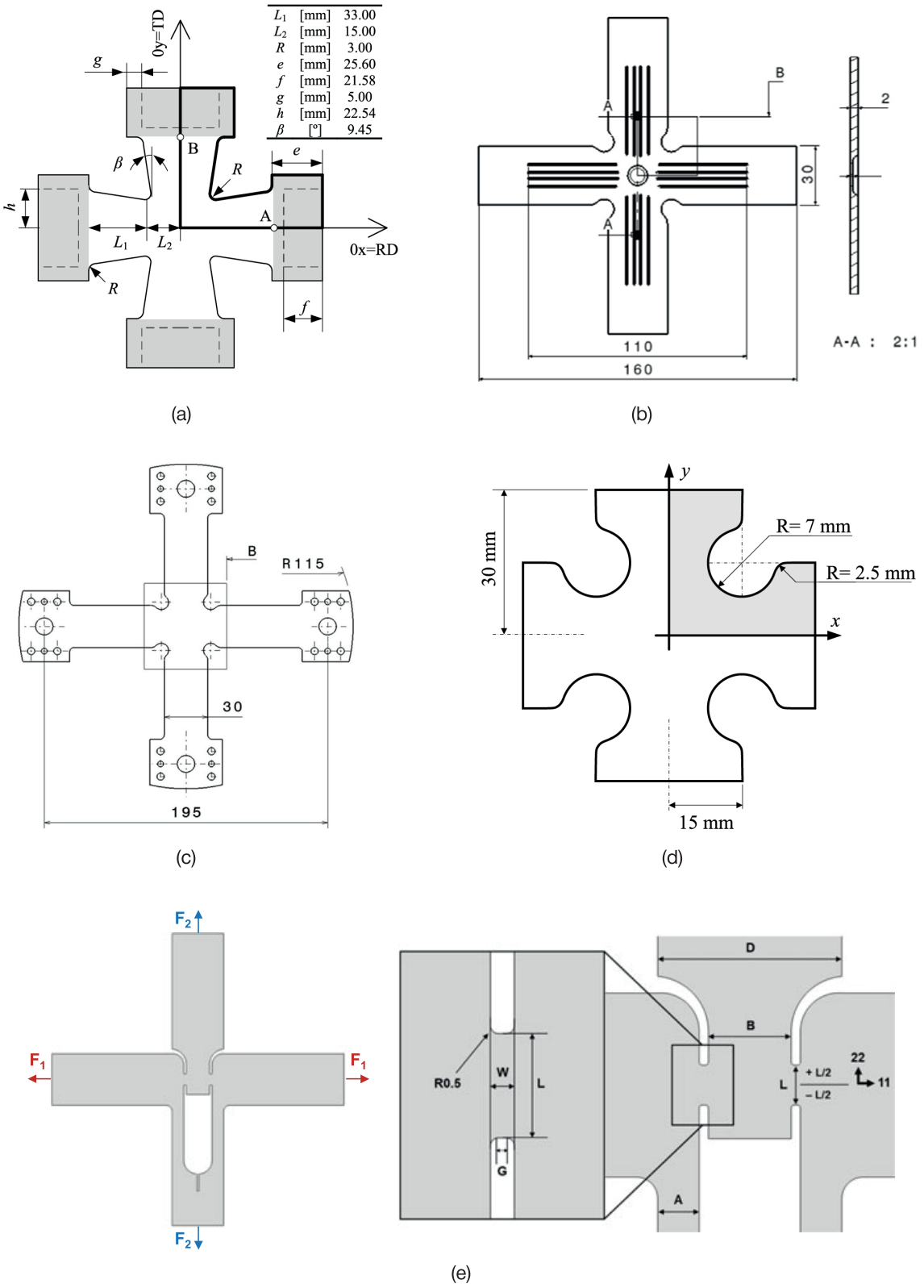

Figure 3.9 Geometry of biaxial loading specimens (dimensions in mm): (a) Prates et al. (2014), (b) Liu et al. (2015), (c) Zhang et al. (2015), (d) Martins et al. (2019), and (e) Kim et al. (2021).

In general, the biaxial test with cruciform specimens results in relatively low values of equivalent plastic strain, while some studies use thickness-reduced center regions of the specimen to increase these. However, the mechanical state usually ranges from equibiaxial to uniaxial tension, with a reduced number or even no strain paths in the shear state.

3.4 Out-of-Plane Loading Tests

POTTIER ET AL. (2012) designed an experimental procedure based on out-of-plane displacements similar to the Nakazima test. However, the specimen geometry is designed to exhibit highly heterogeneous strain paths (see Figure 3.10a), where a hemispherical punch is used to apply the prescribed displacement at the sample center, which is circular, tightly encircled and fastened between the die and the holder. The specimen is designed to exhibit tension (at 0° and 90° from the RD), shear (at 0° and 90°), and expansion, as well as an isoprobability of fracture in the tension and the shear zones (isotropic material). The strain level in expansion remains weaker than in the tension or shear zones, where the maximum levels of strain are relatively high, of 0.62 and 0.95, respectively. From the identification results, the study concludes that the test can lead to the identification of material parameters of an anisotropic plastic model. WANG ET AL. (2019) used this test to characterize the anisotropic behavior of an aluminum alloy at 200 °C, using the Yld2000-2d yield criterion. The obtained results were validated using a deep drawing test, which showed a good agreement between experiments and numerical simulations.

HAPSARI ET AL. (2018) designed a micro incremental deformation test based on the principle of single point incremental forming (see Figure 3.10b). This test consists of locally deforming a clamped blank using a hemispherical tool, where large deformations (approximately 240 %) and multiple strain paths can be achieved. The study characterizes the ductile damage behavior of a copper foil with 0.21 mm of thickness. In a first step, the study identifies the material parameters of a hardening law using classic uniaxial tensile tests up to 0.3 values of deformation. Then, the material parameters of the same hardening law with a damage model are identified by using a FEMU approach, where the objective function was composed of the forming forces between experiments and numerical simulations. The identified material parameters of the hardening law in the second step are similar to those obtained in the first step. Nevertheless, without the second step, it would not have been possible to identify the damage material parameters due to damage growth and necking in the tensile tests.

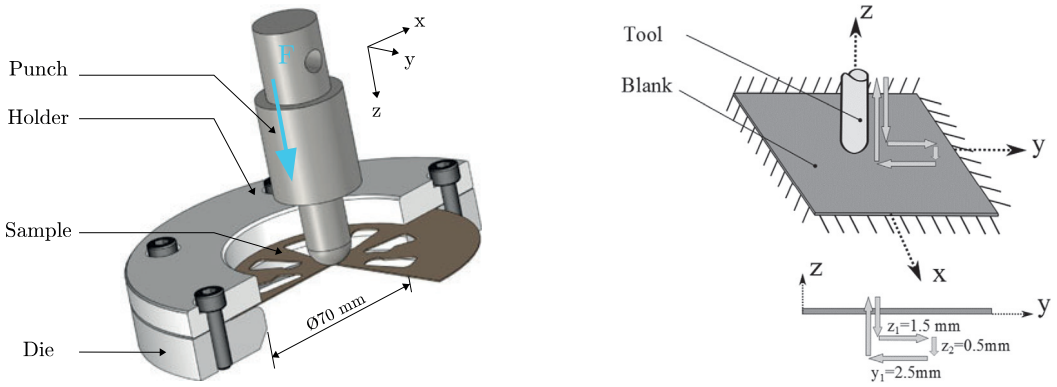

Figure 3.10 Configuration of the out-of-plane loading tests proposed by (a) Pottier et al. (2012) and (b) Hapsari et al. (2018).

3.5 Conclusions

An extensive overview of heterogeneous mechanical tests reported in the literature to characterize the mechanical behavior of sheet metals has been presented. In Figure 3.11, a distribution of designed tests over time is presented, where it is shown that this topic emerged approximately 20 years ago and has since seen more than 40 new tests developed. Historically, the uniaxial loading tests have always been largely developed, though it is seen that the biaxial loading tests have also been similarly investigated up to 2014. However, the trend has been to design uniaxial loading tests using different and innovative methodologies.

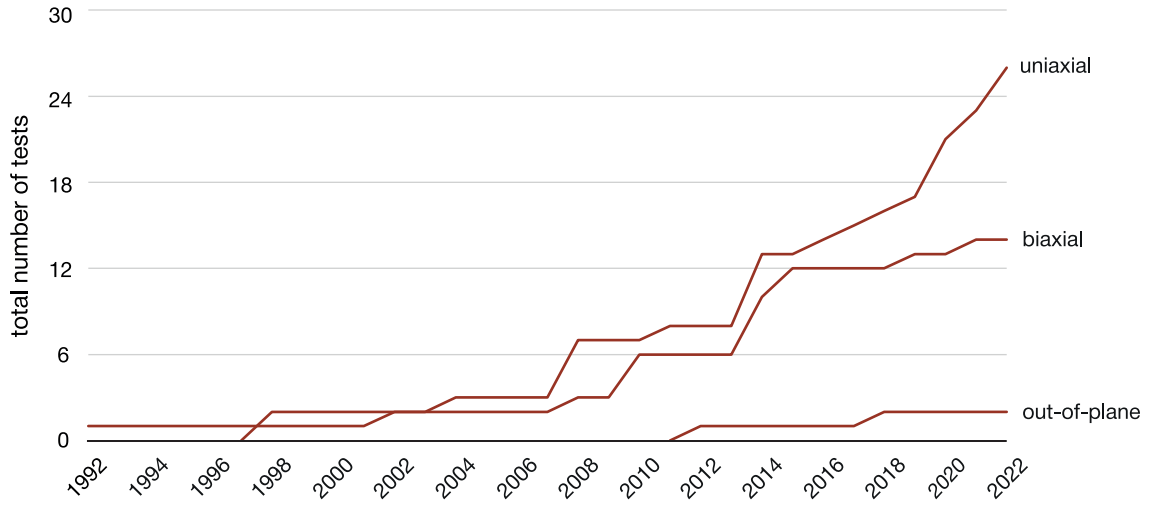

Figure 3.11 Distribution over time of designed heterogeneous mechanical tests for sheet metals, divided in uniaxial, biaxial and out-of-plane loading.

Many studies have focused on the use of cruciform specimens under biaxial loading, where it is possible to achieve mechanical states ranging from uniaxial to equibiaxial tension. To reach large levels of deformation, some studies have experimented with the use of perforated cruciform specimens, thick-reduced zones, or even slots in the arms. However, the levels of strain are still relatively low to fully characterize the hardening behavior of the material. Other studies have used uniaxial loading tests, where it is possible to use complex geometries and achieve various mechanical states (such as shear, uniaxial tension, or biaxial tension). To design the specimen geometries, some studies use innovative methodologies, such as shape or topology optimization. Nevertheless, it was also shown that others are manually proposed based on the authors experience and creativity. However, a single test might not characterize the material behavior or fully retrieve the best material parameters. For that reason, some studies have combined two identical tests with different material orientations to enrich the quality of available data. Moreover, one common problem with these tests is their sensitivity to the material, as the mechanical state and level of deformation can vary. Therefore, it is not an easy task to quantify the richness of the heterogeneous test in a general way.

Regarding the application of heterogeneous tests to identify the material parameters of constitutive models, it is fair to observe that studies tend to focus on simple yield criteria and isotropic hardening laws. Only a single study is reported that identifies the material parameters for a non-linear kinematic hardening law, where reverse loading conditions are necessary. When the identification is performed with finite element based inverse methods (such as FEMU), accurate reproduction of the tests boundary conditions is essential for its success (Kacem et al. 2021). However, the latter is not always easy due to possible sliding between the grips and specimen, lateral loads, or contact between the tools and the specimen.

Furthermore, only a few specimens are analyzed by different studies and conditions, resulting in a lack of information on the proposed tests. The comparison of the proposed specimens is not trivial, as some studies do not present the same information, or their results lack information to assess the richness of the tests. These tests are not yet able to extensively characterize the material behavior, as it is achievable using multiple quasi-homogeneous tests. Nevertheless, the use of heterogeneous mechanical tests is promising in terms of the decrease in the number and cost of experiments, by providing richer mechanical information in a single experiment.

4 Evaluation of Heterogeneous Mechanical Tests

4.1 Introduction

The mechanical design of sheet metal forming parts tends to be more virtual, decreasing associated delays and manufacturing processes costs. Consequently, materials' mechanical characterization has received increased attention due to the need for accurate input data to computational analysis software.

The mechanical behavior of the materials can be numerically described through constitutive models, which can be calibrated using standard quasi-homogeneous mechanical tests (Souto et al. 2015b). Nevertheless, from a single classical mechanical test, it is difficult to extract many material parameters. It requires several tests to identify many material parameters of a single constitutive model (Barlat et al. 2005; Cazacu et al. 2006).

More recently, research has focused on alternative methods based on mechanical tests that induce heterogeneous strain fields, measured through full-field experimental techniques, providing significantly more valuable data (Haddadi and Belhabib 2012; Grédiac et al. 2020). Ideally, a single mechanical test should be enough to characterize the material's mechanical behavior. However, the accuracy of these alternative methods depends on several factors (Pierron and Grédiac 2021): (i) the applied load and shape of the specimen used in the mechanical test (Pierron 2020), (ii) the choice of an appropriate strain field measurement technique (Blaysat et al. 2020), or (iii) the definition of an identification strategy (Prates et al. 2016). Indeed, the heterogeneity does not lead to any analytical post-treatment, and a suitable inverse methodology, such as the FEMU (Aquino et al. 2019) or the VFM (Grédiac et al. 2006; Pierron and Grédiac 2012), is required.

Although many challenges still exist in this field, research still focuses on selecting and designing the most suitable heterogeneous mechanical tests for sheet metals' constitutive model calibration. In recent times, the design of novel heterogeneous mechanical tests using different strategies has increased (see Chapter 3). An innovative approach adopted a shape optimization procedure to design a butterfly-shaped specimen under uniaxial tensile loading (Souto et al. 2016; Souto et al. 2017). A different approach analyzed configurations of notched specimens by evaluating the error between synthetic images and numerical simulations (Rossi et al. 2016a). More recently, some studies used topology optimization, allowing more flexibility in the design process, and resulting in complex geometries (Barroqueiro et al. 2020; Chamoin et al. 2020).

Another study proposed a bridge-like specimen based on the plate buckling theory (Fu et al. 2020). The bridge-like specimen is the first attempt to design a heterogeneous mechanical test that can characterize the mechanical behavior of sheet metals under cyclic loadings.

Generally, the quality and quantity of heterogeneous mechanical tests have increased. However, a qualitative or quantitative comparison is not straightforward, because studies use different materials and representations of output data. To solve this problem, Souto et al. (2015a) proposed a quantitative indicator to evaluate and classify mechanical tests. The indicator evaluates the mechanical test up to rupture and is based on the strain heterogeneity. Although this methodology is innovative, it can depend on the material, and did not consider the sensitivity of the tests to material anisotropy (Martins et al. 2019). Additionally, the sensitivity of heterogeneous mechanical tests to the material parameters is a relevant metric to evaluate their richness (Souto et al. 2015a). In this scope, Hapsari et al. (2018) used an indicator that quantifies the identifiability of a parameters' subset based on the largest and smallest eigenvalue of the dimensionless sensitivity matrix. Nevertheless, this methodology depends highly on the constitutive model and can be computationally expensive. More recently, Zhang et al. (2022b) also investigated the identifiability of the anisotropic material parameters through a sensitivity analysis. The study concluded, among other things, that the material orientation plays a major role in the success of the identification. Moreover, the study recommends against evaluating the identification quality by comparison to the reference parameters or the objective function values. Instead, representations of the material behavior should be used, such as the Lankford coefficients or normalized yield stresses at various material orientations. Another interesting study evaluated the robustness of heterogeneous mechanical tests in terms of measurement biases through virtual experiments (Thoby et al. 2022).

To fill the existing gap in the evaluation of heterogeneous mechanical tests, this study proposes metrics based on the strain and stress states. Within a numerical approach, four heterogeneous mechanical tests are evaluated by considering three different materials. Furthermore, a metric based on the Mohr's circle formulation is proposed to evaluate the tests' sensitivity to material anisotropy.

4.2 Heterogeneous Mechanical Tests

The four heterogeneous mechanical tests selected were selected from the previous survey to include different shapes in the present study (see Chapter 3). In general, these tests were proposed to maximize the strain field heterogeneity. One test resembles a uniaxial tensile test (see Figure 3.2d), another is biaxial loading (see Figure 3.8c), and two others are uniaxial loading with complex geometries (see Figures 3.3b and 3.4d).

The tests are modeled using symmetry conditions to reduce the computational cost of numerical simulations, and the loading is displacement driven. The tests, named A, B, C, and D, and boundary conditions of the finite element models are described and shown in Figure 4.1. It should be noted that the x and y axes correspond to the global coordinate system (x, y), respectively, coincident with the TD and the RD for all tests. The material coordinate system (x', y') rotating with deformation is initially coincident with the global coordinate system.

Test A is a biaxial tensile test with a centered hole, designed to generate a heterogeneous strain field (Schmaltz and Willner 2014). The authors considered that the test could reach levels of deformation able to properly calibrate the hardening behavior, and that it was also able to characterize the anisotropic behavior. The specimen's design is interesting, as the arms are wide and create a short empty region between them. However, the specimen's geometry is not easily modeled because of the lack of given dimensions. The authors concluded that the range of stress states was confined between uniaxial tension and equibiaxial tension states. Nevertheless, the test constitutes a good basis for this analysis because it presents classical characteristics of a

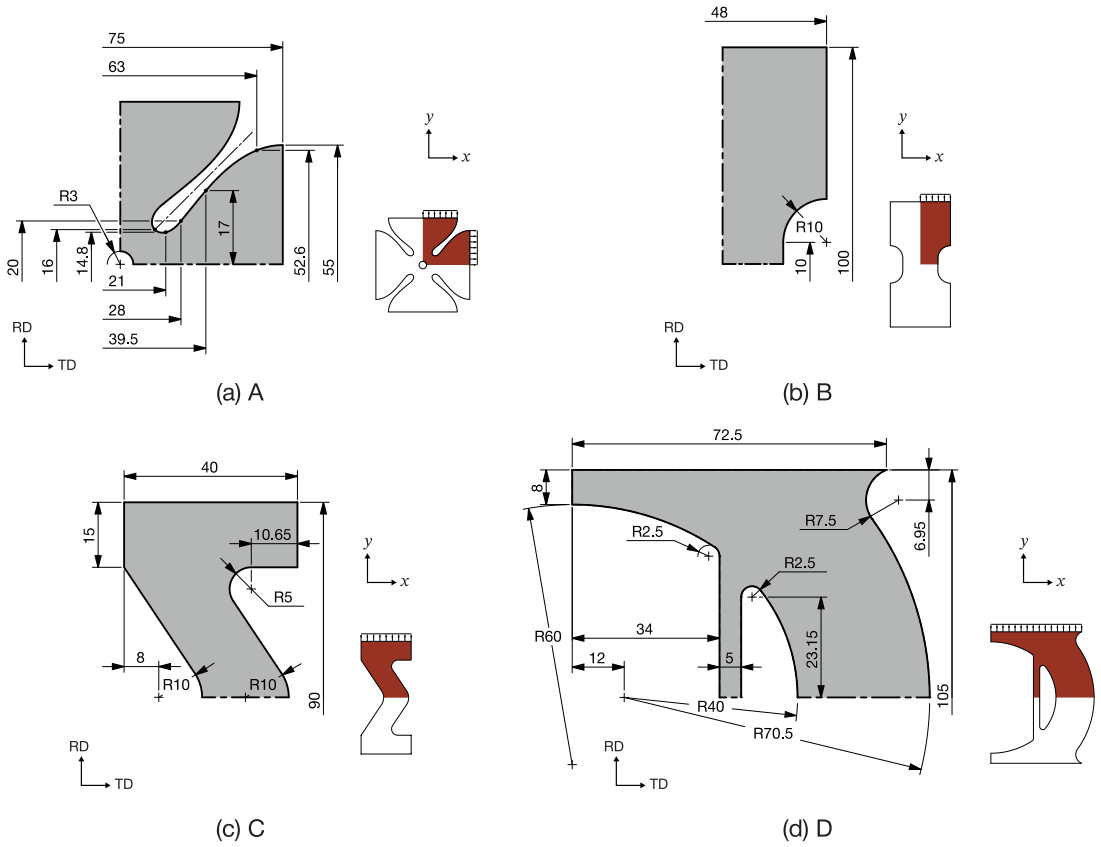

Figure 4.1 Geometry (dimensions in mm) and boundary conditions of the finite element models for the heterogeneous mechanical tests (a) A, (b) B, (c) C, and (d) D. The specimen's geometry is represented using symmetry conditions, while the full geometry is recalled on the right-hand side.

biaxial tensile test and adds features that enhance the heterogeneity of strain and stress states. The numerical model uses symmetry conditions along the x and y axes, with both corresponding to loading directions (see Figure 4.1a).

Test B was designed as a hybrid shape between a uniaxial tensile test and a uniaxial plane strain tensile test (Belhabib et al. 2008). The shape's interest was investigated by comparing it with standard mechanical tests and evaluating the strain field's heterogeneity and sensitivity to material parameters. Additionally, the numerical comparison accounted for the limitations of DIC, by not considering the regions of the sample near the free edges, and where strain level is below DIC accuracy. This study concluded that the new heterogeneous mechanical test performed better than standard mechanical tests in all criteria. Thanks to its simple geometry, test B represents a good benchmark in this analysis, avoiding the complexity of other heterogeneous mechanical tests. The numerical model uses symmetry conditions along the x and y axes, with the latter corresponding to the loading direction (see Figure 4.1b).

Test C is a uniaxial tensile test, designed from empirical knowledge and trial and error, resulting in a geometry resembling a Greek capital letter sigma Σ (Kim et al. 2014). The authors showed that this test exhibits various stress states. Also, combining two tests loaded in different material orientations increased the mechanical information and improved the calibration. Test C is numerically modeled using one symmetry condition along the y axis, aligned to the loading direction (see Figure 4.1c).

Test D is a uniaxial tensile test, designed via an iterative process of finite element analyses (Jones et al. 2018). The process started with a shape based on empirical knowledge, then manu-

ally adjusted to meet several criteria, such as maximizing stress heterogeneity and minimizing large gradients in strain near free edges. The optimized geometry resembles a capital letter "D", and the authors showed that it could cover a reasonable extent of stress states. Similarly to test C, one symmetry condition along the y axis is used in the numerical model of test D, which coincides with the loading direction (see Figure 4.1d).

The numerical models are developed in 2D, assuming a plane stress state formulation. A four-node bilinear plane stress element, with reduced integration and stiffness hourglass control, is used, as well as a large strain formulation. A refined mesh with a maximum element size of 0.1 mm is used, to obtain many material points approaching a continuous state of the material. Furthermore, to account for the limitations of a subset-based DIC system, which does not provide information near the specimen's free edges, the results are analyzed for a region of interest (ROI), defined by an arbitrary boundary of 0.25 mm on the free edges of the specimen. The numerical simulations are performed with automatic time stepping, and a maximum increment size of 0.01. Finally, the numerical simulations are performed with Abaqus/Standard software (Dassault Systèmes 2019), and the constitutive models are implemented through the UMMDp (see Section 2.4).

4.3 Virtual Materials

Three virtual materials are considered to account for the heterogeneous mechanical tests' sensitivity to different materials: (i) an aluminum alloy (AA2090-T3) with a nominal thickness of 1.6 mm (Yoon et al. 2006; Comsa et al. 2011; Abedini et al. 2018); (ii) a dual-phase steel (DP600) with a nominal thickness of 0.8 mm (Ozturk et al. 2014); and (iii) a cold-rolled sheet of 99.9 % pure copper (Cu) with a nominal thickness of 0.1 mm (Pham et al. 2017; Thuillier et al. 2018).

For simplicity's sake, a plane stress state formulation is chosen. The elastic properties of the materials, the material parameters of the Yld2000-2d anisotropic yield criterion, and the Swift isotropic hardening law are provided in Table 4.1 (see Section 2.3 for details on the models formulation). It is worth highlighting that the material parameters of AA2090-T3 and DP600 are selected from the literature. On the other hand, the material parameters of Cu were identified using a classical approach, with quasi-homogeneous mechanical tests using a methodology identical to Souto et al. (2015b). Although the latter identification is not presented in this study, it can be said that a good agreement was obtained between experimental and numerical data. Therefore, the three materials considered in this study come from real experiments, providing a realistic description of the mechanical behavior up to a certain deformation level. Moreover, the same phenomenological models are used for the three materials to have a straightforward and easier comparison between them

Concerning the material's mechanical behavior, DP600 is characterized by a much higher initial yield stress than AA2090-T3 and Cu, while the latter presents a much lower hardening rate than the former (see Figure 4.2). Moreover, Figures 4.3a and 4.3b present the normalized yield stress and the Lankford coefficient for various material orientations. These representations show the considerable variation of both normalized yield stress and Lankford coefficient of AA2090-T3 compared to Cu and DP600. Besides, the latter exhibits, on average, values close to 1 in both representations, while the Lankford coefficients of Cu are below 1, representing a relatively high normal anisotropy. The yield surface projection on the plane of normalized RD-TD and shear-RD stress also highlights the anisotropic behavior, respectively, represented in Figures 4.3c and 4.3d.

4.3.1 Forming Limit Curves

In evaluating heterogeneous mechanical tests, it is relevant to consider the maximum deformation the material can sustain relative to a specific condition. This condition can be, among others, a rupture criterion or a forming limit curve (FLC). The latter is a feature of the forming limit

Table 4.1 Elastic properties of the materials and parameters used in the Yld2000-2d anisotropic yield criterion and the Swift isotropic hardening law, for AA2090-T3 (Yoon et al. 2006; Abedini et al. 2018), DP600 (Ozturk et al. 2014) and Cu.

		Material		
Model	**Parameter**	AA2090-T3	DP600	Cu
Elasticity	E [GPa]	69	210	104
	ν [–]	0.33	0.3	0.28
Yld2000-2d	α_1 [–]	0.860	1.011	0.893
	α_2 [–]	0.929	0.964	1.013
	α_3 [–]	0.957	1.191	0.644
	α_4 [–]	0.977	0.995	0.985
	α_5 [–]	1.063	1.010	0.981
	α_6 [–]	1.039	1.018	0.857
	α_7 [–]	-1.251	0.977	0.958
	α_8 [–]	1.45	0.935	1.322
	a [–]	8	6	8
Swift	σ_0 [MPa]	279.6	355.1	240.2
	K [MPa]	646.0	979.5	350.8
	n [–]	0.227	0.194	0.129

diagram (FLD), typically used to evaluate the formability of sheet metals (Keeler 1961; Zhang et al. 2018). The FLC corresponds to the strain limits the material can sustain without failing. Essentially, the FLC separates the regions where the material may fail (above the FLC), from the regions where it is safe (below the FLC).

With the purpose of a fair comparison between the heterogeneous mechanical tests, an FLC is virtually generated for each material. The adopted shape is a simplified version of real FLCs, but based on typical FLCs and the materials' strain hardening exponent n (see Table 4.1) for the maximum value in the plane strain tensile region ($\varepsilon_2/\varepsilon_1 = 0$), with ε_1 and ε_2, respectively, the major and minor strains (Paul 2013). Moreover, the virtually generated FLCs are characterized by a slope of -1.0 (left-hand side) and 0.5 (right-hand side), as presented in Figure 4.4. Reference data is also added in Figure 4.4 for comparison with the virtually generated FLCs (Comsa et al. 2011; Ozturk et al. 2014; Pham et al. 2017). Although not exact, the virtually generated FLCs are correct approximations of the reference data. Considering the analysis is limited to monotonic loadings, a material point A is expected to present a linear strain path. Thus, if at time instant t the material point A_t is located at a given position in the FLD, the strain path is linear, and the material point is expected to reach the FLC at A_∞. However, the purpose of using the FLC here is simply to know when it is reached. By numerically evaluating the vertical distance (evaluated on the major strain axis, for the same value of minor strain) from the material point A_t to the FLC, represented by the point B_t, it is possible to identify when the limit is reached. Consequently, this distance, represented by W_{FLC}, is numerically evaluated as

$$W_{\mathrm{FLC}} = \frac{\varepsilon_1^{\mathrm{A}_t}}{\varepsilon_1^{\mathrm{B}_t}}, \tag{4.1}$$

where $\varepsilon_1^{\mathrm{A}_t}$ and $\varepsilon_1^{\mathrm{B}_t}$ are, respectively, the major in-plane principal strain at the material point A_t and at the corresponding point B_t on the FLC (see Figure 4.4). Whenever the condition $W_{\mathrm{FLC}} > 1$ is satisfied, the FLC is reached and the test stops.

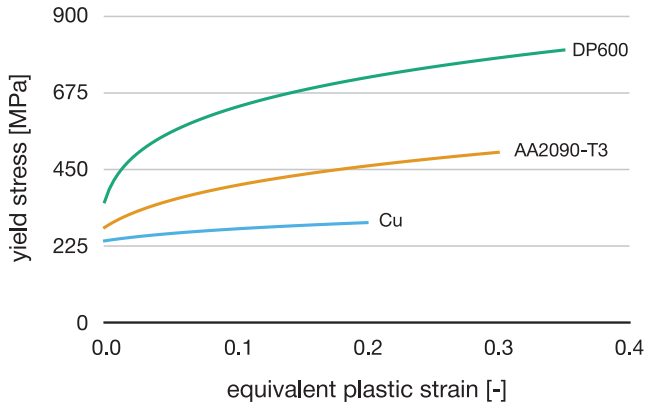

Figure 4.2 Virtual representation of the strain hardening behaviour of AA2090-T3, DP600, and Cu, through the yield stress as a function of the equivalent plastic strain.

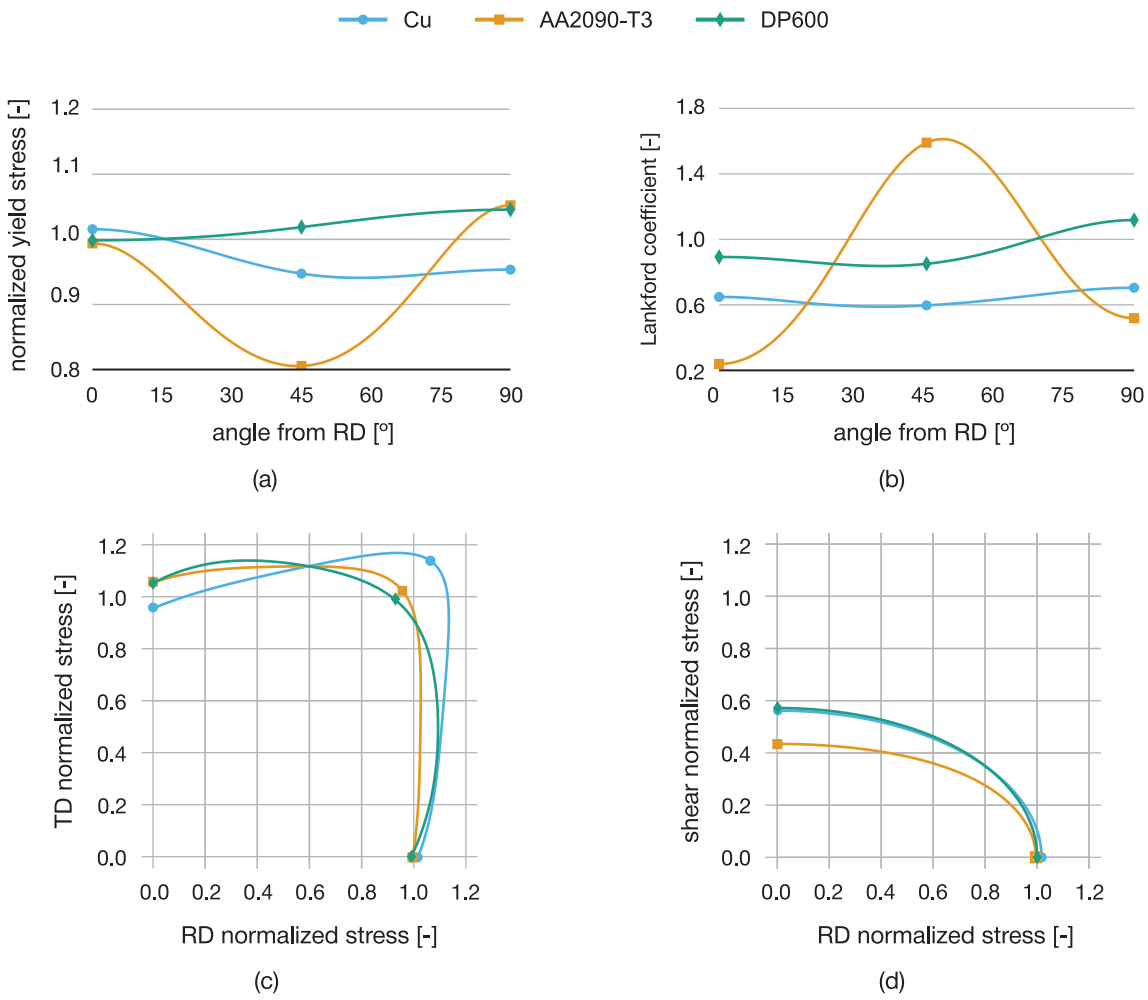

Figure 4.3 Virtual representations of the anisotropic behavior of AA2090-T3, DP600, and Cu: (a) anisotropy of normalized yield stress along material orientations between 0° to 90° from the RD, (b) anisotropy of Lankford coefficient along material orientations between 0° to 90° from the RD, (c) projection of initial yield surface on the plane of RD-TD normalized stress, and (d) projection of initial yield surface on the plane of shear-RD normalized stress.

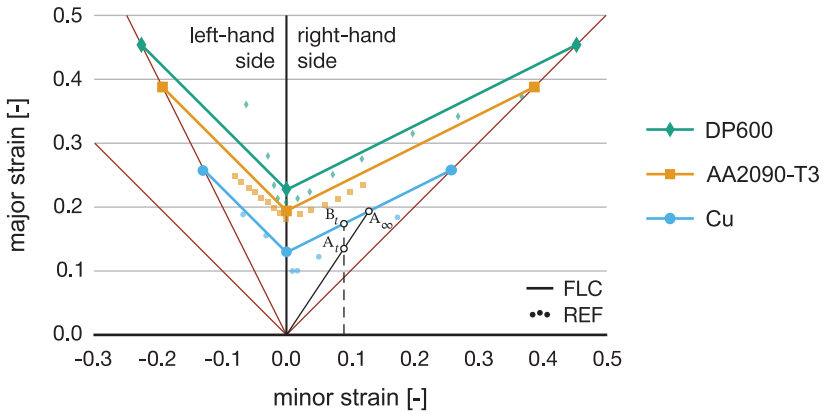

Figure 4.4 Virtual FLCs of AA2090-T3, DP600, and Cu, characterized by the materials' strain hardening exponent n in the plane strain tension region, and by a slope of −1.0 on the left-hand side and 0.5 on the right-hand side of the diagram. Reference data (REF) from the literature is also represented for each material (Comsa et al. 2011; Ozturk et al. 2014; Pham et al. 2017). The position in the FLD of a material point A at the time instant t is represented by A_t, while A_∞ is the position of A when it reaches the FLC on a linear strain path. Material point B_t represents the position used to evaluate the vertical distance from A_t to the FLC.

4.4 Evaluation Metrics

As many heterogeneous mechanical tests already exist, selecting the best one is not a straightforward task. To aid in the decision or design process, studies tend to use standard metrics to evaluate the richness of the tests. This section presents the five metrics selected to evaluate heterogeneous mechanical tests: equivalent plastic strain, major and minor strains, major and minor stresses, stress triaxiality and Lode angle parameter, and rotation angle.

Indeed, total strains can be experimentally measured, and linear strain paths used for the determination of FLDs are easily represented through a strain-based diagram. However, some studies prefer a stress-based representation. To represent the six independent stress tensor components, it is worth using several invariants, such as the principal values, but also the hydrostatic pressure and position in the deviatoric plane. For simplicity's sake, the definition of each metric already assumes a plane stress state formulation.

4.4.1 Equivalent Plastic Strain

The equivalent plastic strain $\bar{\varepsilon}^{\mathrm{p}}$ is a metric that quantifies the level of plastic strain reached during the tests and is given by

$$\bar{\varepsilon}^{\mathrm{p}} = \int_0^t \dot{\bar{\varepsilon}}^{\mathrm{p}} \mathrm{d}t, \tag{4.2}$$

where $\dot{\bar{\varepsilon}}^{\mathrm{p}}$ is the equivalent plastic strain rate (see Equation 2.19). This metric is relevant for metallic materials and in the context of sheet metal forming. Indeed, if more data is available for higher levels of equivalent plastic strain, the calibration accuracy is expected to improve. Concerning heterogeneous mechanical tests, it is beneficial to achieve high equivalent plastic strain levels in many regions. This way, the equivalent plastic strain can also be used as a measure of the heterogeneity of the tests, where a large region of the test presenting high levels of strain is desired, rather than observing strain localization in a reduced region.

4.4.2 Major and Minor Strains

The major and minor strains, respectively, ε_1 and ε_2, with $\varepsilon_1 > \varepsilon_2$, are the principal values of the strain tensor $\boldsymbol{\varepsilon}$ calculated on the sheet plane as

$$\varepsilon_i = \frac{\varepsilon_{xx} + \varepsilon_{yy}}{2} \pm \sqrt{\left(\frac{\varepsilon_{xx} - \varepsilon_{yy}}{2}\right)^2 + \varepsilon_{xy}^2}, \quad \text{with } i = 1, 2, \tag{4.3}$$

where ε_{xx}, ε_{yy}, and ε_{xy} are the strain tensor components calculated on the global coordinate system.

The combination of major and minor strains values can characterize the strain state. This metric analysis is typically presented using the major and minor strains diagram, as shown in Figure 4.5a. Then, as reference values of $\varepsilon_2/\varepsilon_1$ define typical mechanical states for isotropic materials (such as $\varepsilon_2/\varepsilon_1 = -0.5$ defining uniaxial tension and shear by $\varepsilon_2/\varepsilon_1 = -1$, as listed in Table 4.2), the diagram identifies the strain states achieved. The major and minor strains diagram is also known as the FLD.

Moreover, the major and minor strains are relevant to infer the diversity of strain states achieved. A primary characteristic of using the major and minor strains to evaluate heterogeneous mechanical tests is that it can be experimentally measured (Zhang et al. 2015).

4.4.3 Major and Minor Stresses

The major and minor stresses, respectively, σ_1 and σ_2, with $\sigma_1 > \sigma_2$, are the principal values of the stress tensor $\boldsymbol{\sigma}$ calculated on the sheet plane as

$$\sigma_i = \frac{\sigma_{xx} + \sigma_{yy}}{2} \pm \sqrt{\left(\frac{\sigma_{xx} - \sigma_{yy}}{2}\right)^2 + \sigma_{xy}^2}, \quad \text{with } i = 1, 2, \tag{4.4}$$

where σ_{xx}, σ_{yy}, and σ_{xy} are the stress tensor components calculated on the global coordinate system.

Analogously to the major and minor strains, the mechanical state analyzed through the stress tensor represents the stress state. This analysis is typically presented using the major and minor stresses diagram, as shown in Figure 4.5b. Similarly to the major and minor strains, reference values of σ_2/σ_1 represent typical mechanical states (such as uniaxial tension represented by $\sigma_2/\sigma_1 = 0$ and shear by $\sigma_2/\sigma_1 = -1$, as listed in Table 4.2).

These last two metrics are commonly used to evaluate mechanical states' distribution, either through a strain- or stress-based representation. Because the strain fields are obtained from experiments, a strain-based representation is usually associated with experimental data (Belhabib et al. 2008; Güner et al. 2012; Robert et al. 2012; Souto et al. 2015a; Aquino et al. 2019; Wang et al. 2019; Marek et al. 2020). On the other hand, a stress-based representation is more associated with numerical data, because it cannot be directly obtained from experiments (Cooreman et al. 2008; Avril et al. 2008c; Kim et al. 2014; Rossi et al. 2016b; Jones et al. 2018; Barroqueiro et al. 2020; Fu et al. 2020; Thoby et al. 2022). Studies considering both representations are limited (Schmaltz and Willner 2014; Martins et al. 2019).

4.4.4 Stress Triaxiality and Lode Angle Parameter

The stress triaxiality and the Lode angle parameter are two dimensionless indicators that can characterize a mechanical state. Both represent the stress tensor $\boldsymbol{\sigma}$, through stress invariants, and have been used in studies related to ductile fracture (Bai and Wierzbicki 2008; Danas and Ponte Castañeda 2012; Kiran and Khandelwal 2014). Nevertheless, their interest in evaluating the richness of heterogeneous mechanical tests has not yet been investigated. The

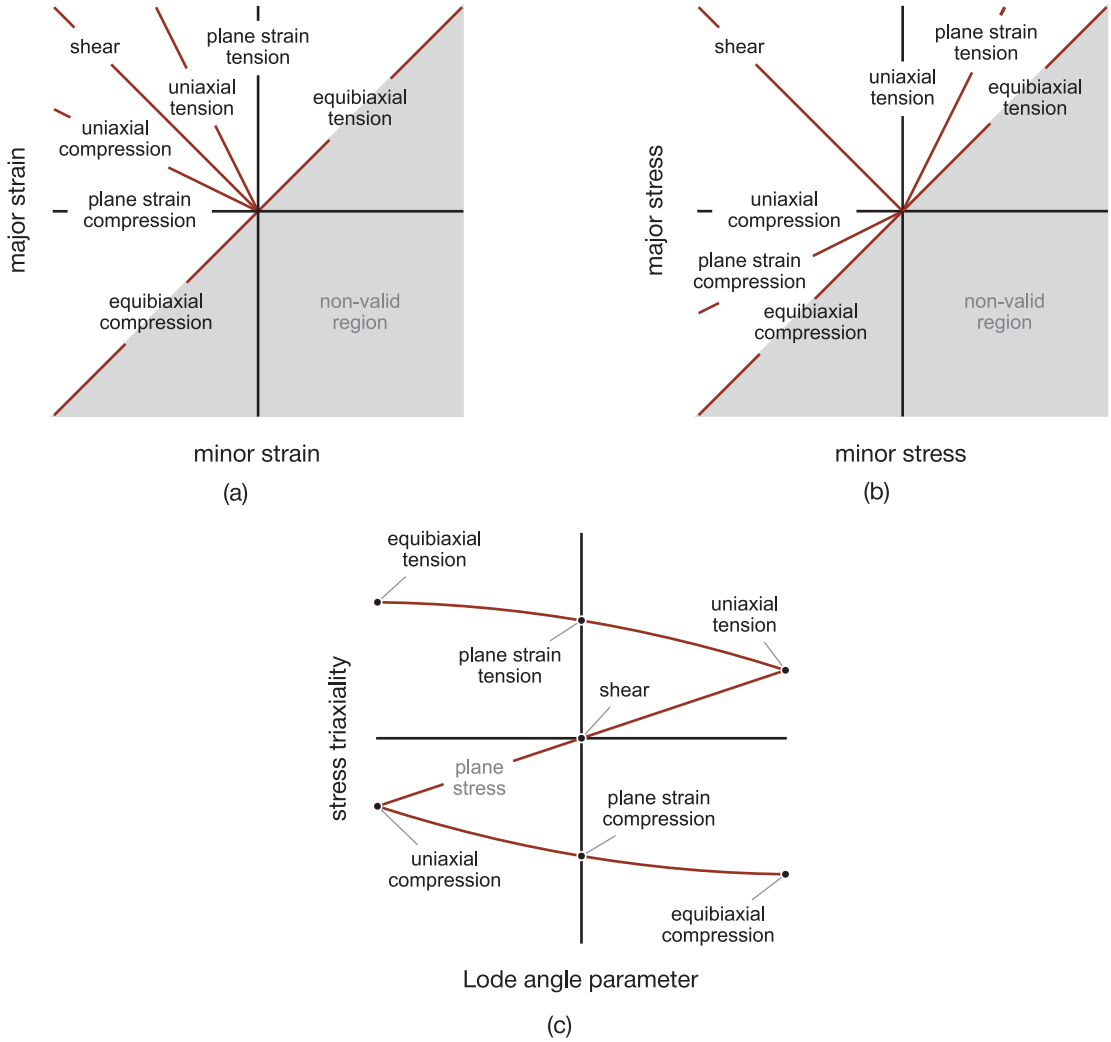

Figure 4.5 An overview of mechanical states, for an isotropic material and plane stress state, represented through the diagrams of (a) major and minor strains, (b) major and minor stresses, and (c) stress triaxiality and Lode angle parameter.

stress triaxiality η represents the distribution of stress in the three orthotropic axes and can be given by

$$\eta = \frac{\sigma_{\mathrm{h}}}{\bar{\sigma}_{\mathrm{VM}}} = \frac{\sigma_{\mathrm{xx}} + \sigma_{\mathrm{yy}}}{3\sqrt{\sigma_{\mathrm{xx}}^2 + \sigma_{\mathrm{yy}}^2 - \sigma_{\mathrm{xx}}\sigma_{\mathrm{yy}} + 3\sigma_{\mathrm{xy}}^2}}, \tag{4.5}$$

where σ_{h} is the hydrostatic stress, and $\bar{\sigma}_{\mathrm{VM}}$ is the von Mises equivalent stress. The range of stress triaxiality values is $-\infty < \eta < +\infty$. However, in the case of plane stress state, the range is reduced to $-2/3 \leq \eta \leq 2/3$. Additionally, stress triaxiality values of $\eta > 0$ characterize tensile states, and of $\eta < 0$ characterize compressive states.

The Lode angle θ, or the Lode parameter L, relates to the third invariant of the deviatoric stress tensor J_3 normalized by the von Mises equivalent stress $\bar{\sigma}_{\mathrm{VM}}$, through

$$L = -\cos(3\theta) = -\left(\frac{J_3}{\bar{\sigma}_{\mathrm{VM}}}\right)^3, \tag{4.6}$$

where J_3 is given by

$$J_3 = -\frac{1}{27}(\sigma_{xx} - 2\sigma_{yy})(\sigma_{yy} - 2\sigma_{xx})(\sigma_{xx} + \sigma_{yy}). \tag{4.7}$$

The range of the Lode angle is $0 \leq \theta \leq \pi/3$, and the Lode parameter's range is $-1 \leq L \leq 1$. Additionally, the Lode angle θ can be normalized as

$$\bar{\theta} = 1 - \frac{2}{\pi} \arccos\left(\frac{J_3}{\bar{\sigma}_{VM}}\right)^3. \tag{4.8}$$

where $\bar{\theta}$ is the Lode angle parameter of range $-1 \leq \bar{\theta} \leq 1$.

A diagram is typically used to represent the stress triaxiality and Lode angle parameter, where the latter is represented on the horizontal axis and the former on the vertical axis. Similarly to the two previous metrics, reference values of η and $\bar{\theta}$ represent typical mechanical states, such as uniaxial tension by $\eta = 1/3$ and $\bar{\theta} = 1$, and shear by $\eta = \bar{\theta} = 0$ (see Figure 4.5c and Table 4.2). Moreover, the relationship between θ and η in a plane stress state ($\sigma_{zz} = 0$) is also represented in Figure 4.5c by the plane stress curve defined by

$$\theta = \cos\left[\frac{\pi}{2}(1 - \bar{\theta})\right] = -\frac{27}{2}\eta(\eta^2 - \frac{1}{3}). \tag{4.9}$$

Table 4.2 An overview of mechanical states represented through the reference values of major and minor strains, major and minor stresses, and stress triaxiality and Lode angle parameter, considering an isotropic material and a plane stress state.

Mechanical state	Major and minor strains	Major and minor stresses	Stress triaxiality and Lode angle parameter
Equibiaxial compression	$\varepsilon_2/\varepsilon_1 = 1$ $\varepsilon_2 < 0$ $\varepsilon_1 < 0$	$\sigma_2/\sigma_1 = 1$ $\sigma_2 < 0$ $\sigma_1 < 0$	$\eta = -2/3$ $\bar{\theta} = 1$
Plane strain compression	$\varepsilon_2 < 0$ $\varepsilon_1 = 0$	$\sigma_2/\sigma_1 = \nu$ $\sigma_2 < 0$ $\sigma_1 < 0$	$\eta = -\sqrt{3}/3$ $\bar{\theta} = 0$
Uniaxial compression	$\varepsilon_2/\varepsilon_1 = -2$ $\varepsilon_2 < 0$ $\varepsilon_1 > 0$	$\sigma_2 < 0$ $\sigma_1 = 0$	$\eta = -1/3$ $\bar{\theta} = -1$
Shear	$\varepsilon_2/\varepsilon_1 = -1$ $\varepsilon_2 < 0$ $\varepsilon_1 > 0$	$\sigma_2/\sigma_1 = -1$ $\sigma_2 < 0$ $\sigma_1 > 0$	$\eta = 0$ $\bar{\theta} = 0$
Uniaxial tension	$\varepsilon_2/\varepsilon_1 = -0.5$ $\varepsilon_2 < 0$ $\varepsilon_1 > 0$	$\sigma_2/\sigma_1 = 0$ $\sigma_2 = 0$ $\sigma_1 > 0$	$\eta = 1/3$ $\bar{\theta} = 1$
Plane strain tension	$\varepsilon_2/\varepsilon_1 = 0$ $\varepsilon_2 = 0$ $\varepsilon_1 > 0$	$\sigma_2/\sigma_1 = \nu$ $\sigma_2 > 0$ $\sigma_1 > 0$	$\eta = \sqrt{3}/3$ $\bar{\theta} = 0$
Equibiaxial tension	$\varepsilon_2/\varepsilon_1 = 1$ $\varepsilon_2 > 0$ $\varepsilon_1 > 0$	$\sigma_2/\sigma_1 = 1$ $\sigma_2 > 0$ $\sigma_1 > 0$	$\eta = 2/3$ $\bar{\theta} = -1$

4.5 Formulation of Rotation Angle

A metric able to evaluate the test's sensitivity to anisotropy has not yet been fully explored to evaluate heterogeneous mechanical tests. A possible representation for this behavior is based on the principal angle between the principal stress base and the material orthotropic axes. The formulation is derived from Mohr's circle equations for a plane stress state and is given by

$$\tan(2\beta) = \frac{2\sigma_{xy}}{\sigma_{xx} - \sigma_{yy}}, \tag{4.10}$$

where β is a principal angle measured in Mohr's circle. Because the tangent function is π-periodic, satisfying $\tan(2\beta) = \tan[2(\beta + \pi/2)]$, there are two principal directions for which Equation 4.10 is fulfilled. These principal directions are β and $\beta + \pi/2$, which are perpendicular. These two principal directions, represented by β_1 and β_2, are, respectively, the principal angles of the major and minor principal stresses. Knowing the values of the stress tensor components, β corresponds to the angle from the material coordinate system x' axis to the closest principal stress axis. For this reason, it is impossible to know from its value if the principal angle is associated with the major or minor principal stress axis. Additionally, the values of 2β range between $-90°$ to $90°$ in Mohr's circle, so that β varies between $-45°$ to $45°$ in the material coordinate system.

Martins et al. (2019) applied this formulation presenting the principal angle related to the major principal stress axis to show that a cruciform specimen exhibited a relatively broad distribution of the principal angle. However, this formulation ignores the case when the mechanical state is predominantly compressive in Mohr's circle by only considering the principal angle related to the major principal stress axis. It also presents different values for β depending on the shear loading direction. Moreover, the presented range of values (from $-45°$ to $135°$) is not readily associated with the material orientation from the RD, typically evaluated between $0°$ to $90°$ for sheet metals.

Therefore, a metric based on the principal angle's formulation is suggested to evaluate the tests' sensitivity to anisotropy. It considers the maximum principal stress in absolute value, and the range of material orientations typically used to calibrate the material's anisotropic behavior. This metric is named rotation angle, represented by γ, and refers to the principal direction associated with the maximum principal stress in absolute value. Its values range between $0°$ to $90°$ and is given by

$$\gamma = \begin{cases} 45 & \text{if } \sigma_{xx} = \sigma_{yy} \text{ and } \sigma_{xy} \neq 0 \\ 45(1-q) + q|\beta| & \text{otherwise} \end{cases}, \tag{4.11}$$

where β is the principal angle (in degrees) calculated from Equation 4.10, and q is an integer of value -1 or 1, calculated as

$$q = \frac{\sigma_{xx} - \sigma_{yy}}{|\sigma_{xx} - \sigma_{yy}|} \frac{|\sigma_1| - |\sigma_2|}{||\sigma_1| - |\sigma_2||} = \text{sign}(\sigma_{xx} - \sigma_{yy})\, \text{sign}(|\sigma_1| - |\sigma_2|), \tag{4.12}$$

where $|.| = \sqrt{(.)^2}$ represents the absolute value, and the stress tensor components are defined in the material coordinate system. This formulation represents all possible states in Mohr's circle, as shown in Figure 4.6. Although each state represents different physical meanings, it is possible to mathematically reduce them to three different conditions, where the rotation angle is:

1. equal to $45°$, when $\sigma_{xx} = \sigma_{yy}$, and $\sigma_{xy} \neq 0$;
2. equal to $|\beta|$, when $\sigma_{xx} < \sigma_{yy}$ for a predominant compressive state ($|\sigma_1| < |\sigma_2|$), and when $\sigma_{xx} > \sigma_{yy}$ for a predominant tensile state ($|\sigma_1| > |\sigma_2|$), respectively, cases 1 and 2 of situations A and B (see Figure 4.6);

3. equal to $90° - |\beta|$, when $\sigma_{xx} > \sigma_{yy}$ for a predominant compressive state ($|\sigma_1| < |\sigma_2|$), and when $\sigma_{xx} < \sigma_{yy}$ for a predominant tensile state ($|\sigma_1| > |\sigma_2|$), respectively, cases 3 and 4 of situations A and B (see Figure 4.6).

Conditions 1 and 2 are schematically illustrated in Figure 4.7. Additionally, a test that demonstrates good sensitivity to material anisotropy should exhibit material points in the complete range of the rotation angle. Ideally, the material points reach the plastic regime and are equally distributed in the range of 0° to 90°.

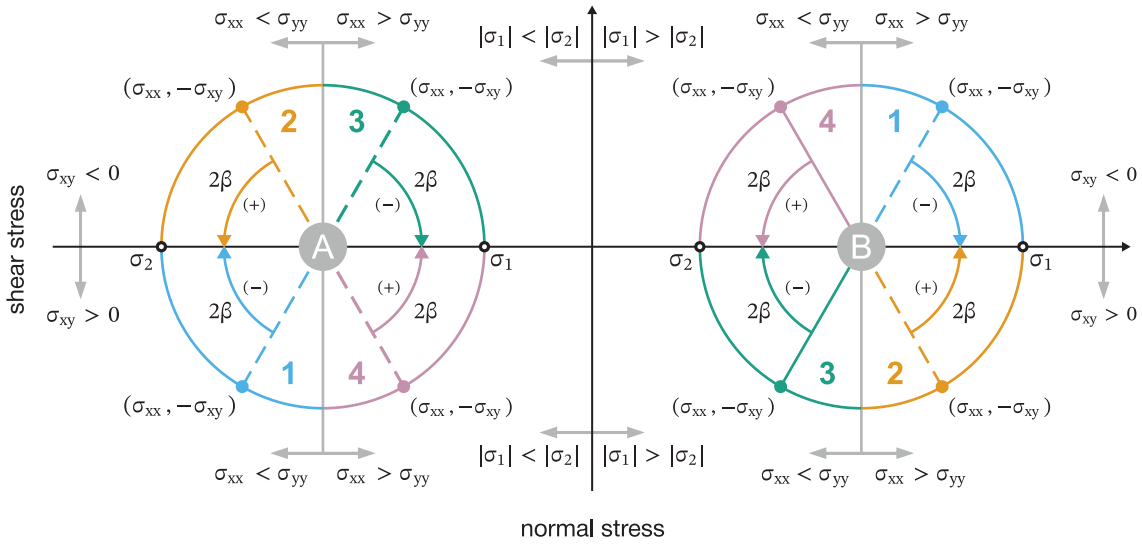

Figure 4.6 Schematic representation of possible states in the Mohr's circle covered by the formulation of the rotation angle. A predominant compressive state characterizes situation A, and situation B by a predominant tensile state. Cases 1, 2, 3, and 4 represent the different possibilities of calculating the principal angle.

4.6 Numerical Evaluation

This section evaluates the heterogeneous mechanical tests A, B, C, and D, considering the three different materials, specifically Cu, DP600, and AA2090-T3. The evaluation is performed using the metrics described above, namely: the equivalent plastic strain, major and minor strains, major and minor stresses, stress triaxiality and Lode angle parameter, and rotation angle. The tests present linear strain paths, without strain-path changes, thus the time instant just before necking defines the maximum heterogeneity of the test. Moreover, this times instant is representative of the heterogeneity observed throughout the test (SOUTO ET AL. 2015B). For that reason, the results are exclusively evaluated for the time instant where the FLC is reached, in other words, when $W_{FLC} = 1$ (see Equation 4.1). Table 4.3 summarizes the displacements obtained at the FLCs of each material for every test.

Equivalent Plastic Strain

The equivalent plastic strain distribution is evaluated using the deformed shape, where the equivalent plastic strain levels are represented through a color map (see Figure 4.8). The finite element mesh is not represented in the shapes, as it would add significant visual noise due to a fine mesh, and the color map would not be visible. Additionally, a distinction in the representations is made between material points in elastic and plastic regimes, with the latter represented through the color scale and the former in a single color. This distinction between regimes enables visualization

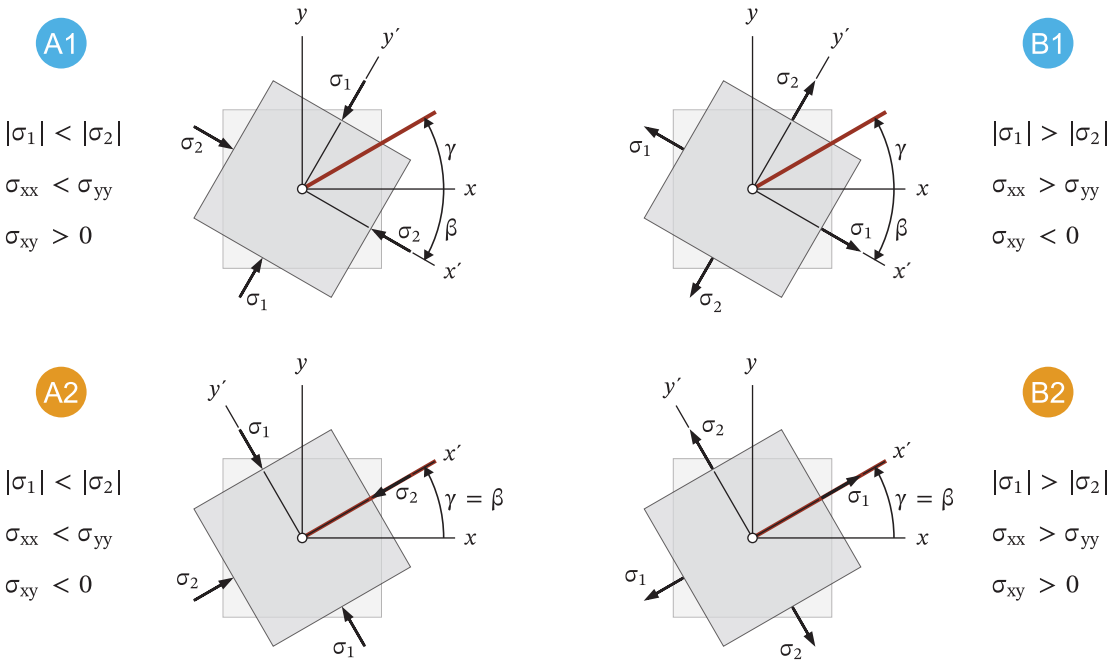

(a)

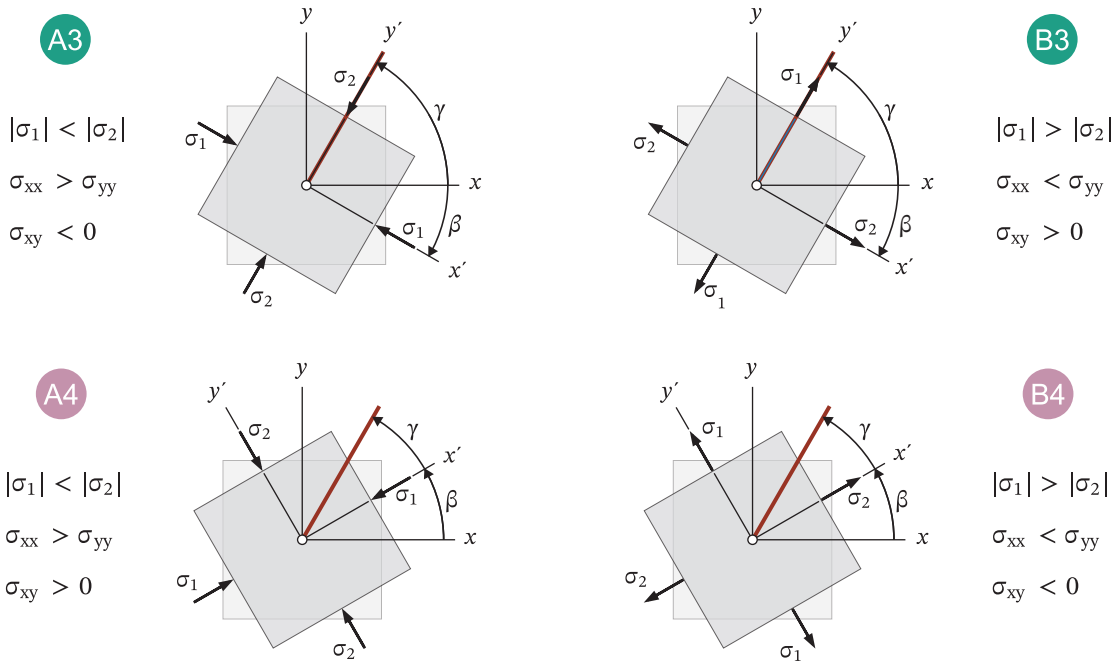

(b)

Figure 4.7 Schematic representation of material points under all possible states in the Mohr's circle, covered by the formulation of the rotation angle, for conditions (a) $\gamma = |\beta|$ and (b) $\gamma = 90° - |\beta|$. The x and y axes represent the global coordinate system (x, y), and x' and y' axes represent the material coordinate system (x', y').

Table 4.3 Displacements (in mm) corresponding to a material point reaching the forming limit curves of Cu, DP600, and AA2090-T3 for tests A, B, C, and D.

	Material		
Test	Cu	AA2090-T3	DP600
A	0.195	0.583	0.571
B	0.514	2.041	2.223
C	0.848	1.924	2.587
D	0.852	2.345	3.266

to focus on material points in the plastic regime, preferable, rather than material points in the elastic regime. Also, this representation provides a visual outline of the mechanical solicitation; and, as will be shown ahead, it is used to connect the metrics.

The comparison of equivalent plastic strain levels between materials is not of huge interest, as the observed differences are intrinsically related to the material itself. Instead, it is more interesting to analyze differences between tests for the same material. Therefore, in this case, the test presenting the highest equivalent plastic strain levels is, in general, test D, for the three materials. Concerning the equivalent plastic strain contour, the variation in the amount of material points under the plastic regime between materials is the lowest for Cu and the highest for DP600. Therefore, more mechanical information is retrieved from the latter before the rupture, which could be related to the strain hardening behavior. Indeed, DP600 exhibits the highest strain hardening rate (see Figure 4.2), and Cu the lowest, leading rapidly to a high localization of deformation.

An important aspect is also the homogeneity of deformation. The deformation in test A mainly localizes between adjacent arms, while most of the specimen's area is under low deformation levels. For test B, the deformation is localized in the vertically centered region, particularly in the central region, and close to the free edges. Although slight differences are observed between materials, test B presents intermediate to high levels of deformation in this region, while the rest of the specimen presents low equivalent plastic strain levels. In opposition, test C presents two primary regions where deformation localizes: one at the left vertically centered region and another at the right-hand side curvature. Low equivalent plastic strain levels are observed between these two regions, while the rest of the specimen is in the elastic regime or close to it. The distinct regions of localized deformation in tests B and C can perhaps be associated with different mechanical states. Lastly, the deformation in test D appears to localize at the right-hand side curvature close to the mechanical grips, and distinct regions present low to intermediate equivalent plastic strain levels.

As the analysis of the equivalent plastic strain is more related to the amount and homogeneity of strain, the following metrics will evaluate the diversity and richness of mechanical states. Nevertheless, each metric is associated with the equivalent plastic strain through a color map.

Major and Minor Strains

The evaluation of the major and minor strains is performed through the strain-based diagram, where a circular marker represents each material point colored by the corresponding level of equivalent plastic strain (see Figure 4.9). In addition, the diagrams are presented with both axes normalized by an arbitrary value, to reduce the visual noise of using different axes limits. This value is specific for each material and is identified in each diagram's bottom left corner.

The major and minor strains results show that the strain states are mainly located between uniaxial and plane strain tension for tests A and B. In the former, for AA2090-T3, the strain states

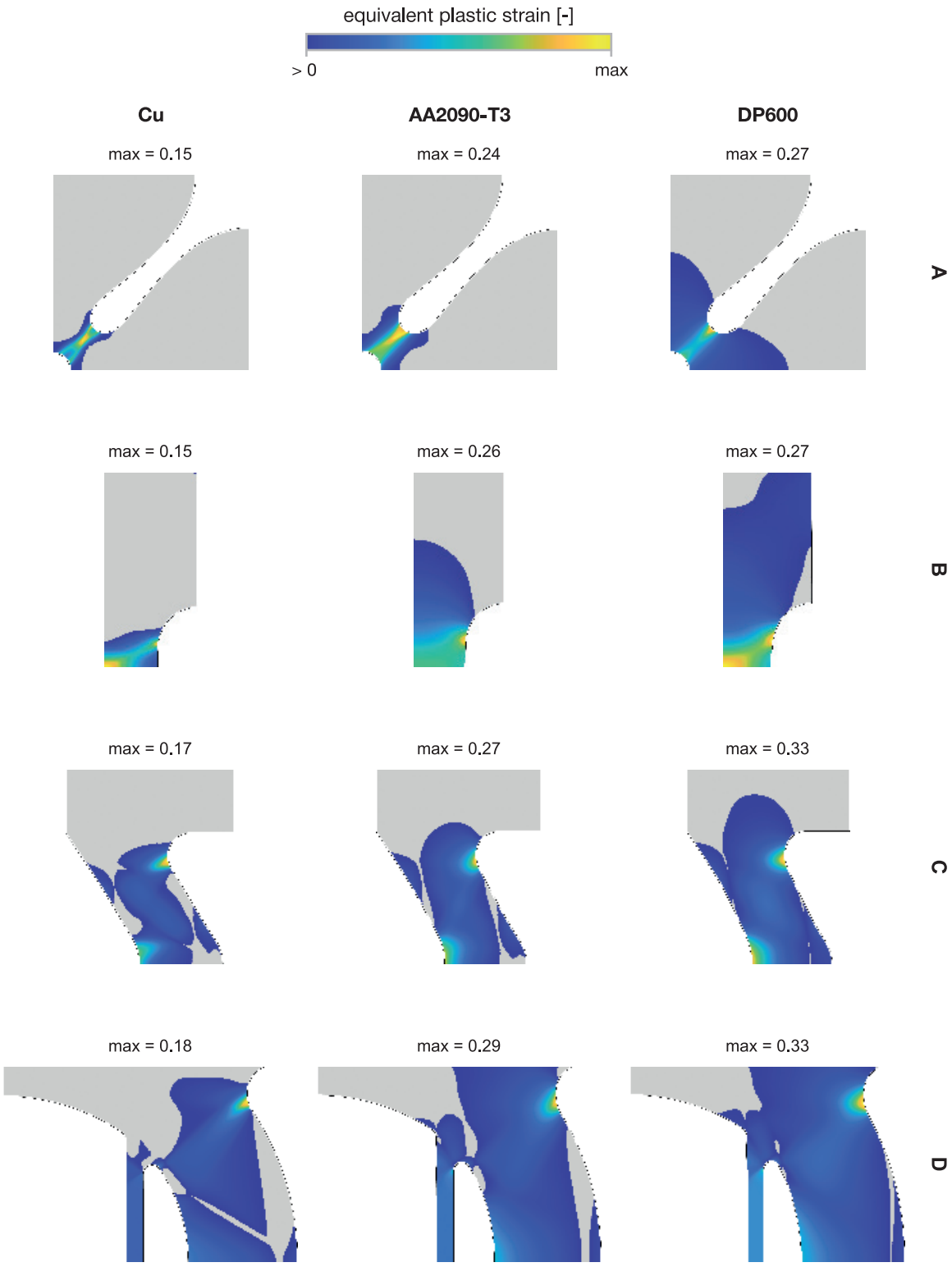

Figure 4.8 Equivalent plastic strain contours. Tests are represented in rows and materials in columns. Material points in the elastic and plastic regimes are distinguished by a gray color and the color map.

tend to uniaxial tension, while for DP600, it tends to plane strain tension. Although some material points with low equivalent plastic strain levels are observed in the equibiaxial tension region, it is disappointing and surprising that a biaxial test presents few material points in this region. In test B, the two regions of high equivalent plastic strain levels are identified, particularly for Cu and DP600, where two peaks of material points are formed, one in the specimen center and another along the free edge. Tests C and D present similar strain states' distributions, ranging from plane strain compression to plane strain tension. However, material points distribution in shear is denser for test C than D, while the opposite is observed in uniaxial compression, even though with low, but not zero, levels of equivalent plastic strain. Concerning test C, the single peak with high equivalent plastic strain levels can suggest that the two main regions previously identified present similar uniaxial tension strain states, therefore not providing additional mechanical information.

Major and Minor Stresses

Similarly to the major and minor strains, the evaluation of the major and minor stresses diagram is performed through the stress-based diagram (see Figure 4.10). The same visualization characteristics are employed, with colored circular markers and normalized axes, which are valuable in this representation, as the magnitude of stress values greatly vary between materials.

The first observation on the major and minor stresses diagram is that material points under or close to the elastic regime are more easily identified than in the strain-based diagram. The opposite is observed for material points under the plastic regime. This observation is certainly explained by the natural shape of typical metallic sheets' stress-strain curve. The curve typically presents an accentuated slope in the elastic regime (proportional to Young's modulus), enhancing stress differences. On the contrary, the curve typically presents a low slope in the plastic regime, enhancing strain differences. This observation is particularly evident for test A, and with less expression for tests C and D. Concerning test B, most material points are close to the uniaxial tension region, presenting the lowest range of stress states from all tests. Between tests C and D, the major and minor stresses diagram is useful to accentuate differences from equibiaxial compression to shear.

Stress Triaxiality and Lode Angle Parameter

The last metric evaluating the diversity of mechanical states is the stress triaxiality and Lode angle parameter diagram, as presented in Figure 4.11. Overall, this representation appears to present less information than the two previous ones, because only a fraction of the material points is visible, though an equal amount of information is represented. Because of the plane stress state formulation, it was expected that all material points fall on the plane stress state curve. Even with a 3D analysis, the same would be expected on most material points, because the stress tensor component σ_{zz} is generally negligible up to necking, and maybe beyond for small thicknesses (see Chapter 7). Therefore, the use of this metric can be more useful in studies of rupture or failure of metallic sheets, because it gives greater importance to σ_{zz}. Nevertheless, it can also be a good way to verify if the plane stress conditions are verified in 3D analysis. But because all the material points are represented on top of the plane stress curve, this metric can be a great complement to the two previous metrics, providing an instant understanding of stress states achieved.

The levels of test A stress triaxiality indicate that all material points are under a tensile state. For DP600, the full range of states from uniaxial to equibiaxial tension is achieved with material points in the plastic regime. On the other hand, for Cu and AA2090-T3, a higher range of stress states with high equivalent plastic strain levels is observed. In relation to tests B, C, and D, it is readily observed that these tests achieve tensile and compressive stress states. Test C lacks material points in shear, under the plastic regime, and equibiaxial to uniaxial compression. Finally, it is seen that test D is the test achieving the highest range of stress states, from equibiaxial compression

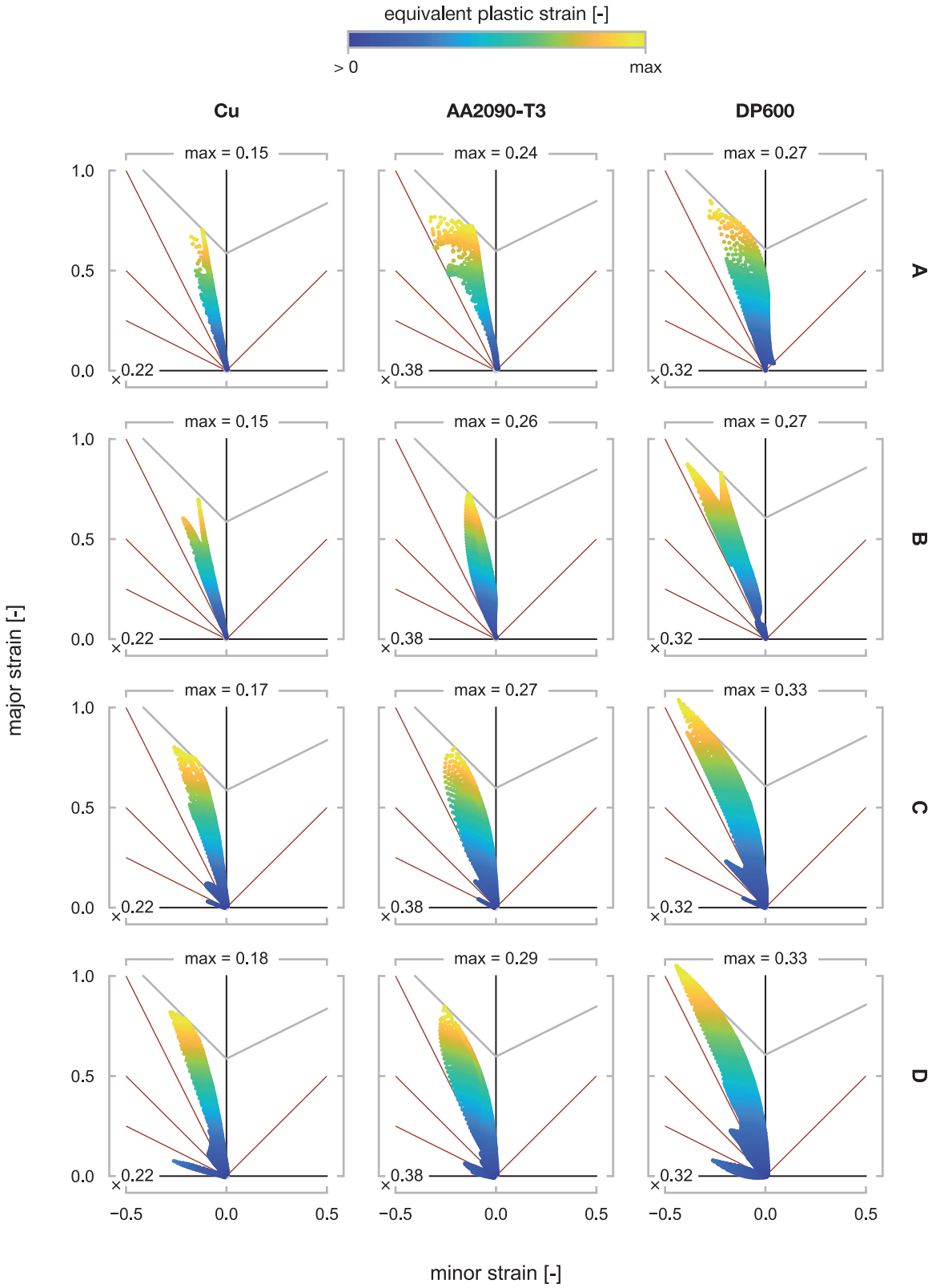

Figure 4.9 Major and minor strains diagrams. Each row is associated with a test, and each column with a material. Material points in the elastic and plastic regimes are distinguished by a single color and the color map. An arbitrary value normalizes both axes, shown in each diagram's bottom left corner. The gray lines represent each material's FLC and the red lines represent reference mechanical states.

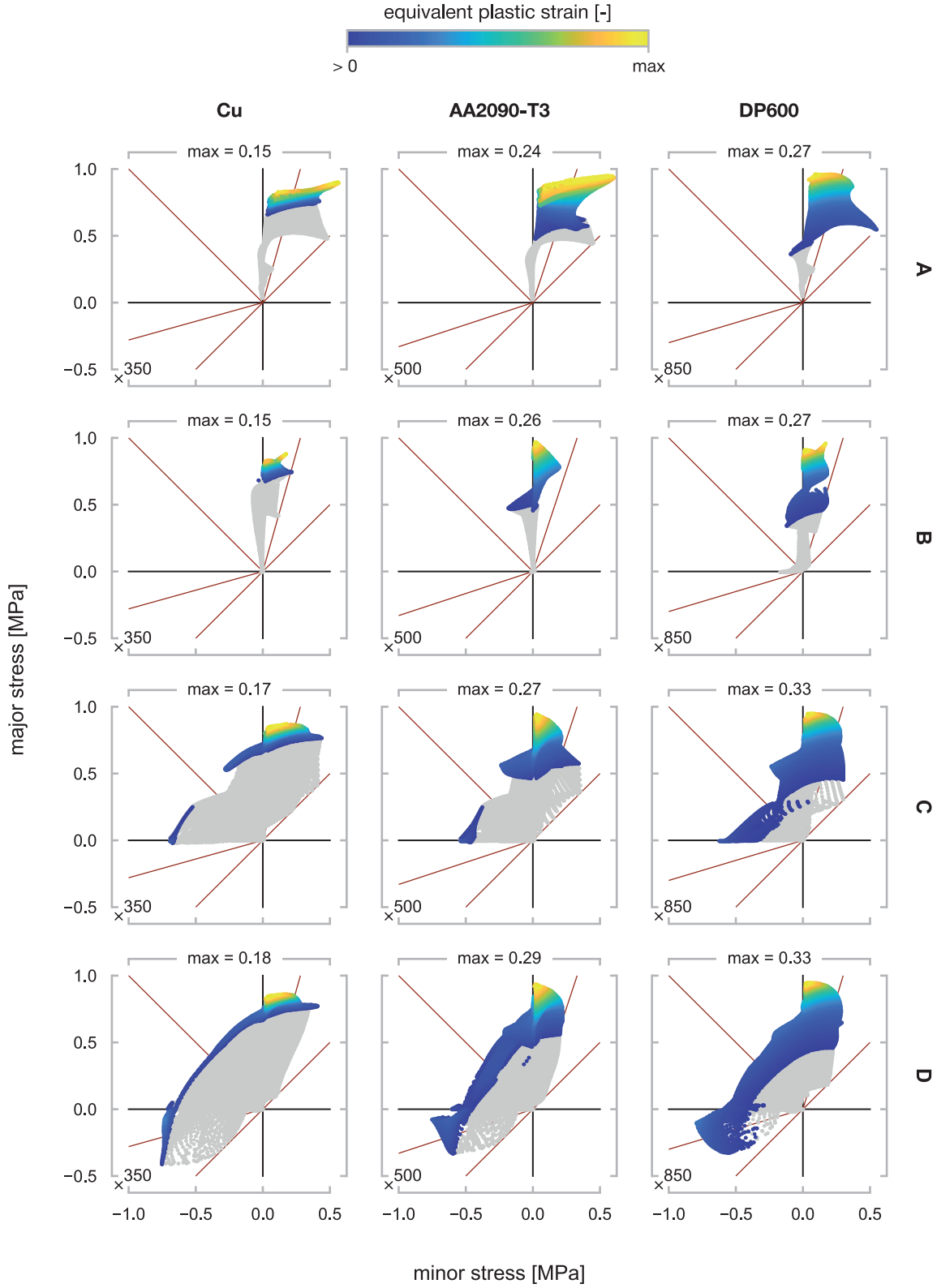

Figure 4.10 Major and minor stresses diagrams. Each row is associated with a test, and each column with a material. Material points in the elastic and plastic regimes are distinguished by a single color and the color map. An arbitrary value normalizes both axes, shown in each diagram's bottom left corner. The red lines represent reference mechanical states.

to equibiaxial tension, with material points in both regimes. In general, this diagram replicates the major and minor stresses diagram through a different stress tensor representation. While the former represents the decomposition of the hydrostatic and deviatoric stress contributions, the latter stands for the principal values. Nevertheless, this metric can complement the previous two, providing an instant understanding of the stress states achieved.

Rotation Angle

Finally, the rotation angle results are presented in Figure 4.12 through a histogram of area densities. The histogram divides the rotation angle entire range of values into 90 equal intervals, representing the specimen's area proportional amount. Using the area density minimizes the finite element mesh influence on the results. Each interval is also discretized by the levels of equivalent plastic strain, similar to the materials points of previous metrics.

Test A presents material points in the full range of rotation angle (both elastic and plastic regimes), indicating a good sensitivity of the test to anisotropy. However, material points presenting high equivalent plastic strain levels are only located between 30° to 60°. It can be noticed that the rotation angle distribution is centered close to 0° for tests B, C and D, which can be related to the material orientation. When changing the material orientation, mainly a shift of the distribution is noticed, but also some spreading of the distribution, especially at 45°, as will be shown ahead. Test B presents the smallest range of values for all materials, exclusively from 0° to 45°. Most material points are also located between 0° and 15°, indicating low sensitivity to anisotropy for a given loading direction. Specifically, for Cu, the density of material points presenting rotation angle levels higher than 15° is low, and the present low levels of equivalent plastic strain. On a positive note, for AA2090-T3 and DP600, the density of material points with rotation angle values higher than 15° tends to increase. Both test C and D achieve the full range of rotation angle values. However, from 45° to 90°, the material points are in the elastic regime or close to it. The ability to cover a high range of values means the density of values will be more evenly distributed. Particularly for test C, this remark reflects the good density of material points in the histogram central region and the low density values (lower than 5 %).

Nevertheless, test C still exhibits the most amount of material points located close to 0°, but material points with high levels of equivalent plastic strain are observed up to 30°. In test D, the rotation angle values are not as equally distributed as in test C, because the histogram's first interval (0° to 1°) aggregates more than 10 % of the specimen's total area. Even so, the density and equivalent plastic strain levels of material points between 0° to 30° are in the same order as for test C. Ultimately, test A is the one that presents the highest range of rotation angle levels for material points in the plastic regime. Therefore, it can be considered the most sensitive test to anisotropy. However, as test A is a biaxial loading test, it is naturally advantageous relative to the other tests. Test C presents the most equal distribution of the four tests, while achieving values up to 45° under the plastic regime.

To demonstrate how the histograms would change for a different material orientation, Figure 4.13 represents the rotation angle histograms of test C and AA2090-T3 for material orientations of 0°, 45°, and 90° from RD. The first case is similar to the one found in Figure 4.12. Concerning the other two cases, it can be observed that for a material orientation of 90° from RD, the histogram is approximately mirrored relatively to the one of 0° from RD. It is not an exact copy, because the material behavior changes with material orientation, but the general distribution is similar. In the case of 45° from RD, it is observed that the region with a higher area density of material points is between 45° and 60° of the rotation angle. Here, it is expected that most material points present rotation angle values in the same order as the material orientation angle. Additionally, the distribution of material points is more spread from 0° to 90° of rotation angle, rather than concentrating near the material orientation angle. The transformation is rather complex than

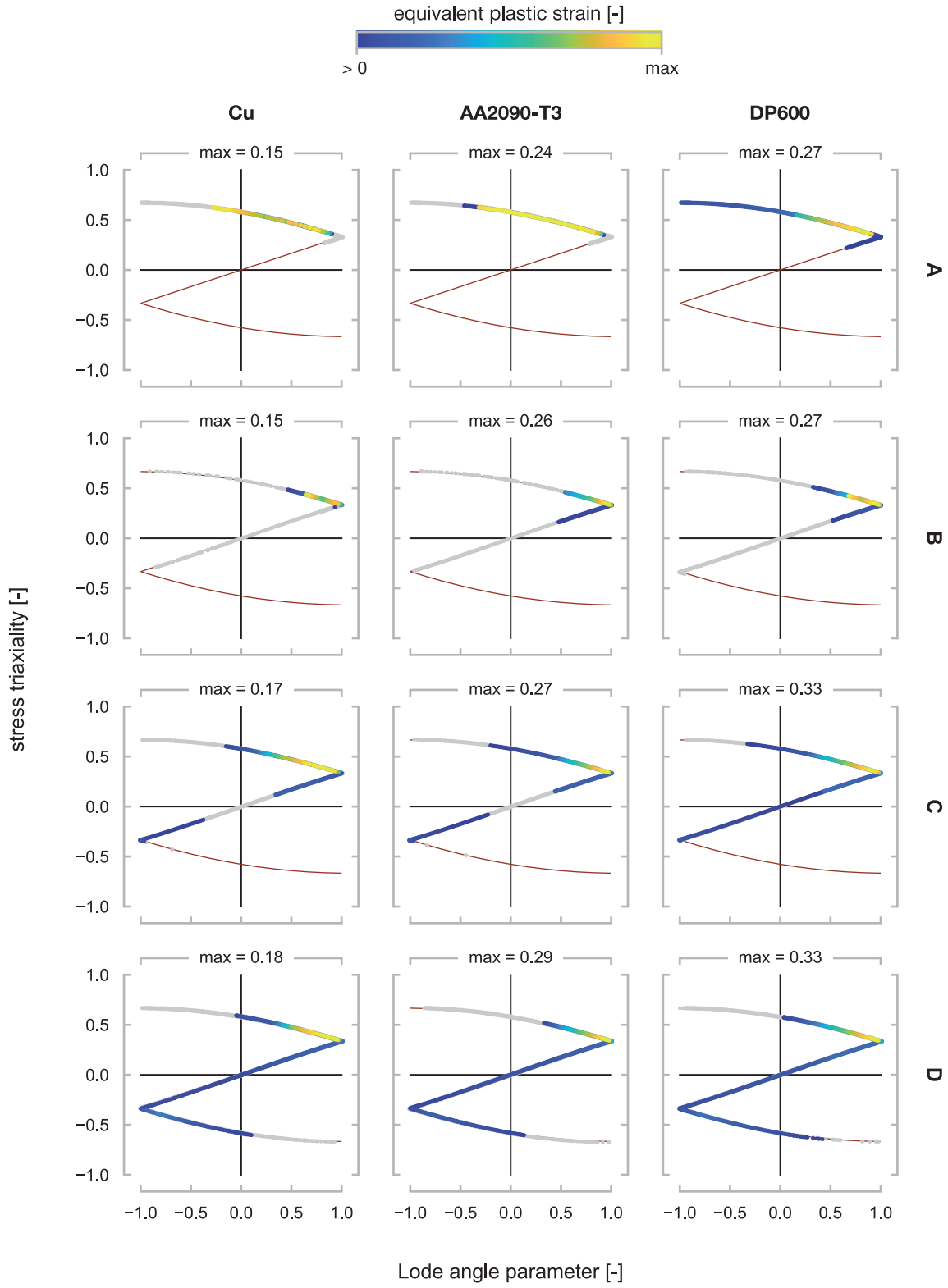

Figure 4.11 Stress triaxiality and Lode angle parameter diagrams. Each row is associated with a test, and each column with a material. Material points in the elastic and plastic regimes are distinguished by a single color and the color map. All the material points are located on top of the plane stress curve represented in red color.

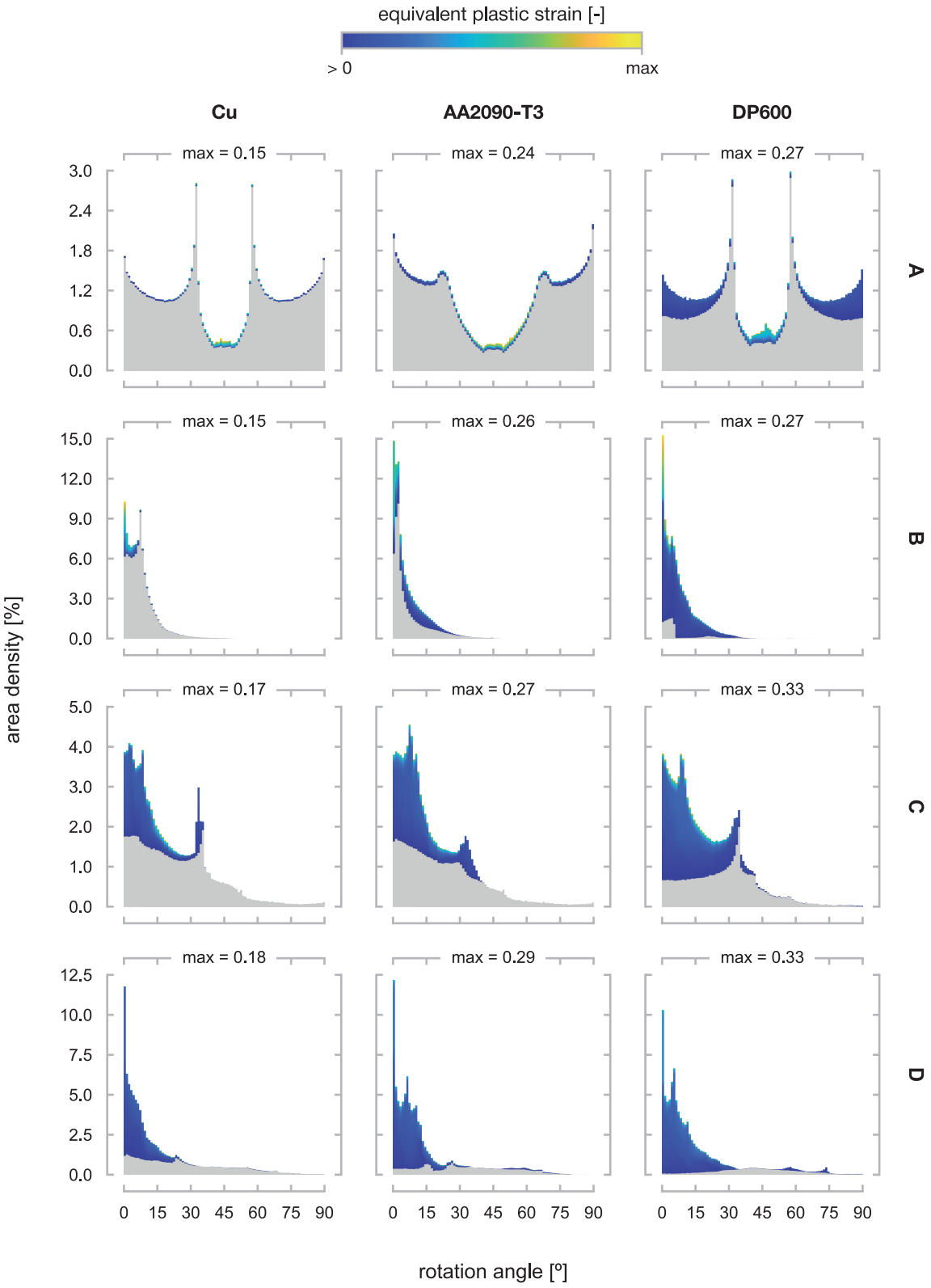

Figure 4.12 Rotation angle histograms. Each row is associated with a test, and each column with a material. The rotation angle's range of values (0° to 90°) is divided into 90 equal intervals. Material points in the elastic and plastic regimes are distinguished by a single color and the color map.

a simple shift in the distribution. However, it is possible to approximately anticipate how the transformation will occur. These results reinforce the idea that at least two tests with different material orientations are needed to fully characterize the anisotropic behavior of sheet metals.

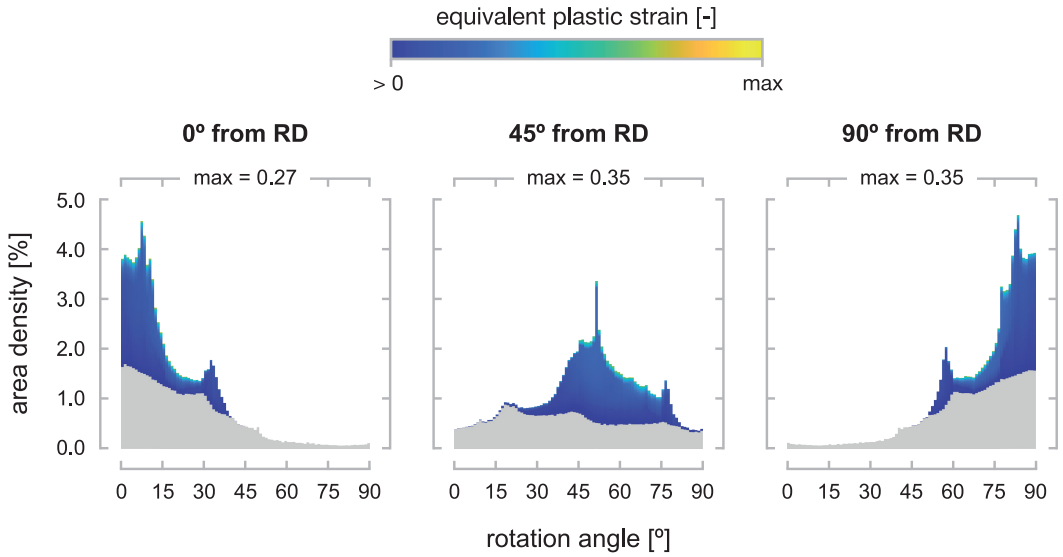

Figure 4.13 Rotation angle histograms of test C and AA2090-T3 for material orientations of 0°, 45°, and 90° from RD, respectively, from left to right. The rotation angle's range of values (0° to 90°) is divided into 90 equal intervals. Material points in the elastic and plastic regimes are distinguished by a single color and the color map. The maximum equivalent plastic strain value is shown above each histogram.

From a global perspective, it appears that these tests individually cannot fully characterize the material's strain hardening and anisotropic behavior. Nevertheless, test D could better characterize the strain hardening than the other tests due to higher equivalent plastic strain levels and diversity of mechanical states. However, test B presents a more homogeneous distribution of deformation and can also be considered a suitable choice for the strain hardening characterization, even if the range of mechanical states is reduced. Regarding the anisotropic behavior of the materials, the rotation angle suggests that test A can better characterize this behavior. However, this test requires a nonstandard testing machine, unlike the other tests, which can be performed on a universal testing machine. Given the possibility of performing two tests, the combination of different material orientations, such as at 0° and 90°, of tests D or C, can increase the anisotropic information observed in the rotation angle.

4.7 Conclusions

In this study, the richness of heterogeneous mechanical tests is evaluated using five metrics. The analysis considers four heterogeneous mechanical tests and three virtual materials, providing additional validation of each test's potential and demonstrating the relevance of evaluating tests for different materials.

The performed evaluation shows that the equivalent plastic strain is relevant to evaluate the levels of strain achieved and the homogeneity of deformation. The diversity of the mechanical states is evaluated using the major and minor strains, the major and minor stresses, and the stress triaxiality and the Lode angle parameter. Although these metrics represent the strain and stress tensors, each one presents characteristics that complement each other. However, the simultaneous use of the three can be considered excessive. To avoid redundant representations, the use of the major and minor strains should be a priority, because it can be experimentally measured.

Additionally, the major and minor stresses are an excellent complement to the major and minor strains and should be used whenever possible. In opposition, the use of the stress triaxiality and Lode angle parameter can be considered optional, as the amount of visible information is lower than in the other two. Lastly, the rotation angle is proposed to evaluate the tests' sensitivity to anisotropy. Through its use, it is possible to assess the range of material orientations achieved. It is expected that this metric can be useful to evaluate the potential of heterogeneous mechanical tests to calibrate the material's anisotropic behavior.

A test achieving a high range of mechanical states, from equibiaxial compression to equibiaxial tension, was identified. Moreover, the biaxial loading test leads to the lowest equivalent plastic strain levels, but is also the most sensitive test to anisotropy. Nevertheless, two uniaxial loading tests also show great potential to characterize the material's anisotropic behavior, if two tests of different material orientations are combined.

In summary, this study provides a basis to evaluate heterogeneous mechanical tests using various metrics. Hopefully, it can contribute to the development of heterogeneous mechanical tests by considering the materials' anisotropic behavior and providing a basis to evaluate their richness. Future studies should validate these findings by applying the suggested metrics to real experiments, and calibrate constitutive models using the selected tests.

5 Efficiency of Optimization Algorithms

5.1 Introduction

The mechanical behavior of sheet metals is usually sensitive to strain, strain rate and temperature effects. Recently, due to the growth of heat-assisted manufacturing processes (KARBASIAN AND TEKKAYA 2010), the effects of strain rate and temperature have gained more impact. Therefore, being able to precisely forecast sheet metals' mechanical response, under a broad variety of strain rates and temperatures, is more and more essential for advanced manufacturing processes. To predict such behavior, thermoelastoviscoplastic constitutive models, characterized by their nonlinearity and many material parameters, can be used. However, the traditional calibration of such models requires an extensive database, with tests performed for various strain rates and temperatures (MARKIEWICZ ET AL. 2017).

The use of full-field measurement techniques, heterogeneous mechanical tests, and inverse methods has reduced the number of required experimental tests (KAJBERG AND WIKMAN 2007). Applying full-field measurements techniques, such as DIC, the entire displacement field on the specimen's surface can be recorded and directly used to calibrate a constitutive model. The information obtained from these tests can be further enriched using temperature measurements. The material parameters can be identified using inverse methods, such as the FEMU (KAVANAGH AND CLOUGH 1971).

Solely using full-field measurements with inverse methodologies does not guarantee suitable material parameters are found. An automatic strategy using optimization algorithms is required to find these material parameters. However, most studies related to constitutive models' calibration tend to overlook the importance of optimization algorithms by resorting to familiar ones, such as gradient-based least-squares algorithms (COOREMAN ET AL. 2008; COPPIETERS ET AL. 2011; SOUTO ET AL. 2015B). These algorithms may perform well and be suitable for nonlinear least-squares problems, such as the ones formulated using the mentioned inverse methodologies, but may also present disadvantages. A few studies have explored the use of other optimization algorithms and strategies, such as direct-search and stochastic methods (DE-CARVALHO ET AL. 2011; COELHO ET AL. 2019; KOWALEWSKI AND GAJEWSKI 2019).

This study aims to implement different optimization algorithms in the calibration of a thermoelastoviscoplastic constitutive model. Three heterogeneous thermomechanical tests performed at different average strain rates are used in this study. This application is selected because it is

considered a challenging application. The FEMU is the inverse methodology, and three optimization algorithms are applied in the optimization procedure. The results obtained with different optimization algorithms are compared in terms of efficiency and robustness.

5.2 Finite Element Model Updating Method

The finite element model updating (FEMU) is used to identify the material parameters of the constitutive model (Kavanagh and Clough 1971). This method is based on the simple idea of iteratively adjusting the unknown material parameters, to minimize the difference between reference and FEA numerical results. The FEMU has been largely adopted in many applications, partly because of its ease of implementation and flexibility (Pottier et al. 2011; Prates et al. 2016). In fact, the FEMU mainly requires the finite element method, which is already widely spread across the scientific community. However, the FEMU requires a finite element model that accurately reproduces the real experiments and its boundary conditions (Kacem et al. 2021). In addition, the high computational cost of the FEMU is a major disadvantage compared to more computationally efficient methods, such as the VFM (Martins et al. 2018a).

The FEMU employs an objective function to be minimized, which can be composed of different data, such as the strain tensor components, the displacement components, or load. This flexibility has contributed to an increase in the number of formulations presented in the literature (Lin et al. 2002; Cao and Lin 2008; Andrade-Campos et al. 2012). Recently, FEMU has been mainly used in combination with full-field measurements (Cooreman et al. 2008; Souto et al. 2015b; Henriques et al. 2022). In that regard, the adopted objective function $\varphi(\boldsymbol{\xi})$, with $\boldsymbol{\xi} = (A, B, n, m, C)$, the vector of material parameters to be identified, includes the three tests with equal weights and can be decomposed in two separate terms as

$$\varphi(\boldsymbol{\xi}) = \frac{1}{3}\sum_{i=1}^{3}\Big[\varphi_1(\boldsymbol{\xi}) + \varphi_2(\boldsymbol{\xi})\Big]_i, \tag{5.1}$$

where the first term φ_1, formed by the numerical and reference strain components ε_{xx}, ε_{yy}, and ε_{xy}, is given by

$$\varphi_1(\boldsymbol{\xi}) = \frac{1}{n_t}\sum_{j=1}^{n_t}\frac{1}{n_p}\sum_{k=1}^{n_p}\left[\left(\frac{\varepsilon_{xx}^{num}(\boldsymbol{\xi}) - \varepsilon_{xx}^{ref}}{\varepsilon_{max}^{ref}}\right)^2 + \left(\frac{\varepsilon_{yy}^{num}(\boldsymbol{\xi}) - \varepsilon_{yy}^{ref}}{\varepsilon_{max}^{ref}}\right)^2 + \left(\frac{\varepsilon_{xy}^{num}(\boldsymbol{\xi}) - \varepsilon_{xy}^{ref}}{\varepsilon_{max}^{ref}}\right)^2\right]_{jk}, \tag{5.2}$$

where n_t and n_p are, respectively, the number of time instants and in-plane measurement points. To distinguish between reference and numerical variables, the superscripts "ref" and "num" are used, respectively. The variable ε_{max}^{ref} represents the maximum strain value of all in-plane components and time instants. Because the displacement field represents the raw data, the strain field is computed from the displacement field using a total Lagrangian formulation. The reference strain field is computed before the calibration procedure, and the updated strain field is computed after every finite element simulation from the extracted numerical displacement field. The second term φ_2 consists of the reference and numerical load normalized by the maximum load value of all time instants F_{max}^{ref} as

$$\varphi_2(\boldsymbol{\xi}) = \frac{1}{n_p}\sum_{j=0}^{n_p}\left[\frac{F^{num}(\boldsymbol{\xi}) - F^{ref}}{F_{max}^{ref}}\right]_j^2. \tag{5.3}$$

5.3 Optimization Algorithms

The optimization algorithms are essential in the FEMU to minimize the objective function (see Equation 5.1) through an iterative procedure. In this study, different algorithms are used to evaluate their performance. The optimization procedure is implemented in Python programming language, using the optimization algorithms from the SciPy library (Virtanen et al. 2020; SciPy 2022b). This library has several optimization algorithms (e.g., gradient-based, stochastic), providing the user with easy implementation in its programs. Three optimization algorithms of different types were selected for the optimization procedure: the Levenberg-Marquardt, the Nelder-Mead, and the Differential Evolution algorithms.

5.3.1 Levenberg-Marquardt Algorithm

The Levenberg-Marquardt (LM) is a gradient-based algorithm that uses the approximated Hessian and Jacobian matrices (Levenberg 1944; Marquardt 1963). It is widely used to calibrate constitutive models (Güner et al. 2012; Marek et al. 2019; Martins et al. 2019) because it is well suited for solving nonlinear least-squares problems. The LM algorithm requires the user to select an initial solution, and if not well chosen, it can lead to convergence difficulties or local minima, instead of the global minimum. Nevertheless, if the problem is well-conditioned and a suitable initial solution $\mathbf{x}_0$ is selected, the algorithm can converge rapidly. For an iteration i, the LM can be written as

$$\left[\mathbf{H}(\mathbf{x}^i) + \lambda \text{diag}\left(\mathbf{H}^i\right)\right]\mathbf{h}^i = -[\mathbf{J}(\mathbf{x}^i)]^{\mathrm{T}}\mathbf{r}(\mathbf{x}^i), \tag{5.4}$$

where $\mathbf{H}(\mathbf{x}^i)$ is the Hessian matrix, λ is the damping factor, $\mathbf{h}^i$ is the increment of identification parameters, and $\mathbf{r}(\mathbf{x}^i)$ is the corresponding residuals vector of the objective function ϕ. Note that $\mathbf{r}(\mathbf{x}^i)$ contains as many rows as number of tests, time instants, and measurement points, for each strain component and load. This is one of the main advantages of the LM algorithm, because it quantifies the influence of each row in the objective function. The damping factor is particularly important in the LM algorithm, because it creates a trust region around the solution. For low values of λ, the algorithm results in a Gauss-Newton algorithm, while for high values it results in the steepest descent algorithm. The Hessian matrix $\mathbf{H}(\mathbf{x}^i)$ can be approximated by

$$\mathbf{H}(\mathbf{x}^i) = [\mathbf{J}(\mathbf{x}^i)]^{\mathrm{T}}\mathbf{J}(\mathbf{x}^i) \tag{5.5}$$

where $\mathbf{J}(\mathbf{x}^i)$ is the Jacobian matrix representing the derivatives of ϕ with respect to $\mathbf{x}^i$. In the scope of this study, $\mathbf{J}$ is calculated by forward finite-differences. Finally, the new solution $\mathbf{x}^{i+1}$ is obtained by

$$\mathbf{x}^{i+1} = \mathbf{x}^i + \mathbf{h}^i. \tag{5.6}$$

More details on the LM algorithm implementation used in this study can be found at Moré (1978) and SciPy (2022d). However, it should be noted that this implementation within SciPy does not provide enough flexibility, because it is essentially a wrapper of the MINPACK project in Fortran (Moré et al. 1984).

5.3.2 Nelder-Mead Algorithm

The Nelder-Mead (NM) is one of the best known and simpler direct-search algorithms used in unconstrained optimization (Nelder and Mead 1965). The NM algorithm employs a simplex that begins with a set of vertices for every identification parameter plus one. In practice, each vertex corresponds to a given solution. Based on a series of transformations of the simplex, the algorithm iteratively reduces the simplex size. The algorithm is known to achieve satisfactory results in

few iterations, but may also present convergence problems. Comparatively to gradient-based algorithms, this algorithm stands out for not requiring derivatives.

At each iteration i, the simplex vertices $\mathbf{x}_1^i, \mathbf{x}_2^i, ..., \mathbf{x}_{n+1}^i$, with n the number of material parameters, are ordered according to the objective function values as

$$\varphi(\mathbf{x}_1^i) \leq \varphi(\mathbf{x}_2^i) \leq ... \leq \varphi(\mathbf{x}_{n+1}^i). \tag{5.7}$$

where $\mathbf{x}_1^i$ represents the best vertex, and consequently, $\mathbf{x}_{n+1}^i$ the worst. Additionally, let us consider that $\mathbf{x}_\mathrm{o}^i$ is the centroid of the n best vertices, given by

$$\mathbf{x}_\mathrm{o}^i = \frac{1}{n}\sum_{j=1}^{n} \mathbf{x}_j^i. \tag{5.8}$$

After the vertices are ordered and the centroid calculated, the algorithm uses four main transformations to improve the simplex: reflection, expansion, contraction and shrink. Each is associated with four scalar parameters ω_r, ω_e, ω_c, and ω_s.

Reflection

The first and mandatory transformation, named reflection, is performed where a new vertex $\mathbf{x}_\mathrm{r}^i$ is found by reflecting the $\mathbf{x}_{n+1}^i$ through $\mathbf{x}_\mathrm{o}^i$ as

$$\mathbf{x}_\mathrm{r}^i = \mathbf{x}_\mathrm{o}^i + \omega_\mathrm{r}(\mathbf{x}_\mathrm{o}^i - \mathbf{x}_{n+1}^i), \tag{5.9}$$

Then, the objective function value of $\mathbf{x}_\mathrm{r}^i$ is calculated and if $\varphi(\mathbf{x}_1^i) \leq \varphi(\mathbf{x}_\mathrm{r}^i) \leq \varphi(\mathbf{x}_n^i)$, a new simplex is obtained where $\mathbf{x}_{n+1}^{i+1} = \mathbf{x}_\mathrm{r}^i$. However, if the latter condition is not observed, multiple transformations can be additionally performed.

Expansion

If $\mathbf{x}_\mathrm{r}^i$ is better than $\mathbf{x}_1^i$, the expansion transformation is performed, where a new vertex $\mathbf{x}_\mathrm{e}^i$ is generated by expanding $\mathbf{x}_\mathrm{r}^i$ as

$$\mathbf{x}_\mathrm{e}^i = \mathbf{x}_\mathrm{o}^i + \omega_\mathrm{e}(\mathbf{x}_\mathrm{r}^i - \mathbf{x}_\mathrm{o}^i), \tag{5.10}$$

If $\varphi(\mathbf{x}_\mathrm{e}^i) < \varphi(\mathbf{x}_\mathrm{r}^i)$, a new simplex is obtained where $\mathbf{x}_{n+1}^{i+1} = \mathbf{x}_e^i$; otherwise, the new simplex is obtained by $\mathbf{x}_{n+1}^{i+1} = \mathbf{x}_\mathrm{r}^i$.

Contraction

If $\varphi(\mathbf{x}_n^i) \leq \phi(\mathbf{x}_\mathrm{r}^i) < \varphi(\mathbf{x}_{n+1}^i)$, an outside contraction is performed, where the reflected point is contracted towards the centroid as

$$\mathbf{x}_\mathrm{oc}^i = \mathbf{x}_\mathrm{o}^i + \omega_\mathrm{c}(\mathbf{x}_\mathrm{r}^i - \mathbf{x}_\mathrm{o}^i), \tag{5.11}$$

If the new vertex is better than the reflected vertex, then $\mathbf{x}_{n+1}^{i+1} = \mathbf{x}_\mathrm{oc}^i$. Instead, if $\varphi(\mathbf{x}_\mathrm{r}^i) \geq \varphi(\mathbf{x}_{n+1}^i)$, an inside contraction is performed as

$$\mathbf{x}_\mathrm{ic}^i = \mathbf{x}_\mathrm{o}^i - \omega_\mathrm{c}(\mathbf{x}_\mathrm{r}^i - \mathbf{x}_\mathrm{o}^i), \tag{5.12}$$

where the new simplex will have $\mathbf{x}_{n+1}^{i+1} = \mathbf{x}_\mathrm{ic}^i$ if the latter is better. However, if the contraction transformation does not yield a better solution, a last transformation is required.

Shrink

Finally, the shrink transformation is performed as a last resort in case contraction fails. Here, a new simplex is obtained by replacing all the vertices, except $\mathbf{x}_1^i$, with new vertices closer to the best solution as

$$\mathbf{x}_j^{i+1} = \mathbf{x}_1^i + \omega_s(\mathbf{x}_j^i - \mathbf{x}_1^i). \tag{5.13}$$

The operations and transformations of the NM algorithm are schematically illustrated in Figure 5.1 for a simplex of size $n = 2$, and considering $\omega_r = 1$, $\omega_e = 2$, $\omega_c = 0.5$, and $\omega_s = 0.5$. Nevertheless, NM implementation used in this study adapts the scalar parameters ω_r, ω_e, ω_c, and ω_s to the dimensionality of the problem at hand (Gao and Han 2012). More details of the implementation used in this study can be found at SciPy (2022a). Nevertheless, implementation-wise, the NM algorithm allows more control over the identification procedure, as it allows the calling of a subroutine at the end of every iteration.

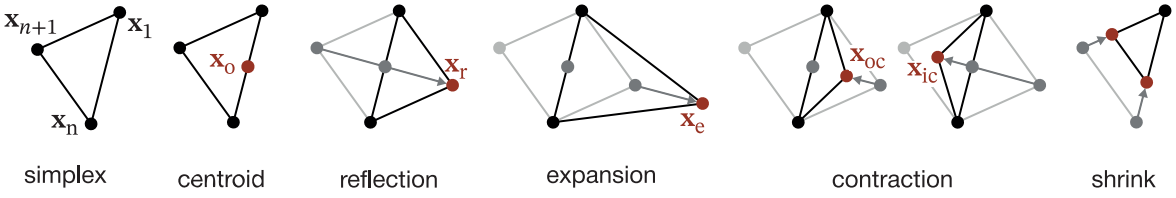

Figure 5.1 Schematic illustration of operations and transformations of the NM algorithm.

5.3.3 Differential Evolution Algorithm

The Differential Evolution (DE) is a population-based stochastic algorithm that generates new solutions from other solutions (Storn and Price 1997). The DE algorithm can be characterized by its ease of implementation, robustness, and finding the global minimum of a problem in most attempts. However, a significant drawback of the DE algorithm is its high computational cost and low convergence rate compared to other optimization algorithms. On the other hand, compared to other population-based stochastic algorithms, the DE algorithm tends to outperform them. As it is common in population-based algorithms, the number of solutions used as the population can significantly impact the convergence and success of the optimization procedure (Piotrowski 2017). Moreover, the DE algorithm requires the definition of bounds for the identification parameters, to generate the initial set of solutions, either manually, randomly or distributed over the search space.

A population of *NP* solutions, each with a size of n material parameters, is initially randomly generated and should try to cover the design space as much as possible. At each iteration i, a solution $\mathbf{x}^i$ is represented in the design space and limited by its upper and lower bounds, respectively, $\mathbf{x}_{max}$ and $\mathbf{x}_{min}$. The generation of the initial population is defined for a given initial solution $\mathbf{x}^0$ by

$$\mathbf{x}^0 = \mathbf{x}_{min} + \mathbf{r}\,(\mathbf{x}_{max} - \mathbf{x}_{min})\,, \tag{5.14}$$

where $\mathbf{r}$ is a vector of random numbers uniformly distributed in the range $[0, 1]$. The optimization process is then initialized, with the DE algorithm divided into three main operations: mutation, crossover and selection.

Mutation

The mutation scheme allows for a more diversified and robust search in the design space. In this step, for every target solution $\mathbf{x}^i$, a mutant solution $\mathbf{v}^{i+1}$ is generated by randomly choosing three

mutually different solutions $\mathbf{x}^i_{r_1}$, $\mathbf{x}^i_{r_2}$ and $\mathbf{x}^i_{r_3}$, r_1, r_1, r_2 and r_3 are integer values from a sample in the range of $[1, 2, ..., n]$. The mutant solution $\mathbf{v}^{i+1}$ is then given by

$$\mathbf{v}^{i+1} = \mathbf{x}^i_{r_1} + F\left(\mathbf{x}^i_{r_2} - \mathbf{x}^i_{r_3}\right), \tag{5.15}$$

where F is a positive integer that controls the ratio in which the population evolves. This parameter is often referred to as the scale factor. The solutions $\mathbf{x}^i_{r_2}$ and $\mathbf{x}^i_{r_3}$ should also be different from the target solution $\mathbf{x}^i$. Depending on the strategy used, $\mathbf{x}^i_{r_1}$ can be randomly chosen from the population or even the best solution from the previous generation.

Crossover

To complement the mutation strategy, the DE algorithm introduces crossover, controlled by a parameter C_r that defines the probability for crossover. In this step, the trial solution $\mathbf{u}^{i+1}$ is generated from two different solutions, the mutant solution $\mathbf{v}^{i+1}$ and the target solution $\mathbf{x}^i$. The type of crossover can either be binomial or exponential. In the binomial crossover, the trial solution $\mathbf{u}^{i+1}$ is generated as

$$\mathbf{u}^{i+1}_j = \begin{cases} \mathbf{v}^{i+1}_j & \text{if } \mathbf{r}_j \leq C_\mathrm{r} \\ \mathbf{x}^i_j & \text{otherwise} \end{cases}, \tag{5.16}$$

where $\mathbf{r}_j$ is a vector of random numbers uniformly distributed in the range $[0, 1]$. Each material parameter of the trial solution $\mathbf{u}^{i+1}$ is determined independently. To determine which solution contributes a given material parameter, C_r is compared to $\mathbf{r}_j$. If $\mathbf{r}_j$ is less than or equal to C_r, the material parameter $\mathbf{u}^{i+1}_j$ is inherited from the mutant solution $\mathbf{v}^{i+1}$, otherwise is inherited from $\mathbf{x}^i_k$. In the exponential crossover, a random material parameter is selected, and starting from that, the trial solution $\mathbf{u}^{i+1}$ receives a material parameter from $\mathbf{v}^{i+1}$ until C_r is less than $\mathbf{r}_j$. From that point forward, $\mathbf{u}^{i+1}$ inherits all the remaining material parameters from $\mathbf{v}^{i+1}$.

Selection

Finally, the selection step decides if the trial solution $\mathbf{u}^{i+1}$ replaces the target solution $\mathbf{x}^i$ in the population. The objective function is evaluated at $\mathbf{u}^{i+1}$, and if its value is less than or equal to the value at $\mathbf{x}^i$, $\mathbf{u}^{i+1}$ replaces $\mathbf{x}^i$ in the population as

$$\mathbf{x}^{i+1} = \begin{cases} \mathbf{u}^{i+1} & \text{if } \varphi(\mathbf{u}^{i+1}) \leq \mathbf{x}^i \\ \mathbf{x}^i & \text{otherwise} \end{cases}. \tag{5.17}$$

This procedure repeats until a termination criterion is satisfied. The operations of DE are schematically illustrated in Figure 5.2, and more details of the implementation used in this study can be found at SciPy (2022c).

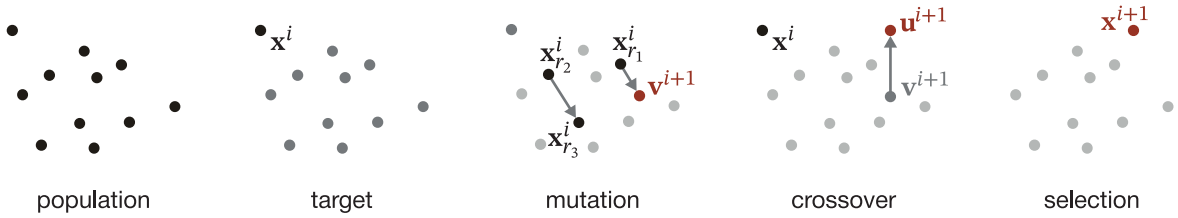

Figure 5.2 Schematic illustration of operations of the DE algorithm.

5.4 Heterogeneous Thermomechanical Test

A numerical database from three heterogeneous thermomechanical tests is used as a reference for the identification procedure, as no real experiments are considered in this study (MARTINS ET AL. 2020B; MARTINS ET AL. 2021). Nevertheless, the reference data is based on real experiments performed on a Gleeble 3500 thermomechanical simulator, using a hydraulic servo system able to impose tension or compression forces, as well as a direct resistance heating system (COËR ET AL. 2011). These tests present both heterogeneous temperature and strain fields, leading to richer mechanical information.

The study considers a virtual material that presents characteristics of a DP980 dual-phase steel with a 1.5 mm of thickness. The tests are uniaxial loading using the specimen geometry as represented in Figure 5.3a. The ROI, defined by a width and length of, respectively, 28 and 60 mm, corresponds to the gauge length of the specimen. A uniaxial tensile load is imposed on the specimens at constant displacement rates of 0.006, 0.06, and 0.6 mm s^{-1}, respectively, for each test. According to the length of the ROI, the displacement rates of each test correspond to, respectively, average strain rates of 10^{-4}, 10^{-3}, and 10^{-2} s^{-1}, which will be used to identify each test. In addition, a heterogeneous temperature field is imposed on the specimens through the direct resistance heating system, controlling and maintaining the temperature at the specimen's center during the test. The remaining part of the specimens present a temperature gradient due to the water-cooling system of the machine's grips. An example of the resulting temperature field is shown in Figure 5.3b for a real experiment. Three thermocouples are used to monitor the temperature field along the gauge length, and the red circles show their relative position in Figure 5.3b. The added value of this procedure is that the temperature gradient triggers a heterogeneous deformation, providing information on the material's mechanical behavior at different temperatures and strain rates.

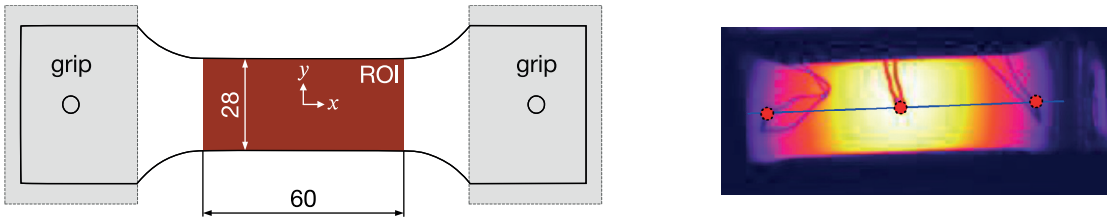

Figure 5.3 Schematic representation of the specimen used in the heterogeneous thermomechanical tests: (a) geometry of the specimens (dimensions in mm) and (b) example of temperature field recorded during real experiments at the surface of the specimens.

The temperature field acquired with the Gleeble equipment usually presents a parabolic shape, symmetrical about the specimen's center (COELHO AND THUILLIER 2022). Measurements of three thermocouples placed at −40, 0, and 40 mm along the x axis during real experiments confirm the approximate symmetrical and parabolic shape of the profile along the specimen's length. Temperature variations along the width of the specimen can be neglected. It was also confirmed that the temperature field remains constant throughout the deformation process (COËR ET AL. 2011; COELHO AND THUILLIER 2022). Because of its parabolic shape, a second-order polynomial can describe each test temperature field. For this study, a temperature field $T(x)$ is numerically generated between −30 and 30 mm along the x axis, and is defined for each test by

$$T(x) = \begin{cases} -0.143x^2 - 0.251x + 506.404 & \text{for} \quad 10^{-4}\,\text{s}^{-1} \\ -0.149x^2 - 0.123x + 499.364 & \text{for} \quad 10^{-3}\,\text{s}^{-1} \\ -0.139x^2 - 0.040x + 509.084 & \text{for} \quad 10^{-2}\,\text{s}^{-1} \end{cases} . \tag{5.18}$$

For the three tests, the temperature field is in range of [360 °C, 510 °C]. The maximum temperature is reached at the specimen's center, decreasing to its lowest at −30 and 30 mm along the x axis as represented in Figure 5.4.

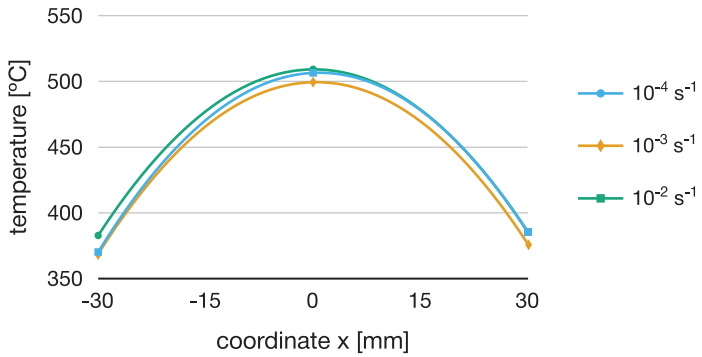

Figure 5.4 Temperature field of the three heterogeneous thermomechanical tests imposed along the x axis and described by second-order polynomials.

The reference data is numerically generated by a FEA simulation of each test. Only the ROI is modeled due to lack of temperature measurements outside this region. The finite element model is built in 2D, assuming a plane stress formulation. Abaqus/Standard (DASSAULT SYSTÈMES 2019) software is used, and the four-node bilinear plane stress quadrilateral element (CPS4) is used, with a large strain formulation. The finite element mesh is composed of 1680 elements. Displacement-driven boundary conditions are imposed on the model extremities, respectively, at −30 and 30 mm along the x axis. In addition, the temperature field is imposed on each node of the finite element model through the second-order polynomial, and kept constant throughout the test (see Figure 5.4).

The virtual material is considered isotropic and its elastic behavior described by the Hooke's law. The elastic properties of the material, namely Young's modulus $E = 210$ GPa and Poisson's ratio $\nu = 0.30$, are known a priori and assumed to be constant in the temperature range of the study. The von Mises yield criterion is assumed, thus anisotropy is not considered in this study. In addition, the Johnson-Cook thermoelastoviscoplastic constitutive model (see Equation 2.23) is used to describe the strain hardening behavior. The models available in Abaqus/Standard are used in the FEA simulations.

The reference materials parameters are characteristic of a DP980 dual-phase steel (MARTINS ET AL. 2020B), and are presented in Table 5.1. Although it is common to identify the material parameters of the Johnson-Cook model, considering each term individually (describing the effects of strain hardening, temperature, and strain rate), in this study the material parameters are simultaneously identified. Nevertheless, some material parameters are considered known a priori

Table 5.1 Reference material parameters used in the Johnson-Cook thermoelastoviscoplastic constitutive model to generate the reference data (Martins et al. 2020b).

A [MPa]	B [MPa]	n [–]	T_{tr} [°C]	T_{m} [°C]	m [–]	C [–]	$\dot{\varepsilon}_0$ [s^{-1}]
205.21	1124.0	0.092	25.0	1000.0	1.36	0.05	0.001

and kept fixed throughout the identification procedure, such as the parameter $\dot{\varepsilon}_0 = 0.001\,\mathrm{s}^{-1}$, the transition temperature $T_{\mathrm{tr}} = 25\,^{\circ}\mathrm{C}$, and the melting temperature $T_{\mathrm{m}} = 1000\,^{\circ}\mathrm{C}$. The latter is a value commonly used for the DP980 (Erice et al. 2018). The transition temperature T_{tr} is set to a low value, as it can describe a wide range of temperatures. Additionally, the value of $\dot{\varepsilon}_0$ is also low, to account for the early sensitivity of the material to strain rate effects. Moreover, by reducing the number of material parameters to be identified, it might reduce the problem of non-uniqueness of the solutions (Notta-Cuvier et al. 2013; Zhang et al. 2022b). As such, the material parameters A, B, n, m, and C are the only ones identified.

In Figure 5.5, the maps of equivalent plastic strain are presented for each test at the last time instant, respectively, at 950, 106, and 11.75 s. It is observed that the increase in average strain rate results in lower levels of equivalent plastic strain achieved. As a result, the strain localization is delayed. The reference database is composed of the displacement field and the evolution of load at each time instant. The evolution of load for each test performed at three different average strain rates is shown in Figure 5.6, where the markers represent the distribution of time instants considered. It is observed that the evolution of the load is sensitive to the average strain rate, as an increase leads to higher values of the maximum load. In addition, it should be noted that different time instants compose the reference database, specifically 62, 58, and 47, respectively, for tests with an average strain rate of 10^{-4}, 10^{-3}, and $10^{-2}\,\mathrm{s}^{-1}$. Therefore, the objective function indirectly assigns different weights to each test. Moreover, a lower weight is assigned to the early stages of each test, as observed by the distribution of time instants considered in the objective function.

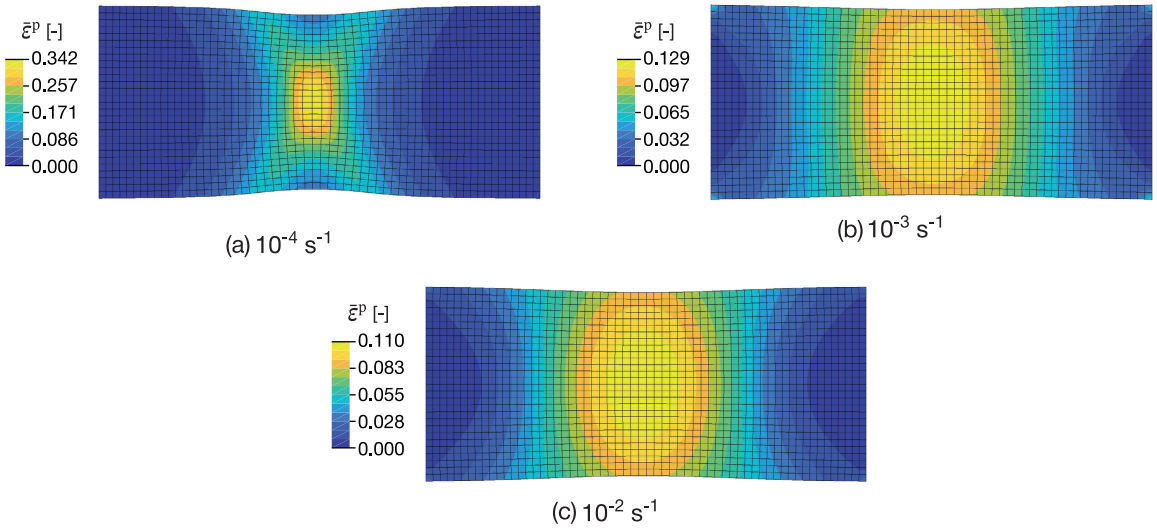

Figure 5.5 Maps of equivalent plastic strain at the last time instant for the thermomechanical heterogeneous tests (a) $10^{-2}\,\mathrm{s}^{-1}$, (b) $10^{-3}\,\mathrm{s}^{-1}$, and (c) $10^{-4}\,\mathrm{s}^{-1}$.

5.5 Numerical Implementation

One of the goals of this study was to develop a parameter identification software in Python programming language, starting from a previously developed Fortran code (Martins et al. 2020b). Python was selected as the main programming language because it is a simple and modern language that allows easy and fast development (Marchand 2022). Moreover, it is already one of the most used languages, and any user can easily learn it and use this code in the future. However, one drawback of Python compared to more advanced programming languages, such as C++ or Java, is the higher computational cost (Oliveira 2018).

To circumvent the computational limitation of Python, a hybrid code with Fortran is adopted,

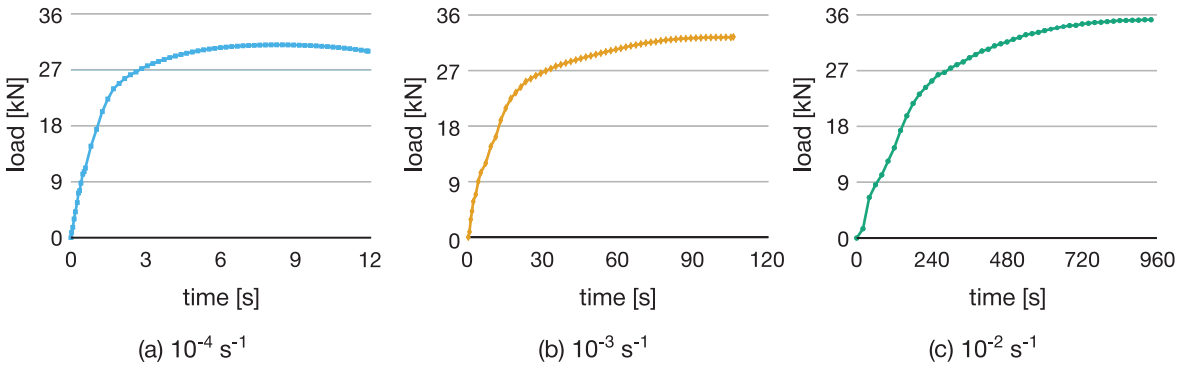

Figure 5.6 Evolution of the load throughout the deformation process of the heterogeneous thermo-mechanical tests at an average strain rate of (a) $10^{-2}\,s^{-1}$, (b) $10^{-3}\,s^{-1}$, and (c) $10^{-4}\,s^{-1}$.

where the latter is used to perform tasks that require more computational effort. There are multiple reasons for selecting Fortran, such as: (i) the availability of previously developed codes, (ii) the wide use in the scientific community, (iii) the low computational cost (ELTON 2015), and (iv) a framework to easily connect with Python. This framework is particularly important in this study, as it allows the use of code already developed and validated without additional development. The framework is called F2PY, and provides a connection between Python and Fortran (PETERSON 2009). Simply, Fortran subroutines can be called from a Python script as if they were Python functions, while only a few modifications are required in Fortran subroutines. It is part of the NumPy package, and more details about its use can be found at (NUMPY 2022).

The flow of implementation is presented in Figure 5.7, where the main tasks are represented, as well as the programming language or software in which they are executed. Initially, the reference data (displacement field and evolution of the load) is read, and then the reference strain field is calculated. The latter task is performed in Fortran because it is one of the most computationally heavy tasks. Then, the optimization algorithm is selected from the ones presented above. It should

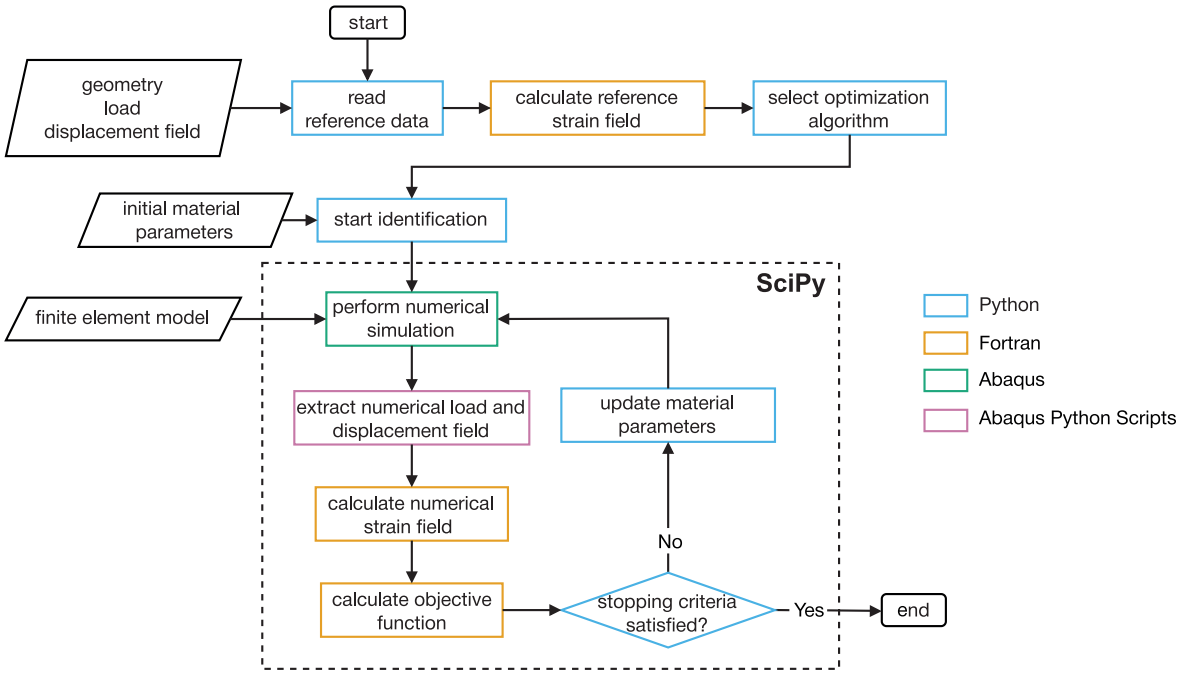

Figure 5.7 Flowchart of FEMU implementation.

be noted that additional algorithms could be made available, but only a few could be selected for this study. The optimization procedure starts by invoking the SciPy functions, at which point the control over the procedure is diminished. Then, all the other tasks are performed within this framework. The FEA simulation is performed with Abaqus/Standard at every iteration, and then an Abaqus-Python script is required to extract the numerical data. Both these tasks must be externally executed to the main Python code. Again, the strain field is calculated from the displacement field in Fortran, as well as the objective function. Although the latter is not of high computational cost, the Fortran code was reused from a previous implementation.

5.6 Numerical Evaluation

Contrary to the DE, the LM and the NM algorithms are suitable for unconstrained problems. However, to limit the search space of the three algorithms, lower and upper bounds are defined for the material parameters (see Table 5.2). The defined bounds are based on the order of magnitude of each parameter, and special attention was taken to not restrict the search space overly. For the DE algorithm, the bounds are directly imposed, while for the LM and the NM algorithms, a transformation of the material parameters is used. For all algorithms, the bounds normalize the material parameters. Considering $\bar{\mathbf{x}} = \mathbf{x}/\mathbf{x}_0$, the vector of material parameters normalized relative to its initial value $\mathbf{x}_0$, the lower and upper bounds $\mathbf{x}^{\min}$ and $\mathbf{x}^{\max}$ are normalized as

$$\bar{\mathbf{x}}_{\min} = \frac{\mathbf{x}_{\min}}{\mathbf{x}^0} \quad \text{and} \quad \bar{\mathbf{x}}^{\max} = \frac{\mathbf{x}_{\max}}{\mathbf{x}^0}, \tag{5.19}$$

where $\bar{\mathbf{x}}_{\min}$ and $\bar{\mathbf{x}}_{\max}$ are the normalized bounds. Then, the transformed material parameters $\bar{\mathbf{X}}$ for $\bar{\mathbf{x}} \geq 1$ correspond to

$$\bar{\mathbf{X}} = 1 + (\bar{\mathbf{x}}_{\max} - 1)\left[1 - \exp\left(\frac{1 - \bar{\mathbf{x}}}{\bar{\mathbf{x}}_{\max} - 1}\right)\right], \tag{5.20}$$

$\bar{\mathbf{x}} < 1$ corresponds to

$$\bar{\mathbf{X}} = 1 + (\bar{\mathbf{x}}_{\min} - 1)\left[1 - \exp\left(\frac{1 - \bar{\mathbf{x}}}{\bar{\mathbf{x}}_{\min} - 1}\right)\right]. \tag{5.21}$$

The use of these transformations guarantees that the algorithms achieve feasible solutions, i.e. solutions that lie within the search space.

To mimic image noise from actual full-field measurements, random noise from a normal Gaussian distribution is added to the reference displacement field, while, for simplicity's sake, the load signals are kept noiseless. To evaluate the robustness of the methodology and performance of algorithms, three data sets are used as reference data for the calibration: (i) without noise, (ii) with noise of amplitude 10^{-5} mm, and (iii) with noise of amplitude 10^{-3} mm. The objective function values using the reference material parameters are 0.0, 3.13×10^{-9}, and 3.017×10^{-5}, respectively, for each data set.

Because the LM and the NM algorithms are sensitive to the initial solution, five different initial sets are generated using the Latin hyperspace sampling method (McKay et al. 1979), generating solutions evenly distributed over the search space (see Table 5.2). The number of initial sets was arbitrarily selected as equal to the number of material parameters. This sampling method does not consider the reference material parameters, avoiding an initial bias towards the global minimum. The distribution of the material parameters of each generated initial set over the search space is shown in Figure 5.8. These five initial sets are used for the LM and the NM algorithms, while for the DE algorithm, a population of 50 solutions, ten times the number of material parameters, is generated using the same sampling method. This number is considered sufficiently high to avoid a significant impact on the performance of the DE algorithm (Piotrowski 2017; Oliveira 2018).

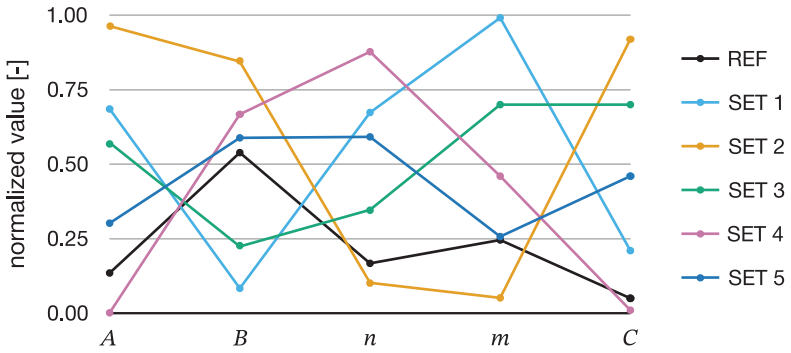

Figure 5.8 Distribution in the search space of the material parameters, normalized by the bounds, in each initial set for the LM and the NM algorithms. The reference material parameters are also represented.

The three algorithms are, in general, used with the default settings defined in the SciPy library. The exception is the step size for the finite difference approximation of the Jacobian in the LM algorithm, set equal to 10^{-3}. The adaptive setting in the NM algorithm is also set, enabling the algorithm to adapt its parameters to the problem's dimensionality.

The final solutions and objective function values obtained in the optimization procedures are summarized in Table 5.3 for the three algorithms. Additionally, in Figure 5.9, the evolution of the objective function throughout the function evaluations is represented for the three algorithms.

Let us consider, for the purpose of analysis, that the final solutions with all material parameters within 0.1 % of error from the reference ones achieve the global minimum. As such, it is observed that the LM algorithm presents the worst performance of the three algorithms. Overall, the LM algorithm achieves the global minimum only twice, whereas the NM algorithm achieves the global minimum six times, and the DE algorithm can find the global minimum in two out of three attempts. The fact that the LM algorithm cannot achieve the global minimum more often can be related to the step size for the finite difference approximation of the Jacobian, which is probably not small enough. The algorithm could benefit from starting a new optimization procedure, using the obtained solution as the initial solution, and reducing the step size.

The results of the LM and the NM algorithms confirm their sensitivity to the initial solution,

Table 5.2 Reference set, upper and lower bounds for material parameters. The sets of material parameters represent the initial solutions used for the LM and the NM algorithms.

	Parameter				
	A [MPa]	B [MPa]	n [–]	m [–]	C [–]
Reference	205.210	1124.000	0.092	1.360	0.050
Bounds					
Lower	50.000	100.000	0.010	0.500	0.000
Upper	1200.000	2000.000	0.500	4.000	1.000
Sets					
1	838.230	258.620	0.340	3.970	0.210
2	1158.140	1704.400	0.060	0.680	0.680
3	707.870	525.550	0.180	2.950	0.700
4	51.600	1368.290	0.440	2.110	0.010
5	397.470	1218.310	0.300	1.400	0.460

Table 5.3 Final solutions and objective function values of the LM, the NM, and the DE algorithms. The highlighted values indicate a relative error of 0.1% of the identified material parameters.

		Parameter					
Algorithm	**Set**	A [MPa]	B [MPa]	n [–]	m [–]	C [–]	φ [–]
LM	*without noise*						
	1	205.779	**1123.565**	**0.092**	**1.360**	**0.050**	1.860×10^{-11}
	2	1200.000	2000.000	0.500	0.705	0.055	4.900×10^{-4}
	3	269.893	1147.581	0.100	1.235	0.051	1.371×10^{-6}
	4	**205.228**	**1123.986**	**0.092**	**1.360**	**0.050**	1.134×10^{-12}
	5	356.294	1029.529	0.113	1.292	0.051	1.371×10^{-6}
	with noise of amplitude 10^{-5} mm						
	1	205.860	**1123.511**	**0.092**	**1.360**	**0.050**	3.153×10^{-9}
	2	1200.000	2000.000	0.500	0.705	0.053	4.900×10^{-4}
	3	205.202	1123.965	**0.092**	**1.360**	**0.050**	3.134×10^{-9}
	4	205.530	1123.770	**0.092**	**1.360**	**0.050**	3.139×10^{-9}
	5	375.103	1020.996	0.116	1.280	0.051	1.778×10^{-6}
	with noise of amplitude 10^{-3} mm						
	1	210.709	1120.125	0.093	1.358	**0.050**	3.017×10^{-5}
	2	50.000	2000.000	0.082	0.729	0.053	8.433×10^{-5}
	3	280.799	1074.003	0.102	1.328	**0.050**	3.046×10^{-5}
	4	200.753	**1127.190**	0.091	1.362	**0.050**	3.017×10^{-5}
	5	357.248	1029.400	0.113	1.291	0.051	3.155×10^{-5}
NM	*without noise*						
	1	**205.211**	**1123.999**	**0.092**	**1.360**	**0.050**	3.781×10^{-14}
	2	1200.000	1749.794	0.201	0.501	0.057	6.991×10^{-5}
	3	**205.211**	**1123.998**	**0.092**	**1.360**	**0.050**	4.990×10^{-14}
	4	50.000	1242.019	0.076	1.409	0.049	7.780×10^{-7}
	5	**205.210**	**1124.000**	**0.092**	**1.360**	**0.050**	1.069×10^{-16}
	with noise of amplitude 10^{-5} mm						
	1	**205.218**	**1123.991**	**0.092**	**1.360**	**0.050**	3.131×10^{-9}
	2	1200.000	1749.755	0.201	0.501	0.057	6.991×10^{-5}
	3	**205.210**	**1124.000**	**0.092**	**1.360**	**0.050**	3.130×10^{-9}
	4	124.777	1183.018	0.083	1.388	0.050	2.440×10^{-7}
	5	**205.206**	**1124.002**	**0.092**	**1.360**	**0.050**	3.131×10^{-9}
	with noise of amplitude 10^{-3} mm						
	1	206.206	**1123.279**	**0.092**	**1.360**	**0.050**	3.017×10^{-5}
	2	1200.000	1751.275	0.200	**0.500**	0.057	9.888×10^{-5}
	3	206.326	**1123.261**	**0.092**	**1.360**	**0.050**	3.017×10^{-5}
	4	50.000	1241.590	0.076	1.410	0.049	3.094×10^{-5}
	5	257.939	1082.608	0.099	1.348	**0.050**	3.032×10^{-5}
DE	*without noise*						
		205.210	**1124.000**	**0.092**	**1.360**	**0.050**	1.690×10^{-16}
	with noise of amplitude 10^{-5} mm						
		308.679	1043.777	0.106	1.336	0.051	5.824×10^{-7}
	with noise of amplitude 10^{-3} mm						
		205.152	**1123.997**	**0.092**	**1.360**	**0.050**	3.017×10^{-5}

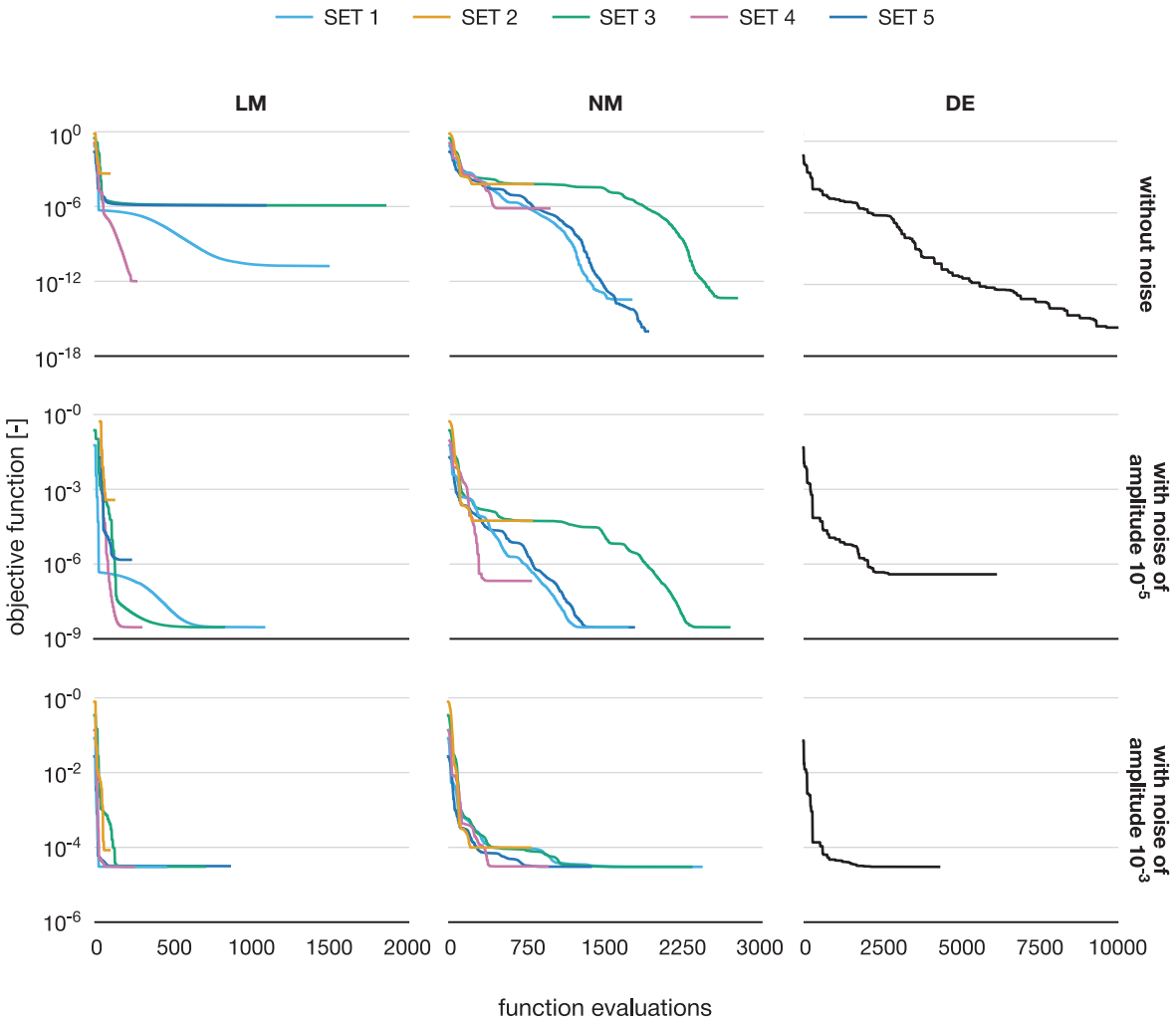

Figure 5.9 Evolution of objective function throughout function evaluations using the LM, the NM, and the DE algorithms, represented from left to right. Results correspond to data sets without noise, with noise of amplitude 10^{-5} mm, and with noise of amplitude 10^{-3} mm, from top to bottom.

with different results depending on the initial set. This is particularly evident when the parameter A of the initial set is close to its upper bound, as it is the case of set 2. In this situation, the solution stagnates early, either in the upper and lower bound of parameter A. Based on these results, it can be said that avoiding initial solutions close to the parameter's bounds can potentially decrease the chance of the algorithm converging there. In general, parameters n, m, and C present higher success rates in achieving the reference solution. However, the results of set 5 with the LM algorithm appear to have converged to local minima. In fact, one disadvantage of the LM algorithm is the susceptibility to converge to local minima.

The effect of noise on the results is interesting, as it is observed that noise can benefit the algorithm. In the case of the LM and NM algorithms, the final achieved solutions are, in general, very similar between the data sets without noise and with noise of amplitude 10^{-5} mm. However, with the LM algorithm and set 3, it is observed that noise benefits the algorithm in achieving a better solution than without noise. When the noise is increased to an amplitude of 10^{-3} mm, both the LM and the NM algorithms are not as efficient in achieving the reference solution, but the NM algorithm appears less negatively affected by the presence of an additional noise. The DE algorithm appears less affected by noise regarding the final solution, as each parameter

solution of the data set with noise of amplitude 10^{-3} mm is within 0.1 % of error from the reference solution. However, the final solution for the data set with noise of amplitude 10^{-5} mm is not close to the reference one, but it can be related to a local minimum. To further investigate the effect of noise in DE, more attempts should be performed, as the DE algorithm is not deterministic, and a component of randomness always exists. Noise also affects the objective function convergence. For example, for the LM algorithm with the initial set 1, where the final solutions are relatively similar, the algorithm converges around 1000, 600, and 50 function evaluations, respectively, for data sets without noise, with noise of amplitude 10^{-5} and 10^{-3} mm.

In summary, the differences between the LM and the NM algorithms are more evident in terms of the convergence rate, where the first tends to converge rapidly, whereas the former typically requires more function evaluations. Although only a single run was performed for the DE algorithm with each data set, it appears more robust than the other two algorithms. Nevertheless, it generally requires more function evaluations to converge to the global optimum. Using the LM or the NM algorithms in a multiple starting approach can lead to similar results to the DE algorithm.

5.7 Conclusions

A methodology to calibrate a thermoelastoviscoplastic constitutive model based on full-field measurements, and the FEMU is considered to reduce the number of thermomechanical tests involved. Three heterogeneous thermomechanical tests performed at different average strain rates are used as reference data required by the calibration procedure. By using a modern programming language library, three optimization algorithms are easily implemented in the calibration process, namely the LM, the NM, and the DE algorithms.

The identification results of each algorithm were compared for three data sets, involving different noise levels introduced in the reference displacement field. The DE algorithm has demonstrated to be the most robust algorithm by reaching or being close to the global minimum in two of the three data sets. However, it is also susceptible to local minima, even though it appears less than the LM and the NM algorithms. Moreover, the number of function evaluations required for convergence by the DE is higher than the other algorithms. The latter is particularly relevant when dealing with the FEMU. Using a computationally efficient algorithm can potentially compensate for the required effort of the FEMU. A multiple starting approach could be used to circumvent the sensitivity of the LM and the NM algorithms to initial solutions. Additionally, it would be interesting to explore the use of the DE algorithm early on to reduce the search space, and then use the LM or the NM algorithms to fine-tune the solution. Nevertheless, this approach could be susceptible to local minima in the vicinities of the global optimum.

In the scope of the present study, a parameter identification software was developed in Python and Fortran programming languages, by combining the benefits of both. In addition, by using the optimization library within Python, it will allow an easier implementation and combination of optimization algorithms in the future. Later, the NM algorithm is used in the VFM, because it is computationally more efficient than DE. Compared to the implementation of the LM algorithm, it allows more flexibility to control the identification procedure.

6 Volume Reconstruction from 3D Full-Field Measurements

6.1 Introduction

From a macroscopic point of view, it is essential to characterize and model the mechanical behavior of metallic parts up to large deformations, enabling an accurate simulation of manufacturing processes. However, the occurrence of plastic instabilities at large deformations, such as diffuse and localized necking (Bayoumi and Joshi 1992; Hill 2001), introduces additional challenges to the experimental techniques and inverse methodologies. Necking makes the deformation non-uniform and the stress state inside the specimen triaxial, eventually leading to fracture (Bridgman 1952; Tvergaard 1993). Besides, plastic deformation becomes highly heterogeneous and concentrates within the necking region. A classical method to characterize the mechanical behavior is based on the information up to necking, but it can limit the strain range drastically. Alternatively, by combining full-field measurements with inverse methods, it is possible to calibrate a constitutive model beyond necking where deformation is no longer homogeneous, such as using FEMU (Pradeau et al. 2016). The VFM can potentially be used as an alternative to FEMU, but it has been mainly used in the 2D space where plane stress conditions are assumed. However, because the stress state is triaxial, using the VFM considering plane stress assumptions is no longer valid, and a 3D analysis is required (Rossi and Pierron 2012b; Kim et al. 2013; Coppieters et al. 2017; Martins et al. 2019). Nevertheless, it would be interesting to know which thicknesses can be applied to the VFM in a 2D framework, but no previous study has investigated it.

In the field of material testing and characterization, full-field measurement techniques are being used more and more frequently as the standard procedure. Pierron and Grédiac (2021) give a comprehensive overview of this topic and introduce the concept of "Material Testing 2.0". One advantage of these techniques is that they allow for the measurement of displacement and strain fields on the entire surface of the specimen. It enables the transition from classical mechanical tests to more complex ones, leading to more and richer data acquisition from a single test. Consequently, it reduces the cost and effort of material testing and improves the accuracy of calibrated constitutive models (Cooreman et al. 2008).

Among full-field measurement techniques, the DIC is the most widespread and fast-growing method in solid mechanics (Sutton et al. 2009). The most common optical setup nowadays is a two-camera setup that can acquire the surface displacement field in the 3D space (stereo-DIC). However, using the DIC to obtain information in the bulk of the material is still a big challenge

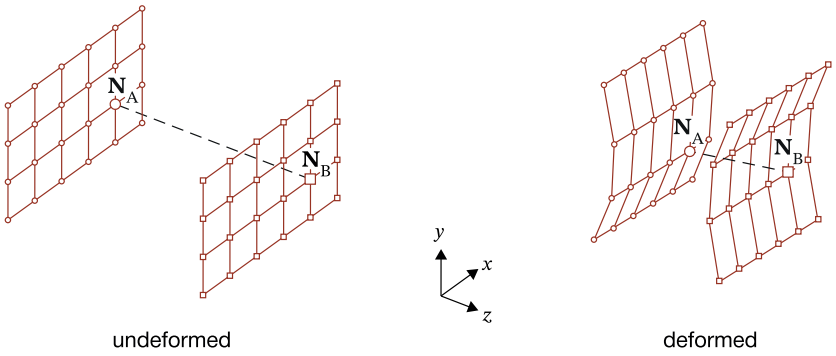

Figure 6.1 Schematic illustration of measurement points at the front and back surfaces of the specimen, in the undeformed and deformed configurations.

(Buljac et al. 2018), but something required to use the VFM in a 3D framework. In the absence of bulk measurements, plane stress conditions have been commonly assumed to estimate the deformation in the thickness direction for sheet metals. While technology is still limited to surface displacements, efforts have been made to, at least, reconstruct the 3D displacement field over the whole external surface of solids (Badel et al. 2012; Genovese et al. 2016). For example, Li et al. (2017) used a multiple camera DIC system, with two cameras in the front and another two in the back of the specimen, to measure the whole-field thickness strain.

Starting from surface full-field measurements, a volume reconstruction method able to reconstruct the volume displacement field of a homogeneous solid was introduced with the aim of using the VFM in a 3D framework Rossi and Pierron (2012a). The potential benefits of this proposed method is that it could eventually replace more advanced and costly techniques, such as the DVC. However, an in-depth study of the uncertainties associated with this method is required.

The final aim of using the volume reconstruction method is to accurately reconstruct the strain field, from real experiments, over the whole volume of the specimen. Then, it is intended to identify the material parameters through the VFM in a 3D framework. To achieve that, this study performs an in-depth analysis of the uncertainty associated with the internal mesh generation (IMG). At first, the volume is directly reconstructed from FEA data, and afterwards, virtual experiments mimicking real experiments are employed (Lava et al. 2009). The interest in using virtual experiments is to reduce the gap to experimentally acquired measurements without having to perform the real experiment.

6.2 Internal Mesh Generation

The IMG method was proposed to reconstruct the volume displacement field inside a solid by starting from surface measurements (Rossi and Pierron 2012b; Rossi et al. 2013; Rossi et al. 2018b). It can be applied to flat or cylindrical specimens, but only the first one is considered here. In the undeformed configuration, flat specimens are assumed to have a constant thickness and two opposite parallel faces, one in the back and another in front of the specimen. A requirement of IMG is that the displacement field is known a priori on both surfaces, named here surfaces A and B. The coordinate system is chosen so that the z axis is perpendicular to the thickness in the undeformed configuration.

Let us consider that $\mathbf{N}_\mathrm{A} = (N_{\mathrm{A}_x}, N_{\mathrm{A}_y}, N_{\mathrm{A}_z})$ and $\mathbf{N}_\mathrm{B} = (N_{\mathrm{B}_x}, N_{\mathrm{B}_y}, N_{\mathrm{B}_z})$ are points located in surfaces A and B, respectively. In the undeformed configuration, $\mathbf{N}_\mathrm{A}$ and $\mathbf{N}_\mathrm{B}$ share the same coordinates along the x axis ($N_{\mathrm{A}_X} = N_{\mathrm{B}_X}$) and along the y axis ($N_{\mathrm{A}_y} = N_{\mathrm{B}_y}$), but different coordinates along the z axis. A schematic illustration of points $\mathbf{N}_\mathrm{A}$ and $\mathbf{N}_\mathrm{B}$ on surfaces A and B, both in undeformed and deformed configurations, is shown in Figure 6.1.

The IMG adopts quadratic Bézier curves to construct points inside the specimen. The Bézier curve is defined by one point on each surface, $\mathbf{N}_A$ and $\mathbf{N}_B$, and an internal point $\mathbf{P} = (P_x, P_y, P_z)$ inside the volume and located in a plane between points $\mathbf{N}_A$ and $\mathbf{N}_B$. The Bézier curve is denoted $\mathbf{B}$ and mathematically defined as

$$\mathbf{B}(z) = (1-z)^2\mathbf{N}_A + 2(1-z)\mathbf{P} + z^2\mathbf{N}_B, \tag{6.1}$$

with $0 \leq z \leq 1$ defining the position of each internal point along the Bézier curve, so that $\mathbf{B}(0) = \mathbf{N}_A$ and $\mathbf{B}(1) = \mathbf{N}_B$. The distribution of internal points $\mathbf{z}$ along the Bézier curve is linearly defined. Additionally, the curve is tangent to segment $\overline{\mathbf{N}_A\mathbf{P}}$ at $\mathbf{B}(0)$ and to segment $\overline{\mathbf{N}_B\mathbf{P}}$ at $\mathbf{B}(1)$.

The methodology behind the IMG is schematically illustrated in Figure 6.2, for the undeformed and deformed configurations. For clarity, the point of view is chosen perpendicular to the x axis. However, points and vectors are considered in the 3D space. The internal point $\mathbf{P}$ is defined as the intersection between the straight line perpendicular to surface A (or surface B) in $\mathbf{N}_A$ (or $\mathbf{N}_B$) and the middle plane perpendicular to segment $\overline{\mathbf{N}_A\mathbf{N}_B}$. In the undeformed configuration, $\mathbf{P}$ is simply defined as the average of the surface points $\mathbf{N}_A$ and $\mathbf{N}_B$:

$$\mathbf{P} = \frac{\mathbf{N}_A + \mathbf{N}_B}{2}, \tag{6.2}$$

yielding a straight line from $\mathbf{N}_A$ to $\mathbf{N}_B$. However, in the deformed configuration, the specimen is not flat anymore, and two different internal points $\mathbf{N}_A$ and $\mathbf{N}_B$ are obtained by starting from $\mathbf{N}_A$ and $\mathbf{N}_B$, respectively. According to geometrical considerations, the internal points $\mathbf{P}_A$ and $\mathbf{P}_B$ are defined as

$$\mathbf{P}_A = \mathbf{N}_A - \frac{|\mathbf{N}_A - \mathbf{N}_B|^2}{2\,(\mathbf{N}_A - \mathbf{N}_B)\cdot\hat{\mathbf{n}}_A}\hat{\mathbf{n}}_A, \tag{6.3}$$

$$\mathbf{P}_B = \mathbf{N}_B - \frac{|\mathbf{N}_B - \mathbf{N}_A|^2}{2\,(\mathbf{N}_B - \mathbf{N}_A)\cdot\hat{\mathbf{n}}_B}\hat{\mathbf{n}}_B, \tag{6.4}$$

where $\cdot$ is the scalar product, and $\hat{\mathbf{n}}_A$ and $\hat{\mathbf{n}}_B$ are the surface normals of points $\mathbf{N}_A$ and $\mathbf{N}_B$, respectively. The internal point $\mathbf{P}$ is then computed as

$$\mathbf{P} = \frac{\mathbf{P}_A + \mathbf{P}_B}{2}. \tag{6.5}$$

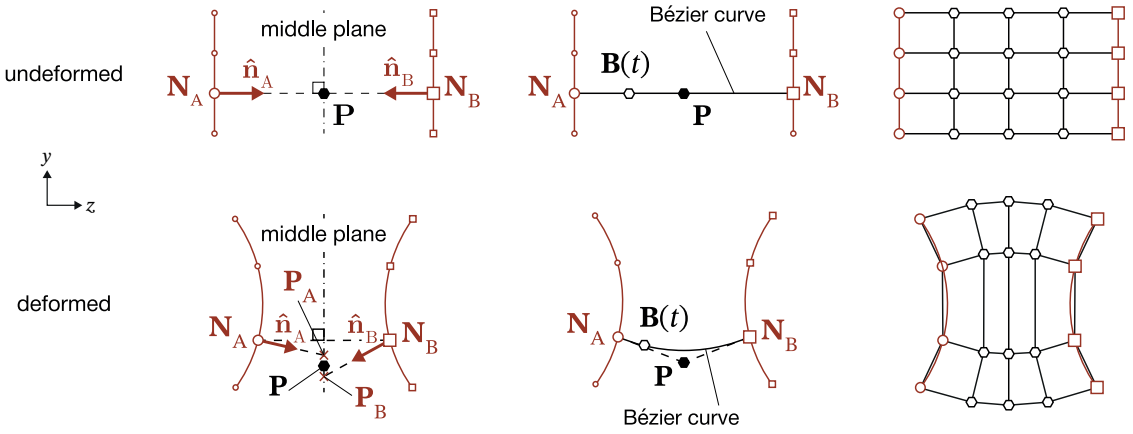

Figure 6.2 Schematic of the IMG for flat specimens in the undeformed and deformed configurations.

It can be pointed out that if the deformation is symmetrical, then $\mathbf{P}_A \equiv \mathbf{P}_B \equiv \mathbf{P}$, as it theoretically occurs in isotropic materials. However, due to measurement errors and possible anisotropy of heterogeneous materials, the former is usually not true.

Finally, a 3D regular mesh is obtained with n_x, n_y, and n_z nodes along the x, y, and z axes, respectively. Consequently, there will be $m_x = n_x - 1$, $m_y = n_y - 1$, and $m_z = n_z - 1$ elements along the x, y, and z axes, respectively. Deciding the number of internal points is similar to deciding the number of elements through the thickness in a 3D finite element model. The more points through the thickness, the finer the mesh is, and more precision is obtained. However, the computational time of future operations, such as strain calculation, will increase proportionally. It is important to balance the required precision and computational time, and ideally a convergence study can be used to determine the most suitable number of internal points. However, the number of nodes of the surface mesh is more dependent on the number of measurement points coming from experiments. In the end, the volume displacement and strain fields are calculated using the shape functions of hexahedral elements, as illustrated in the last schematic of Figure 6.2. From an implementation point of view, the steps of IMG can be defined as:

1. Read the experimental coordinates field of undeformed configuration $\mathbf{X}_{E_0}$ and 3D displacement field of deformed configuration $\mathbf{u}_{E_1}$, for every considered time instant;
2. Define the coordinates field of regular grid over the specimen surfaces in the undeformed configuration $\mathbf{X}_{S_0}$. The regular grid coordinates field can be calculated based on the sparsity and coordinates field of experimental points;
3. Interpolate the displacement field $\mathbf{u}_{E_1}$ over regular grid $\mathbf{X}_{S_0}$ to obtain the interpolated displacement field $\mathbf{u}_{S_1}$ through an interpolation function $\mathcal{I}$ defined as

$$\mathbf{u}_{S_1} = \mathcal{I}(\mathbf{u}_{E_1}, \mathbf{X}_{E_0}, \mathbf{X}_{S_0}), \tag{6.6}$$

   and obtain the regular grid coordinates field in the deformed configuration $\mathbf{X}_{S_1}$ as

$$\mathbf{X}_{S_1} = \mathbf{X}_{S_0} + \mathbf{u}_{S_1}. \tag{6.7}$$

4. Calculate the surface normals of the regular grid in the deformed configuration $\hat{\mathbf{n}}_{S_1}$ through a function $\mathcal{S}$ as

$$\hat{\mathbf{n}}_{S_1} = \mathcal{S}(\mathbf{X}_{S_1}). \tag{6.8}$$

5. Then, calculate the middle plane between the front and back surfaces defined over the regular grid in the undeformed configurations;
6. Reconstruct the internal points through the Bézier curve definition of Equation 6.1 to obtain the reconstructed points coordinates field $\mathbf{X}_{IMG}$. Then, the reconstructed displacement field of the deformed configuration $\mathbf{u}_{IMG_1}$ are obtained as

$$\mathbf{u}_{IMG_1} = \mathbf{X}_{IMG_1} - \mathbf{X}_{IMG_0}, \tag{6.9}$$

   where $\mathbf{X}_{IMG_0}$ and $\mathbf{X}_{IMG_1}$ represent, respectively, the reconstructed points coordinates field in the undeformed and deformed configurations.
7. Finally, calculate the reconstructed strain field $\boldsymbol{\varepsilon}_{IMG_1}$ using hexahedral shape functions $\mathcal{F}$ as

$$\boldsymbol{\varepsilon}_{IMG_1} = \mathcal{F}(\mathbf{X}_{R_0}, \mathbf{u}_{IMG_1}). \tag{6.10}$$

Lastly, the IMG is numerically implemented in Python programming language, using an array-based approach.

6.3 Plane Strain Tensile Test

To evaluate the accuracy of the IMG when applied to real experiments, a FEA simulation is used for which the whole volume deformation history is known. The finite element model reproduces the necking evolution in specimens under severe plastic deformation. In this study, a 20 mm thick flat specimen, as represented in Figure 6.3a, is considered under a plane strain tensile test and an initial rectangular section. The finite element model is modeled in 3D, and the commercial software Abaqus/Standard is used (DASSAULT SYSTÈMES 2019). The bottom extremity of the test is fixed, and a vertical displacement is imposed on the top extremity. Moreover, an eight-node brick element with reduced integration is used, as well as a large strain formulation. The global element size is 1 mm, and a structured mesh is used in the volume of interest (VOI) between $76 \times 20\,\text{mm}^2$ in the xy plane, resulting in 1520 elements and 1617 nodes in the VOI. The dimensions of the latter were defined based on the equivalent plastic strain distribution, as it is observed that it mainly localizes in the center region of the specimen (see Figure 6.3c).

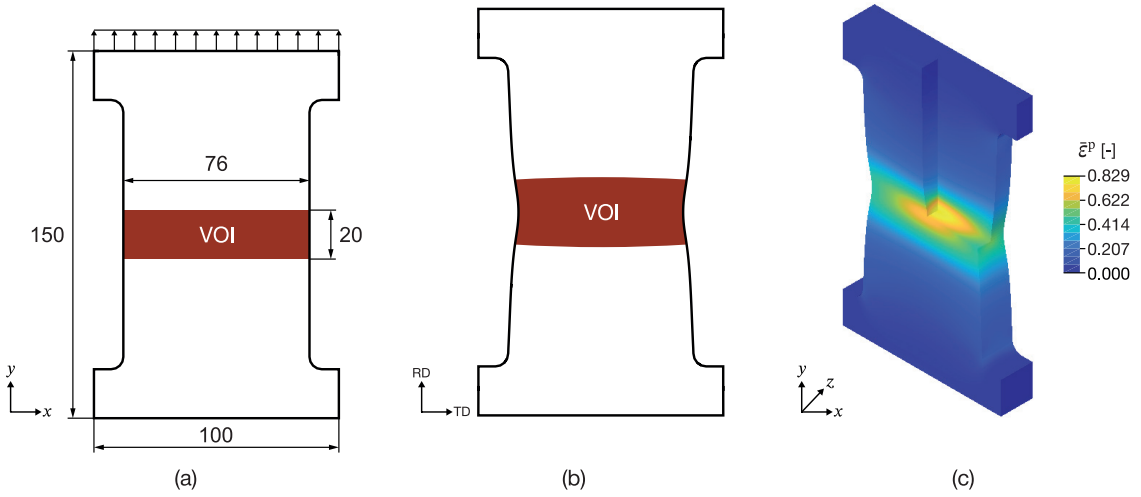

Figure 6.3 Finite element model of plane strain tensile test in the (a) undeformed configuration, (b) deformed configuration, and (c) 3D view cut of the equivalent plastic strain distribution in the deformed configuration. Dimensions in mm.

A virtual material is considered, where the constitutive models and material parameters are selected to resemble the behavior of a metal with high anisotropy. The Hill 1948 yield criterion is used to describe the yield surface, and Swift's hardening law is selected to describe the strain hardening curve (see Section 2.3). The material parameters, including Young's modulus E and Poisson's ratio ν, are provided in Table 6.1.

The FEA simulation is displacement-driven, with a maximum imposed vertical displacement

Table 6.1 Elastic properties of the material and parameters of the constitute models used for the virtual material.

Elasticity		Hill 1948						Swift		
E [GPa]	ν [–]	F [–]	G [–]	H [–]	N [–]	M [–]	L [–]	σ_0 [MPa]	K [MPa]	n [–]
70	0.3	0.252	0.826	0.174	2.242	1.500	1.500	226.7	310.5	0.08

of 16 mm in the top extremity, and is composed of 100 time instants. At the last time instant, the maximum values of equivalent plastic strain are approximately 0.8 which falls in the range of the fracture strain observed for ductile metals, as observed in the deformed configuration of Figure 6.3c. In this representation, it is possible to notice that a severe necking occurs at the center of the specimen. The necking is associated with a complex 3D deformation field, as illustrated over the cross-sections. The maximum strain is obtained at the inner part of the specimen and therefore cannot be directly evaluated by surface measurements.

Analyzing the distribution of the components of the strain tensor, it is observed that the test is largely dominated by the components ε_{yy} and ε_{zz} (see Figure 6.4). The latter components achieve its highest values in the middle of the specimen, 0.542 and -0.422 for ε_{yy} and ε_{zz}, respectively. Also, both strain components present a considerable gradient increasing towards the middle of the specimen. The other components present considerably smaller magnitudes, particularly ε_{xz} and ε_{yz}, for which the maximum achieved values are lower than 0.1. Although the strain component ε_{xx} presents low values comparatively to ε_{yy}, its maximum values are close to the free edges of the specimen, which might be difficult regions to reconstruct. The strain field obtained from the FEA simulation is used in the following sections as the reference strain field $\boldsymbol{\varepsilon}_{\text{REF}}$. The next step is to use the IMG to reconstruct the internal displacement field, and compare the reconstructed strain field to $\boldsymbol{\varepsilon}_{\text{REF}}$.

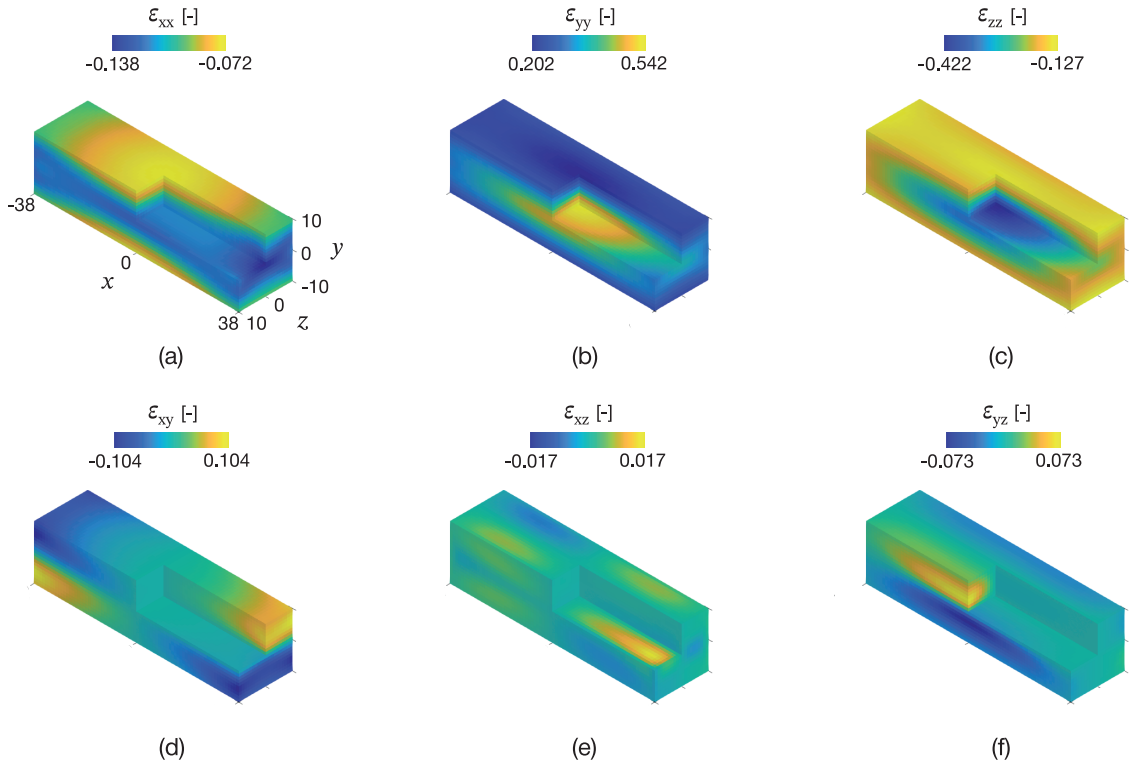

Figure 6.4 Maps of the 3D cross-sections for strain tensor components (a) ε_{xx}, (b) ε_{yy}, (c) ε_{zz}, (d) ε_{xy}, (e) ε_{xz}, and (f) ε_{yz}, at the last time instant and represented on the reference configuration. For simplicity's sake, the axes and coordinates are only represented in the top-left map.

6.4 Volume Reconstruction from Finite Element Analysis

The necking occurs in the central part of the specimen, where the stress state is triaxial and cannot be inferred from surface measurements. The VOI used to verify the reconstruction algorithm is the central zone where localized necking occurs. A regular grid of 77×21 nodes, respectively,

along the specimen's width (x axis), and length (y axis), is selected in the reconstruction algorithm to coincide with the number of nodes of the finite element model. Therefore, it is not necessary to interpolate the displacement fields to the regular grid, because these are coincident, i.e., $\mathbf{u}_{S_1} = \mathbf{u}_{E_1}$ (see Equation 6.6). Moreover, 21 nodes are used in the reconstruction of the internal points, to have a direct correspondence between the reference and the reconstruction. In terms of computational effort, the IMG is very fast at reconstructing the displacement field. In this study, it takes approximately two minutes to reconstruct the displacement field of all 100 time instants.

The reconstructed volume is evaluated by comparing the reconstructed strain field $\boldsymbol{\varepsilon}_{\mathrm{IMG}}$ to the reference strain field $\boldsymbol{\varepsilon}_{\mathrm{REF}}$, for every time instant. The absolute error and the average absolute error are used to express the difference between the two strain fields. Mathematically, for a given time instant t and material point i, the absolute error $\boldsymbol{\delta}$ is given by

$$\boldsymbol{\delta}(t,i) = \left|\boldsymbol{\varepsilon}_{\mathrm{IMG}}(t,i) - \boldsymbol{\varepsilon}_{\mathrm{REF}}(t,i)\right|. \tag{6.11}$$

while the average absolute error $\bar{\boldsymbol{\delta}}$ of all material points is given by

$$\bar{\boldsymbol{\delta}}(t) = \frac{1}{n_{\mathrm{p}}} \sum_{i=1}^{n_{\mathrm{p}}} \boldsymbol{\delta}(t,i), \tag{6.12}$$

where n_{p} is the total number of material points.

In Figure 6.5, the evolution of $\boldsymbol{\delta}$ is represented for each strain tensor component throughout all time instants. All material points of the VOI are represented within the plotted area, while the superior boundary represents the maximum observed error, and the intermediate white line represents $\bar{\boldsymbol{\delta}}$. A first observation can be made regarding the increase of error with deformation. The higher the deformation, the more the IMG is susceptible to error. Nevertheless, a reasonable

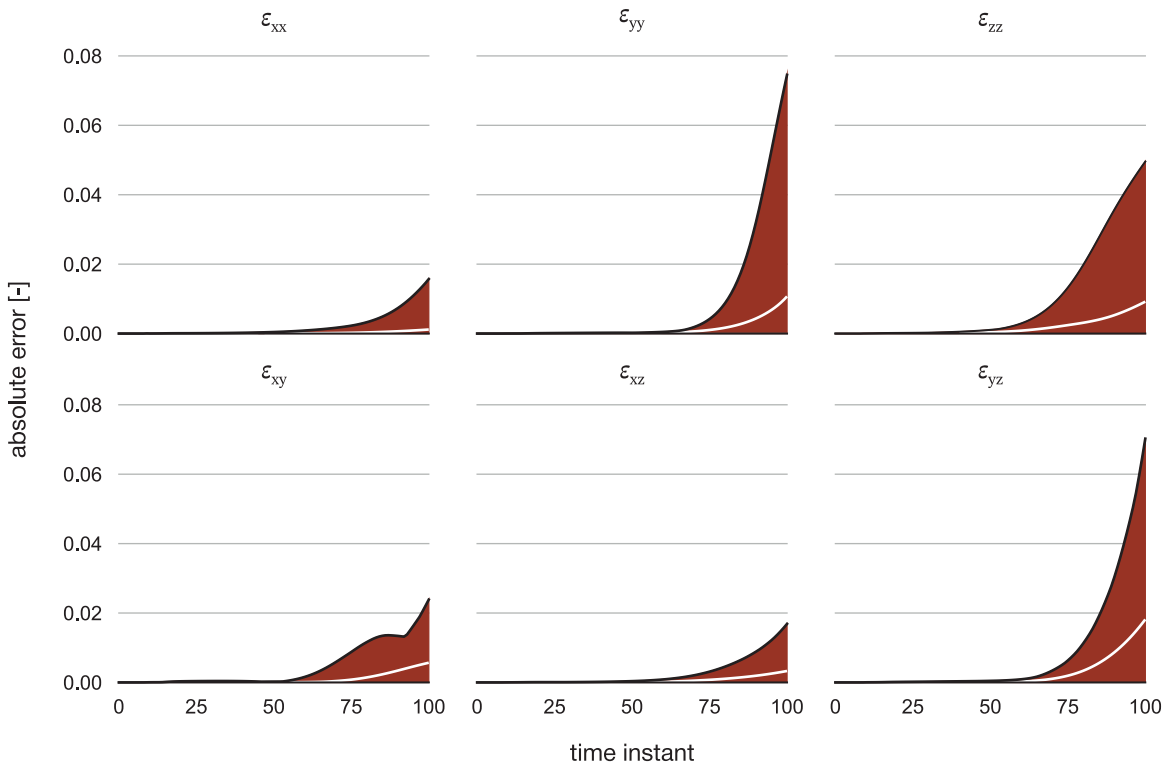

Figure 6.5 Evolution of the absolute error for each reconstructed strain tensor component throughout all time instants. The superior bound represents the maximum absolute error, and the white line represents the average absolute error.

agreement is observed between the reference and reconstruction, with maximum errors of up to 0.08 in the ε_{yy} and ε_{yz} components. Even though the maximum errors are relatively high compared to the observed strain values, the average values are much closer to the minimum than the maximum. The error evolution of the thickness strain ε_{zz} is distinct from the other components, as the error increases more gradually, rather than abruptly, towards the end of the test. This is a sign that the source of error in ε_{zz} is not just related to the increase of deformation, as discussed further ahead.

The 3D maps also present the spatial absolute error in Figure 6.6. Overall, ε_{xx} and ε_{yy} are well reconstructed, as a large region presents low errors. However, ε_{xx} presents large errors towards the free edges of the specimen, and ε_{yy} towards the middle of the specimen. Nevertheless, the accentuated error on the free edges can also be related to the surface normals estimation close to the free edges, as no data is available beyond the specimen's boundaries. The use of additional information from the specimen's sides could potentially improve the accuracy of the IMG towards the free edges. However, using the sides' information would have added more complexity to the methodology, both in terms of data acquisition and integration of the data within the IMG methodology.

The absolute error spatial distribution of ε_{zz} is more complex (see Figure 6.6c). It is observed that the highest error is at the center of the specimen's surface. Moreover, following a path towards the middle of the specimen, the error decreases between the specimen's surface and middle plane, but then increases again towards the middle. This behavior indicates that the reconstructed strain ε_{zz} is approximately homogeneous through the thickness, representing an average of the reference gradient values. The source of this behavior is the linear distribution of internal points along the Bézier curve. The combination of linear distribution with perpendicular surface normals to the

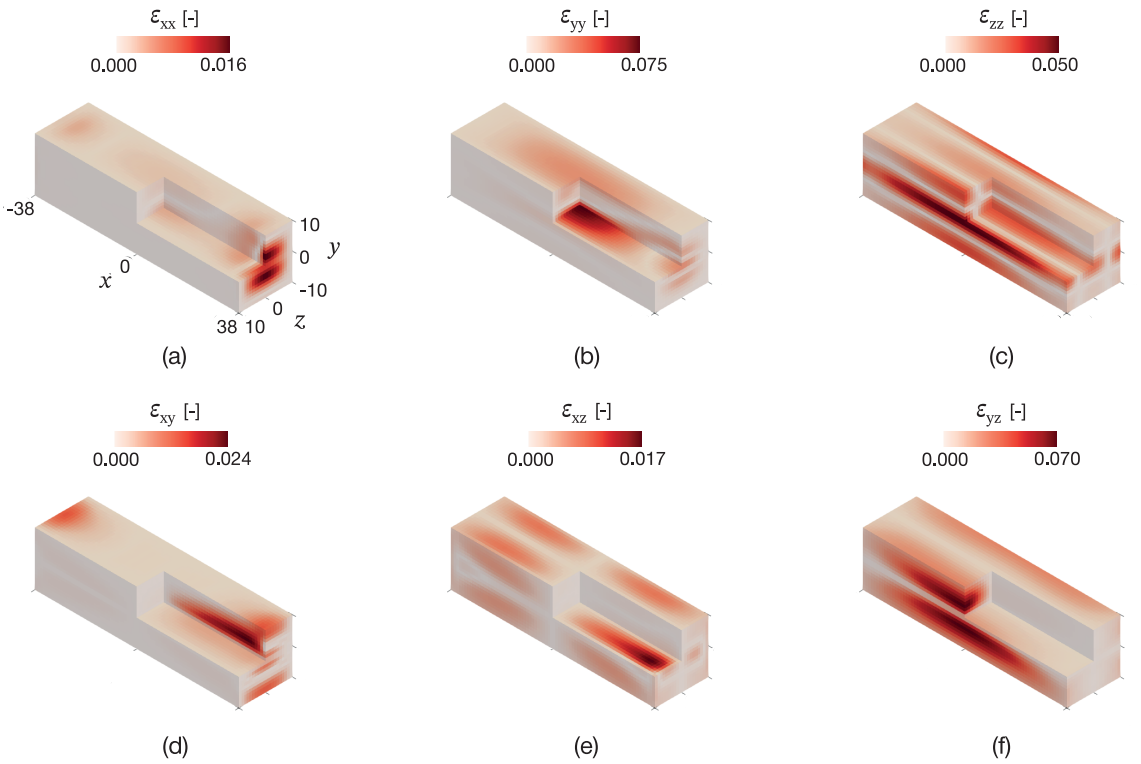

Figure 6.6 Maps of the 3D cross-sections of absolute error for reconstructed strain tensor components (a) ε_{xx}, (b) ε_{yy}, (c) ε_{zz}, (d) ε_{xy}, (e) ε_{xz}, and (f) ε_{yz}, at the last time instant and represented on the undeformed configuration. For simplicity's sake, the axes and coordinates are only represented in the top-left map.

undeformed surfaces leads to Bézier curves with little or no curvature. Although the latter is less observed at distances away from the specimen's center, the most problematic is still the region of higher deformations. However, this drawback of the IMG has not been previously described nor identified.

An investigation of the specimen's global volume evolution, calculated as the sum of all elements volume, shows a discrepancy between the reconstruction and the reference, as shown in Figure 6.7a. During the elastic regime, which corresponds to the initial rapid evolution, and beginning of the plastic regime, the reconstruction shows a global volume approximately identical to the reference. However, starting from the time instant of maximum load, the global volume of reconstruction presents a rapid increase and deviation from the reference values, which are approximately constant afterwards. Additionally, a local analysis of the volume of the elements showed a high discrepancy. In the reference, the initial volume of the elements is approximately preserved, with a residual increase coming from the elastic deformation. On the other hand, the reconstruction shows that the elements' volume starts deviating from the initial volume at values of equivalent plastic strain of approximately 0.13, which are rather low relative to the maximum values at the last time instant. This is shown in Figure 6.7b, where the volume's evolution of two elements, one located on the specimen's surface and another on the middle of the surface (between two opposite surfaces) is represented. These two deviations from reference, global and local volume, are thought to be a source of error of the IMG, leading to incorrect reconstructed strain fields. Therefore, the next section focuses on improving the IMG by integrating two types of correction.

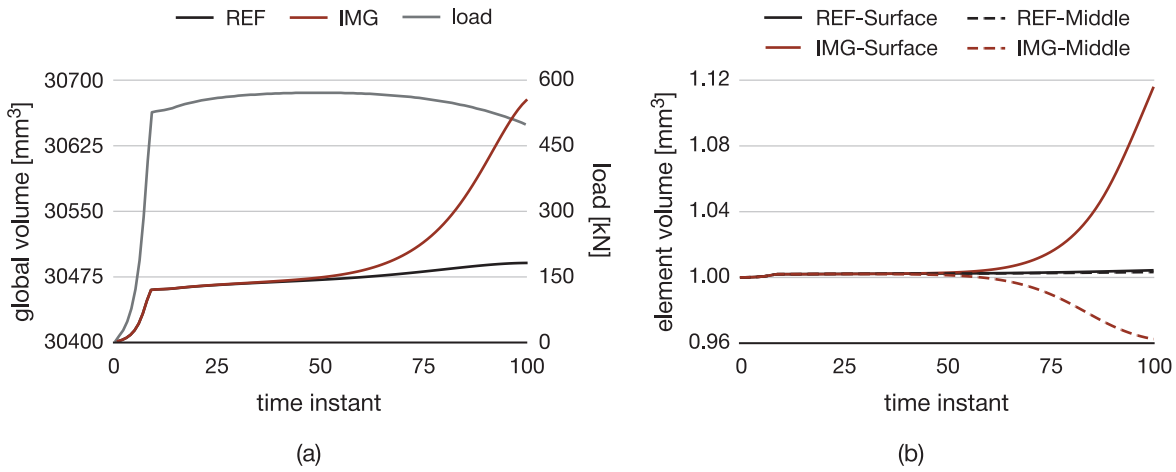

Figure 6.7 Evolution throughout time instants of (a) global volume of reference and reconstruction, with the reference load for comparison, and (b) volume of elements in the surface, and another in the middle for reference and reconstruction.

6.5 Improvements to Internal Mesh Generation

The analysis of the reconstructed strain field relative to the reference identified two possible sources of error of the IMG: the increase in the geometry's global volume and the local element's volume deviation from its initial value. This section proposes two strategies to improve the accuracy of the IMG in reconstructing the strain field.

6.5.1 Correction of Global Volume

As previously observed in Figure 6.7a, the reconstructed global volume deviates abruptly from the reference after a certain amount of deformation. On the other hand, the reference global

volume evolves approximately linearly after the onset of plastic deformation. The proposed solution attempts to correct the global volume after it starts deviating from the reference. However, to generalize the algorithm to applications where the reference is unknown, the threshold is identified after the abrupt increase is detected in the global volume evolution.

The global volume is, mathematically, the sum of all elements volume, but in the IMG, it can also be seen as the volume enclosed by the geometry's external surfaces. This way, by adjusting the enclosing surfaces, it is possible to correct the global volume. However, the front and back surfaces are the only known information of the specimen (either from the FEA simulation or experimental measurements), while all the other surfaces are reconstructed using the IMG. In turn, the IMG is based on the normals of the front and back points surface, which govern the unknown enclosing surfaces. Therefore, the proposed algorithm attempts to correct the global volume by adjusting the front and back points normals to the surface (see Figure 6.8).

The first part of the algorithm identifies the threshold of abrupt increase and determines the predicted global volume of subsequent time instants. Initially, the global volume evolution is only due to elastic deformation. After the onset of plastic deformation, the evolution rate changes, and is necessary to quantify it. Therefore, the global volume evolution is incrementally fitted by a second order polynomial regression, and the coefficient of determination R^2 is calculated. Whenever R^2 drops below 0.99, it is considered that the given time instant is the onset of plastic deformation. From this time instant onward, the global volume evolution is incrementally fitted

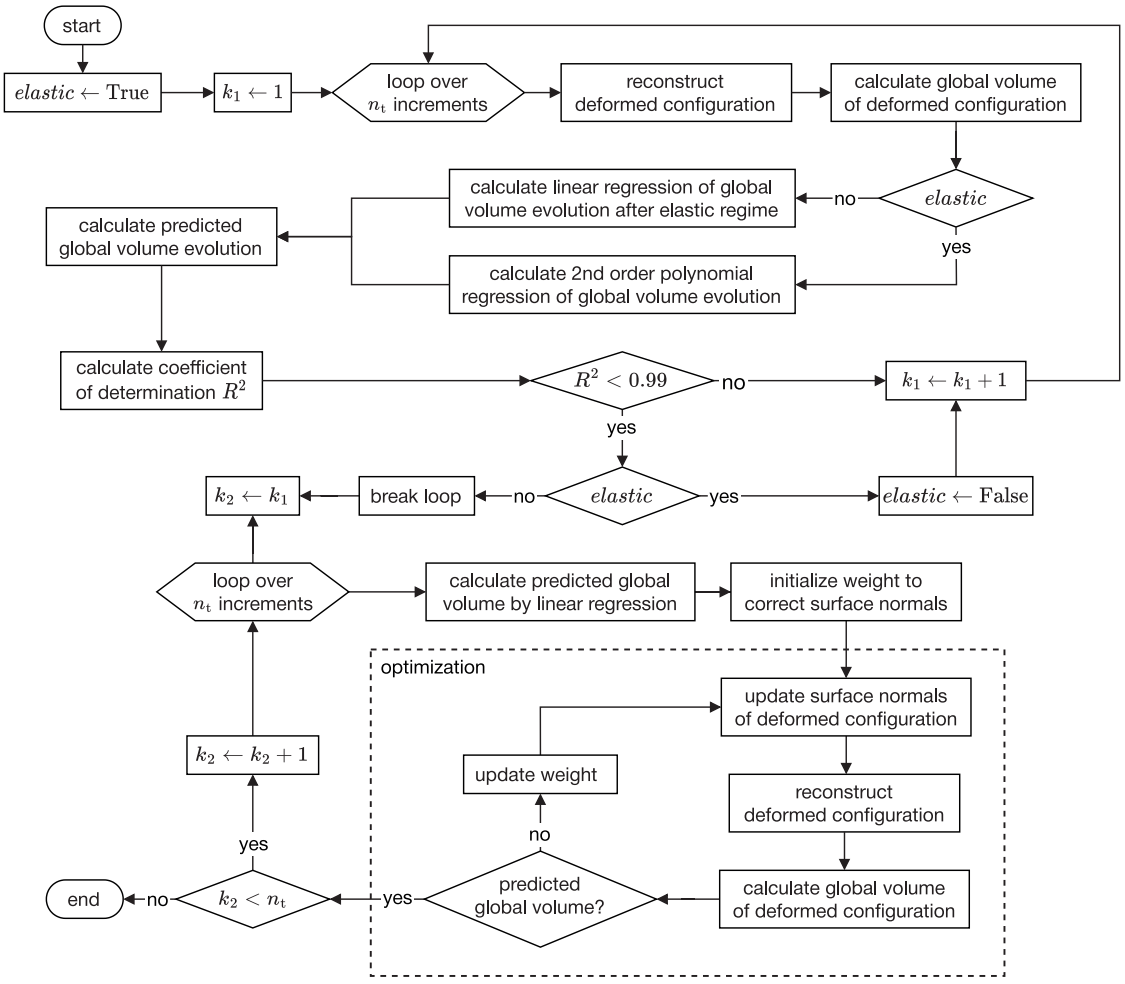

Figure 6.8 Flowchart of the algorithm to correct the global volume in the IMG.

by a linear regression. Similarly, whenever R^2 drops below 0.99, it is considered an abrupt increase. Then, the linear regression is used to predict the global volume of subsequent time instants and correct it to a linear evolution. This first part of the algorithm is schematically represented in the top section of Figure 6.8.

The second part of the algorithm is dedicated to correcting the global volume evolution by adjusting the surfaces' normals. Let us consider that $\hat{\mathbf{n}}$ represents the surface normal of any given point. The corrected surface normal $\hat{\mathbf{n}}_c$ is obtained by multiplying $\hat{\mathbf{n}}$ by a given weight $\mathbf{w} = (w_x, w_y, w_z)$, for each component, as

$$\hat{\mathbf{n}}_c = (w_x \hat{n}_x, w_y \hat{n}_y, w_z \hat{n}_z), \tag{6.13}$$

which is then normalized by its magnitude to transform it into a unit normal vector.

The search for the optimal weight is performed using the Levenberg-Marquardt algorithm from Python's optimization library (see Section 5.3). The optimization algorithm starts from the known solution, where $\mathbf{w} = (1, 1, 1)$, and iteratively searches for the optimum weight by comparing the corrected global volume with the one predicted using the linear regression. The optimization procedure stops whenever the corrected global volume drops below the predicted global volume. This second part of the algorithm is schematically presented at the bottom section of Figure 6.8.

Different combinations of weights are implemented to investigate which one yields the best results. These combinations are differentiated by the surfaces normal component or components adjusted by a given weight, in particular by optimizing the individual weights associated with the x component (IMG-Global-X), y component (IMG-Global-Y), z component (IMG-Global-Z), and another combination where the three components are simultaneously adjusted by optimizing three different weights (IMG-Global-XYZ). Mathematically, these combinations result in corrected surface normals given by

$$\hat{\mathbf{n}}_c = \begin{cases} (w_x \hat{n}_x, \quad \hat{n}_y, \quad \hat{n}_z) & \text{with IMG-Global-X} \\ (\quad \hat{n}_x, w_y \hat{n}_y, \quad \hat{n}_z) & \text{with IMG-Global-Y} \\ (\quad \hat{n}_x, \quad \hat{n}_y, w_z \hat{n}_z) & \text{with IMG-Global-Z} \\ (w_x \hat{n}_x, w_y \hat{n}_y, w_z \hat{n}_z) & \text{with IMG-Global-XYZ} \end{cases}. \tag{6.14}$$

The combination IMG-Global-XYZ is a bigger challenge than the three others in terms of optimization, because three different weights are optimized instead of only one. In Figure 6.9, the corrected global volume evolution by using the four combinations is represented. The only combination that failed to correct was when only optimizing the weight given to $\hat{n}_x$, while the others successfully

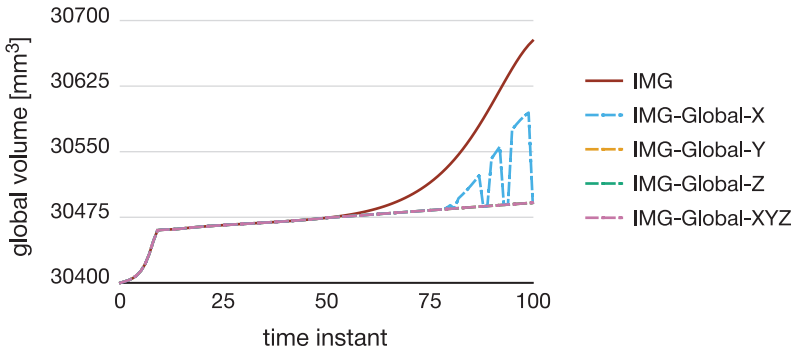

Figure 6.9 Comparison of the global volume evolution throughout time instants between the IMG with different combinations of the corrected global volume.

corrected to the linearly predicted values. The evolution of the latter is overlapped in Figure 6.9, thus only the evolution of IMG-Global-XYZ is visible.

Although three combinations of the weights succeeded in correcting the global volume, it does not mean it yielded three similar solutions. To decide which combination is best suited to improve the IMG, the evolution of the strain tensor components average absolute error for each combination is analyzed and presented in Figure 6.10. Comparatively to the average absolute error obtained with the IMG without correction, it is observed that the only combinations that perform worst for any component are IMG-Global-X and IMG-Global-XYZ, in particular, for ε_{xx}, ε_{xy}, and ε_{xz}. The average absolute error of ε_{zz} has barely changed for any combination, but improvements are observed in the other components when using the combinations IMG-Global-Y and IMG-Global-Z. The differences are slight between these two combinations, but both decrease by 50 %, or more, the average absolute error of ε_{yy}, ε_{xy}, and ε_{yz}. In further analyses, the combination IMG-Global-Z is adopted because it corrects the component through the thickness. Therefore, it is a more general approach that can be applied in different tests. Computationally, the correction of global volume takes approximately 15 minutes for all time instants. Comparatively to the time required by the IMG without global correction, it is a substantial increase, but it can still be considered computationally fast.

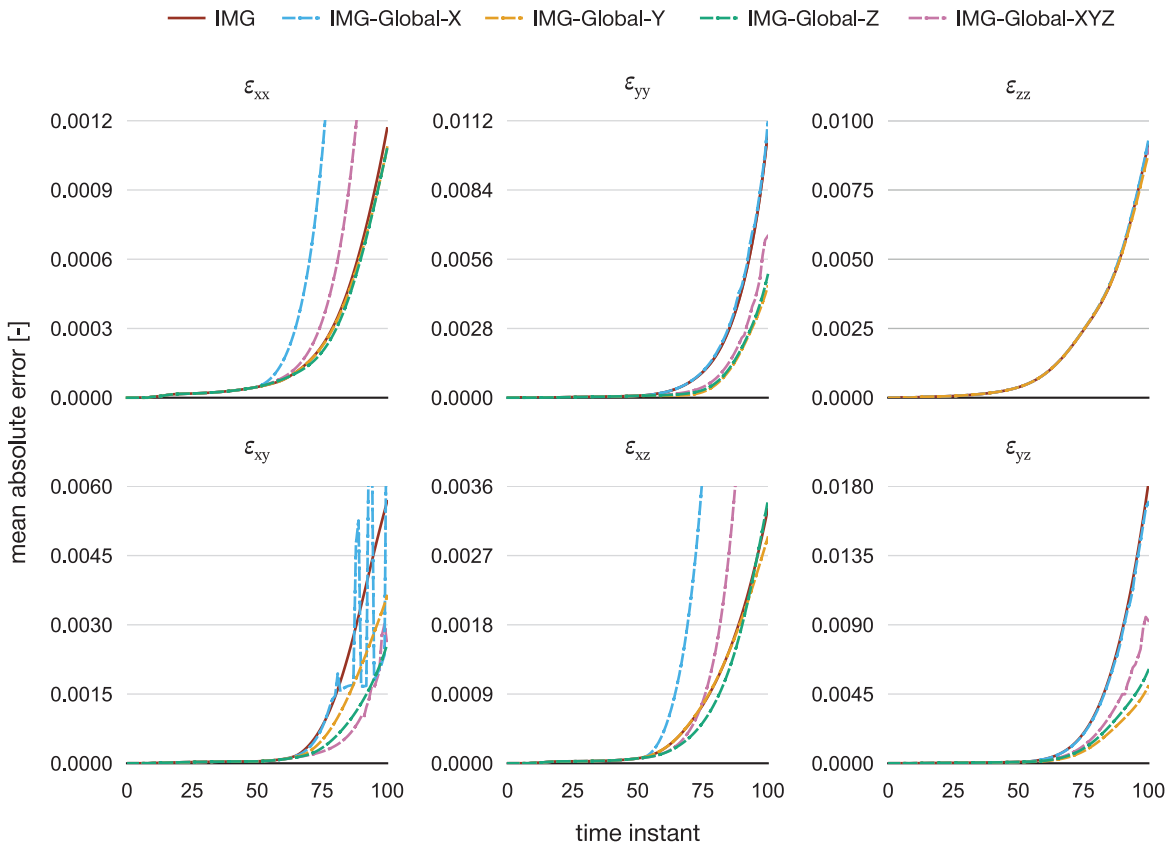

Figure 6.10 Evolution of the average absolute error for each reconstructed strain tensor component throughout time instants, between the IMG and different combinations of the corrected global volume.

6.5.2 Correction of Local Volume

Due to the global volume increase, it would be expected that the volume of the elements also changes, as demonstrated in Figure 6.7b. However, the volume of the elements does not increase proportionally, but instead some elements increase their volume while others decrease it. This

behavior is a consequence of the linear distribution of nodes through the thickness along the Bézier curves. By assuming ε_{xx} and ε_{yy} are correctly reconstructed, then the ε_{zz} is either over- or underestimated, resulting in an incorrect evolution of the elements volume. By adjusting the distribution of nodes through the thickness along the Bézier curve, the proposed solution attempts to correct the local volume of the reconstructed elements.

The algorithm adopts a node by node approach, where the distribution of nodes along the Bézier curve is iteratively optimized to improve the elements volume in its neighborhood. Meaning that the updated nodes will affect the volume of the element to which they belong. Therefore, an individual cost function is used to guide the optimization towards the optimum distribution. This individual cost function is given by the sum of the maximum absolute volume change (relative to a given reference) along the z axis. Considering that the nodes distribution associated to a given pair of surface nodes (one in the back and another in the front surface) is denoted by $\mathbf{z}$, such that, the distribution of the nodes between points $\mathbf{N}_A$ and $\mathbf{N}_B$ illustrated in Figure 6.2 is given by $\mathbf{z}_{ij} = [0.0, 0.25, 0.5, 0.75, 1.0]$. Each pair of nodes ij is associated with m_s number of elements on each surface, corresponding to $m_s \times m_z$ elements through the thickness. Then, the individual cost function ϕ_I, for a given distribution $\mathbf{z}_{ij}$, is given by

$$\phi_I(\mathbf{z}_{ij}) = \sum_{l=1}^{m_s} \max_z \left| \mathbf{V}_I(\mathbf{z}_{ij}, l) - \mathbf{V}_{I_0}(l) \right|, \tag{6.15}$$

where $\mathbf{V}_I$ represents the optimized volume of each element affected by $\mathbf{z}_{ij}$, and $\mathbf{V}_{I_0}$ the corresponding reference volume. As such, $\mathbf{V}_I(l)$ stands for the set of the elements volume along a given surface element l. The optimization procedure is simplified by adopting symmetry conditions along the thickness between the front and back surfaces. This way, the nodes distribution is optimized for only half of the specimen's thickness, while the other half distribution will be identical. Moreover, the location of nodes on the front and back surfaces is unchanged, as well as the node in the middle between the two outer surfaces.

Nevertheless, the optimization of individual nodes distribution could lead to global solutions worse than the reference. Thus, after all nodes are individually optimized, a global cost function ϕ_G is calculated to evaluate if the global solution has improved. The global cost function is defined as the sum of the maximum absolute volume change along the z axis for all elements (relative to a given reference), and is mathematically expressed as

$$\phi_G(\mathbf{Z}) = \sum_{i}^{m_x} \sum_{j}^{m_y} \max_z \left| \mathbf{V}_G(\mathbf{Z}, i, j) - \mathbf{V}_{G_0}(i, j) \right| \tag{6.16}$$

where $\mathbf{Z}$ represents the set of all nodes optimized distribution $\mathbf{z}_{ij}$, $\mathbf{V}_G$ represents the optimized volume of each element in the VOI, and $\mathbf{V}_{G_0}$ the corresponding reference volume. As such, $\mathbf{V}_{G_0}(i, j)$ stands for the set of the elements volume along a given surface element ij. The optimization procedure is repeated until the global solution no longer improves. The structure of the algorithm to correct the elements volume is schematically presented in Figure 6.11.

Additionally, the methodology to find the optimal nodes distribution along the Bézier curve could potentially be performed in different ways. Two strategies are here proposed, named, biased and optimized.

Biased Strategy

The biased distribution uses a logarithmic function to distribute the nodes along the Bézier curve with a certain bias in one direction, either towards the middle of the specimen or towards the external surfaces. The position of node $\mathbf{z}_{ij}(k) \in [0, 0.5]$ along the biased distribution is given by

$$\mathbf{z}_{ij}(k,w) = \frac{1}{2|w|}\left[10^{\frac{\log_{10}(|w|+1)}{n_\mathrm{b}}k} - 1\right], \quad \text{with} \quad k = 1, 2, ..., n_\mathrm{b}, \tag{6.17}$$

where $n_\mathrm{b} = (n_\mathrm{z} + 1)/2$ represents the number of nodes in the biased distribution, assuming symmetry along the z axis, and $w \neq 0$ is the bias weight. The bias weight w can either take negative or positive values, with its absolute value governing the bias magnitude and its sign governing the bias direction. Nevertheless, Equation 6.17 is formulated to generate a bias towards the outer surfaces of the specimen. Therefore, to also consider a bias towards the middle of the specimen, $\mathbf{z}_{ij}$ is inverted when $w < 0$. Mathematically, the two bias directions are given by

$$\mathbf{z}_{ij} = \begin{cases} \mathbf{z}_{ij} & \text{if } w > 0 \\ \mathrm{flip}(|\mathbf{z}_{ij} - 0.5|) & \text{if } w < 0 \end{cases} \tag{6.18}$$

where flip(·) stands for the reverse order of the vector components. The advantage of this strategy is that there is only one optimization variable, independently of the number of nodes through the thickness. The initial solution of the optimization algorithm is a linear nodes distribution $\mathbf{z}_{ij}^{\mathrm{linear}}$.

Optimized Strategy

The optimized distribution targets each node along the Bézier curve individually. In this approach, the number of optimization variables is equal to the number of nodes through the thickness

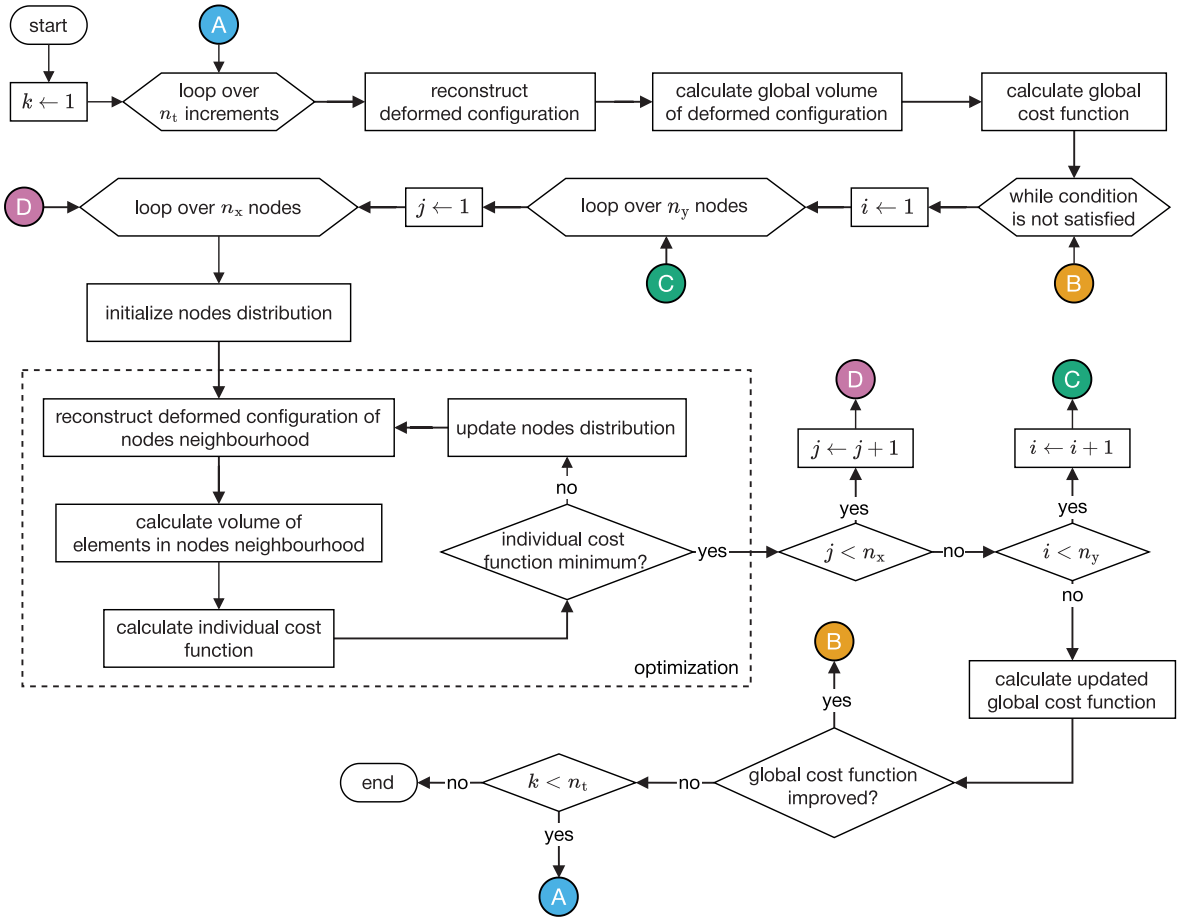

Figure 6.11 Flowchart of the algorithm to correct the elements volume in the IMG.

(considering symmetry condition and excluding surface and middle nodes). Thus, the higher the number of nodes, the more complex the optimization problem. Moreover, because this approach optimizes the position of each node individually, there is a risk that it can lead to unfeasible meshes. Therefore, there is the need to impose bounds constraints to the nodes distribution as

$$z_{ijk}^{\text{linear}} - \delta_z \leq z_{ijk} \leq z_{ijk}^{\text{linear}} + \delta_z, \tag{6.19}$$

where δ_z represents an interval of accepted values given by

$$\delta_z = \frac{0.5}{n_z - 1}. \tag{6.20}$$

Similarly to the bias strategy, the initial solution of the optimization algorithm is a linear distribution. Moreover, the Nelder-Mead algorithm is employed in the optimization procedure (see Section 5.3).

The local volume correction was tested for both strategies, without considering the global volume correction. Additionally, a total and an incremental approach are used on the reference to guide the optimization procedure. The former uses the initial undeformed configuration as reference, and the latter the last deformed configuration. Four different combinations are tested: using the biased (IMG-Local-B) and optimized (IMG-Local-O) strategies, with total (-T) and incremental (-I) approaches.

The evolution of the average absolute error for each strain tensor component is presented in Figure 6.12, for all combinations. It is observed that the IMG-Local-B-I combination completely

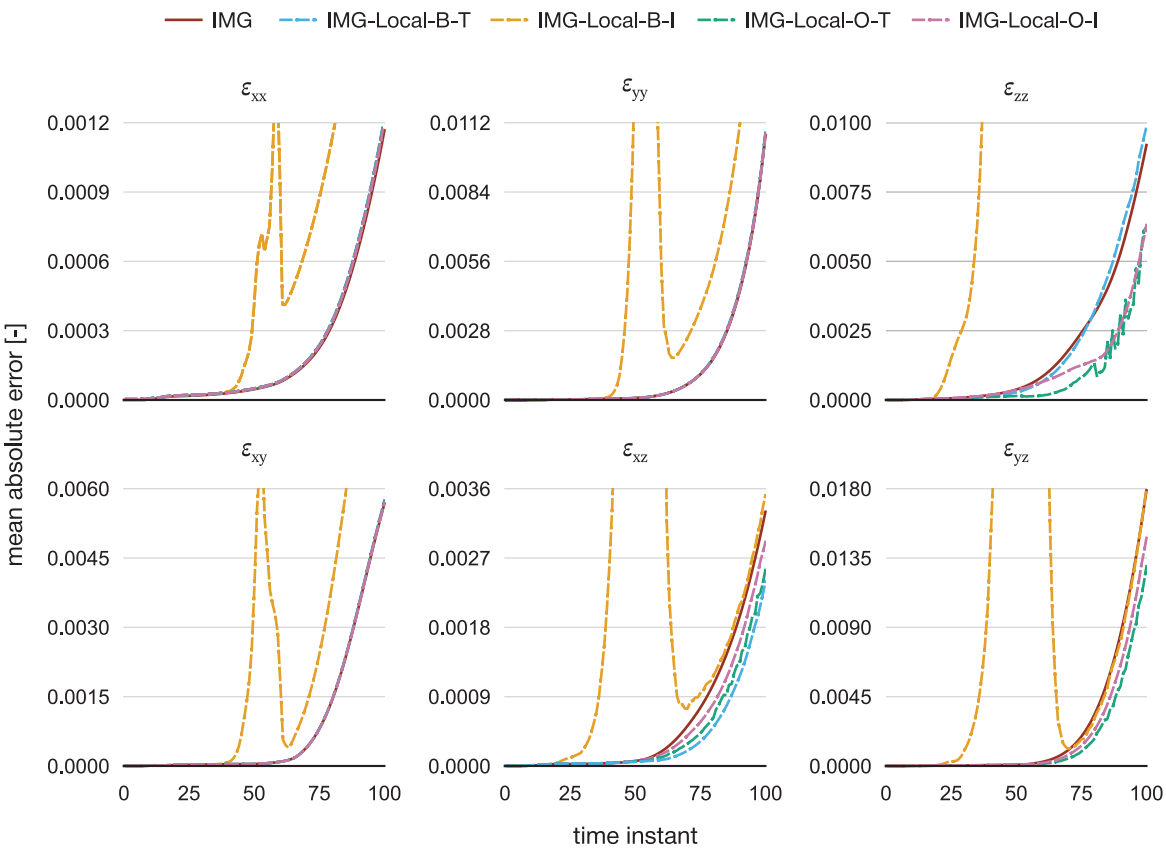

Figure 6.12 Evolution of the average absolute error for each reconstructed strain tensor component throughout time instants, for the IMG, both standard and different combinations of local volume correction.

fails to correct the local volume, as the error vastly increases relative to the IMG combination. In this particular combination, it happened that the bias distribution started to excessively converge towards the middle surface. In this case, either the adopted cost function failed to penalize the solutions, or bounds constraints should be adopted for the weights. Except for this combination, all the others decrease or maintain the error. Specifically, the average absolute error associated with the thickness strain substantially decreases when adopting the optimized approach, either with a total or incremental approach. A drawback of the local volume correction is its high computational cost, which could require a few hours to correct all time instants.

6.5.3 Correction to Global and Local Volume

Here, the combination of global and local volume corrections (IMG-Mixed) is analyzed. Again, four different combinations are tested where the local volume strategy is changed. In Figure 6.13, the evolution of the average absolute error for each reconstructed strain component is presented. The combination using the bias strategy with an incremental approach should be discarded, as it completely fails again. Using the other combinations, the results are encouraging for all strain components, except for ε_{xx}, which is unchanged. It is interesting to observe that the bias strategy with a total approach decreases the error, though it was not the case using both corrections individually. Nevertheless, the optimized strategy with a total approach is the one that decreases the error the most.

In Figure 6.14, the profile of the strain component ε_{zz} is plotted along the thickness direction for the center elements, corresponding to 20 elements. It is observed that the reference produces

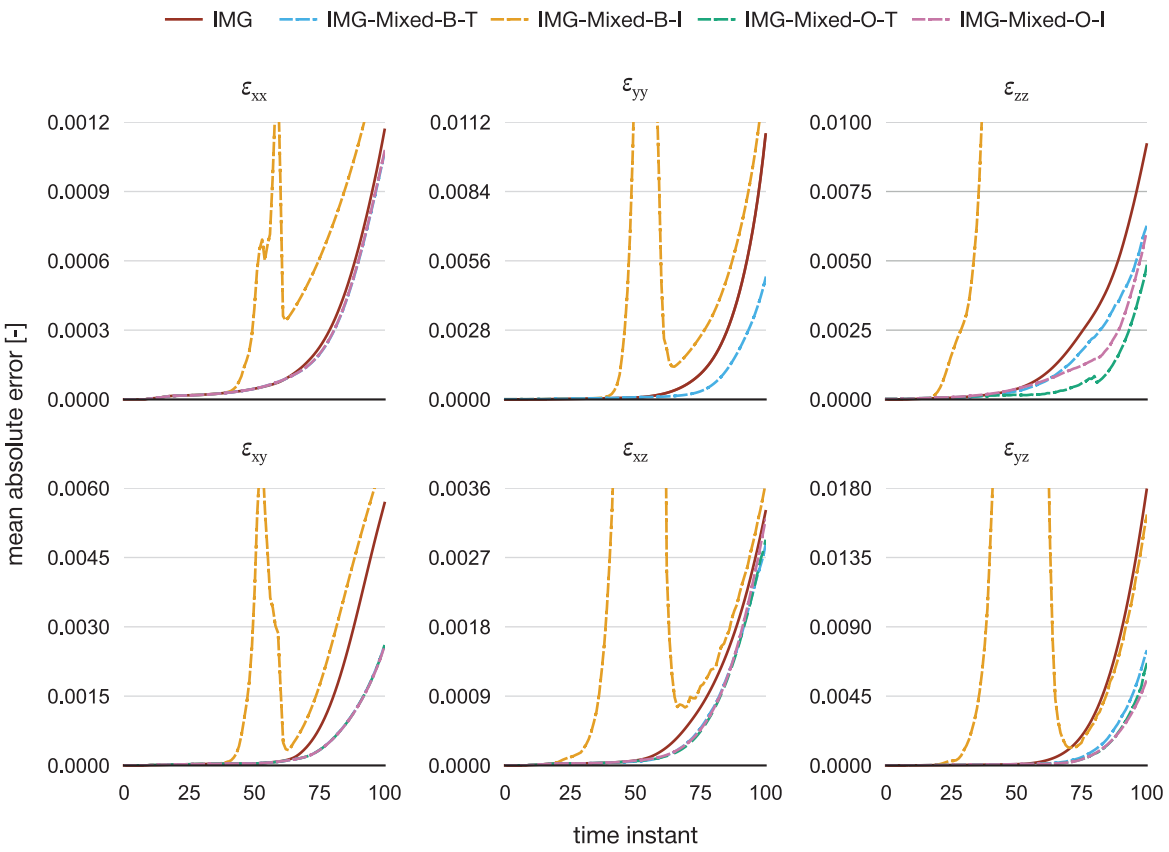

Figure 6.13 Evolution of the average absolute error for each reconstructed strain tensor component throughout all time instants, for the IMG, both standard and different combinations of global and local volume corrections.

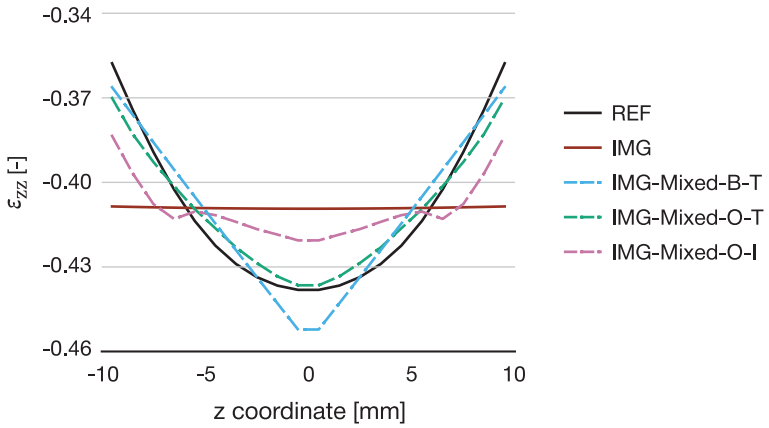

Figure 6.14 Profile of the strain component ε_{zz}, along the intersections of middle planes xz-yz, of the reference and the IMG, both in standard and different combinations of global and local volume corrections.

a curved profile, while using IMG an approximately linear profile is obtained. When applying the volume corrections, the reconstructed profile is no longer linear and is more similar to the reference. However, the reconstructed profile of combination IMG-Mixed-O-I is irregular along the thickness, with a few peals observed. Although the error decreases, its reconstructed profile is still far from the reference. Based on this result, the total approach appears to be the best, for both bias and optimized strategies. Between these two combinations, both reconstructed paths are similar to the reference. However, using the bias strategy, the maximum value of ε_{zz} is overestimated, and the gradient evolves linearly towards the center. Consequently, combining the global volume correction with the local volume correction using the optimized strategy with a total approach is the best combination.

Figure 6.15 shows the element's volume map and thickness strain map of the reconstructed volume of interest at the last time instant, using the IMG-Mixed-O-T combination. Although the corrected values are still far from the reference, the maximum and minimum values have improved (see Figure 6.7b). Nevertheless, the existing improvements resulted in the thickness strain map of Figure 6.15b, which is almost identical to the reference (see Figure 6.4c).

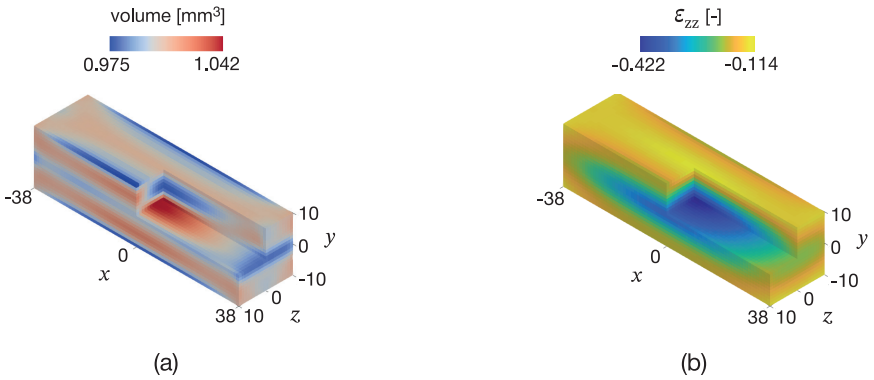

Figure 6.15 Maps of the 3D cross-sections of the reconstruction using IMG-Mixed-O-T for the (a) volume of the elements and the (b) strain component ε_{zz}, at the last time instant and represented on the undeformed configuration.

Lastly, to show that the proposed global and local volume corrections improve the IMG, Figure 6.16 presents the values of the normal strain components along different paths. It is observed in all cases that the combination IMG-Mixed-O-T improves the strain reconstruction

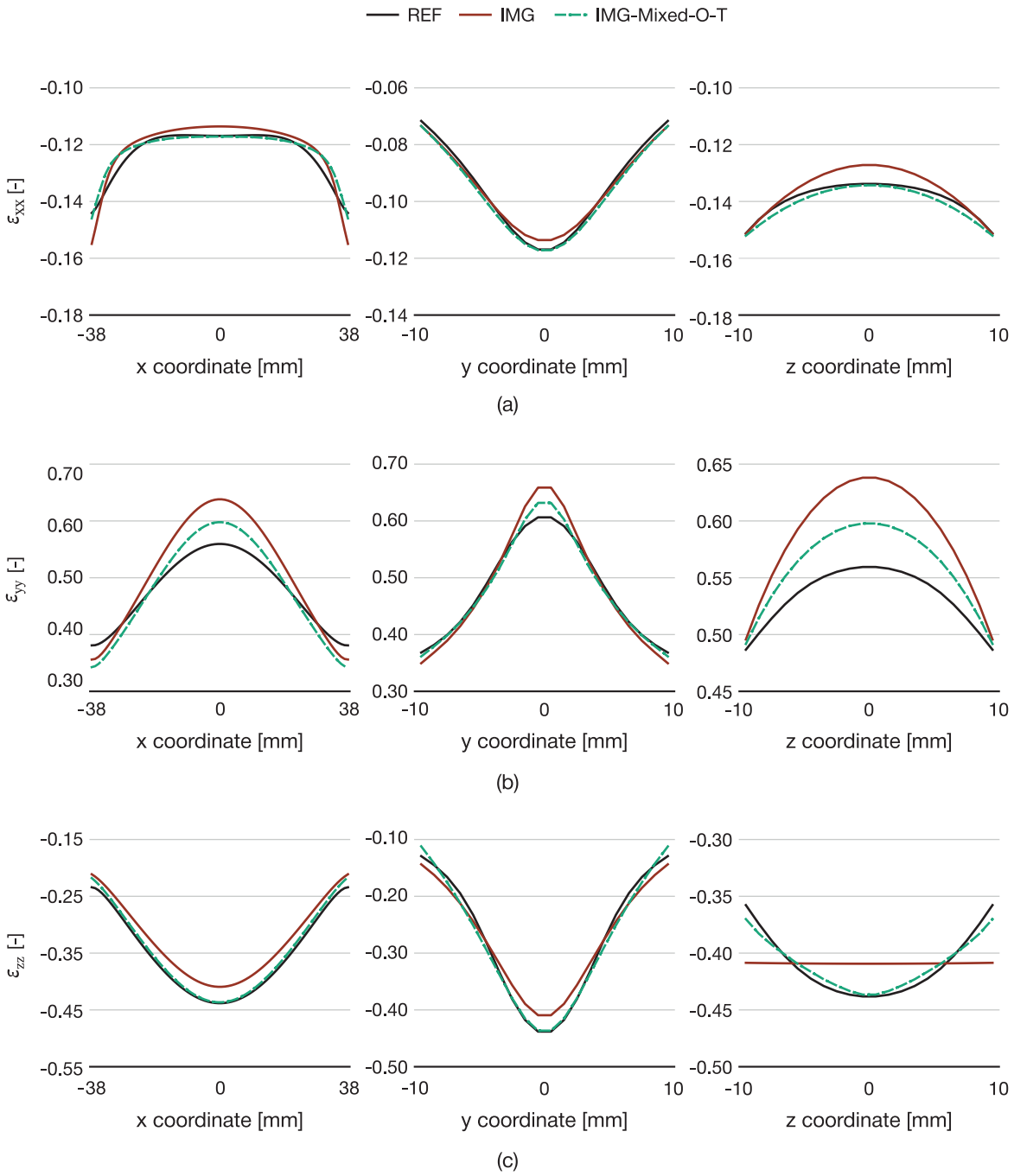

Figure 6.16 Profile of the strain tensor components (a) ε_{xx}, (b) ε_{yy}, and (c) ε_{zz}, along the intersections of middle planes xy-xz, xy-yz, and xz-yz, respectively, from left to right.

relative to the reference.

Up to this point, the error coming from the IMG itself has been established and improved. Nevertheless, the previous studies only considered the displacement field from FEA simulations, which does not contain any "imperfections". However, the aim of the IMG is to be applied with real experiments, where many sources of error exist, which could lead to increased errors in the reconstructed fields. As such, it is important to also estimate the errors that would be obtained when using real experiments. With that purpose, the following section estimates the uncertainty of the IMG using virtual experiments that mimic real experiments.

6.6 Uncertainty Quantification

The IMG was developed to be applied to real experiments, but many experimental conditions can influence the measurements quality, and consequently influence the quality of reconstructed displacement and strain fields (Oliveira et al. 2022a). To include these conditions in the volume reconstruction, virtual experiments are introduced to evaluate the uncertainty of IMG under various experimental conditions. In particular, virtual experiments mimicking a stereo-DIC setup are used to measure more accurately the out-of-plane displacements. These virtual experiments are useful to study the influence of experimental conditions or DIC settings, without ever performing the real experiments (Lava et al. 2020; Henriques et al. 2022). Consequently, it leads to a decrease in time and cost relative to performing the same study with real experiments.

6.6.1 Generation of Stereo-DIC Virtual Experiments

To simulate the measurement chain associated with a virtual stereo-DIC setup, four virtual cameras are used to measure the displacement field in the front and back surfaces of the specimen, two for each. The virtual experiments are generated from displacement fields coming from FEA simulation, and used to deform a reference speckle pattern image. This image can be numerically generated. Further details on the procedure and mathematical formulation can be found in Balcaen et al. (2017b) and Balcaen et al. (2017a). Nevertheless, the necessary steps to obtain virtual experiments for each surface of the specimen are as follows:

1. Export the FEA mesh and associated 3D displacement fields of outer surfaces;
2. Impose the FEA mesh onto a reference speckle pattern image;
3. Generate the synthetically deformed stereo-DIC images;
4. Perform the stereo-DIC measurements;
5. Export the stereo-DIC measurements to the IMG.

These steps are illustrated in Figure 6.17 for a large region of the plane strain tensile test. As previously established, Abaqus/Standard was used to perform the FEA simulation. Then, all the steps were performed using MatchID suite software (MatchID 2022a). In particular, step 1 was performed through MatchID FEA Converter (MatchID 2022b), which easily allows the extraction of mesh coordinates and displacement fields from Abaqus output database files (see Figure 6.17a). Using this software, the obtained output files are directly compatible with MatchID software. In step 2, the FEA mesh is imposed onto the speckle pattern image from the point of view of camera 0 (see Figure 6.17b). Then, in step 3, the FEA mesh and displacement fields are interpolated to camera 1 using stereo-camera calibration parameters (see Figure 6.17c). Steps 2 and 3 are performed through the virtual images generation module from MatchID Stereo software (MatchID 2022c). Using this module, it is possible to use any speckle pattern image and easily impose the FEA mesh on top of it. Finally, full-field measurements are obtained in step 4 through MatchID Stereo (MatchID 2022d) and exported in a convenient structure to be used in IMG (see Figures 6.17d and 6.17e).

One key aspect of stereo-DIC virtual experiments is the definition of calibration parameters. Without these parameters, it is impossible to generate virtual experiments, because they are responsible for interpolating data from one camera to the other. In opposition, generating virtual experiments for a 2D-DIC application is much simpler, because there is no need to define these calibration parameters. These parameters can be obtained from a standard calibration procedure, where more than 50 real images are captured for each camera. Then, through a calibration software, intrinsic and extrinsic parameters are obtained. The intrinsic parameters of a camera describe the way images are acquired, such as resolution or focal length. On the other hand,

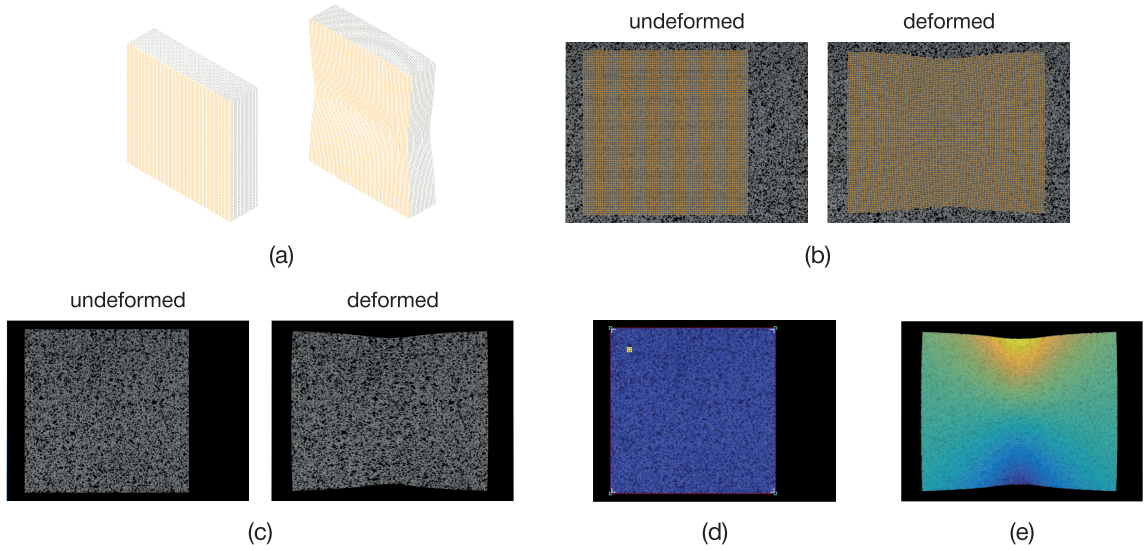

Figure 6.17 Schematic illustrations of the steps involved in the generation of virtual experiments for each surface: (a) export of FEA mesh and displacement field of outer surface, (b) FEA mesh imposed on the speckle pattern image from the point of view of camera 0, in undeformed and deformed configurations, (c) generated synthetic images from the point of view of camera 0, in undeformed and deformed configurations, (d) pre-processing of stereo-DIC measurements from the point of view of camera 0, in the undeformed configuration, and (e) measured displacement field component from the point of view of camera 0.

the extrinsic parameters describe the position and orientation of a camera relative to another. Normally, the extrinsic parameters of camera 1 are defined relative to a reference camera, named camera 0.

Calibration parameters can also be manually defined, even though they will not be a complete representation of a real acquisition. Nevertheless, an image of a real speckle pattern is used as a reference to generate all virtual experiments, as shown in Figure 6.18. This image was obtained using a real camera with a resolution of $1040 \times 1392\,\mathrm{px}^2$, respectively, the width r_x and height r_y of the camera sensor in pixels. Therefore, some calibration parameters are inherited from this camera, assuming perfect conditions exist, in particular c_x and c_y defining the coordinates of the detector's center are set to, respectively, half-width and half-height. Additionally, a camera lens with a focal length $f = 50\,\mathrm{mm}$ is here considered. From the camera resolution and focal length, it is possible to obtain parameters f_x and f_y, governing the focal length along the x and

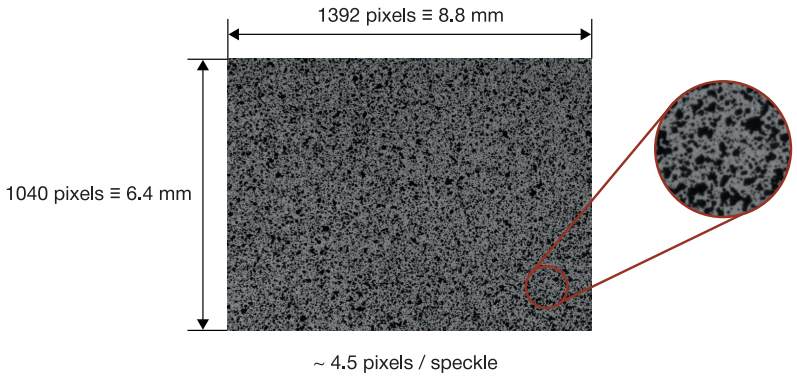

Figure 6.18 Image of the real speckle pattern used as reference to generate the virtual experiments.

y axes. Additionally, by considering perfect conditions, it is assumed that the cameras do not present skewing of the axes and no lens distortions. Thus, the skewing factor f_s, radial distortion coefficients κ_1, κ_2, and κ_3 of the camera lens, as well as tangential distortion coefficients of the camera lens p_1 and p_2 are equal to zero.

Perfect conditions are also assumed in the definition of the extrinsic parameters, meaning that camera 1 is perfectly aligned and oriented relative to camera 0. Therefore, the position of camera 1 is only governed by its relative orientation with respect to camera 0 around the x axis, and its magnitude defined by θ_x, which will be referred to as stereo-angle. The other two orientations θ_y and θ_z represent, respectively, the relative orientation of camera 1 with respect to camera 0 around y and z axes, and are set to zero. Consequently, distance T_x of camera 1 relative to camera 0 in the x axis will be zero. Distances T_y and T_z of camera 1 relative to camera 0, respectively, along the y and z axes depend of θ_x and are calculated as

$$T_y(S_o, \theta_x) = S_o \sin \theta_x \tag{6.21}$$

and

$$T_z(S_o, \theta_x) = S_o(1 - \cos \theta_x), \tag{6.22}$$

where S_o is the distance from camera 0 to the specimen along the z axis given by

$$S_o = f\frac{L_{FOV}}{L_{CS}} \tag{6.23}$$

where L_{FOV} is the dominant length of the field of view, and L_{CS} is the correspondent length of the camera sensor in millimeters (Jones and Iadicola 2018). A schematic of the position and orientation of cameras 0 and 1 is shown in Figure 6.19, for a generic situation of a stereo-vision system. In addition, the intrinsic and extrinsic parameters used in the generation of the synthetic images are presented in Table 6.2. It should be noted that the intrinsic parameters correspond to all four cameras involved: cameras 0, 1, 2, and 3. Moreover, the extrinsic parameters correspond to both stereo-vision systems, in front (cameras 0 and 1) and back (cameras 2 and 3) of the specimen.

6.6.2 Design of Experiments

When using stereo-vision systems in real experiments, many factors can influence the accuracy of the final measurements (Forsström et al. 2020). Evaluating the influence of all of them in the volume reconstruction method would be a hard and long task. A design of experiments (DOE) can be used to evaluate the variation of results under different conditions (Mason et al. 1979).

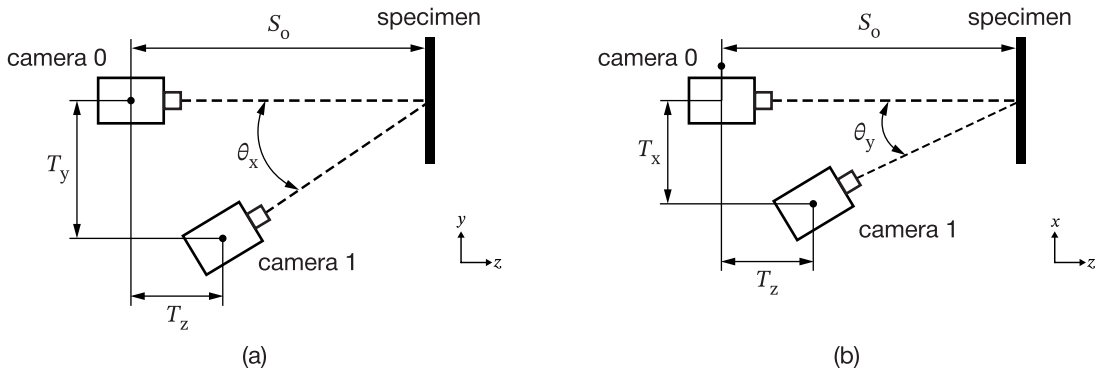

Figure 6.19 Schematic illustration of the position and orientation of cameras in a generic stereo-vision system, in the (a) yz plane and the (b) xz plane.

Table 6.2 Calibration parameters for the stereo-vision system considered in this study.

Intrinsic				Extrinsic					
c_x [px]	c_y [px]	f_x [px]	f_y [px]	θ_x [°]	θ_y [°]	θ_z [°]	T_x [mm]	T_y [mm]	T_z [mm]
520	696	7909	7909	θ_x	0	0	0	$T_y(S_o, \theta_x)$	$T_z(S_o, \theta_x)$

Therefore, a DOE is performed by selecting five factors which can influence the final stereo-DIC measurements and consequently the volume reconstruction: field of view, stereo-angle, noise, subset size, and step size. All these factors are introduced at some step along the procedure chain presented above. Moreover, three levels are evaluated for each factor to obtain a quadratic response (Mason et al. 1979). Table 6.3 presents the different levels defined for each factor. In total, the DOE is composed of 243 virtual experiments.

Table 6.3 Factors and levels for the design of experiments to evaluate the volume reconstruction from virtual experiments.

	Factors				
Level	Field of view [mm^2]	Stereo-angle [°]	Noise [–]	Subset size [px^2]	Step size [px]
1	76 × 112	15/16	0	17 × 17	3
2	76 × 148	20/21	5	21 × 21	5
3	76 × 160	25/26	10	25 × 25	7

The field of view of the cameras is usually determined by the specimen ROI and its relative motion and deformation (Jones and Iadicola 2018). Ideally, the ROI should almost fill the field of view to optimize the spatial resolution of measurements. The better the spatial resolution, the more accurate the measurements will be. Thus, it is important to estimate the total motion of the specimen to better define the field of view. Practically, the field of view will determine the distance the cameras should be located from the specimen. In the virtual experiments, the field of view effect is introduced when imposing the FEA mesh onto the speckle pattern image (step 2), by increasing or decreasing the space by the FEA mesh, as shown in Figure 6.20. It should be noted that the ROI in the generation of virtual experiments differs from the VOI defined previously and considered for analysis. The ROI here corresponds to 76×76 mm^2 area centered on the specimen.

The stereo-angle between two cameras depends on the measurement quantities most important in a given experiment (Jones and Iadicola 2018). Smaller stereo-angles will lead to more accurate in-plane displacements, while larger stereo-angles are often associated with better out-of-plane displacement accuracy (Reu 2013; Balcaen et al. 2017b). Thus, defining the stereo-angle results from a compromise between in-plane and out-of-plane accuracy. In the present study, because the out-of-plane accuracy is important to better reconstruct the out-of-plane deformation fields, angles between 15° to 26° are considered. It should be noted that the stereo-angle values shown in Table 6.3 correspond to the front and back stereo-vision systems, respectively. This difference was considered to have different results between front and back measurements. A schematic representation of the different levels is presented in Figure 6.20.

In real experiments, the presence of noise in the obtained measurements is always considered. Noise can come from various sources, such as the quality of speckle pattern, lightning, cleanliness of cameras and sensors, among others. In virtual experiments, most possible sources of noise are avoided. Nevertheless, by using a real image of a speckle pattern, some noise is already present. To go even further, artificial noise can be added to virtual experiments by changing the gray level of pixels (Rossi et al. 2015). Therefore, three levels of artificial noise are defined as the

standard deviation of a Gaussian distribution for an 8-bit image (step 3). The first level does not add artificial noise, while the noise distribution of second and third levels is, respectively, defined with a standard deviation of 5 and 10 gray levels, approximately 2 % and 4 % of the gray level range.

While the first three factors are related to the setup of acquisition, the subset size and step size are related to the post-processing settings of the stereo-DIC software (step 4). The subset size is important for the software to correlate the motion of a subregion of ROI throughout the test. In theory, the subset should be large enough that it contains sufficient information, such that one subset can be distinguished from all other subsets in the ROI. Generally, it is recommended that a subset contains at least three transitions between dark and light features of the speckle pattern (LAVA ET AL. 2009; LAVA ET AL. 2010). The step size governs the density of measurement points obtained by the stereo-DIC software, and directly affects the spatial resolution of measurements. The smaller the step size, the more measurement points will be obtained. However, many measurement points will also lead to higher computational costs, and

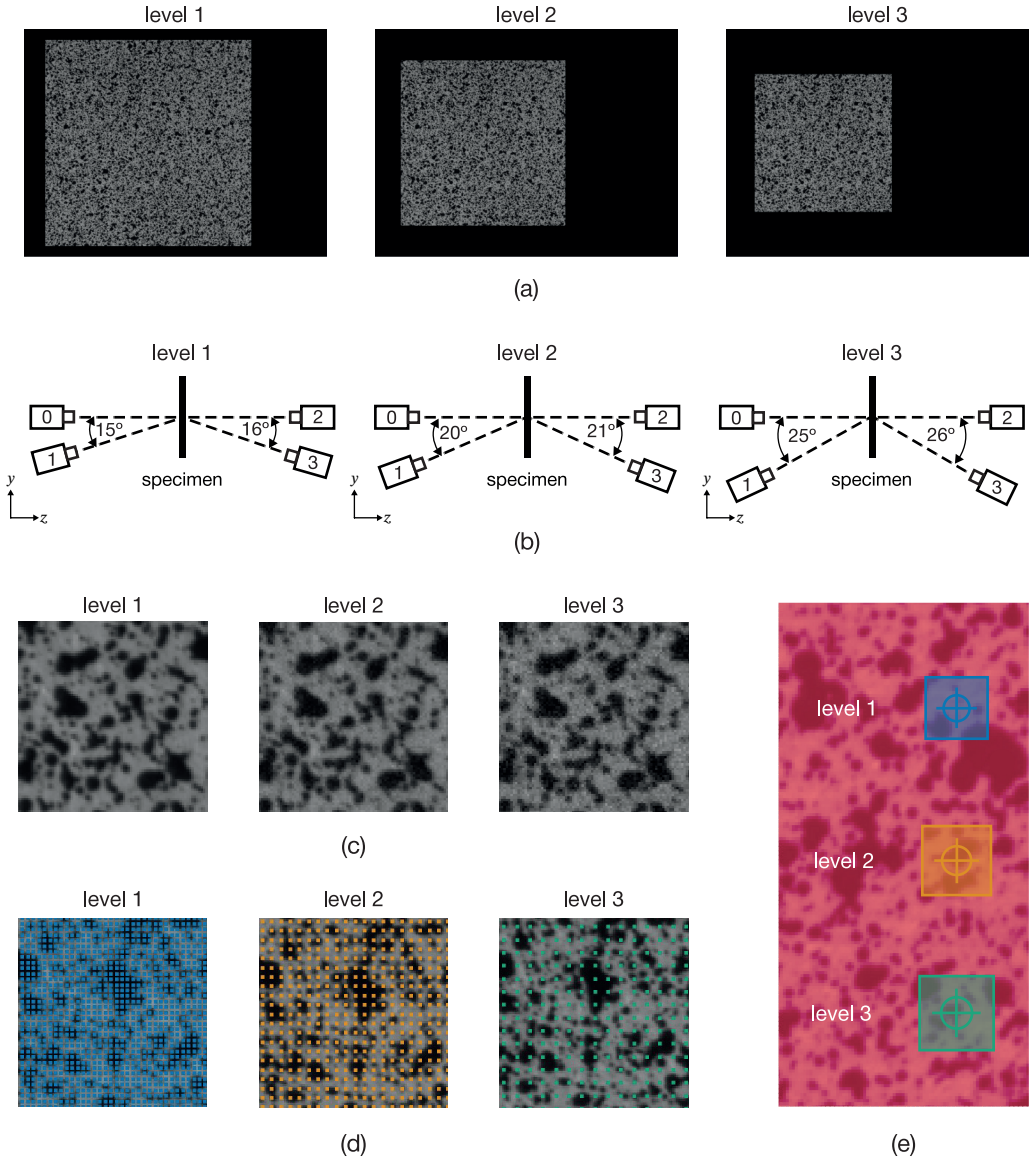

Figure 6.20 Schematic illustrations of the factors and levels considered in the DOE: (a) field of view, (b) stereo-angle, (c) noise, (d) subset size, and (e) step size.

is not a guarantee of improving spatial resolution if subsets are largely overlapped. Nevertheless, using a smaller step size allows obtaining measurement points closer to the free edges of the specimen, which are important for better volume reconstruction as previously established. The three different subset and step sizes considered in the DOE are shown in Figure 6.20.

As already established, MatchID software is used to generate virtual experiments and perform stereo-DIC measurements. However, manually generating 243 virtual experiments can be a long task. For that reason, a Python program was developed to automatically generate virtual experiments for different conditions and also perform the stereo-DIC measurements. This was only possible using MatchID in batch mode, which enables performing all necessary tasks through the command line in the background. It was only necessary to build a template for a single case and replicate it for the others.

6.6.3 Results

To isolate the influence of introducing virtual experiments in the IMG, the error is computed as the absolute difference between the reconstruction from FEA and virtual experiments, mathematically identical to Equation 6.11. Additionally, the relative error is also investigated with respect to the maximum values observed in each component. The results of the displacement field are presented in Figure 6.21a and of the strain field in Figure 6.21b. The presented results analyze the major effects of each factor, allowing a comparison of its influence on the error. Therefore, each level within each factor corresponds to the average result of 81 experiments. Moreover, for simplicity, only the average of error of all the points or elements in the VOI is represented. It is considered that the average absolute error can describe the influence of each factor on an average.

It is observed that an increase in the field of view leads to an error increase in all the components of displacement and strain. Moreover, it appears the field of view is the factor with the biggest impact out of the five factors evaluated, as variations between levels are more pronounced. For example, for u_y, the average error is approximately two times higher from the first to the third level of the field of view. The increase of noise also leads to an increase in the average error, even though its impact on the displacement components is low and more evident in the strain components. On the other hand, the subset size appears to have a low impact on the error, at least for the range of values considered. To further understand its impact, the range values could have been enlarged to higher values. The impact of stereo-angle is not well understood, and some conflicting results are observed. Perhaps the stereo-angle could be analyzed as a function of lenses focal length, because the impact of stereo-angle on measurements accuracy is also affected by the choice of lenses. Overall, the error is relatively low for all factors. However, these low variations can also be explained by the range of values selected for each factor. Expanding the range of values can potentially yield different results, but it is not expected that the error will increase drastically.

6.7 Conclusions

This study analyses the accuracy of a volume reconstruction method, named internal mesh generation. This method reconstructs the volume of a solid starting from surface measurements, and is purely based on geometrical considerations. A finite element model of a plane strain tensile test with 20 mm of thickness was used as a reference. The ability of the IMG to reconstruct the deformed volume is good, with reduced computational effort. However, the accuracy of the reconstructed strain field is not perfect, particularly when a large strain gradient is observed through the thickness. To improve the accuracy of the IMG, two strategies are proposed. The first aims to correct the global volume evolution of the reconstructed geometry, and consequently, has been shown to improve the accuracy of the reconstructed strain field. The second strategy focuses on correcting the elements' local volume by adjusting the position of nodes through the thickness. Using the latter strategy, it has been shown that the strain tensor component εzz is well

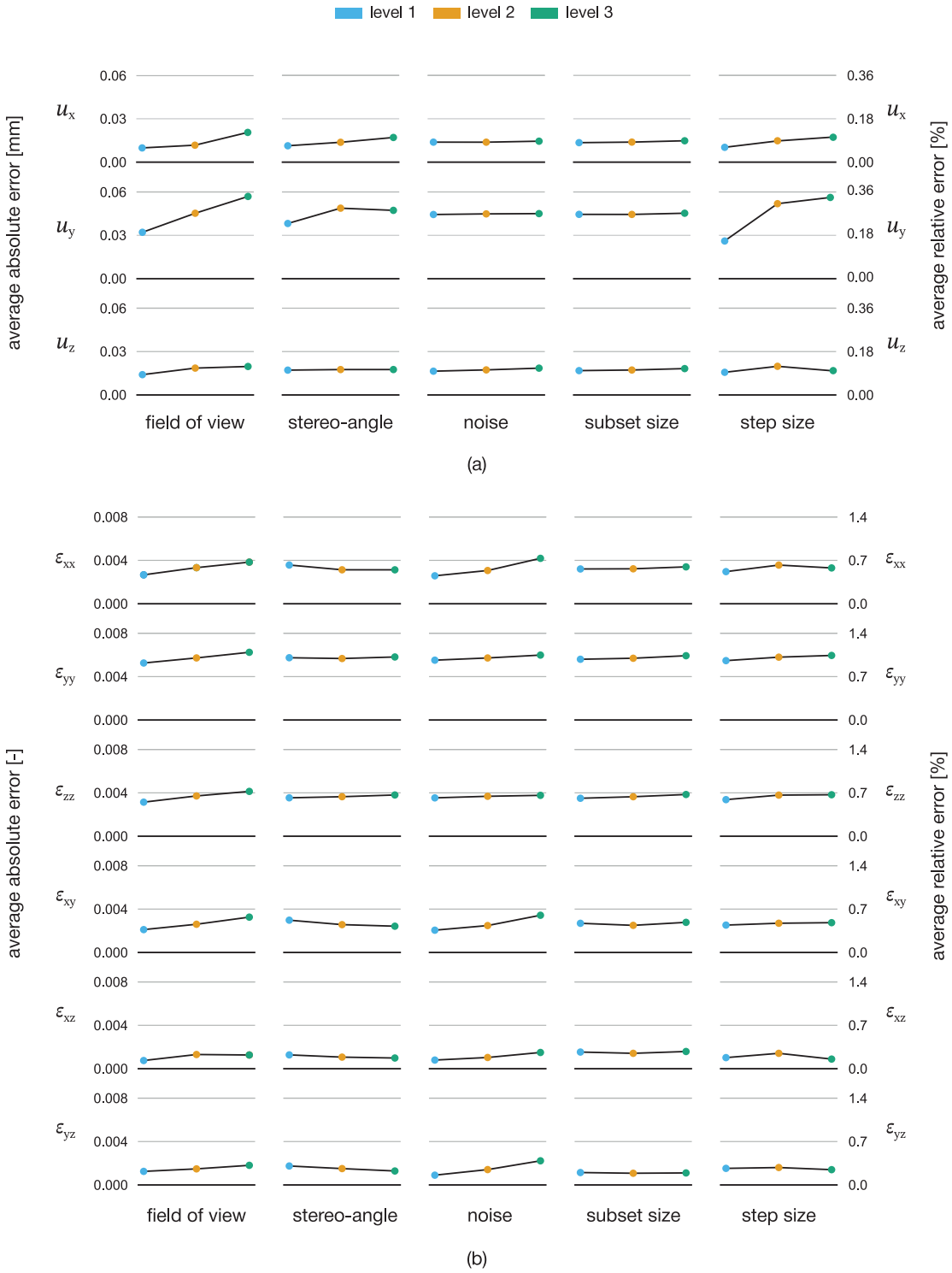

Figure 6.21 Average absolute and relative errors of the VOI between reconstruction using FEA and virtual experiments for the (a) displacement field components and (b) strain field components. Each column corresponds to a different factor in the DOE.

reconstructed. Future developments could attempt to improve the reconstructed displacement field by including information of all surfaces, front, back and sides.

Using this method with real experiments is the final aim. However, real experiments are susceptible to varying conditions that ultimately affect the final measurements and, consequently, the reconstruction itself. Therefore, the uncertainty of the IMG under different experimental conditions and stereo-DIC settings was successfully estimated using virtual experiments. In particular, a DOE was performed with five factors, each with three levels. The study showed that the field of view is the primary factor influencing the error, but that all factors considered have a rather low influence.

Globally, a volume reconstruction method that is computationally efficient and able to estimate the displacement field inside a solid and from the surfaces displacement field within a reasonable error has been evaluated. However, applying the method to real experiments with different materials of varying thicknesses is still lacking. Moreover, investigating the stress reconstruction from the reconstructed strain field is of utmost importance to use this method in the context of parameter identification. In the end, the interest of this method is to use the VFM in the identification of material parameters, with improved accuracy.

7 Virtual Fields Method in a 3D Framework

7.1 Introduction

Conventionally, the elastoplastic behavior of sheet metals is characterized through standard uniaxial tensile tests. From these tests, it is possible to extract the true stress-strain curve essential to characterize the strain hardening behavior. The former is important, because many sheet metal forming processes achieve plastic strains beyond the point of maximum uniform elongation. Moreover, to simulate these processes in FEA software, the key requirement is the definition of the true stress-strain curve. Without an accurate characterization of this curve, numerical simulations will not be representative of the real material behavior.

However, diffuse necking is observed after the point of maximum uniform elongation in the standard uniaxial tensile tests (HILL 1952; HUTCHINSON AND MILES 1974; NICHOLS 1980). The diffuse necking leads to a non-uniform deformation concentrated within the necking region (TVERGAARD 1993; TONG AND ZHANG 2001), which does not allow measuring the deformation through a conventional extensometer. Commonly, localized necking is also observed in sheet metals after diffuse necking. While the former phenomenon is associated with a decrease in the specimen width, in the latter, a rapid decrease of the thickness is observed. A triaxial stress state also develops within this necking region, which eventually leads to fracture of the material (DUNAND AND MOHR 2010; TARDIF AND KYRIAKIDES 2012).

By measuring deformation through an extensometer, it will underestimate the resulting strain values after the onset of necking. Therefore, several studies have proposed solutions to determine the true stress-strain curve beyond this point (TU ET AL. 2020). Usually, the hardening behavior is extrapolated from the pre-necking stress-strain curve, but can lead to large errors. BRIDGMAN (1952) was one of the first studies to tackle the problem of characterizing the post-necking hardening behavior. In this pioneering study, the authors proposed an analytical method based on geometrical parameters of the necking profile to correct and compensate for necking in a round bar. Although this method has shown to perform well for round tensile specimens, it requires significant experimental work and could not be applied to specimens of rectangular cross-sections. However, rounded specimens are not practical for thin sheets applications. Later, ZHANG ET AL. (1999) proposed a method that can be applied to specimens of rectangular cross-section by determining a relationship between the area and thickness reduction of the cross-section. A drawback of this method is the required use of small specimens with thin sheets. Also, MIRONE

(2004) proposed a material-independent method that characterizes the necking behavior with reduced errors and much less experimental effort compared to the method of Bridgman.

With the advance of full-field measurement techniques combined with inverse methodologies, it has allowed the development of complete solutions that consider the stress and strain of all measured material points in the identification procedure. Most proposed solutions use a finite element based inverse method for the identification of the post-hardening behavior (Koc and Štok 2004; Tao et al. 2009; Dunand and Mohr 2010; Pottier et al. 2011; Tardif and Kyriakides 2012). Nevertheless, building a finite element model that accurately predicts the occurrence of necking is a hard task, for which several aspects need to be considered. The finite element models should be capable of predicting the location of diffuse necking, which is often also a difficulty in real experiments. Special attention should also be paid to building a finite element mesh to avoid highly distorted elements, due to the large strains involved in post-necking (Kajberg and Lindkvist 2004). Employing information about the test's actual boundary conditions in the finite element model can lead to more accurate results (Denys et al. 2016; Kacem et al. 2021), but getting this information is not straightforward. Another drawback of such methodologies, which is often pointed out, is their high computational cost.

More recently, alternatives to finite element based methodologies are becoming more popular by avoiding their shortcomings and directly using the measured strain fields. Rossi et al. (2018a) proposed an identification method, known as linear stress-strain curve identification method (LSSCI), that uses a piecewise linear function to describe the stress-strain curve even beyond necking. This method has been successfully applied, provided that good full-field measurements are obtained up to the free edges of the specimen. Nevertheless, to fully characterize the elasto-plastic behavior (strain hardening and anisotropy) of sheet metals, a decoupled identification approach is required. In this approach, the LSSCI method is used to characterize the hardening behavior, and the VFM is used to identify the parameters of a yield criterion (Lattanzi et al. 2020). Coppieters et al. (2011) proposed an energy method, based on the observation that under quasi-static conditions, the internal work is equal to the external work, assuming the hardening behavior is correctly described. Using real experiments, it has been shown that this method is computationally efficient, without the need to perform any FEA simulations (Coppieters and Kuwabara 2014).

The latter method is not drastically different from the VFM, and can be seen as a special case of the latter. The VFM is based on the PVW and employs virtual displacement fields instead of actual displacement fields to balance the internal virtual work with the external virtual work (Pierron and Grédiac 2012). It is one of the most prominent inverse methodologies and has already been applied to various applications (Avril et al. 2008a; Notta-Cuvier et al. 2015; Jones et al. 2019; Martins et al. 2019; Marek et al. 2020; Fu et al. 2021; Rossi et al. 2022a). In particular, it has already been successfully applied in the characterization of the strain hardening behavior of thin sheets up to large deformations (Rossi et al. 2016b). However, some studies have highlighted that after diffuse necking, a deviation between internal and external virtual works is observed (Coppieters et al. 2017; Martins et al. 2021), violating the validity of the VFM, leading to an inaccurate description of the hardening behavior. The triaxial stress state can explain the observed deviation that develops in the necking region (Kim et al. 2013). This rich information about the necking behavior is not used in the VFM because of the plane stress limitations imposed by the lack of available 3D full-field measurements. In fact, in sheet metal characterization, the VFM is limited to be used in combination with surface measurements, as techniques are not yet available to capture the 3D behavior inside the material. To circumvent this limitation, the IMG method investigated in Chapter 6 might provide the necessary 3D displacement fields for using the VFM in a 3D framework. However, this topic has not been extensively investigated, and at the best of the author's knowledge, only one study is found that it extended the use of the VFM to a

3D framework (Rossi and Pierron 2012a), assuming no plane stress or plane strain conditions.

Considering the amount of studies already using the VFM in the identification of material parameters, its interest and potential is undeniable. Yet, it lacks a better understanding of the consequences of its limitations, particularly the use of a 2D instead of a 3D framework. Although several problems might exist in the latter, such as the lack of volumetric full-field measurements, it might encourage the scientific community to develop new methodologies. Therefore, this study investigates the application of the VFM in 2D and 3D frameworks, respectively, 2D-VFM and 3D-VFM to the identification of a hardening law up to large deformations. Even though only simulated experiments are considered, the application of the VFM is investigated in materials of varying thicknesses to understand its influence.

The following section introduces the formulation of the VFM general to any 3D application, as well as its numerical implementation. Then, the simulated tests and virtual materials used in this study are presented and analyzed. A section dedicated to the definition of virtual fields follows, and finally, the results of an analysis of predicted load and identifications of a hardening law are presented.

7.2 Virtual Fields Method

Let us consider, in the Euclidean space, a body $\mathcal{B}$ subject to a general deformation process at a time instant t. According to the finite deformation theory (Dunne and Petrinic 2005), the position of its particles in the undeformed or reference configuration $\mathcal{B}_0$ (Lagrangian description) is given by $\mathbf{X}$, while in the deformed or current configuration $\mathcal{B}_t$ (Eulerian description) by $\mathbf{x}$. The motion of each material point can be described as a function of $\mathbf{x} = \chi(\mathbf{X}, t)$, mapping the position of each particle in the undeformed to the deformed configuration. The displacement field $\mathbf{u} = (u_x, u_y, u_z)$ is defined as the difference between the deformed and undeformed configurations as

$$\mathbf{u}(\mathbf{X}, t) = \chi(\mathbf{X}, t) - \mathbf{X} = \mathbf{x} - \mathbf{X}. \tag{7.1}$$

Spatial derivatives can be used to calculate the deformation gradient $\mathbf{F}$ as

$$\mathbf{F} = \frac{\partial \mathbf{x}}{\partial \mathbf{X}} = \frac{\partial \mathbf{u}}{\partial \mathbf{X}} + \mathbf{I}, \tag{7.2}$$

where $\mathbf{I}$ is the second order identity tensor. The deformation gradient $\mathbf{F}$ provides a complete description of deformation, including stretch and rigid body rotations. The latter does not contribute to shape or size change, thus not contribute to the strain tensor. Therefore, it is necessary to separate the stretch from the rigid body rotations in the deformation gradient. Using the theorem of polar decomposition (de Souza Neto et al. 2008), $\mathbf{F}$ can be decomposed as

$$\mathbf{F} = \mathbf{RU} = \mathbf{VR}, \tag{7.3}$$

where $\mathbf{U}$ is the right stretch tensor, $\mathbf{V}$ is the left stretch tensor, and $\mathbf{R}$ is the orthogonal rotation tensor. A consequence of such mathematical description is that for every material point, a local coordinate system $(1, 2, 3)$, also known as corotational coordinate system, rotates during deformation, as schematically represented in Figure 7.1.

The VFM is based on the PVW, which represents an integral form of mechanical equilibrium, written either in the undeformed or deformed configurations. Using the deformed configuration, neglecting body forces, and quasi-static conditions, the PVW can be given as

$$\int_{\mathcal{B}_t} \boldsymbol{\sigma} : \frac{\partial \mathbf{u}^*}{\partial \mathbf{x}} \, d\mathcal{B}_t + \int_{\partial \mathcal{B}_t} (\boldsymbol{\sigma}\mathbf{n}) \cdot \mathbf{u}^* \, d\partial\mathcal{B}_t = 0, \tag{7.4}$$

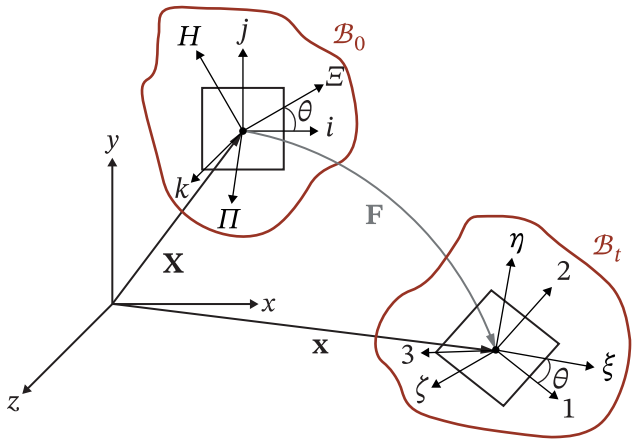

Figure 7.1 Description of the motion of a material body $\mathcal{B}$ in the Euclidean space defined by the global coordinate system (x, y, z), its undeformed configuration, deformed configuration at a time instant t, and definition of a material point coordinate systems: (i, j, k) is the global coordinate system defined in the undeformed configuration, $(1, 2, 3)$ is the local coordinate system defined in the deformed configuration, (Ξ, H, Π) and (ξ, η, ζ) are the material coordinate systems, respectively, in the undeformed and deformed configurations. The angle θ represents the material orientation.

where $\boldsymbol{\sigma}$ is the Cauchy stress tensor, $\mathbf{u}^*$ is the virtual displacements field, and $\mathbf{n}$ the outward vector of $\partial\mathcal{B}_t$. Alternatively, the PVW can be formulated in the undeformed configuration as

$$\underbrace{\int_{\mathcal{B}_0} \mathbf{P} : \frac{\partial \mathbf{U}^*}{\partial \mathbf{X}}\, d\mathcal{B}_0}_{W_{\text{int}}} + \underbrace{\int_{\partial\mathcal{B}_0} (\mathbf{PN}) \cdot \mathbf{U}^*\, d\partial\mathcal{B}_0}_{W_{\text{ext}}} = 0, \tag{7.5}$$

where $\mathbf{P}$ is the first Piola-Kirchhoff stress tensor, the virtual displacements' field is now represented by $\mathbf{U}^*$, and $\mathbf{N}$ is the outward vector of $\partial\mathcal{B}_0$. The PVW written in the undeformed configuration is more suitable for practical implementation, as $\mathbf{U}^*$ does not need to be updated with virtual boundary conditions (Marek et al. 2019; Lattanzi et al. 2020).

The first Piola-Kirchhoff stress tensor $\mathbf{P}$ relates forces applied in the deformed configuration to volumes in the undeformed configuration, and is defined as

$$\mathbf{P} = \det(\mathbf{F})\boldsymbol{\sigma}\mathbf{F}^{-\mathrm{T}}, \tag{7.6}$$

where $\det(\mathbf{F})$ is the determinant of $\mathbf{F}$ and $\mathbf{F}^{-\mathrm{T}}$ the transpose of its inverse. The Cauchy stress tensor $\boldsymbol{\sigma}$ is calculated from the strain tensor $\boldsymbol{\varepsilon}$ by means of a constitutive model combined with a given set of material parameters $\boldsymbol{\xi}$.

According to Equation 7.5, the PVW states that, in equilibrium and for a continuous virtual field, the internal virtual work W_{int} is equal to the external virtual work W_{ext} in absolute value, which must be satisfied for any time instant. Let us now consider that the body $\mathcal{B}$ can be discretized by a given number of material points (similarly to a finite element mesh), then W_{int} can be approximated by a discrete sum as

$$W_{\text{int}}(\boldsymbol{\xi}, \mathbf{U}^*, t) = \sum_{i=1}^{n_{\text{p}}} \left(\mathbf{P}_k(\boldsymbol{\xi}, t) : \frac{\partial \mathbf{U}_i^*}{\partial \mathbf{X}_i} V_i \right), \tag{7.7}$$

where n_{p} represents the number of material points and V_i is the volume covered by i-th material point. Due to the formulation of the PVW in the undeformed configuration, V_i is constant for every time instant. Additionally, the external virtual work W_{ext} can be simplified by selecting a virtual field that is constant along the boundary $\partial\mathcal{B}_0$ as

$$\begin{aligned} W_{\text{ext}}\left(\mathbf{U}^*, t\right) &= \int_{\partial\mathcal{B}_0} (\mathbf{PN}) \cdot \mathbf{U}^* \, d\partial\mathcal{B}_0 \\ &= \mathbf{U}^* \int_{\partial\mathcal{B}_0} (\mathbf{PN}) \, d\partial\mathcal{B}_0 \\ &= \mathbf{U}^* \cdot \mathbf{L}(t), \end{aligned} \tag{7.8}$$

where $\mathbf{L}$ is the resultant of the load acting on $\partial\mathcal{B}_0$, recorded during the test. Because the load distribution on $\partial\mathcal{B}_0$ is usually unknown, this simplification is crucial for the VFM.

Finally, the VFM is used to identify the best set of material parameters by minimizing the difference between the internal and external virtual work, through an objective function φ written in a least-squares formulation as

$$\varphi(\boldsymbol{\xi}) = \sum_{t=1}^{n_\text{t}} \sum_{j=1}^{n_\text{v}} \left[W_{\text{int}}\left(\boldsymbol{\xi}, \mathbf{U}_j^*, t\right) - W_{\text{ext}}\left(\mathbf{U}_j^*, t\right) \right]^2, \tag{7.9}$$

where n_v is the number of virtual fields and n_t the total number of time instants. Various time instants and different virtual fields can be used to enrich the objective function. Usually, an optimization algorithm is used to iteratively adjust the material parameters.

7.2.1 Stress Reconstruction from the Strain Fields

As previously established, the VFM requires, at each iteration, the calculation of $\mathbf{P}$, which is effectively dependent on the strain tensor. Therefore, it is convenient to use a measure of strain that is independent of rigid body rotations and dependent on stretch alone, given by

$$\boldsymbol{\varepsilon} = \ln \mathbf{V}, \tag{7.10}$$

where $\mathbf{V}$ is defined in the global coordinate system (i, j, k) in the undeformed configuration. However, constitutive equations are generally defined in the material coordinate system (ξ, η, ζ), aligned with material texture. Thus, the calculated strain tensor $\boldsymbol{\varepsilon}^{(i,j,k)}$ must be projected to the material coordinate system (ξ, η, ζ) according to

$$\boldsymbol{\varepsilon}^{(\xi,\eta,\zeta)} = \mathbf{R}_{\text{mat}}^{\text{T}} \left(\mathbf{R}^{\text{T}} \boldsymbol{\varepsilon}^{(i,j,k)} \mathbf{R} \right) \mathbf{R}_{\text{mat}}, \tag{7.11}$$

where $\mathbf{R}_{\text{mat}}$ is the material rotation tensor given by

$$\mathbf{R}_{\text{mat}} = \begin{bmatrix} \cos\theta & -\sin\theta & 0 \\ \sin\theta & \cos\theta & 0 \\ 0 & 0 & 1 \end{bmatrix}, \tag{7.12}$$

which is responsible for rotating the local coordinate system to the material one as a function of the material orientation θ, constant throughout deformation.

The projected strain tensor $\boldsymbol{\varepsilon}^{(\xi,\eta,\zeta)}$ is used to reconstruct the stress tensor $\boldsymbol{\sigma}^{(\xi,\eta,\zeta)}$ via an implicit integration algorithm, similarly to the ones found in FEA software. However, many time instants should be used to guarantee the stability and convergence of the algorithm. Alternatively, other algorithms could be used, such as the direct method proposed by Rossi et al. (2020), that provide a computationally faster reconstruction but cannot be incorporated in a FEA software.

Afterwards, the stress tensor $\boldsymbol{\sigma}^{(\xi,\eta,\zeta)}$ defined in the material coordinate system (ξ, η, ζ) should be projected to the global coordinate system (i, j, k) as

$$\boldsymbol{\sigma}^{(i,j,k)} = \mathbf{R}_{\text{mat}} \left(\mathbf{R} \boldsymbol{\sigma}^{(\xi,\eta,\zeta)} \mathbf{R}^{\text{T}} \right) \mathbf{R}_{\text{mat}}^{\text{T}}, \tag{7.13}$$

and used in Equation 7.5 to calculate the first Piola-Kirchhoff stress tensor $\mathbf{P}$ defined the global coordinate system (i, j, k) in the undeformed configuration.

This formulation is general to any 3D application. However, the VFM is commonly used with full-field measurements limited to the surface of the specimen. These measurements only provide in-plane kinematic quantities, and often plane stress conditions are assumed, provided the specimen's thickness is small relative to its width and height. Thus, the application is considered 2D, and out-of-plane stress components are negligible ($\sigma_{zz} = \sigma_{xz} = \sigma_{yz} = 0$), but the deformation gradient $\mathbf{F}$ is in reality fully 3D. It results that the calculation of $\mathbf{P}$ requires additional assumptions (Marek et al. 2019). Assuming a thin specimen, the out-of-plane shear components can be neglected ($F_{xz} = F_{yz} = F_{zx} = F_{zz} = 0$), and the determinant of $\mathbf{F}$ is redefined as

$$\det(\mathbf{F}) = F_{zz}(F_{xx}F_{yy} - F_{xy}F_{yz}), \tag{7.14}$$

where F_{xx}, F_{yy}, F_{xy}, and F_{yx} are the in-plane components of $\mathbf{F}$, and F_{zz} is the out-of-plane component. The in-plane components are obtained from the displacement field. However, F_{zz} is unknown, but it can be approximated by the out-of-plane strain component for each time instant $\varepsilon_{zz}(t)$ as

$$F_{zz}(t) = 1 + \varepsilon_{zz}(t) = 1 + \int_0^t \dot{\varepsilon}_{zz}\, dt. \tag{7.15}$$

Finally, assuming isotropic elastic behavior using Hooke's law and the isochoric behavior of plasticity, $\dot{\varepsilon}_{zz}$ can be determined as

$$\dot{\varepsilon}_{zz} = -\frac{\nu}{1-\nu}(\dot{\varepsilon}^{\text{e}}_{xx} + \dot{\varepsilon}^{\text{e}}_{yy}) - (\dot{\varepsilon}^{\text{p}}_{xx} + \dot{\varepsilon}^{\text{p}}_{yy}), \tag{7.16}$$

where $\dot{\varepsilon}^{\text{e}}_{xx}$ and $\dot{\varepsilon}^{\text{e}}_{yy}$ represent the components of elastic strain rate, and $\dot{\varepsilon}^{\text{p}}_{xx}$ and $\dot{\varepsilon}^{\text{p}}_{yy}$ the components of plastic strain rate.

7.2.2 Numerical Implementation

The VFM is numerically implemented in a code fully developed in Python programming language. In terms of computational efficiency, the code is developed with array-based calculations, instead of using loops over the material points, as was the case in the FEMU from Chapter 5. Using arrays to directly perform the operations, such as calculating the logarithmic strain of all material points, largely speeds up the computation and reduces differences into an implementation in Fortran. Comparatively to the implementation of Chapter 5, the small loss in computational speed is compensated in simplicity. Moreover, the array-based calculation easily allows the program to perform the operations in either a 2D or 3D framework.

As schematically presented in Figure 7.2, the VFM requires the input of the geometry (coordinates of undeformed configuration), displacement fields, evolution of load, and constitute model. It should be noted that this implementation uses a finite element mesh and shape functions similar to a FEA software (such as Abaqus/Standard). In the pre-processing stage, the deformation gradient is calculated, and the logarithmic strain tensor is obtained from the polar decomposition of the deformation gradient. The latter operation is performed using a function available in the NumPy library (Numpy 2022). The logarithmic strain tensor calculated in global coordinate system is rotated to the material coordinate system in the undeformed configuration. Then, the manual virtual fields are generated.

The identification procedure uses the gradient-free NM algorithm (see Section 5.3) included in the SciPy library (SciPy 2022a). This algorithm was chosen, in part, because it allows more

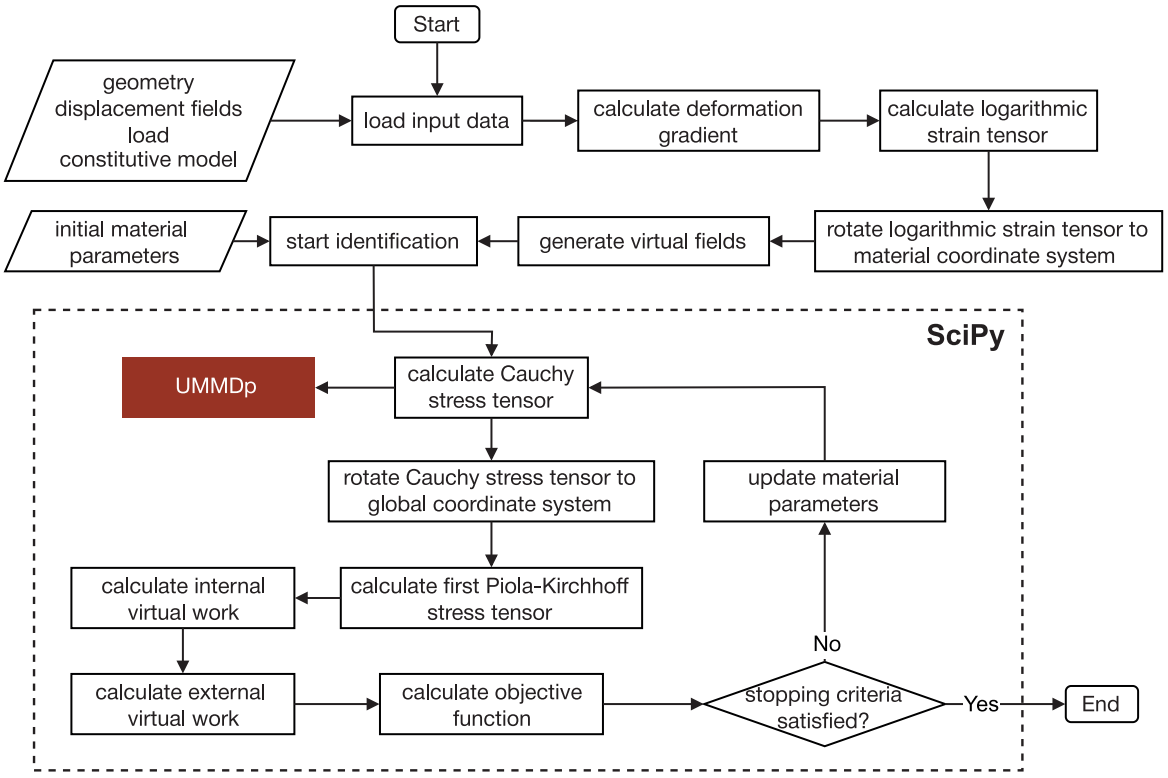

Figure 7.2 Flowchart of the VFM implementation.

control over the optimization procedure compared to the implementation of the LM algorithm. For example, using the NM it is possible to call a function at the end of each iteration, which is not available for all algorithms of the SciPy library. This functionality is important to allow updates during the optimization procedure. Inside the identification procedure, the first and main operation is the calculation of the Cauchy stress tensor. Specifically, UMMDp is integrated in the VFM to reconstruct the stress field through the backward-Euler scheme combined with an elastic predictor and plastic corrector (see Section 2.4). The major advantages of using UMMDp is to guarantee that the same constitutive model is used both in the identification procedure and future FEA simulations, and easily identify different constitutive models. A driver code for UMMDp is developed that allows the communication with the main program through the F2PY framework (NumPy 2022). This operation requires the most computational effort, because using an array-based calculation is impossible. The stress tensor is history dependent, so the calculation is performed iteratively for each material point and time instant. Afterwards, the Cauchy stress tensor is rotated to the global coordinate system, and the first Piola-Kirchhoff stress tensor is calculated. The internal and external virtual works are calculated, and finally, the objective function. Finally, the stopping criteria are evaluated, and the program either ends or updates the material parameters and continues the optimization procedure.

7.3 Simulated Tensile Tests

7.3.1 Specimen Geometry and Finite Element Model

This study only considers numerical simulations of a uniaxial tensile test. A specimen with varying cross-section is selected (Kim et al. 2013; Martins et al. 2018b) and its geometry is presented in Figure 7.3. Relatively to a classic uniaxial tensile specimen, this geometry has the advantage of generating a heterogeneous strain field over a large area, providing richer mechanical information

for the identification of material parameters (see Chapter 3). Moreover, the varying cross-section will trigger necking in the center region of the specimen, facilitating the setup of acquisition cameras during real experiments.

The test is simulated with Abaqus/Standard (DASSAULT SYSTÈMES 2019), considering a fully 3D model of the test, without assuming symmetry conditions. The finite element mesh is built using the 8-node brick elements with reduced integration (C3D8R), and considering three layers through the thickness. Ideally, more layers could have been used to describe more accurately the deformations along the thickness. However, it was found that increasing the number of layers also largely increased the computational time of numerical simulations and post-processing procedures. The finite element mesh was generated with an in-plane global element size of 0.2 mm, resulting in a total of 197 955 elements. Nevertheless, the center region of the specimen is the richest part of the specimen, thus a VOI (shaded region in Figure 7.3) is defined and constituted by 97 307 elements. The in-plane mesh size was defined after performing a convergence study evaluating the maximum equivalent plastic strain, by considering only three layers of elements through the thickness. The selected mesh size provided the best balance between an accurate description of the equivalent plastic strain and the computational effort.

A Cartesian coordinate system is defined with the x axis along d_w, the y axis along d_h, and the z axis along d_t. The constants d_w and d_h represent, respectively, half of the width and length of the VOI, while d_t is the material thickness. The origin of the coordinate system is located in the front surface of the specimen ($x = y = z = 0$), while $z = d_t$ defined the back surface (see Figure 7.3). The numerical simulations are displacement-driven, with an imposed constant vertical displacement u_y of 5 mm applied across the top edge, which was additionally fixed along the x and z axess to simulate the effect of the grip of a testing machine. The bottom edge of the model was fixed. The numerical simulations are performed at a constant time step, resulting in 200 time instants. Finally, a large strain formulation is adopted, and the constitutive model is implemented using UMMDp (see Section 2.4).

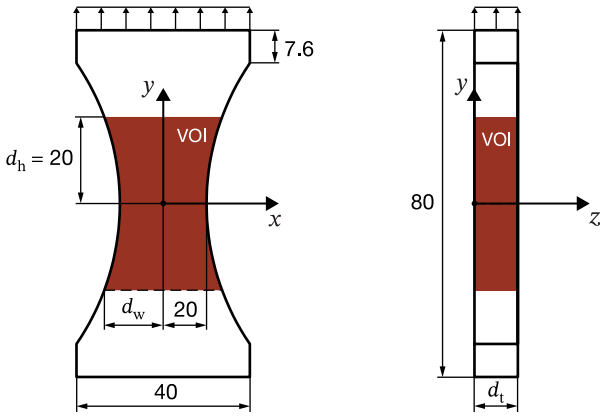

Figure 7.3 Geometry and finite element model of the specimen used in the numerical simulations of the simulated tensile test (dimensions in mm).

7.3.2 Virtual Materials

The materials considered in this study are based on the real characteristics of a DP780 dual-phase steel with a nominal thickness of 1.5 mm. This material was experimentally tested using quasi-static classical uniaxial tensile tests at different material orientations. The results showed that the material exhibited anisotropy, and the recorded longitudinal strain just before rupture was approximately 0.65. However, it should be emphasized that the goal of this study is not to characterize this material, but only to use it as a basis for the virtual materials considered

throughout. Many virtual materials of varying thicknesses are used in this study, but using the same description of the elastoplastic behavior.

The elastic isotropic behavior of the materials is described by Hooke's law, and the elastoplastic behavior is described by the von Mises isotropic yield criterion and the Swift isotropic hardening law (see Sections 2.2 and 2.3). The latter model was selected for its simplicity and wide use in the scientific community. The elastic properties of the materials and the Swift's law material parameters are provided in Table 7.1. The parameters of Swift law were obtained by fitting the experimental stress-strain curve of DP780. Additionally, in Figure 7.4, the hardening behavior according to the Swift's law is presented up to 0.75 of equivalent plastic strain.

Table 7.1 Elastic properties of the materials and reference parameters used in the Swift isotropic hardening law.

Elasticity		**Swift hardening law**		
E [GPa]	ν [–]	K [MPa]	σ_0 [MPa]	n [–]
200.0	0.3	1250.0	350.0	0.150

The materials are defined with thicknesses of 1.5, 2, 2.5, 3, 4, 6, 8, and 10 mm. The vertical displacement of 5 mm is used in all numerical simulations to have a direct comparison between the materials. As a result, only the numerical model of the 1.5 mm thick material is, approximately, modeled to reach rupture around the same magnitude of values of the real material. The equivalent plastic strain map for this material, on the surface ($z = 0$) and on the middle plane ($z = d_t$), is shown in Figure 7.5c at the last time instant corresponding to $u_y = 5$ mm. A large concentration of deformation is observed in the central region, indicating a severe localization of necking just before rupture. At a time instant of $u_y = 4$ mm (see Figure 7.5a), it can be observed that the material was already in diffuse necking, though the values of equivalent plastic strain are much lower than at the last time instant. This difference shows that large deformations are developed in the later stages of the test. On the other hand, the tests with materials of large thicknesses (such as 8 mm or 10 mm) do not even reach localized necking. It is observed that the necking is delayed as a function of the material's thickness. This is observed in the equivalent plastic strain maps for the 10 mm thick material presented in Figure 7.5b. The values of equivalent plastic strain at the last time instant are only comparable to the ones observed at $u_y = 4$ mm for the 1.5 mm thick material. The evolution of load as a function of the vertical displacement is also shown in Figure 7.6 for all materials. As expected, the load increase is proportional to the thickness of the materials.

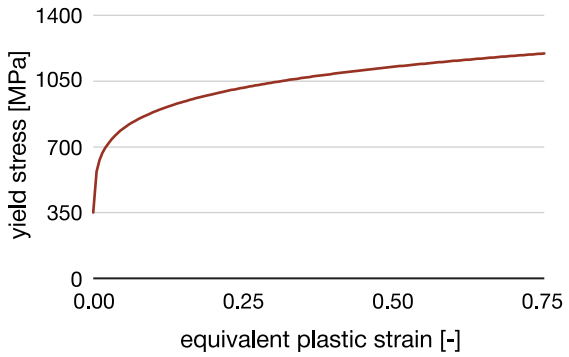

Figure 7.4 Virtual representation of the materials strain-hardening behavior using the Swift isotropic hardening law and reference parameters.

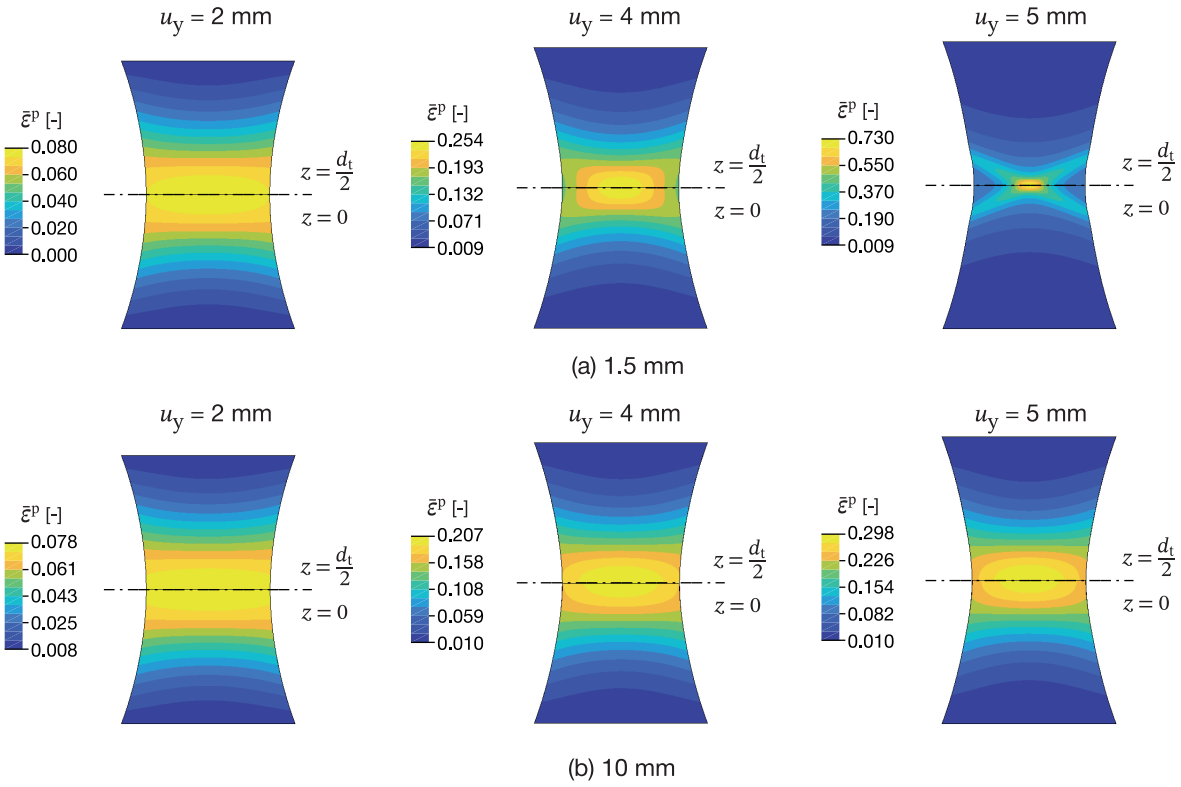

Figure 7.5 Maps of equivalent plastic strain at time instants corresponding to vertical displacements of 2, 4, and 5 mm for materials with (a) 1.5 mm and (b) 10 mm of thickness. Maps on the surface ($z = 0$) and middle plane ($z = d_t/2$) are both represented.

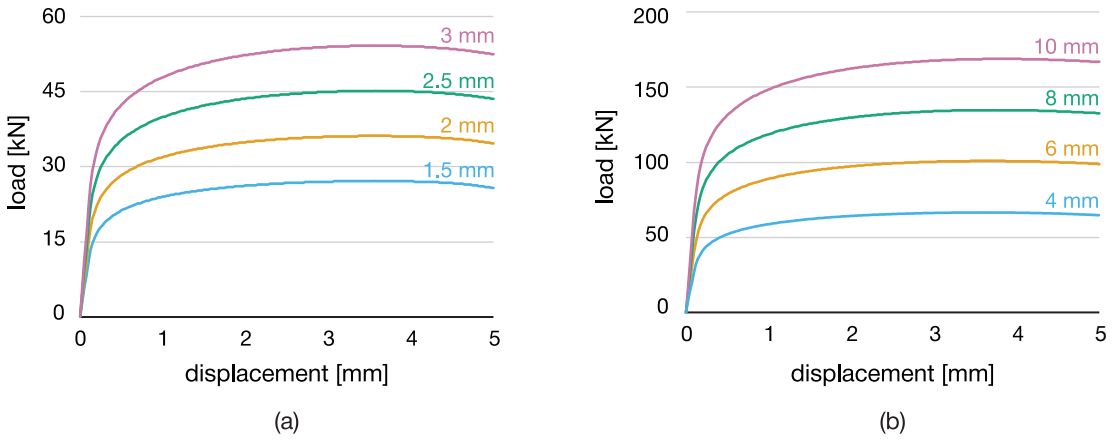

Figure 7.6 Evolution of the load as a function of the vertical displacement for the simulated tests with materials of thickness (a) 1.5, 2, 2.5, and 3 mm, and (b) 4, 6, 8, and 10 mm.

7.3.3 Extraction of the Displacement Fields

The simulated tests are modeled in 3D, but the 2D-VFM uses information from the surface of the specimen, thus only in-plane kinematic fields are considered. For the 3D-VFM, the displacement field is extracted from the nodes of the finite element mesh in the VOI of the simulated tests. This mesh is already regularized, thus can be directly used as input to the 3D-VFM. For the 2D-VFM, the in-plane displacement field is extracted from the nodes on the surface of the 3D test, and a 2D finite element mesh is generated by rearranging the elements' connectivity.

7.4 Definition of the Virtual Fields

The main area of development and discussion around the VFM is probably the selection of virtual fields. Because its definition assigns weights to material points, it directly affects the objective function and can lead to different identification results. Nevertheless, one thing all methodologies agree is that the virtual fields must be kinematically admissible, continuous and differentiable over the entire domain (Pierron and Grédiac 2012).

In the framework of plasticity, two strategies can be distinguished according to the way virtual fields are generated. The most common strategy is based on manually defined virtual fields. This strategy usually employs polynomial or harmonic functions defined by the user and adapted to the geometry and boundary conditions of the application (Rossi et al. 2016b; Fu et al. 2020; Martins et al. 2021). For this reason, this strategy depends highly on the user experience and understanding of the application, even though it is simpler from an implementation point of view. The other strategy is based on the automatic generation of virtual fields, and was developed to overcome the problems of the first. A major advantage is that it reduces the user dependence of the first strategy, making the method more automatic and suited for integration in parameter identification software. A first implementation, named optimized virtual fields, relied on the minimization of noise effects in the material parameters (Pierron et al. 2010). Later, Marek et al. (2017) proposed the sensitivity-based virtual fields. This implementation relies on the sensitivity of the stress field to each material parameter, and it has been shown to outperform the manual virtual fields, particularly when dealing with experimental data (Marek et al. 2020; Lattanzi et al. 2020). Nevertheless, it has been shown that increasing the number of manual virtual fields can lead to interesting results (Martins et al. 2020a).

Considering that 3D-VFM is still less explored than 2D-VFM, only the manual defined virtual fields are employed in this study because of its simplicity and ease of implementation. The generic form of the virtual displacement fields $\mathbf{U}$, for the general case of 3D, is given by

$$\mathbf{U}^* = \begin{bmatrix} U_x^* \\ U_y^* \\ U_z^* \end{bmatrix}, \tag{7.17}$$

where $U_z^* = 0$ in the 2D-VFM, and the gradient of virtual displacement fields $\frac{\partial \mathbf{U}}{\partial \mathbf{X}}$ by

$$\frac{\partial \mathbf{U}^*}{\partial \mathbf{X}} = \begin{bmatrix} \frac{\partial U_x^*}{\partial X} & \frac{\partial U_x^*}{\partial Y} & \frac{\partial U_x^*}{\partial Z} \\ \frac{\partial U_y^*}{\partial X} & \frac{\partial U_y^*}{\partial Y} & \frac{\partial U_y^*}{\partial Z} \\ \frac{\partial U_z^*}{\partial X} & \frac{\partial U_z^*}{\partial Y} & \frac{\partial U_z^*}{\partial Z} \end{bmatrix}, \tag{7.18}$$

where $\partial U_x^*/\partial Z = \partial U_z^*/\partial X = \partial U_y^*/\partial Z = \partial U_z^*/\partial Y = \partial U_z^*/\partial Z = 0$ in the 2D-VFM.

Three manual virtual fields are defined in this study, and their components are presented in Table 7.2. The first virtual field $\mathbf{U}_1^*$ is commonly used in various applications of the VFM because it includes the load's contribution. The external virtual work is proportional to the load and is balanced by the internal virtual work calculated from the stress component yy, aligned with the loading direction. In theory, it is the only virtual field that gives a non-zero value in the calculation of the internal virtual work. Moreover, the resulting gradient presents a constant spatial distribution across all VOI.

The second and third virtual fields, respectively, denoted by $\mathbf{U}_2^*$ and $\mathbf{U}_3^*$ present non-constant spatial distributions, with different weights assigned to the stress components in the calculation of the internal virtual work. These are null on the boundary of the applied load, which gives a zero

Table 7.2 Components of the virtual displacements and gradient of the virtual displacements for the three virtual fields.

	Virtual field		
Component	1	2	3
Virtual displacements			
U_x^*	0	$\frac{1}{\pi}\sin(\frac{\pi}{d_w}x)\cos(\frac{\pi}{2d_h}y)$	$\frac{1}{\pi}\sin(\frac{\pi}{d_w}x)\cos(\frac{\pi}{2d_h}y)\cos(\frac{\pi}{2d_t}z)$
U_y^*	$\frac{y}{d_h}$	$\frac{1}{\pi}\sin(\frac{\pi}{d_w}x)\cos(\frac{\pi}{2d_h}y)$	$\frac{1}{\pi}\sin(\frac{\pi}{d_w}x)\cos(\frac{\pi}{2d_h}y)\cos(\frac{\pi}{2d_t}z)$
U_z^*	0	0	$\frac{1}{\pi}\sin(\frac{\pi}{d_w}x)\cos(\frac{\pi}{2d_h}y)\sin(\frac{\pi}{2d_t}z)$
Gradient of virtual displacements			
$\frac{\partial U_x^*}{\partial X}$	0	$\frac{1}{d_w}\cos(\frac{\pi}{d_w}x)\cos(\frac{\pi}{2d_h}y)$	$\frac{1}{d_w}\cos(\frac{\pi}{d_w}x)\cos(\frac{\pi}{2d_h}y)\cos(\frac{\pi}{2d_t}z)$
$\frac{\partial U_x^*}{\partial Y}$	0	$-\frac{1}{2d_h}\sin(\frac{\pi}{d_w}x)\sin(\frac{\pi}{2d_h}y)$	$-\frac{1}{2d_h}\sin(\frac{\pi}{d_w}x)\sin(\frac{\pi}{2d_h}y)\cos(\frac{\pi}{2d_t}z)$
$\frac{\partial U_x^*}{\partial Z}$	0	0	$-\frac{1}{2d_t}\sin(\frac{\pi}{d_w}x)\cos(\frac{\pi}{2d_h}y)\sin(\frac{\pi}{2d_t}z)$
$\frac{\partial U_y^*}{\partial X}$	0	$\frac{1}{d_w}\cos(\frac{\pi}{d_w}x)\cos(\frac{\pi}{2d_h}y)$	$\frac{1}{d_w}\cos(\frac{\pi}{d_w}x)\cos(\frac{\pi}{2d_h}y)\cos(\frac{\pi}{2d_t}z)$
$\frac{\partial U_y^*}{\partial Y}$	$\frac{1}{d_h}$	$-\frac{1}{2d_h}\sin(\frac{\pi}{d_w}x)\sin(\frac{\pi}{2d_h}y)$	$-\frac{1}{2d_h}\sin(\frac{\pi}{d_w}x)\sin(\frac{\pi}{2d_h}y)\cos(\frac{\pi}{2d_t}z)$
$\frac{\partial U_y^*}{\partial Z}$	0	0	$-\frac{1}{2d_t}\sin(\frac{\pi}{d_w}x)\cos(\frac{\pi}{2d_h}y)\sin(\frac{\pi}{2d_t}z)$
$\frac{\partial U_z^*}{\partial X}$	0	0	$\frac{1}{d_w}\cos(\frac{\pi}{d_w}x)\cos(\frac{\pi}{2d_h}y)\sin(\frac{\pi}{2d_t}z)$
$\frac{\partial U_z^*}{\partial Y}$	0	0	$-\frac{1}{2d_h}\sin(\frac{\pi}{d_w}x)\sin(\frac{\pi}{2d_h}y)\sin(\frac{\pi}{2d_t}z)$
$\frac{\partial U_z^*}{\partial Z}$	0	0	$\frac{1}{2d_t}\sin(\frac{\pi}{d_w}x)\cos(\frac{\pi}{2d_h}y)\cos(\frac{\pi}{2d_t}z)$

value in the calculation of external virtual work. The second virtual field was adopted from other studies using 2D-VFM, where its use has proven to be successful (Rossi et al. 2016b; Marek et al. 2019; Lattanzi et al. 2020). It only considers the in-plane components of the stress tensor, neglecting the out-of-plane components. Also, $\mathbf{U}_2^*$ does not depend on z, leading to a constant spatial distribution across the thickness.

Lastly, $\mathbf{U}_3^*$ assigns weight to all the stress tensor components and also generates a non-constant spatial distribution across the thickness. The third virtual field can be considered an extension of the second to 3D-VFM, because it simplifies to the latter when $z = 0$. However, it should be noted that this virtual field would not be useful if the origin of the coordinate system was positioned in the middle of the specimen, because the kinematic fields are symmetrical across the thickness. Thus, leading to a combination of symmetrical stress fields with symmetrical virtual fields across the thickness, resulting in a null value of the internal virtual work. The former is only true because this study only considers simulated tests, while in real experiments unsymmetrical kinematic fields across the thickness would be expected. A graphical representation of the three virtual fields displacement maps is shown in Figure 7.7. The presented maps of $\mathbf{U}_1^*$ and $\mathbf{U}_2^*$ are representative of the whole VOI, while for $\mathbf{U}_3^*$ are presented the maps at the front ($z = 0$) and back ($z = d_t$) surfaces.

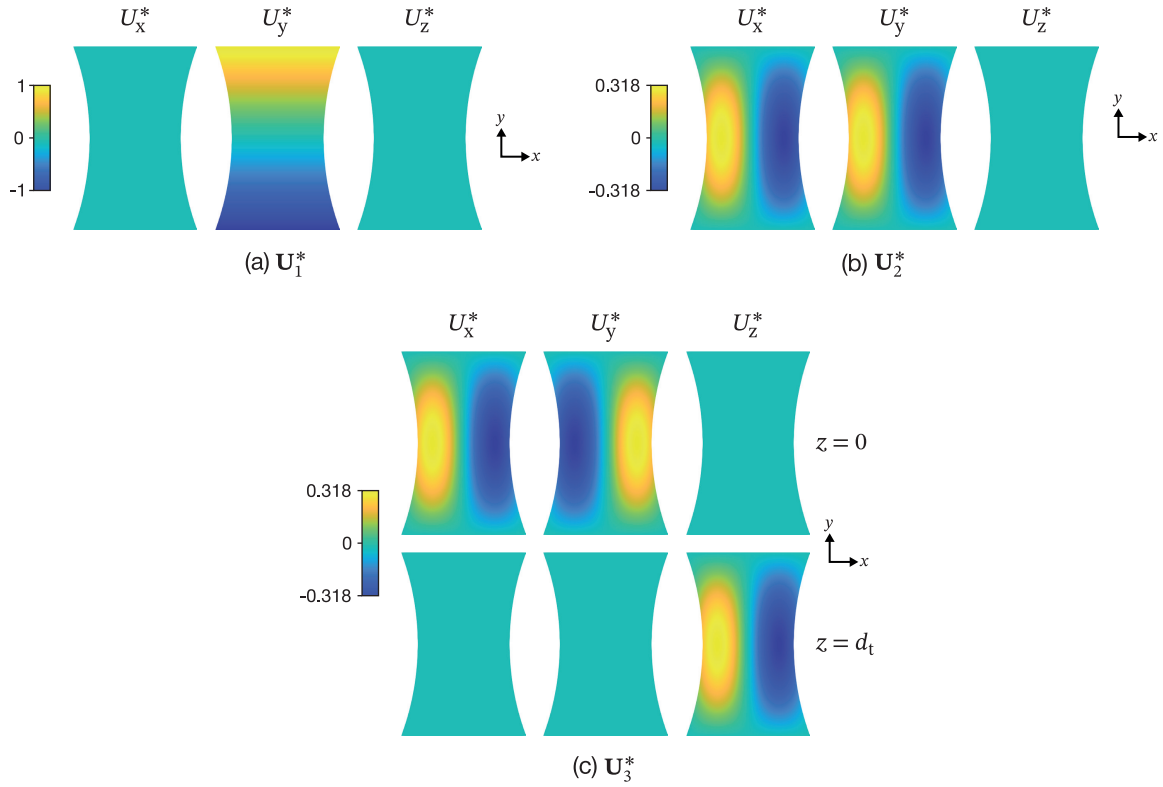

Figure 7.7 Maps of virtual displacement fields represented for three virtual fields (a) $\mathbf{U}_1^*$, (b) $\mathbf{U}_2^*$, and (c) $\mathbf{U}_3^*$. The maps of $\mathbf{U}_1^*$ are represented on the front ($z = 0$) and back ($z = d_t$) surfaces, while the maps of $\mathbf{U}_1^*$ and $\mathbf{U}_3^*$ are representative of the whole VOI.

7.5 Results

7.5.1 Analysis of the Predicted Load

Because this study only considers numerical data, the reference parameters and reference test data are known. By taking advantage of that, it is possible to analyze the predicted load using the 2D-VFM and the 3D-VFM, and compare with the reference load obtained from the numerical simulations. In particular, the evolution of load can be extracted from numerical simulations and used in the external virtual work term, as shown in Equation 7.8, provided a constant virtual field over the boundary is used. Also, considering the test is uniaxially loaded along the y axis, the evolution of load can be simplified to its y component, denoted by $L^{\text{ref}}(t)$. Using the first virtual field $\mathbf{U}_1^*$, the external virtual work $W_{\text{ext}}(\mathbf{U}_1^*, t)$ can be simplified to

$$\begin{aligned} W_{\text{ext}}(\mathbf{U}_1^*, t) &= \frac{y}{d_{\text{h}}} \cdot L^{\text{ref}}(t) \\ &= L^{\text{ref}}(t), \end{aligned} \tag{7.19}$$

where $\mathbf{U}_{1_y}^* = y/d_{\text{h}} = 1$ on the boundary of applied load. Consequently, the evolution of predicted load $L(\boldsymbol{\xi}, t)$ can be calculated from the internal virtual work $W_{\text{int}}(\boldsymbol{\xi}, \mathbf{U}_1^*, t)$ as

$$
\begin{aligned}
L(\boldsymbol{\xi}, t) &= \frac{1}{2} W_{\text{int}}(\boldsymbol{\xi}, \mathbf{U}_1^*, t) \\
&= \frac{1}{2} \int_{\mathcal{B}_0} \mathbf{P}(\boldsymbol{\xi}, t) : \frac{\partial \mathbf{U}_1^*}{\partial \mathbf{X}} \, d\mathcal{B}_0 \\
&= \frac{1}{2} \int_{\mathcal{B}_0} P_{\text{yy}}(\boldsymbol{\xi}, t) \cdot \frac{1}{d_{\text{h}}} \, d\mathcal{B}_0,
\end{aligned}
\tag{7.20}
$$

where P_{yy} represents the yy component of the Piola-Kirchhoff stress tensor. The constant 1/2 is necessary to account for the reaction load on the fixed boundary.

The relative error $\delta_{\text{re}}(\boldsymbol{\xi}, t)$ between evolution of predicted and reference load given by

$$
\delta_{\text{re}}(\boldsymbol{\xi}, t) = 100 \times \frac{\left| L(\boldsymbol{\xi}, t) - L^{\text{ref}}(t) \right|}{L^{\text{ref}}(t)},
\tag{7.21}
$$

is used as the indicator to compare the results using the 2D-VFM and the 3D-VFM.

In Figure 7.8, the evolution of the relative error is presented for all materials. It is observed that using the 3D-VFM, the maximum relative error is lower than 0.5 % for all thicknesses, and

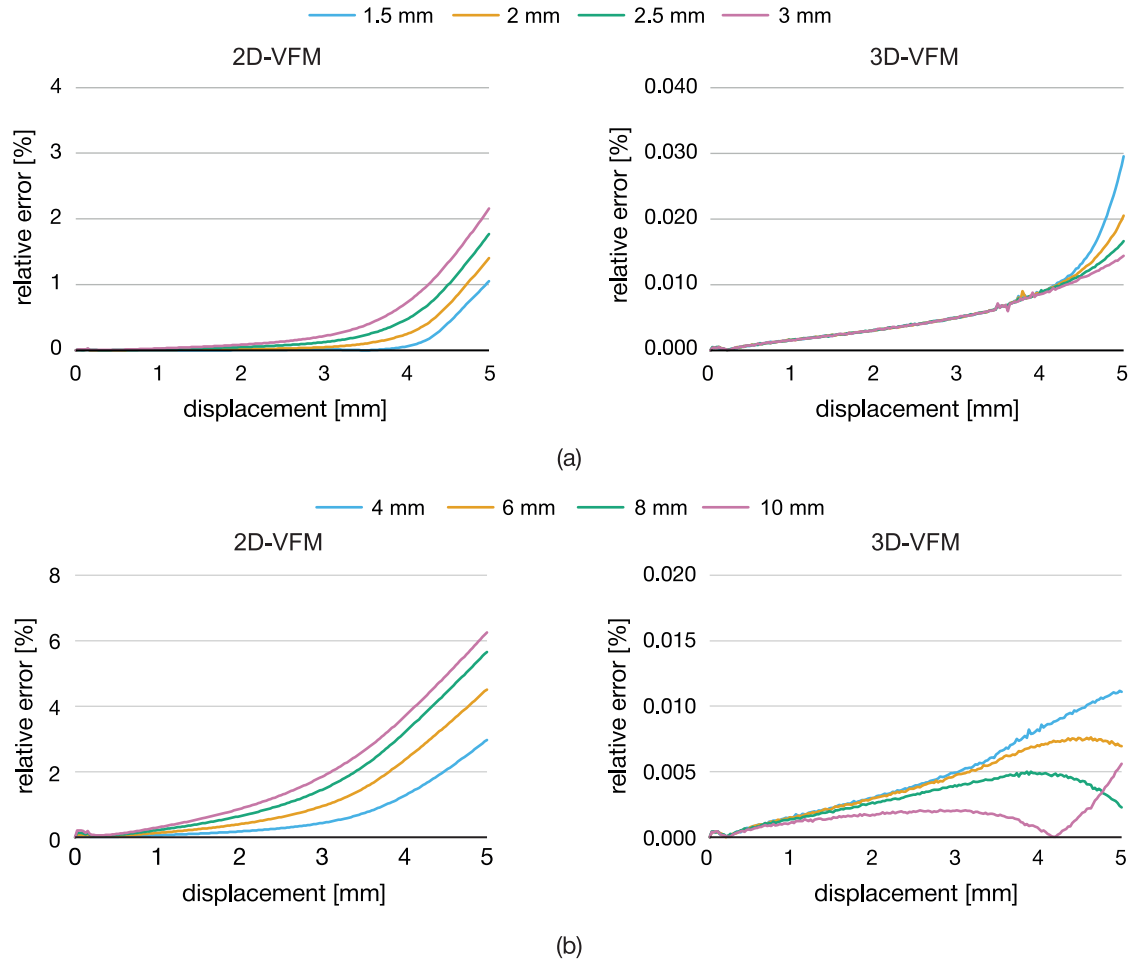

Figure 7.8 Evolution of the relative error for predicted load using the 2D-VFM and the 3D-VFM with the reference material parameters, for tests with materials of thickness (a) 1.5, 2, 2.5, and 3 mm, and (b) 4, 6, 8, and 10 mm.

tends to decrease with the increase in thickness. Thus, it can be considered that the relative error of 3D-VFM is negligible, and that the evolution of load is successfully predicted. However, the same is not observed using the 2D-VFM, where the relative error is not negligible. Overall, the relative error increases with the increase in thickness. For 1.5 mm, the evolution of relative error is close to zero, up to 4 mm of displacement, instant where the error rapidly increases up to 1 %. It was shown before that the time instant corresponding to $u_y = 4$ mm is when the equivalent plastic strain values rapidly increase, leading to the rupture of the material. Increasing the material's thickness, an increase in the relative error is observed sooner in the test, even though the same displacement corresponds to lower deformations in the thicker tests. For the thicker material of 10 mm, the relative error is as high as 6 % at the last time instant, though it can be expected that it would be higher for later stages of the test leading to rupture. In general, the increase in relative error appears proportional to the material's thickness.

To better understand the origin of these deviations, the evolution of the stress components xx, yy, and zz is investigated for two material points, one in the center of the front surface, denoted P_S, and another in the center of the middle plane, denoted P_M. The exact location of these two material points in the finite element mesh of all tests is shown in Figure 7.9, for the 1.5 mm thick material as an example.

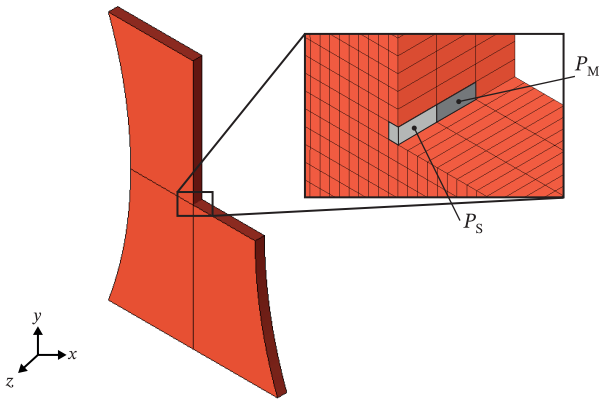

Figure 7.9 Location of the material points P_S and P_M, represented on the finite element mesh of the 1.5 mm thick material test.

This analysis is only performed for the materials of thickness 1.5, 3, and 10 mm, as presented in Figure 7.10. It can be seen that there is a dominant stress component σ_{yy} associated with the loading direction, which is expected from an uniaxial tensile test. More interestingly, it can be seen for the 1.5 mm thick material that the time instant where the error rapidly increases is consistent with the appearance of the stress component σ_{zz} (see Figure 7.10a). In fact, this is also consistent with the onset of localized necking, as previously observed in Figure 7.4. For larger thicknesses, the development of σ_{zz} is not as sudden and intense, but more as a constant increase from the initial time instant, in particular for the 10 mm thick material (see Figure 7.10c). Moreover, for the three materials, there is a difference in the stress values between the two material points.

Additionally, an analysis of the evolution of the ratio of stress components is also performed between the two material points. Its formulation is given by

$$R_{ii} = \frac{\sigma_{ii}(P_M)}{\sigma_{ii}(P_S)} \quad \text{with } i = \text{x, y, z.} \tag{7.22}$$

This analysis shows that the magnitude of σ_{zz} in P_M is two times higher than in P_S (see Figure 7.11). The same behavior is observed for all materials, as shown in Table 7.3, where the maximum values of the ratio of stress are presented. Interesting is also the observed tendency of R_{xx} to increase for

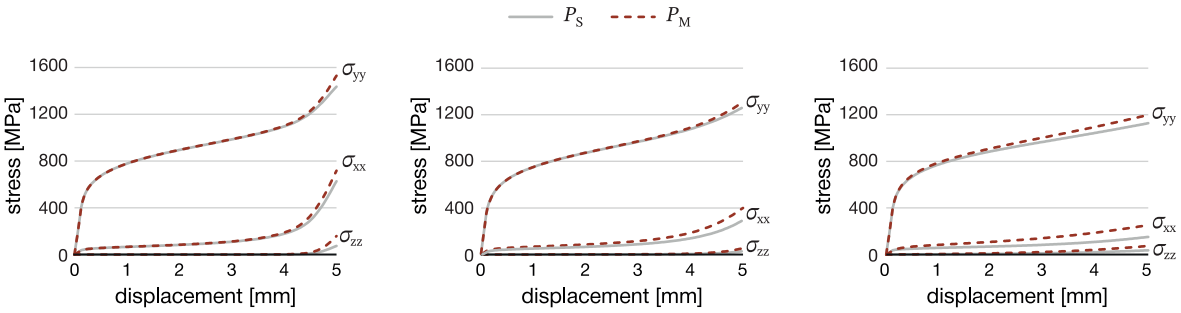

(a) 1.5 mm (b) 3 mm (c) 10 mm

Figure 7.10 Evolution of the stress components σ_{xx}, σ_{yy}, and σ_{zz} for the material points P_S and P_M, respectively, located on the center of the surface and in the center of the middle plane, for materials with thicknesses of (a) 1.5 mm, (b) 3 mm, and (c) 10 mm.

higher thicknesses. Since the 2D-VFM only considers the in-plane stress components and the surface material points in the calculation of the internal virtual work, it is not able to capture these behaviors, leading to the errors in the calculation of the internal virtual work, and consequently, errors in the predicted load.

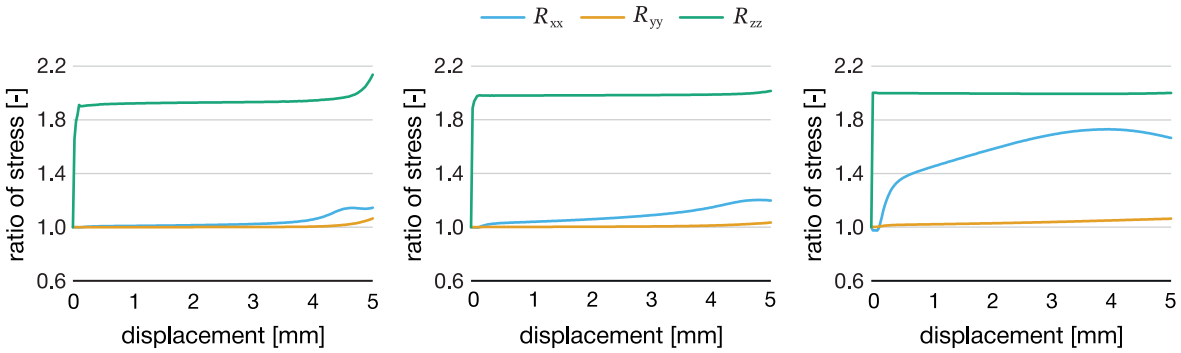

(a) 1.5 mm (b) 3 mm (c) 10 mm

Figure 7.11 Evolution of ratio of stress components σ_{xx}, σ_{yy}, and σ_{zz} between material points P_S and P_M, for materials with thicknesses of (a) 1.5 mm, (b) 3 mm, and (c) 10.0 mm.

Although errors will exist when using the 2D-VFM, it is important to understand if it's an acceptable error. For example, a relative error of 1 % (1.5 mm) can be considered acceptable for an application not requiring high accuracy. As such, it can also be considered that for thicknesses up to 1.5 mm, using the 2D-VFM is acceptable. However, for larger thicknesses, a larger deviation in the internal virtual work should be expected, leading to larger errors in the predicted load.

Table 7.3 Maximum values of the ratio of stress components σ_{xx}, σ_{yy}, and σ_{zz} between material points P_S and P_M, for all materials.

	Thickness [mm]							
Ratio of stress [–]	1.5	2	2.5	3	4	6	8	10
R_{xx}	1.15	1.16	1.18	1.20	1.25	1.37	1.54	1.73
R_{yy}	1.07	1.04	1.04	1.03	1.03	1.04	1.05	1.06
R_{zz}	2.14	2.04	2.02	2.02	2.01	2.01	2.00	2.00

7.5.2 Identification of the Swift Hardening Law

The developed VFM code in Python programming language is applied to identify the material parameters of the Swift's law, with $\boldsymbol{\xi} = (K, \sigma_0, k)$. The adopted termination criteria of the optimization procedure are set to a maximum number of iterations of 500, or when the absolute difference between parameters in consecutive iterations is lower than or equal to 1×10^{-8}. The identification is carried out for only the three thicknesses 1.5, 3, and 10 mm.

In a first part, the identification is carried out using both the 2D-VFM and the 3D-VFM. Only the first virtual field is used here. The three material parameters of Swift's law are identified, and the starting guess is equal to the reference parameters (see Table 7.1). This way, it will be easier to verify if the reference parameters are the global minimum solution used by numerical simulations. It is expected that the optimization is easily carried out, without taking many iterations or stopping at local minima.

The results of this identification are summarized in Table 7.4, where it is observed that using the 3D-VFM, the final material parameters are identical to the reference ones. In fact, considering the objective function is not normalized, the initial and final values are of low magnitude. These results reinforce the previous analysis, where very low errors were obtained for the predicted load using the 3D-VFM.

Table 7.4 Results of the identification starting from the reference material parameters and using the 2D-VFM and the 3D-VFM, for tests with thicknesses of 1.5, 3, and 10 mm. Only the first virtual field is employed in the identification.

	Parameter			Objective function	
Thickness	K [MPa]	σ_0 [MPa]	n [–]	Initial [–]	Final [–]
initial parameters	1250.000	350.000	0.150	—	—
2D-VFM					
1.5 mm	1240.609	340.502	0.148	3.00×10^{6}	2.10×10^{6}
3 mm	1217.838	318.345	0.143	9.10×10^{7}	3.30×10^{7}
10 mm	1137.783	5.049	0.128	1.58×10^{10}	2.40×10^{9}
3D-VFM					
1.5 mm	1250.591	350.365	0.150	3.31×10^{3}	8.20×10^{2}
3 mm	1250.463	350.255	0.150	7.76×10^{3}	8.30×10^{2}
10 mm	1249.936	349.863	0.150	7.11×10^{3}	5.40×10^{3}

However, the results using the 2D-VFM are completely different. By comparison, the initial objective function values are higher than those observed using the 3D-VFM, which directly indicates a worse prediction of the load using the reference material parameters. For the 1.5 mm thick material, the identified material parameters are not that far from the reference ones, even though it directly represents that these are suitable parameters. In fact, the objective function values have not largely improved, and its values are still much higher than those observed using the 3D-VFM. Moreover, the 2D-VFM uses a third of the material points considered in the 3D-VFM, thus proportionally the objective function values using 2D-VFM would be even higher. For the 3 and 10 mm thick materials, the identified parameters are far from the reference parameters. In particular, the identified value of σ_0 for the 10 mm thick material is not even physically acceptable. Bounds could have been imposed to avoid the unfeasible solutions, though it would not change the conclusions of the identification.

In Figure 7.12, the evolution of the relative error for predicted load (see Equation 7.21) is represented using both the reference and identified material parameters from Table 7.4 using the

2D-VFM. For the 1.5 mm thick material, it is observed that the predicted load with the identified parameters has improved in the range of necking (from approximately 4 mm of displacement). In spite of that, the relative error increases in early stages of the test, where the error was close to zero using the reference parameters. The same phenomenon is observed for the 3 and 10 mm thick materials with even more emphasis. It can be concluded that the identification using the 2D-VFM results in identified material parameters that are not representative of the materials' hardening behavior when applied to materials with large thicknesses.

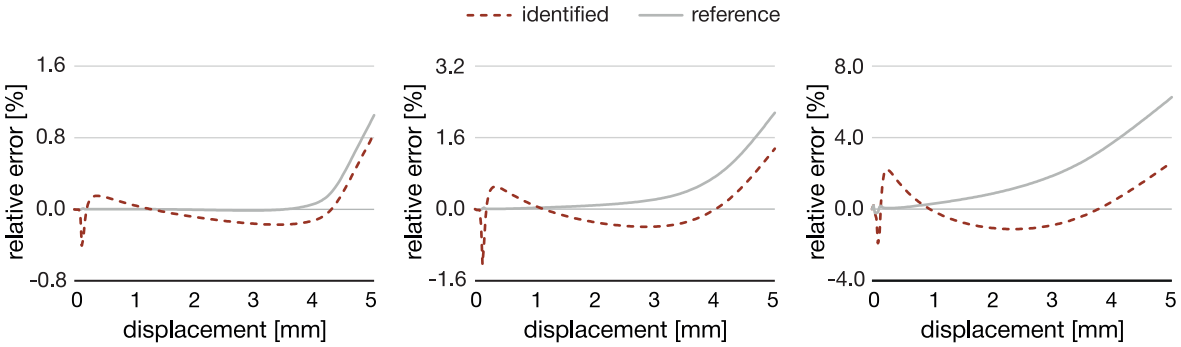

Figure 7.12 Evolution of the relative error for predicted load using the reference and the identified material parameters using the 2D-VFM, for tests with thicknesses of (a) 1.5 mm, (b) 3 mm, and (c) 10.0 mm.

To analyze the influence of each virtual field (see Table 7.2), more identifications are performed, but only using the 3D-VFM. In the identifications, various combinations of virtual fields are used. Three identifications evaluate the influence of each virtual field individually, and three more are performed by combining the first with the second virtual field, the second with the third, and a final identification combining the three of them. Again, the identifications are performed only for the 1.5, 3, and 10 mm thick materials. However, the initial material parameters are different from the reference ones to investigate the effect on the efficiency of convergence. The selected initial material parameters correspond to 1.5 times the reference ones.

Overall, the identification results are good, as summarized in Table 7.5. A common result between all identifications is the exact identification of the parameter n, while for the parameters K and σ_0 the exact values are not identified, but almost identical. The values of the identified parameters are all within 1 % of the reference ones, which is more than an acceptable result. Nevertheless, for the sake of comparing the influence of different virtual fields, it can be said that the best results are achieved using the first virtual field, either alone or in combination with others. In fact, this virtual field is the only one that leads to a non-zero value in external virtual work, including valuable information to the identification of hardening material parameters. When using either the second or third virtual fields alone, the identified parameters K and σ_0 tend to not reach the exact solution. Nevertheless, it does not mean these virtual fields are not suitable, but only reinforces the idea that using manual virtual fields, increasing its number leads to better and more stable results (Martins et al. 2020a). Interestingly, for the 10 mm thick material, the results using the second virtual field are slightly worst compared to the results of the 1.5 and 3 mm thick materials. This finding suggests that when out-of-plane stress components are not negligible, using virtual fields similar to the second leaves out important information that could be captured in the objective function. In terms of computational efficiency, the number of iterations required for the convergence of the identification procedure does not suggest any major differences between the combination of virtual fields.

Table 7.5 Results of the identification using the 3D-VFM and combining different virtual fields, for tests with thicknesses of 1.5, 3, and 10 mm.

		Parameter				Objective function	
Thickness	**Virtual fields**	K [MPa]	σ_0 [MPa]	n [–]	**Iterations**	Initial [–]	Final [–]
	initial parameters	1875.000	525.000	0.225	—	—	—
1.5 mm	1	1250.591	350.365	0.150	217	7.64×10^{9}	8.21×10^{2}
	2	1247.688	348.374	0.150	226	1.97×10^{8}	9.68×10^{2}
	3	1247.355	348.439	0.150	217	8.25×10^{7}	8.72×10^{2}
	1 + 2	1250.454	350.240	0.150	218	7.89×10^{9}	3.71×10^{3}
	1 + 3	1250.525	350.307	0.150	240	6.73×10^{9}	2.70×10^{3}
	1 + 2 + 3	1250.394	350.187	0.150	232	6.93×10^{9}	5.52×10^{3}
3 mm	1	1250.463	350.255	0.150	234	3.06×10^{10}	8.32×10^{2}
	2	1248.317	348.930	0.150	208	9.13×10^{8}	7.28×10^{2}
	3	1248.670	349.627	0.150	217	3.80×10^{8}	3.88×10^{1}
	1 + 2	1250.357	350.160	0.150	216	3.15×10^{10}	6.45×10^{3}
	1 + 3	1250.423	350.223	0.150	221	3.10×10^{10}	2.56×10^{3}
	1 + 2 + 3	1250.321	350.132	0.150	220	3.19×10^{10}	8.04×10^{3}
10 mm	1	1249.936	349.863	0.150	240	3.51×10^{11}	5.39×10^{3}
	2	1246.999	347.853	0.150	210	9.40×10^{9}	1.67×10^{4}
	3	1249.914	349.843	0.150	275	3.09×10^{11}	1.09×10^{4}
	1 + 2	1249.792	349.726	0.150	248	3.62×10^{11}	1.18×10^{5}
	1 + 3	1249.914	349.843	0.150	275	3.09×10^{11}	1.09×10^{4}
	1 + 2 + 3	1249.773	349.710	0.150	260	3.19×10^{11}	1.22×10^{5}

7.6 Conclusions

The purpose of this study is to better understand the limitations of using the VFM in a 2D framework compared to a 3D framework. The study only considers data from numerical simulations, and the methodology was applied to the identification of a hardening law, beyond necking and up to rupture. The simulated tests are performed with a uniaxial tensile test of varying cross-sections, generating a heterogeneous strain field over a large area. Moreover, various materials of different thicknesses are considered to understand its influence on the use of the VFM. Although these materials present different thicknesses, their hardening behavior is based on the real behavior of a dual-phase steel with 1.5 mm of thickness.

Three manual virtual fields are implemented in this study, because of its simplicity and lack of studies in a 3D framework. The first virtual field is commonly used in the VFM, because it's the only one that includes the external virtual work in the calculation of the objective function. The second virtual field only assigns weight to in-plane stress components. It is also widely used in the VFM in a 2D framework. The third, and last, virtual field is an extension of the second to a 3D framework, and can be considered a novel contribution of this study. The advantage of the latter is that it assigns non-zero weights to all stress components and is not constant along the thickness.

In a first part, the evolution of the predicted load was analyzed using the 2D-VFM and the 3D-VFM, for all materials. The relative error between predicted and reference load from numerical simulations was used as an indicator. The results showed that the relative error was negligible when using the 3D-VFM, successfully predicting the evolution of the load. On the contrary, using the 2D-VFM, the relative error was no longer negligible, ranging from 1 % for the 1.5 mm thick

material up to 6 % for the 10 mm thick material, at the last time instant. With this analysis, it has been shown that the relative error increases proportionally to the increase of materials' thickness. Moreover, the source of the error can be related to the development of non-negligible out-of-plane stress components not considered in the 2D-VFM, as well as considerable differences in the stress values between the surface and middle of the specimen.

In a second part, the identification of the Swift hardening law material parameters was investigated. Initially, the identification was carried out using both VFM frameworks, only one virtual field, and starting from the reference material parameters. The results have shown that the reference material parameters correspond to the global optimum solution using the 3D-VFM, but using the 2D-VFM led to solutions diverging from the reference, and one unfeasible solution was also found. A verification of the predicted load using the identified parameters has shown that these do not lead to better results, but rather improve the prediction at some stages at the expense of others. Lastly, the three virtual fields were employed in the identification of the material parameters using the 3D-VFM. This time, a starting solution far away from the reference was chosen to analyze the convergence efficiency using different combinations of virtual fields. Nevertheless, few differences were observed between identifications, with all reaching solutions within 1 % of the reference values or in some cases identical.

Finally, it can be said that this study performed a pioneering analysis of the limitations of the VFM in a 2D framework compared to a 3D framework. However, this was only a preliminary numerical study that can be enlarged and extended to materials developing pronounced out-of-plane stress fields.

8 Final Remarks

8.1 Conclusions

The ultimate objective of this thesis was to develop and investigate efficient and accurate methodologies for the characterization of metallic sheets. Following the "Material Testing 2.0" paradigm, the parameter identification of constitutive models of metallic sheets can be divided in three pillars: (i) material testing, (ii) constitutive models, and (iii) inverse methodologies. It is considered that this thematic follows a multiplicative system, meaning that if one of the pillars fails, the outcome of the parameter identification will not be successful. Thus, this thesis aimed to contribute to each of the three pillars, by investigating the use of heterogeneous mechanical tests, techniques to reconstruct the kinematic fields, advanced constitutive models, and inverse methodologies.

The starting point for this thesis dealt with the use of advance constitutive models, because scientific and industrial communities need accurate models to describe multiple phenomena of the materials. However, implementing and validating a single model is an arduous task that can take months of work. For that reason, studies generally tend to use well known models, which are, in some cases, relatively simple and have already been implemented and tested. Nevertheless, with the recent development of an open source user subroutine library of constitutive models, named Unified Material Model Driver for Plasticity (UMMDp), an opportunity to easily access advanced models opened up. This library contains various isotropic and kinematic hardening laws, more than 10 advanced yield criteria, and it is compatible with five different FEA software. Moreover, its programming structure is highly modular, allowing its expansion with an easy integration of other models. However, at the start of this thesis, few validations of the library were reported. Therefore, the validity and performance of the UMMDp was investigated by comparing it with an already developed and validated user material subroutine and one of the most used FEA software, Abaqus/Standard. In particular, the use of the advanced Yld2004-18p anisotropic yield criterion and a non-linear mixed hardening law was analyzed for single-element homogeneous tests and a deep drawing cup test. Results showed that the UMMDp yields identical results compared to the used references, validating its use, but with added computational effort. Nevertheless, the latter disadvantage is compensated by its practicality and potential. These outcomes have led to the adoption of the UMMDp throughout this thesis. Moreover, this investigation also led to the use of the UMMDp by several other studies, other research teams, as well as its integration in the VFM module of MatchID commercial software (MatchID 2022e).

Afterwards, an extensive overview of heterogeneous mechanical tests, reported in the literature, was performed, with its focus on the type and amount of information provided. This survey was

justified by the large amount of heterogeneous tests designed in the last decade. However, as more and more tests were proposed, it raised the question of which was best, i.e. which test provided the widest range of mechanical states and a larger degree of deformation, leading to more accurate parameter identification. The survey divided the tests between uniaxial, biaxial and out-of-plane loading, showing that the first type corresponds to most developed tests, which may be related to the fact that only a common uniaxial testing machine is required. These tests can achieve various mechanical states, mainly in the shear and uniaxial tension regions. Moreover, having only two edges of the specimen fixed leads to more flexibility in the design process, which in turn leads to complex shapes obtained by different methodologies. On the other hand, biaxial and out-of-plane loading tests require more complex experimental apparatus, thus are found in a less number. Nevertheless, the biaxial tests have been largely investigated for a long time, but its interest has recently dropped because it has been shown that the range of mechanical states is reduced and low levels of deformation are achieved.

The previous survey also led to the conclusion that there is a lack of information on the proposed tests, as only a few are analyzed by different studies and conditions. Comparing heterogeneous mechanical tests is not a trivial task, as there are no clear standards or metrics to evaluate them. Therefore, a study was performed where the richness of four heterogeneous mechanical tests is numerically evaluated through five different metrics. These metrics are the equivalent plastic strain, the major and minor strains, the major and minor stresses, the stress triaxiality and Lode angle parameter, and, lastly, the rotation angle. It has been shown that the first metric is relevant to evaluate the levels of deformation achieved, as well as its homogeneity over the specimen surface. The other three metrics evaluate the diversity of mechanical states achieved, providing different representations. However, it is suggested that major and minor strains are always used, because they can be directly calculated from experiments. The last metric is proposed to evaluate the range of anisotropy that can be characterized from a single test. Also, the use of three virtual materials is considered in the analysis. This has shown the importance of evaluating the tests for different materials, as the results can vary. Finally, the study has shown that these can be suitable metrics to qualitatively evaluate and compare heterogeneous mechanical tests, without the complexity of quantitative indicators.

Concerning the inverse methodologies, optimization algorithms are transversal to most of them, but studies often overlook its importance. Often, studies tend to use a gradient-based least squares algorithm without exploring other possibilities. Thus, the following study evaluated the use of different optimization algorithms within the finite element model updating (FEMU). The FEMU was implemented using Python and Fortran programming languages, by combining the benefits of both. Also, by using the optimization library within Python, three optimization algorithms were employed in the calibration of a thermoelastoviscoplastic model, namely the Levenberg-Marquardt (LM), the Nelder-Mead (NM), and the Differential Evolution (DE) algorithms. Artificial noise was introduced in the numerical data to evaluate the robustness of the algorithms. The results showed that the most robust algorithm is the DE algorithm. However, the latter requires many function evaluations, leading to a high computational cost. The LM and NM algorithms are more computationally efficient, but often are not able to achieve the best solution. Their robustness can be improved by considering a multiple starting approach. Although it was not explored in this study, the best methodology could be to combine the DE algorithm with either the LM or the NM algorithms in a sequential approach.

Then, it was intended to investigate the use of the virtual fields method (VFM) up to rupture. However, a few studies dealing with the VFM in a 2D framework have shown that after necking, the validity of the VFM is compromised, leading to inaccurate descriptions of the material hardening behavior. This study highlighted that the cause of deviations in the VFM was due to the appearance of a triaxial stress state in the necking region. They have suggested to extend the VFM to a 3D

framework. However, the VFM requires the input of the experimental strain field, which is limited to the specimen surface.

To circumvent the latter limitation, a numerical method, named internal mesh generation (IMG), was proposed a few years ago to reconstruct the volume displacement field inside a solid material. This method, which only uses surface measurements, is purely based on geometrical considerations, and showed a great potential. However, only a few studies investigated it, and its uncertainty was not yet fully quantified. For that reason, a study was performed with the intent to estimate the error resulting from the application of the IMG. Initially, the reconstructed strain field of a plane strain tensile test was compared with the reference from FEA simulations. The results showed that there was a good agreement between the reference and the reconstructed field. However, a limitation of the method to accurately reconstruct the strain field through the thickness was identified when large strain gradients are observed. To solve this limitation and further improve the method, two strategies were proposed. The first one corrects the global volume, leading to, on average, more accurate strain values. The second one corrects the local volume, which is the volume of each element, by adjusting the position of nodes through the thickness. It has been shown that combining both strategies leads to the best results. The latter improves the reconstruction of the normal strain components, particularly the through-thickness gradient of the strain tensor component ε_{zz}. This study only deals with numerical data, but the final aim is to apply the IMG to real experiments. Thus, it was attempted to estimate the uncertainty of the method under different experimental conditions and varying DIC settings. A design of experiments was carried out with five factors using virtual experiments from a dedicated software. The results showed that the investigated factors have a relatively low influence, meaning the error is mainly from the IMG itself.

Thanks to the IMG, it will be possible to use the VFM in a 3D framework with real experiments, which is a great advance. A fully numerical study to investigate the limitations of the VFM in 2D framework, and consequently, the advantages of a 3D framework, is performed. Particularly, the influence of the materials thickness was analyzed regarding, at first, the evolution of the predicted load, and afterward, the identification of the material parameters of the Swift hardening law. In the first part, the evolution of the predicted load using the reference parameters was compared to the one obtained from the FEA simulations. For the 3D-VFM, the relative error was negligible, accurately predicting the evolution of the load. However, using the 2D-VFM resulted in non-negligible relative errors after necking, showing that the error is proportional to the thickness. The source of error was related to non-negligible out-of-plane stress components and the considerable differences between the stress values at the surface and inside the material. In the second part, the identification of the Swift law was carried out using different combinations of three manually defined virtual fields. While two of them are commonly used in other 2D applications, a third one specific to 3D was extended from the 2D one. Although the material parameters identified with the 2D-VFM did not match the reference parameters, the 3D-VFM was able to correctly identify them in every instance. The purpose of this study was to explore the potential benefits of using the VFM in a 3D framework. It is expected that future studies will build on the findings of this research.

Generically, this thesis has contributed to the three main pillars of parameter identification of constitutive models for metallic sheets, and has demonstrated how important it is to consider all of them as part of the entire process. Nevertheless, the field of parameter identification in the paradigm of “Material Testing 2.0” is fairly wide and relatively recent, as proven by the variety of studies here presented. Consequently, some topics lack clear standards or are still underdeveloped. Thus, it is expected that further research leads to clear standards to convince more communities of its advantages. Finally, even though the studies here presented only included numerical data, it is hoped that these can be extended to real experiments in the future.

8.2 Perspectives of Future Studies

Considering the studies developed in this thesis, it is expected that the field of parameter identification of constitutive models will continue to receive more attention from scientific and industrial communities. Therefore, some perspectives of future studies may be outlined. Additionally, several computational tools developed within this thesis are available open source and can be used as a basis for future studies. The following points represent ideas and suggestions for future studies:

- The investigation of the UMMDp has led to its validation and spread across the scientific community. The large range of models it includes can be a great tool for various studies, reducing the arduous task of model implementation. Nevertheless, it is expected that the UMMDp will be enlarged with models from the community and continuously shared. Particularly, it is expected to extend it with thermoelastoviscoplastic models. Moreover, the UMMDp can be the starting point for research studies, leading to better model selection;

- Following the overview and evaluation of heterogeneous mechanical tests, it is suggested to clearly define ways to compare and evaluate heterogeneous mechanical tests. In the future, more tests will be designed with even more innovative methodologies. Therefore, it will be important to dedicate time and effort to the definition of standard metrics, allowing them to easily compare and even rank different tests. Additionally, if different research groups agree to such metrics, it could lead to easier adoption, as well as cultivating a sense of healthy competition. As a suggestion, this discussion could be initiated through informal sessions organized within international conferences;

- Concerning the IMG, its potential to reconstruct the strain field inside the materials has been shown. However, this study was purely numerical and must be extended for real experiments to consolidate its potential. Although not included in this thesis, real experiments of the DP780 dual-phase steel have already been performed and are expected to be included in future studies. Nevertheless, the IMG should be applied to different materials of varying thickness to understand its robustness. In addition, the method can be further improved by integrating measurements of the four surfaces, which are the front, the back and the sides. Moreover, it is expected to use the IMG in combination with inverse methodologies, in particular with the VFM, to characterize the material behavior up to rupture. A starting point could be the use of reconstructed fields from virtual experiments, and then continue with real experiments;

- Some limitations of the 2D-VFM comparatively to the 3D-VFM have been identified when dealing with large deformations up to rupture and larger material thicknesses. However, this study can still be considered preliminary, creating the path for more research about this topic. To avoid general assumptions and conclusions based on a single study, it is suggested to investigate the 3D effects of different materials, particularly with a more predominant out-of-plane stress field.

- Furthermore, the VFM code developed within this thesis can be the basis for future studies, in particular extending the sensitivity-based virtual fields to a 3D framework.

Bibliography

Abedini A, Butcher C, Rahmaan T, Worswick MJ. Evaluation and calibration of anisotropic yield criteria in shear loading: Constraints to eliminate numerical artefacts. *International Journal of Solids and Structures*, 151:118–134, 2018.

Adams V, Askenazi A. *Building Better Products with Finite Element Analysis*. OnWord Press, Santa Fe, NM, USA, 1999.

ADINA R&D. *ADINA Theory and Modeling Guide*. ADINA R&D, Inc, Watertown, MA, USA, 2021.

An YG, Vegter H, Elliott L. A novel and simple method for the measurement of plane strain work hardening. *Journal of Materials Processing Technology*, 155-156:1616–1622, 2004.

Andrade-Campos A, Thuillier S, Pilvin P, Teixeira-Dias F. On the determination of material parameters for internal variable thermoelastic–viscoplastic constitutive models. *International Journal of Plasticity*, 23(8):1349–1379, 2007.

Andrade-Campos A, de-Carvalho R, Valente RAF. Novel criteria for determination of material model parameters. *International Journal of Mechanical Sciences*, 54(1):294–305, 2012.

Andrade-Campos A, Bastos N, Conde M, Gonçalves M, Aquino J, Lourenço R, Martins JMP, Oliveira MG, Prates P, Rumor L. On the inverse identification methods for forming plasticity models using full-field measurements. *IOP Conference Series: Materials Science and Engineering*, 1238(1):012059, 2022.

ANSYS, Inc. *Ansys Mechanical User's Guide*. ANSYS, Inc., Canonsburg, PA, USA, 2021.

Aquino J, Andrade-Campos A, Martins JMP, Thuillier S. Design of heterogeneous mechanical tests: Numerical methodology and experimental validation. *Strain*, 55(4):e12313, 2019.

Avril S, Huntley JM, Pierron F, Steele DD. 3D Heterogeneous stiffness reconstruction using MRI and the virtual fields method. *Experimental Mechanics*, 48(4):479–494, 2008.

Avril S, Bonnet M, Bretelle AS, Grédiac M, Hild F, Ienny P, Latourte F, Lemosse D, Pagano S, Pagnacco E, Pierron F. Overview of identification methods of mechanical parameters based on full-field measurements. *Experimental Mechanics*, 48(4):381–402, 2008.

Avril S, Pierron F, Pannier Y, Rotinat R. Stress reconstruction and constitutive parameter identification in plane-stress elasto-plastic problems using surface measurements of deformation fields. *Experimental Mechanics*, 48(4):403–419, 2008.

Badel P, Genovese K, Avril S. 3D residual stress field in arteries: Novel inverse method based on optical full-field measurements. *Strain*, 48(6):528–538, 2012.

Bai Y, Wierzbicki T. A new model of metal plasticity and fracture with pressure and Lode dependence. *International Journal of Plasticity*, 24(6):1071–1096, 2008.

Balcaen R, Wittevrongel L, Reu PL, Lava P, Debruyne D. Stereo-DIC calibration and speckle image generator based on FE formulations. *Experimental Mechanics*, 57(5):703–718, 2017.

Balcaen R, Reu PL, Lava P, Debruyne D. Stereo-DIC uncertainty quantification based on simulated images. *Experimental Mechanics*, 57(6):939–951, 2017.

Banabic D. *Sheet Metal Forming Processes: Constitutive Modelling and Numerical Simulation*. Springer, Berlin, Germany, 2010.

Banabic D, Barlat F, Cazacu O, Kuwabara T. Advances in anisotropy of plastic behaviour and formability of sheet metals. *International Journal of Material Forming*, 13(5):749–787, 2020.

Barlat F, Brem JC, Yoon JW, Chung K, Dick RE, Lege DJ, Pourboghrat F, Choi SH, Chu E. Plane stress yield function for aluminum alloy sheets-part 1: Theory. *International Journal of Plasticity*, 19:1297–1319, 2003.

Barlat F, Aretz H, Yoon JW, Karabin ME, Brem JC, Dick RE. Linear transfomation-based anisotropic yield functions. *International Journal of Plasticity*, 21(5):1009–1039, 2005.

Barroqueiro B, Andrade-Campos A, Dias-de-Oliveira J, Valente RAF. Design of mechanical heterogeneous specimens using topology optimization. *International Journal of Mechanical Sciences*, 181:105764, 2020.

Bay BK, Smith TS, Fyhrie DP, Saad M. Digital volume correlation: Three-dimensional strain mapping using x-ray tomography. *Experimental Mechanics*, 39:217–226, 1999.

Bayoumi AE, Joshi R. On the formabllity/instability of stretch-forming sheet metals. *Applied Mechanics Reviews*, 45(3):S154–S164, 1992.

Belhabib S, Haddadi H, Gaspérini M, Vacher P. Heterogeneous tensile test on elastoplastic metallic sheets: comparison between FEM simulations and full-field strain measurements. *International Journal of Mechanical Sciences*, 50(1):14–21, 2008.

Blaysat B, Neggers J, Grédiac M, Sur F. Towards criteria characterizing the metrological performance of full-field measurement techniques. *Experimental Mechanics*, 60(3):393–407, 2020.

Boger RK, Wagoner RH, Barlat F, Lee MG, Chung K. Continuous, large strain, tension/compression testing of sheet material. *International Journal of Plasticity*, 21(12):2319–2343, 2005.

Bridgman PW. *Studies in Large Plastic Flow and Fracture: With Special Emphasis on the Effects of Hydrostatic Pressure*. McGraw Hill, New York, NY, USA, 1952.

Brosius A, Yin Q, Güner A, Tekkaya AE. A new shear test for sheet metal characterization. *steel research international*, 82(4):323–328, 2011.

Buljac A, Jailin C, Mendoza A, Neggers J, Taillandier-Thomas T, Bouterf A, Smaniotto B, Hild F, Roux S. Digital volume correlation: Review of progress and challenges. *Experimental Mechanics*, 58(5):661–708, 2018.

Cao J, Lin J. A study on formulation of objective functions for determining material models. *International Journal of Mechanical Sciences*, 50(2):193–204, 2008.

Carbonnière J, Thuillier S, Sabourin F, Brunet M, Manach PY. Comparison of the work hardening of metallic sheets in bending–unbending and simple shear. *International Journal of Mechanical Sciences*, 51(2):122–130, 2009.

de-Carvalho R, Valente RAF, Andrade-Campos A. Optimization strategies for non-linear material parameters identification in metal forming problems. *Computers & Structures*, 89(1):246–255, 2011.

Cazacu O, Plunkett B, Barlat F. Orthotropic yield criterion for hexagonal closed packed metals. *International Journal of Plasticity*, 22(7):1171–1194, 2006.

Chaboche JL. Time-independent constitutive theories for cyclic plasticity. *International Journal of Plasticity*, 2(2):149–188, 1986.

Chamoin L, Jailin C, Diaz M, Quesada L. Coupling between topology optimization and digital image correlation for the design of specimen dedicated to selected material parameters identification. *International Journal of Solids and Structures*, 193-194:270–286, 2020.

Chapelier M, Bouclier R, Passieux J. Spline-based specimen shape optimization for robust material model calibration. *Advanced Modeling and Simulation in Engineering Sciences*, 9(1):4, 2022.

Coelho B, Andrade-Campos A, Martins JMP, Silva T, Thuillier S. Inverse identification processes of elastoplastic constitutive models using advanced optimisation strategies. *Proceedings of NUMIFORM 2019: The 13th International Conference on Numerical Methods in Industrial Forming Processes*, Portsmouth, NH, USA, 23–27 June, 2019.

Coelho B, Thuillier S. On the use of the Gleeble® test as a heterogeneous test: sensitivity analysis on temperature, strain and strain rate. *IOP Conference Series: Materials Science and Engineering*, 1238(1):012058, 2022.

Coër J, Bernard C, Laurent H, Andrade-Campos A, Thuillier S. The effect of temperature on anisotropy properties of an aluminium alloy. *Experimental Mechanics*, 51(7):1185–1195, 2011.

Comsa DS, Paraianu L, Bichis I, Banabic D. A new formulation of the MMFC to avoid the numerical instability. *Proceedings of the 4th Forming Technology Forum*, Zurich, Switzerland, 17–18 May, 2011.

Conde M, Oliveira MG, Martins JMP, Andrade-Campos A. Design of heterogeneous interior notched specimens for material mechanical characterization. *Proceedings of the 24th International ESAFORM Conference on Material Forming*, Liège, Belgium, 14–16 April, 2021.

Conde M, Henriques J, Coppieters S, Andrade-Campos A. Parameter identification of Swift law using a FEMU-based approach and an innovative heterogeneous mechanical test. *Key Engineering Materials*, 926:2238–2246, 2022.

Cooreman S, Lecompte D, Sol H, Vantomme J, Debruyne D. Elasto-plastic material parameter identification by inverse methods: Calculation of the sensitivity matrix. *International Journal of Solids and Structures*, 44(13):4329–4341, 2007.

Cooreman S, Lecompte D, Sol H, Vantomme J, Debruyne D. Identification of mechanical material behavior through inverse modeling and DIC. *Experimental Mechanics*, 48(4):421–433, 2008.

Cooreman S. *Identification of the plastic material behaviour through full-field displacement measurements and inverse methods*. Doctoral Thesis, Vrije Universiteit Brussel, 2008.

Coppieters S, Cooreman S, Sol H, Van Houtte P, Debruyne D. Identification of the post-necking hardening behaviour of sheet metal by comparison of the internal and external work in the necking zone. *Journal of Materials Processing Technology*, 211(3):545–552, 2011.

Coppieters S, Kuwabara T. Identification of post-necking hardening phenomena in ductile sheet metal. *Experimental Mechanics*, 54(8):1355–1371, 2014.

Coppieters S, Kim JH, Denys K, Cooreman S, Debruyne D. On complete solutions for the problem of diffuse necking in sheet metal. *Procedia Engineering*, 207:2012–2017, 2017.

Danas K, Ponte Castañeda P. Influence of the Lode parameter and the stress triaxiality on the failure of elasto-plastic porous materials. *International Journal of Solids and Structures*, 49(11):1325–1342, 2012.

Dassault Systémes. *Abaqus 6.14 Analysis User's Guide*. Dassault Systèmes Simulia Corp., Providence, RI, USA, 2014.

Dassault Systèmes. *Abaqus/Standard*. v2019, 2019.

de Borst R, Crisfield MA, Remmers JJC, Verhoosel CV. *Non-Linear Finite Element Analysis of Solids and Structures*. John Wiley & Sons, Chichester, West Sussex, UK, 2012.

de Souza Neto EA, Perić D, Owen DRJ. *Computational Methods for Plasticity: Theory and Applications*. John Wiley & Sons, Chichester, West Sussex, UK, 2008.

Denys K, Coppieters S, Seefeldt M, Debruyne D. Multi-DIC setup for the identification of a 3D anisotropic yield surface of thick high strength steel using a double perforated specimen. *Mechanics of Materials*, 100:96–108, 2016.

Dunand M, Mohr D. Hybrid experimental–numerical analysis of basic ductile fracture experiments for sheet metals. *International Journal of Solids and Structures*, 47(9):1130–1143, 2010.

Dunne F, Petrinic N. *Introduction to Computational Plasticity*. Oxford University Press, New York, NY, USA, 2005.

Elton D. *Why physicists still use Fortran*. moreisdifferent.com, http://www.moreisdifferent.com/2015/07/16/why-physicsts-still-use-fortran, 2015.

Erice B, Roth CC, Mohr D. Stress-state and strain-rate dependent ductile fracture of dual and complex phase steel. *Mechanics of Materials*, 116:11–32, 2018.

Farnam Street. *Multiplicative Systems: Understanding The Power of Multiplying by Zero*. fs.blog, https://fs.blog/multiplicative-systems/, 2016.

Forsström A, Bossuyt S, Scotti G, Hänninen H. Quantifying the effectiveness of patterning, test conditions, and DIC parameters for characterization of plastic strain localization. *Experimental Mechanics*, 60(1):3–12, 2020.

Frederick CO, Armstrong PJ. A mathematical representation of the multiaxial Bauschinger effect. *Materials at High Temperatures*, 24(1):1–26, 2007.

Fu J, Xie W, Zhou J, Qi L. A method for the simultaneous identification of anisotropic yield and hardening constitutive parameters for sheet metal forming. *International Journal of Mechanical Sciences*, 181:105756, 2020.

Fu J, Zhu K, Nie X, Tang Y, Yang Z, Qi L. Inertia-based identification of elastic anisotropic properties for materials undergoing dynamic loadings using the virtual fields method and heterogeneous impact tests. *Materials & Design*, 203:109594, 2021.

Gao F, Han L. Implementing the Nelder-Mead simplex algorithm with adaptive parameters. *Computational Optimization and Applications*, 51(1):259–277, 2012.

Genovese K, Cortese L, Rossi M, Amodio D. A 360-deg digital image correlation system for materials testing. *Optics and Lasers in Engineering*, 82:127–134, 2016.

Gilles G, Hammami W, Libertiaux V, Cazacu O, Yoon JH, Kuwabara T, Habraken AM, Duchêne L. Experimental characterization and elasto-plastic modeling of the quasi-static mechanical response of TA-6V at room temperature. *International Journal of Solids and Structures*, 48(9):1277–1289, 2011.

Goga V. New specimen for determination of the state of plane stress. *Applied Mechanics and Materials*, 486:227–232, 2014.

Gonçalves M, Andrade-Campos A, Thuillier S. On the topology design of a mechanical heterogeneous specimen using geometric and material nonlinearities. *IOP Conference Series: Materials Science and Engineering*, 1238(1):012055, 2022.

Grédiac M, Pierron F, Avril S, Toussaint E. The virtual fields method for extracting constitutive parameters from full-field measurements: A review. *Strain*, 42(4):233–253, 2006.

Grédiac M, Hild F. *Full-Field Measurements and Identification in Solid Mechanics*. John Wiley & Sons, Hoboken, NJ, USA, 2012.

Grédiac M, Blaysat B, Sur F. On the optimal pattern for displacement field measurement: Random speckle and DIC, or checkerboard and LSA? *Experimental Mechanics*, 60(4):509–534, 2020.

Grilo TJ, Souto N, Valente RAF, Andrade-Campos A, Thuillier S, de Sousa RJA. On the development and computational implementation of complex constitutive models and parameters' identification procedures. *Key Engineering Materials*, 554-557:936–948, 2013.

Grilo TJ. *Development of computational anisotropic hypoelastic- and hyperelastic-based models including nonlinear kinematic hardening*. Doctoral Thesis, Universidade de Aveiro, 2015.

Grilo TJ, Vladimirov IN, Valente RAF, Reese S. On the modelling of complex kinematic hardening and nonquadratic anisotropic yield criteria at finite strains: application to sheet metal forming. *Computational Mechanics*, 57(6):931–946, 2016.

Güner A, Soyarslan C, Brosius A, Tekkaya AE. Characterization of anisotropy of sheet metals employing inhomogeneous strain fields for Yld2000-2D yield function. *International Journal of Solids and Structures*, 49(25):3517–3527, 2012.

Ha GX, Oliveira MG, Andrade-Campos A, Manach PY, Thuillier S. Prediction of coupled 2D and 3D effects in springback of copper alloys after deep drawing. *International Journal of Material Forming*, 14(5):1171–1187, 2021.

Haddadi H, Belhabib S. Improving the characterization of a hardening law using digital image correlation over an enhanced heterogeneous tensile test. *International Journal of Mechanical Sciences*, 62(1):47–56, 2012.

Hannon A, Tiernan P. A review of planar biaxial tensile test systems for sheet metal. *Journal of Materials Processing Technology*, 198(1):1–13, 2008.

Hapsari G, Richard F, Ben Hmida R, Malécot P, Thibaud S. Instrumented incremental sheet testing for material behavior extraction under very large strain: Information richness of continuous force measurement. *Materials & Design*, 140:317–331, 2018.

Hencky H. Zur theorie plastischer deformationen und der hierdurch im material hervorgerufenen nachspannungen. *Zamm-zeitschrift Fur Angewandte Mathematik Und Mechanik*, 4:323–334, 1924.

Henriques J, Xavier J, Andrade-Campos A. Identification of orthotropic elastic properties of wood by a synthetic image approach based on digital image correlation. *Materials*, 15(2):625, 2022.

Hill R. A theory of the yielding and plastic flow of anisotropic metals. *Proceedings of the Royal Society of London. Series A. Mathematical and Physical Sciences*, 193(1033):281–297, 1948.

Hill R. On discontinuous plastic states, with special reference to localized necking in thin sheets. *Journal of the Mechanics and Physics of Solids*, 1(1):19–30, 1952.

Hill R. Constitutive modelling of orthotropic plasticity in sheet metals. *Journal of the Mechanics and Physics of Solids*, 38(3):405–417, 1990.

Hill R. On the mechanics of localized necking in anisotropic sheet metals. *Journal of the Mechanics and Physics of Solids*, 49:2055–2070, 2001.

Huber MT. Przyczynek do podstaw wytorymalosci. *Czasopismo Techniczne*, 22:34–81, 1904.

Hutchinson JW, Miles JP. Bifurcation analysis of the onset of necking in an elastic/plastic cylinder under uniaxial tension. *Journal of the Mechanics and Physics of Solids*, 22(1):61–71, 1974.

Ida T, Takizawa H, Kuwabara T. Development of plug-ins for bridging variables between advanced finite element codes and 'UMMDp'. *Journal of Physics: Conference Series*, 1063:012100, 2018.

Inoue T, Takizawa H, Kuwabara T. Practical examples of sheet metal forming simulations using the subroutine library 'UMMDp'. *Journal of Physics: Conference Series*, 1063:012102, 2018.

Johnson GR, Cook WH. A constitutive model and data for materials subjected to large strains, high strain rates, and high temperatures. *Proceedings of the 7th International Symposium on Ballistics*, The Hague, Netherlands, 19–21 April, 1983.

Jones EMC, Carroll JD, Karlson KN, Kramer SLB, Lehoucq RB, Reu PL, Turner DZ. Parameter covariance and non-uniqueness in material model calibration using the virtual fields method. *Computational Materials Science*, 152:268–290, 2018.

Jones EMC, Karlson KN, Reu PL. Investigation of assumptions and approximations in the virtual fields method for a viscoplastic material model. *Strain*, 55(4):e12309, 2019.

Jones EMC, Iadicola MA (Eds.). *A Good Practices Guide for Digital Image Correlation*. International Digital Image Correlation Society, 2018.

Kacem A, Laurent H, Thuillier S. Influence of experimental boundary conditions on the calibration of a ductile fracture criterion. *Engineering Fracture Mechanics*, 248:107686, 2021.

Kajberg J, Lindkvist G. Characterisation of materials subjected to large strains by inverse modelling based on in-plane displacement fields. *International Journal of Solids and Structures*, 41(13):3439–3459, 2004.

Kajberg J, Wikman B. Viscoplastic parameter estimation by high strain-rate experiments and inverse modelling – Speckle measurements and high-speed photography. *International Journal of Solids and Structures*, 44(1):145–164, 2007.

Karbasian H, Tekkaya AE. A review on hot stamping. *Journal of Materials Processing Technology*, 210(15):2103–2118, 2010.

Kavanagh KT, Clough RW. Finite element applications in the characterization of elastic solids. *International Journal of Solids and Structures*, 7(1):11–23, 1971.

Keeler SP. *Plastic instability and fracture in sheets stretched over rigid punches*. Doctoral Thesis, Massachusetts Institute of Technology, 1961.

Kim JH, Serpantié A, Barlat F, Pierron F, Lee MG. Characterization of the post-necking strain hardening behavior using the virtual fields method. *International Journal of Solids and Structures*, 50(24):3829–3842, 2013.

Kim JH, Barlat F, Pierron F, Lee MG. Determination of anisotropic plastic constitutive parameters using the virtual fields method. *Experimental Mechanics*, 54(7):1189–1204, 2014.

Kim M, Ha J, Bonica S, Korkolis YP. Design of a new cruciform-like specimen for combined tension and shear of metal sheets. In: Daehn G, Cao J, Kinsey B, Tekkaya E, Vivek A, Yoshida Y (Eds.). *Forming the Future*. The Minerals, Metals & Materials Series, Springer, Cham, Switzerland, 2021.

Kim M, Ha J, Korkolis YP. Shape optimization of a cruciform-like specimen for combined tension and shear loading. In: Inal K, Levesque J, Worswick M, Butcher C (Eds.). *NUMISHEET 2022*. The Minerals, Metals & Materials Series, Springer, Cham, Switzerland, 2022.

Kiran R, Khandelwal K. A triaxiality and Lode parameter dependent ductile fracture criterion. *Engineering Fracture Mechanics*, 128:121–138, 2014.

Koc P, Štok B. Computer-aided identification of the yield curve of a sheet metal after onset of necking. *Computational Materials Science*, 31(1):155–168, 2004.

Kowalewski Ł, Gajewski M. Assessment of optimization methods used to determine plasticity parameters based on DIC and back calculation methods. *Experimental Techniques*, 43(4):385–396, 2019.

Küsters N, Brosius A. Damage characterization on heterogeneous tensile tests. *Procedia Manufacturing*, 29:458–463, 2019.

Kuwabara T, Ikeda S, Kuroda K. Measurement and analysis of differential work hardening in cold-rolled steel sheet under biaxial tension. *Journal of Materials Processing Technology*, 80-81:517–523, 1998.

Lankford WT, Snyder SC, Bauscher JA. New criteria for predicting the press performance of deep-drawing sheets. *Transactions of the American Society of Metals*, 42:1197–1232, 1950.

Lattanzi A, Barlat F, Pierron F, Marek A, Rossi M. Inverse identification strategies for the characterization of transformation-based anisotropic plasticity models with the non-linear VFM. *International Journal of Mechanical Sciences*, 173:105422, 2020.

Lava P, Cooreman S, Coppieters S, De Strycker M, Debruyne D. Assessment of measuring errors in DIC using deformation fields generated by plastic FEA. *Optics and Lasers in Engineering*, 47(7):747–753, 2009.

Lava P, Cooreman S, Debruyne D. Study of systematic errors in strain fields obtained via DIC using heterogeneous deformation generated by plastic FEA. *Optics and Lasers in Engineering*, 48(4):457–468, 2010.

Lava P, Jones EMC, Wittevrongel L, Pierron F. Validation of finite-element models using full-field experimental data: Levelling finite-element analysis data through a digital image correlation engine. *Strain*, 56(4):12350, 2020.

Levenberg K. A method for the solution of certain non-linear problems in least squares. *Quarterly of Applied Mathematics*, 2(2):164–168, 1944.

Li J, Xie X, Yang G, Zhang B, Siebert T, Yang L. Whole-field thickness strain measurement using multiple camera digital image correlation system. *Optics and Lasers in Engineering*, 90:19–25, 2017.

Lin J, Cheong BH, Yao X. Universal multi-objective function for optimising superplastic-damage constitutive equations. *Journal of Materials Processing Technology*, 125-126:199–205, 2002.

Liu W, Guines D, Leotoing L, Ragneau E. Identification of sheet metal hardening for large strains with an in-plane biaxial tensile test and a dedicated cross specimen. *International Journal of Mechanical Sciences*, 101-102:387–398, 2015.

Livermore Software Technology. *LS DYNA Keywords User's Manual*. Livermore Software Technology, Livermore, CA, USA, 2021.

Logan RW, Hosford WF. Upper-bound anisotropic yield locus calculations assuming <111> -pencil glide. *International Journal of Mechanical Sciences*, 22(7):419–430, 1980.

Maček A, Starman B, Mole N, Halilovič M. Calibration of advanced yield criteria using uniaxial and heterogeneous tensile test data. *Metals*, 10(4):542, 2020.

Makinde A, Thibodeau L, Neale KW. Development of an apparatus for biaxial testing using cruciform specimens. *Experimental Mechanics*, 32(2):138–144, 1992.

Marchand WR. *The Rising Popularity of Python*. pythoncircle.com, https://pythoncircle.com/post/763/the-rising-popularity-of-python/, 2022.

Marek A, Davis FM, Pierron F. Sensitivity-based virtual fields for the non-linear virtual fields method. *Computational Mechanics*, 60(3):409–431, 2017.

Marek A, Davis FM, Rossi M, Pierron F. Extension of the sensitivity-based virtual fields to large deformation anisotropic plasticity. *International Journal of Material Forming*, 12(3):457–476, 2019.

Marek A, Davis FM, Kim JH, Pierron F. Experimental validation of the sensitivity-based virtual fields for identification of anisotropic plasticity models. *Experimental Mechanics*, 60(5):639–664, 2020.

Markiewicz E, Langrand B, Notta-Cuvier D. A review of characterisation and parameters identification of materials constitutive and damage models: From normalised direct approach to most advanced inverse problem resolution. *International Journal of Impact Engineering*, 110:371–381, 2017.

Marquardt DW. An algorithm for least-squares estimation of nonlinear parameters. *Journal of the Society for Industrial and Applied Mathematics*, 11(2):431–441, 1963.

Martins JMP, Andrade-Campos A, Thuillier S. Comparison of inverse identification strategies for constitutive mechanical models using full-field measurements. *International Journal of Mechanical Sciences*, 145:330–345, 2018.

Martins JMP, Thuillier S, Andrade-Campos A. Identification of material parameters for plasticity models: A comparative study on the finite element model updating and the virtual fields method. *AIP Conference Proceedings*, 1960:110007, 2018.

Martins JMP, Andrade-Campos A, Thuillier S. Calibration of anisotropic plasticity models using a biaxial test and the virtual fields method. *International Journal of Solids and Structures*, 172-173:21–37, 2019.

Martins JMP, Thuillier S, Andrade-Campos A. Calibration of anisotropic plasticity models with an optimized heterogeneous test and the virtual fields method. In: Baldi A, Kramer SLB, Pierron F, Considine J, Bossuyt S, Hoefnagels J (Eds.). *Residual Stress, Thermomechanics & Infrared Imaging and Inverse Problems*, Volume 6. Conference Proceedings of the Society for Experimental Mechanics Series, Springer, Cham, Switzerland, 2020.

Martins JMP, Andrade-Campos A, Thuillier S. Calibration of Johnson-Cook model using heterogeneous thermo-mechanical tests. *Procedia Manufacturing*, 47:881–888, 2020.

Martins JMP, Thuillier S, Andrade-Campos A. Calibration of a modified Johnson-Cook model using the virtual fields method and a heterogeneous thermo-mechanical tensile test. *International Journal of Mechanical Sciences*, 202-203:106511, 2021.

Mason RL, Gunst RF, Hess JL. *Statistical Design and Analysis of Experiments: With Applications to Engineering and Science*. John Wiley & Sons, New York, NY, USA, 1979.

MatchID. *MatchID*. v2022.1.2, 2022.

MatchID. *MatchID FEA Converter*. v2022.1.0, 2022.

MatchID. *MatchID FEDEF*. v2022.1.2, 2022.

MatchID. *MatchID Stereo*. v2022.1.2, 2022.

MatchID. *MatchID VFM*. v2022.1.2, 2022.

McKay MD, Beckman RJ, Conover WJ. A comparison of three methods for selecting values of input variables in the analysis of output from a computer code. *Technometrics*, 21(2):239–245, 1979.

Meuwissen MHH. *An inverse method for the mechanical characterisation of metals*. Doctoral Thesis, Technische Universiteit Eindhoven, 1998.

Meuwissen MHH, Oomens CWJ, Baaijens FPT, Petterson R, Janssen JD. Determination of the elasto-plastic properties of aluminium using a mixed numerical-experimental method. *Journal of Materials Processing Technology*, 75:204–211, 1998.

Mirone G. A new model for the elastoplastic characterization and the stress-strain determination on the necking section of a tensile specimen. *International Journal of Solids and Structures*, 41(13):3545–3564, 2004.

Moré JJ. The Levenberg-Marquardt algorithm: Implementation and theory. *Proceedings of the 7th Dundee Biennial Conference on Numerical Analysis*, Dundee, Scotland, 28 June – 1 July, 1978.

Moré JJ, Sorensen DC, Hillstrom KE, Garbow BS. The MINPACK Project. In: Cowell WJ (Ed.). *Sources and Development of Mathematical Software*. Prentice-Hall Series in Computational Mathematics, Prentice-Hall, Englewood Cliffs, NJ, USA, 1984.

Nelder JA, Mead R. A simplex method for function minimization. *The Computer Journal*, 7(4):308–313, 1965.

Nichols FA. Plastic instabilities and uniaxial tensile ductilities. *Acta Metallurgica*, 28(6):663–673, 1980.

Notta-Cuvier D, Langrand B, Markiewicz E, Lauro F, Portemont G. Identification of Johnson-Cook's viscoplastic model parameters using the virtual fields method: Application to titanium alloy Ti6Al4V. *Strain*, 49(1):22–45, 2013.

Notta-Cuvier D, Langrand N, Lauro F, Markiewicz E. An innovative procedure for characterising a coupled elastoplastic damage model of behaviour using the virtual fields method. *International Journal of Solids and Structures*, 69-70:415–427, 2015.

NumPy. *F2PY user guide and reference manual — NumPy v1.23 Manual*. numpy.org, https://numpy.org/doc/stable/f2py/#f2py-user-guide-and-reference-manual, 2022.

Numpy. *numpy.linalg.svd — NumPy v1.23 Manual*. numpy.org, https://numpy.org/doc/stable/reference/generated/numpy.linalg.svd.html, 2022.

Oide K, Takizawa H, Kuwabara T. Implementation of anisotropic yield functions into the subroutine library "UMMDp". *Journal of Physics: Conference Series*, 1063:012101, 2018.

Oliveira MG. *On the use of advanced optimization methods in mechanical design*. Master Thesis, Universidade de Aveiro, 2018.

Oliveira MG, Thuillier S, Andrade-Campos A. Analysis of heterogeneous tests for sheet metal mechanical behavior. *Procedia Manufacturing*, 47:831–838, 2020.

Oliveira MG, Martins JMP, Coelho B, Thuillier S, Andrade-Campos A. On the optimisation efficiency for the inverse identification of constitutive model parameters. *Proceedings of the 24th International ESAFORM Conference on Material Forming*, Liège, Belgium, 14–16 April, 2021.

Oliveira MG, Lattanzi A, Thuillier S, Andrade-Campos A, Rossi M. Error estimation of the 3D reconstruction of a displacement field from DIC measurements. *Key Engineering Materials*, 926:2129–2136, 2022.

Oliveira MG, Thuillier S, Andrade-Campos A. Evaluation of heterogeneous mechanical tests for model calibration of sheet metals. *Journal of Strain Analysis for Engineering Design*, 57(3):208–224, 2022.

Ozturk F, Toros S, Kilic S. Effects of anisotropic yield functions on prediction of forming limit diagrams of DP600 advanced high strength steel. *Procedia Engineering*, 81:760–765, 2014.

Paul SK, Manikandan G, Verma RK. Prediction of entire forming limit diagram from simple tensile material properties. *The Journal of Strain Analysis for Engineering Design*, 48(6):386–394, 2013.

Paul SK. Theoretical analysis of strain- and stress-based forming limit diagrams. *Journal of Strain Analysis for Engineering Design*, 48(3):177–188, 2013.

Peterson P. F2PY: a tool for connecting Fortran and Python programs. *International Journal of Computational Science and Engineering*, 4(4):296–305, 2009.

Pham CH, Thuillier S, Manach PY. Experimental and numerical investigation of the formability of an ultra-thin copper sheet. *Journal of Physics: Conference Series*, 896(1):012109, 2017.

Pierron F, Avril S, Tran VT. Extension of the virtual fields method to elasto-plastic material identification with cyclic loads and kinematic hardening. *International Journal of Solids and Structures*, 47(22):2993–3010, 2010.

Pierron F, Grédiac M. *The Virtual Fields Method: Extracting Constitutive Mechanical Parameters from Full-field Deformation Measurements*. Springer, New York, NY, USA, 2012.

Pierron F. Test design for identification from full-field measurements: A concise review. In: Baldi A, Kramer SL, Pierron F, Considine J, Bossuyt S, Hoefnagels J (Eds.). *Residual Stress, Thermomechanics & Infrared Imaging and Inverse Problems*, Volume 6. Conference Proceedings of the Society for Experimental Mechanics Series, Springer, Cham, Switzerland, 2020.

Pierron F, Grédiac M. Towards material testing 2.0. A review of test design for identification of constitutive parameters from full-field measurements. *Strain*, 57(1):e12370, 2021.

Piotrowski AP. Review of differential evolution population size. *Swarm and Evolutionary Computation*, 32:1–24, 2017.

Pottier T, Toussaint F, Vacher P. Contribution of heterogeneous strain field measurements and boundary conditions modelling in inverse identification of material parameters. *European Journal of Mechanics - A/Solids*, 30(3):373–382, 2011.

Pottier T, Vacher P, Toussaint F, Louche H, Coudert T. Out-of-plane testing procedure for inverse identification purpose: application in sheet metal plasticity. *Experimental Mechanics*, 52(7):951–963, 2012.

Pradeau A, Thuillier S, Yoon JW. Prediction of failure in bending of an aluminium sheet alloy. *International Journal of Mechanical Sciences*, 119:23–35, 2016.

Prager W. The theory of plasticity: A survey of recent achievements. *Proceedings of the Institution of Mechanical Engineers*, 169(1):41–57, 1955.

Prates PA, Oliveira MC, Fernandes JV. A new strategy for the simultaneous identification of constitutive laws parameters of metal sheets using a single test. *Computational Materials Science*, 85:102–120, 2014.

Prates PA, Pereira AFG, Sakharova NA, Oliveira MC, Fernandes JV. Inverse strategies for identifying the parameters of constitutive laws of metal sheets. *Advances in Materials Science and Engineering*, 2016:e4152963, 2016.

Reis LC, Prates PA, Oliveira MC, Santos AD, Fernandes JV. Inverse identification of the Swift law parameters using the bulge test. *International Journal of Material Forming*, 10(4):493–513, 2017.

Reu P. Stereo-rig design: Stereo-angle selection – Part 4. *Experimental Techniques*, 37(2):1–2, 2013.

Reyne B, Barlat F. A new concept for continuum distortional plasticity. *International Journal of Plasticity*, 155:103303, 2022.

Robert L, Velay V, Decultot N, Ramde S. Identification of hardening parameters using finite element models and full-field measurements: Some case studies. *The Journal of Strain Analysis for Engineering Design*, 47(1):3–17, 2012.

Rossi M, Pierron F. Identification of plastic constitutive parameters at large deformations from three dimensional displacement fields. *Computational Mechanics*, 49(1):53–71, 2012.

Rossi M, Pierron F. Identification of the plastic behaviour in the post-necking regime using a three dimensional reconstruction technique. *Key Engineering Materials*, 504-506:703–708, 2012.

Rossi M, Chiappini G, Sasso M. Characterization of aluminum alloys using a 3D full field measurement. In: Proulx T (Ed.). *Application of Imaging Techniques to Mechanics of Materials and Structures*, Volume 4. Conference Proceedings of the Society for Experimental Mechanics Series, Springer, New York, NY, USA, 2013.

Rossi M, Lava P, Pierron F, Debruyne D, Sasso M. Effect of DIC spatial resolution, noise and interpolation error on identification results with the VFM. *Strain*, 51(3):206–222, 2015.

Rossi M, Badaloni M, Lava P, Debruyne D, Pierron F. A procedure for specimen optimization applied to material testing in plasticity with the virtual fields method. *AIP Conference Proceedings*, 1769:200016, 2016.

Rossi M, Pierron F, Štamborská M. Application of the virtual fields method to large strain anisotropic plasticity. *International Journal of Solids and Structures*, 97–98:322–335, 2016.

Rossi M, Lattanzi A, Barlat F. A general linear method to evaluate the hardening behaviour of metals at large strain with full-field measurements. *Strain*, 54(3):12265, 2018.

Rossi M, Cortese L, Genovese K, Lattanzi A, Nalli F, Pierron F. Evaluation of volume deformation from surface DIC measurement. *Experimental Mechanics*, 58(7):1181–1194, 2018.

Rossi M, Lattanzi A, Cortese L, Amodio D. An approximated computational method for fast stress reconstruction in large strain plasticity. *International Journal for Numerical Methods in Engineering*, 121(14):3048–3065, 2020.

Rossi M, Lattanzi A, Morichelli L. Integrated thermomechanical characterization of metals using the virtual fields method. *Key Engineering Materials*, 926:2222–2227, 2022.

Rossi M, Lattanzi A, Morichelli L, Martins JMP, Thuillier S, Andrade-Campos A, Coppieters S. Testing methodologies for the calibration of advanced plasticity models for sheet metals: A review. *Strain*, —:e12426, 2022.

Rusinek A, Klepaczko JR. Shear testing of a sheet steel at wide range of strain rates and a constitutive relation with strain-rate and temperature dependence of the flow stress. *International Journal of Plasticity*, 17(1):87–115, 2001.

Schmaltz S, Willner K. Comparison of different biaxial tests for the inverse identification of sheet steel material parameters. *Strain*, 50(5):389–403, 2014.

SciPy. *minimize(method='Nelder-Mead') — SciPy v1.9.2 Manual*. docs.scipy.org, https://docs.scipy.org/doc/scipy-1.9.2/reference/optimize.minimize-neldermead.html, 2022.

SciPy. *Optimization and root finding (scipy.optimize) — SciPy v1.9.2 Manual*. docs.scipy.org, https://docs.scipy.org/doc/scipy/reference/optimize.html, 2022.

SciPy. *scipy.optimize.differential_evolution — SciPy v1.9.2 Manual*. docs.scipy.org, https://docs.scipy.org/doc/scipy-1.9.2/reference/generated/scipy.optimize.differential_evolution.html#scipy.optimize.differential_evolution, 2022.

SciPy. *scipy.optimize.least_squares — SciPy v1.9.2 Manual*. docs.scipy.org, https://docs.scipy.org/doc/scipy-1.9.2/reference/generated/scipy.optimize.least_squares.html#scipy.optimize.least_squares, 2022.

Souto N. *Computational design of a mechanical test for material characterization by inverse analysis*. Doctoral Thesis, Universidade de Aveiro, 2015.

Souto N, Thuillier S, Andrade-Campos A. Design of an indicator to characterize and classify mechanical tests for sheet metals. *International Journal of Mechanical Sciences*, 101–102:252–271, 2015.

Souto N, Andrade-Campos A, Thuillier S. Material parameter identification within an integrated methodology considering anisotropy, hardening and rupture. *Journal of Materials Processing Technology*, 220:157–172, 2015.

Souto N, Andrade-Campos A, Thuillier S. A numerical methodology to design heterogeneous mechanical tests. *International Journal of Mechanical Sciences*, 107:264–276, 2016.

Souto N, Andrade-Campos A, Thuillier S. Mechanical design of a heterogeneous test for material parameters identification. *International Journal of Material Forming*, 10(3):353–367, 2017.

Storn R, Price K. Differential evolution – A simple and efficient heuristic for global optimization over continuous spaces. *Journal of Global Optimization*, 11(4):341–359, 1997.

Sutton MA, Orteu JJ, Schreier H. *Image Correlation for Shape, Motion and Deformation Measurements: Basic Concepts, Theory and Applications*. Springer, New York, NY, USA, 2009.

Takizawa H, Oide K, Suzuki K, Yamanashi T, Inoue T, Ida T, Nagai T, Kuwabara T. Development of the user subroutine library "Unified Material Model Driver for Plasticity (UMMDp)" for various anisotropic yield functions. *Journal of Physics: Conference Series*, 1063:012099, 2018.

Tao H, Zhang N, Tong W. An iterative procedure for determining effective stress–strain curves of sheet metals. *International Journal of Mechanics and Materials in Design*, 5(1):13–27, 2009.

Tardif N, Kyriakides S. Determination of anisotropy and material hardening for aluminum sheet metal. *International Journal of Solids and Structures*, 49(25):3496–3506, 2012.

Teaca M, Charpentier I, Martiny M, Ferron G. Identification of sheet metal plastic anisotropy using heterogeneous biaxial tensile tests. *International Journal of Mechanical Sciences*, 52(4):572–580, 2010.

Thoby JD, Fourest T, Langrand B, Notta-Cuvier D, Markiewicz E. Robustness of specimen design criteria for identification of anisotropic mechanical behaviour from heterogeneous mechanical fields. *Computational Materials Science*, 207:111260, 2022.

Thuillier S, Manach PY, Menezes LF. Occurence of strain path changes in a two-stage deep drawing process. *Journal of Materials Processing Technology*, 210(2):226–232, 2010.

Thuillier S, Pham CH, Manach PY. 2D springback and twisting after drawing of copper alloy sheets. *Journal of Physics: Conference Series*, 1063:012124, 2018.

Tong W, Zhang N. An experimental investigation of necking in thin sheets. *Proceedings of the ASME 2001 International Mechanical Engineering Congress and Exposition*, New York, NY, USA, 11-16 November, 2001.

Tu T, Ren X, He J, Zhang Z. Stress–strain curves of metallic materials and post-necking strain hardening characterization: A review. *Fatigue & Fracture of Engineering Materials & Structures*, 43(1):3–19, 2020.

Tvergaard V. Necking in tensile bars with rectangular cross-section. *Computer Methods in Applied Mechanics and Engineering*, 103:273–290, 1993.

van den Boogaard AH. *Thermally enhanced forming of aluminium sheet*. Doctoral Thesis, Universiteit Twente, 2002.

Vegter H, van den Boogaard AH. A plane stress yield function for anisotropic sheet material by interpolation of biaxial stress states. *International Journal of Plasticity*, 22(3):557–580, 2006.

Vincze G, Rauch EF, Gracio JJ, Barlat F, Lopes AB. A comparison of the mechanical behaviour of an AA1050 and a low carbon steel deformed upon strain reversal. *Acta Materialia*, 53(4):1005–1013, 2005.

Virtanen P et al. SciPy 1.0: Fundamental algorithms for scientific computing in Python. *Nature Methods*, 17(3):261–272, 2020.

von Mises R. Mechanik der festen Körper im plastisch-deformablen Zustand. *Nachrichten von der Gesellschaft der Wissenschaften zu Göttingen, Mathematisch-Physikalische Klasse*, 4:582–592, 1913.

Wang Z, Zang S, Chu X, Zhang S, Lionel L. Identification of 7B04 aluminum alloy anisotropy yield criteria with conventional test and Pottier test at elevated temperature. *Results in Physics*, 15:102655, 2019.

Yoon JW, Barlat F, Dick RE, Karabin ME. Prediction of six or eight ears in a drawn cup based on a new anisotropic yield function. *International Journal of Plasticity*, 22(1):174–193, 2006.

Yoshida F, Uemori T. A model of large-strain cyclic plasticity describing the Bauschinger effect and workhardening stagnation. *International Journal of Plasticity*, 18(5):661–686, 2002.

Yu Y, Wan M, Wu XD, Zhou XB. Design of a cruciform biaxial tensile specimen for limit strain analysis by FEM. *Journal of Materials Processing Technology*, 123(1):67–70, 2002.

Zhang R, Shao Z, Lin J. A review on modelling techniques for formability prediction of sheet metal forming. *International Journal of Lightweight Materials and Manufacture*, 1(3):115–125, 2018.

Zhang S, Léotoing L, Guines D, Thuillier S. Potential of the cross biaxial test for anisotropy characterization based on heterogeneous strain field. *Experimental Mechanics*, 55(5):817–835, 2015.

Zhang Y, Gothivarekar S, Conde M, de Velde AV, Paermentier B, Andrade-Campos A, Coppieters S. Enhancing the information-richness of sheet metal specimens for inverse identification of plastic anisotropy through strain fields. *International Journal of Mechanical Sciences*, 214:106891, 2022.

Zhang Y, Van Bael A, Andrade-Campos A, Coppieters S. Parameter identifiability analysis: Mitigating the non-uniqueness issue in the inverse identification of an anisotropic yield function. *International Journal of Solids and Structures*, 243:111543, 2022.

Zhang ZL, Hauge M, Ødegård J, Thaulow C. Determining material true stress–strain curve from tensile specimens with rectangular cross-section. *International Journal of Solids and Structures*, 36(23):3497–3516, 1999.

Zidane I, Guines D, Léotoing L, Ragneau E. Development of an in-plane biaxial test for forming limit curve (FLC) characterization of metallic sheets. *Measurement Science and Technology*, 21(5):055701, 2010.

Ziegler H. A modification of Prager's hardening rule. *Quarterly of Applied Mathematics*, 17(1):55–65, 1959.